

VRIJE UNIVERSITEIT

Signatures of gluon saturation in high energy scattering

ACADEMISCH PROEFSCHRIFT

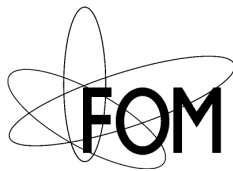
ter verkrijging van de graad Doctor aan
de Vrije Universiteit Amsterdam,
op gezag van de rector magnificus
prof.dr. L.M. Bouter,
in het openbaar te verdedigen
ten overstaan van de promotiecommissie
van de faculteit der Exacte Wetenschappen
op woensdag 17 juni 2009 om 10.45 uur
in de aula van de universiteit,
De Boelelaan 1105

door

Erik Wessels

geboren te Assen

promotor: prof.dr. P.J.G. Mulders
copromotor: dr. D. Boer



The work described in this thesis was carried out at the 'Vrije Universiteit Amsterdam' and is part of the research program of the 'Stichting voor Fundamenteel Onderzoek der Materie' (FOM), which is financially supported by the 'Nederlandse Organisatie voor Wetenschappelijk Onderzoek' (NWO).

This thesis is partly based on the following publications:

The Saturation scale and its x -dependence from Lambda polarization studies.

Daniël Boer, Andre Utermann and Erik Wessels

Phys. Lett. **B671**, 91 (2009)

Geometric Scaling at RHIC and LHC.

Daniël Boer, Andre Utermann and Erik Wessels

Proceedings of 14th High-Energy Physics International Conference in Quantum Chromodynamics (QCD 08), Montpellier, France, 7-12 Jul 2008.

Nucl. Phys. **B (Proc. Suppl.)** 186, 90 (2009), arXiv:0810.0113 [hep-ph]

Geometric Scaling at RHIC and LHC.

Daniël Boer, Andre Utermann and Erik Wessels

Phys. Rev. **D77**, 054014 (2008)

Investigating the extended geometric scaling region at LHC with polarized and unpolarized final states.

Daniël Boer, Andre Utermann and Erik Wessels

Proceedings of Workshop on Heavy Ion Collisions at the LHC: Last Call for Predictions, Geneva, Switzerland, 14 May - 8 Jun 2007.

J. Phys. **G35**, 054001 (2008), arXiv:0711.0974 [hep-ph]

x -Evolution of Phenomenological Dipole Cross Sections.

Daniël Boer, Andre Utermann and Erik Wessels

Proceedings of 15th International Workshop on Deep-Inelastic Scattering and Related Subjects (DIS2007), Munich, Germany, 16-20 Apr 2007.

Published in 'Munich 2007, Deep-inelastic scattering' 413

arXiv:0706.1666 [hep-ph]

Compatibility of phenomenological dipole cross sections with the Balitsky-Kovchegov equation.

Daniël Boer, Andre Utermann and Erik Wessels

Phys. Rev. **D75**, 094022 (2007)

Contents

1	Introduction	1
2	QCD at high energy	5
2.1	Definition of QCD	5
2.2	The running coupling	6
2.3	Deep inelastic scattering	9
2.3.1	DIS in terms of structure functions	10
2.3.2	Parton distribution functions	11
2.4	Small- x evolution	15
2.5	The dipole picture	18
2.6	Geometric scaling	21
2.6.1	DIS at small x	21
2.6.2	Nucleon-nucleus scattering at small x	23
2.7	Outline of this thesis	25
3	The colour glass condensate	29
3.1	Scattering off the Weizsäcker-Williams field	30
3.1.1	The Weizsäcker-Williams field	30
3.1.2	Scattering of electrons off the Weizsäcker-Williams field	32
3.2	Scattering off the colour glass condensate	34
3.2.1	The classical colour field	34
3.2.2	Cross-section of a quark-colour glass condensate scattering	36
3.2.3	Evolution in x : the JIMWLK equation	38
3.3	Summary	40
4	BFKL evolution	43
4.1	BFKL equation in the colour dipole formalism	43
4.2	Solution of the BFKL equation and the small- x problem	49
4.3	The small- r_{\perp}^2 limit and the initial condition	51
4.4	Behaviour of the saddle point	53
4.5	The BFKL equation with a saturation boundary condition	55
4.5.1	The saturation scale	55

4.5.2	Geometric scaling window	57
4.6	Summary	58
5	BK evolution	59
5.1	Introduction	59
5.2	The BK equation	60
5.3	Travelling waves	62
5.3.1	The travelling wave approximation	62
5.3.2	Travelling wave at subasymptotic rapidity	64
5.3.3	The role of the initial condition	65
5.4	Summary	66
6	Models for the dipole amplitude	67
6.1	Dipole models for deep inelastic scattering	68
6.1.1	Geometric scaling	68
6.1.2	The GBW model	69
6.1.3	The IIM model	71
6.2	Dipole models for nucleon-nucleus scattering	72
6.2.1	The MV model	74
6.2.2	The KKT model	76
6.2.3	The DHJ model	78
7	Compatibility of phenomenological models with the BK equation	81
7.1	Numerical solution of the BK equation	82
7.2	Anomalous dimension from the numerical solution	84
7.2.1	Anomalous dimension as a function of r	84
7.2.2	Anomalous dimension as a function of k	86
7.2.3	The saturation scale	88
7.2.4	The initial condition	90
7.3	Conclusions	92
8	Compatibility of phenomenological models with RHIC data	95
8.1	Hadron collisions in the dipole formalism	96
8.1.1	DHJ models versus new model	97
8.1.2	Comparison with RHIC data	99
8.1.3	Compatibility with deep inelastic scattering	102
8.2	LHC predictions	104
8.2.1	Hadron production	104
8.2.2	Nuclear modification factor	106
8.2.3	Geometric scaling in jet production	106
8.3	Conclusions	108

9 Polarization of Λ hyperons and the saturation scale	109
9.1 Introduction	110
9.2 Λ polarization in $p + A \rightarrow \Lambda + X$	112
9.3 Gaussian fragmentation functions	114
9.4 Measuring \mathcal{P}_Λ	115
9.5 Transverse Λ polarization in phenomenological dipole models	117
9.6 Transverse Λ polarization results	121
9.7 Conclusions	125
10 Summary	127
A Colour glass condensate	131
A.1 Average of U and $U^\dagger U$	131
A.1.1 $\langle U \rangle_\rho$	131
A.1.2 $\langle U^\dagger U \rangle_\rho$	133
A.2 Scattering off the WW-field	135
A.3 Lagrangian density for CGC	139
B CGC and DGLAP descriptions	143
B.1 Cross section in CGC and DGLAP	143
B.2 Kinematics: average values of x	144
C Definitions of gluon distributions	149
C.1 Unintegrated gluon distributions	149
C.2 Limit of small r_\perp	150
C.3 Relation with the dipole scattering amplitude	150
Samenvatting	153
Dankwoord	157
Bibliography	159

Chapter 1

Introduction

According to present knowledge, matter is built out of elementary particles. Of the four kinds of interaction between these elementary particles, the electromagnetic, weak and strong interactions are described collectively by a quantum gauge theory that is known as the Standard Model. The remaining interaction, gravity, is described independently by the theory of General Relativity. While the unification of gravity with the other interactions is a major current challenge of theoretical physics, gravity is usually negligible in the description of elementary particles.

Matter is arranged in the form of atoms, which consist of electrons shrouding a nucleus that is composed of protons and neutrons. While the composition of the electron cloud of an atom is in principle rather well understood in terms of quantum electrodynamics (QED), i.e. the part of the Standard Model that deals with the electromagnetic interaction, the structure of the nuclei poses a much more difficult problem. The particles that make up nuclei and in general all other hadrons, are the quarks and the gluons. These particles are governed by the part of the Standard Model that describes the strong interaction, quantum chromodynamics (QCD), which is a so-called non abelian gauge theory. As a consequence, the gluons, unlike the photons, can interact with each other directly, making the theory highly non-linear and difficult to solve. The tool of choice for performing calculations is perturbation theory. This means that the desired quantity is expanded as a power series in terms of a small parameter, for which one uses the coupling constant. While in QED, the coupling constant, the fine structure constant $\alpha_{\text{em}} \approx 1/137$, increases with energy, in practice it is small enough for the application of such a technique. In QCD however, the coupling constant *decreases* with energy—one can also say that it decreases as smaller distances are considered—and turns out to be too large on the length scale of hadrons to use perturbation theory. Hence, one cannot calculate the exact composition of hadrons in terms of quarks and gluons from first principles using analytic techniques.

The structure of hadrons on very small length scales can however be analysed using perturbation theory, since in this case the coupling constant is small. This may be the case in high energy scattering. In deep inelastic scattering (DIS) for instance, an electron and a proton are accelerated to high energy and made to collide, which means that the

electron interacts with the proton predominantly by the exchange of a virtual photon. If the mass of the virtual photon is Q^2 , the spatial resolution at which the proton is probed is roughly given by $1/Q^2$. If Q^2 is large, the results can be well understood in terms of the photon scattering off a single quark or gluon inside the proton. Hence, the virtual photon probes the density of quarks and gluons inside the proton. Since before the formulation of QCD, the constituent particles of hadrons received the name partons, these densities are known as parton distribution functions. They depend not only on Q^2 , but also on the longitudinal momentum fraction x of the proton that is carried by the struck parton. Since perturbation theory does not allow a direct computation of the parton distribution functions, they must be taken from experiments. However, it is possible to calculate the Q^2 dependence of the distribution functions perturbatively in QCD, which leads to the so-called DGLAP equations. This perturbative QCD picture of high energy scattering provides a very successful description of experimental results. However, in spite of this success, there may be a kinematic region at high energy in which this picture breaks down.

The parton distribution functions depend not only on Q^2 , but also on the longitudinal momentum fraction x of the probed parton. If the centre of mass energy, which is usually denoted with \sqrt{s} , of the scattering process increases, the momentum fraction of the probed partons decreases. In DIS, the momentum fraction x that is probed scales like $x \sim Q^2/(Q^2 + s)$. Apart from the non-perturbative region, at high energy we can distinguish two kinematic regions. In the so-called Bjorken limit of fixed x and $Q^2 \rightarrow \infty$, the proton is described as a collection of free partons, since the strong coupling constant vanishes—the parton distribution function then depend on x only. At finite values of Q^2 , the parton picture remains valid, the Q^2 dependence of the parton distribution function being described by the DGLAP equations. Another possible limit is the small- x limit, or high energy limit, in which $\sqrt{s} \rightarrow \infty$ so that $x \rightarrow 0$. In this limit, the x dependence of the gluon distribution function is thought to be described by the so-called BFKL equation, which predicts that if x becomes very small, the gluon density rises so fast that it will eventually violate unitarity of the scattering amplitude. Hence, it is expected that by some mechanism that is not described by the BFKL equation, the fast rise of the gluon density is tempered, so that the density saturates as $x \rightarrow 0$. Physically, one imagines that the gluons start to overlap, so that their mutual interactions slow down the rise of the density. This leads to a new picture of a scattering experiment at such small values of x that high densities are probed. Instead of scattering of a single parton, i.e. a gluon, due to the very high density of gluons we have to consider scattering off many gluons. In DIS, the corresponding picture is known as the dipole picture. In this picture, the virtual photon fluctuates into a quark-antiquark pair, colour dipole, that interacts with the proton through multiple scattering. The scattering of the dipole off the proton is described by the so-called dipole scattering amplitude. In this picture, saturation of the gluon density means saturation of the dipole amplitude.

Scattering of a nucleon off a nucleus can also be described in terms of the dipole scattering amplitude. In the perturbative picture, a parton from the nucleon scatters off a parton, i.e. a gluon if small values of x are probed, from the nucleus. If the gluon density in the nucleus becomes large, one has to take into account scattering off more than one gluon. At very small values of x , the gluon content of the nucleus can be described as

a classical colour field that is known as a colour glass condensate. The scattering off a parton from the nucleon off this colour field turns out to be described by the same dipole amplitude that is used in DIS.

Since high energy scattering can be described in the dipole picture, gluon saturation can be formulated in terms of saturation of the dipole scattering amplitude. The linear BFKL equation, which predicts a too strong growth of the dipole amplitude, is expected to be supplanted by a non-linear equation, such as the so-called BK equation, of which the non-linear term can account for saturation. In this thesis, we will investigate theoretical approaches to saturation of the dipole amplitude, with an emphasis on the BK equation. In the dipole picture of high energy scattering, we derive an expression for the dipole scattering amplitude, known as the MV model, in the colour glass condensate formalism. Turning to the x -evolution of the dipole amplitude, we give a derivation of the BFKL equation. Further, we show how it leads to a rapid rise of the gluon density, and introduce the non-linear BK equation as a possible replacement. In the absence of analytic solutions of the BK equation, we discuss a number of phenomenological models that incorporate features that arise from small- x evolution. Using numerical solutions of the BK equation, we investigate to what extent these properties actually arise from BK evolution. We identify a number of experimental signatures that result from the small- x features of the dipole models, and use these to study whether saturation may be observed in data from high energy scattering experiments. We will see that present data is inconclusive. Contrarily, at the new Large Hadron Collider (LHC) protons and lead nuclei are accelerated to much higher energies than previously available. We present theoretical analyses showing that LHC is able to probe values of x that are expected to be small enough for small- x effects to be resolved, so that LHC offers the first possibility of experimental tests of saturation.

Chapter 2

QCD at high energy

2.1 Definition of QCD

The quantum field theory that describes the strong interaction among quarks is known as quantum chromodynamics, or QCD. Formally, it is a Yang-Mills theory [1] with the gauge group $SU(3)$ describing the interactions between colour charged fields, in which each flavour of quarks transforms according to the fundamental representation of the gauge group. The lagrangian density of QCD can be written as¹

$$\mathcal{L}_{\text{QCD}} = -\frac{1}{4}F_{\mu\nu}^a F_a^{\mu\nu} + \sum_f \bar{q}_f (i\gamma_\mu D^\mu - m_f) q_f, \quad (2.1)$$

where the sum runs over all quark flavours. The covariant derivative is given by $D_\mu = \partial_\mu - ig t^a A_\mu^a$, where the coupling constant g sets the strength of the interactions between the quark field q and the gauge field A_μ^a . The t -matrices are the generators of the gauge group in the fundamental representation, since D acts on the quark fields. The t 's are normalized as follows,

$$\text{tr } t^a t^b = \delta^{ab} / 2 \quad (2.2)$$

leading to the properties

$$(t^a t^a)_{bc} = C_F \delta_{bc}; \quad C_F = \frac{N^2 - 1}{2N}. \quad (2.3)$$

The field strength tensor of the gauge field A_μ^a , the quanta of which are called gluons, is defined as

$$F_{\mu\nu}^a = \partial_\mu A_\nu^a - \partial_\nu A_\mu^a - g f^{abc} A_\mu^b A_\nu^c, \quad (2.4)$$

¹We ignore additional gauge fixing and ghost terms that are introduced in order to quantize the theory [2, 3].

2.2. The running coupling

where f denotes the structure constants of the Lie algebra of the gauge group, i.e. $[t^a, t^b] = if^{abc}t^c$. The structure constants themselves define a representation of the group, the adjoint representation, which is constructed as follows: $(T^a)_{bc} = -if^{abc}$. Its normalization is given by

$$\text{tr}T^aT^b = f^{acd}f^{bdc} = C_A\delta^{ab}; \quad C_A = N \quad (2.5)$$

where for $SU(3)$ $C_F = 4/3$ and $C_A = 3$.

We see that the non-abelian term in F , which is proportional to the coupling constant g , will give rise to self couplings of the gauge fields, which means that the gluons themselves carry colour charge, like the quarks. A crucial symmetry of the lagrangian density (2.1), which is one of the properties that ensures the renormalizability of the quantized theory, is gauge invariance. The theory is invariant under local transformations generated by the gauge group,

$$\begin{aligned} q(x) &\rightarrow U(x)q(x) \\ A_\mu &\equiv t^a A_\mu^a \rightarrow U(x)A_\mu U^{-1}(x) - \frac{i}{g}(\partial_\mu U(x))U^{-1}(x) \\ F_{\mu\nu} &\equiv t^a F_{\mu\nu}^a \rightarrow U(x)F_{\mu\nu}U^{-1}(x) \end{aligned} \quad (2.6)$$

where the operator $U(x) = \exp(i\lambda^a(x)t^a)$ describes a rotation in the group space, characterized by the parameters $\lambda^a(x)$, where a runs from 1 to the number of generators—i.e. $N^2 - 1$ in the case of $SU(N)$. The transformation is local since $\lambda^a(x)$ depends on the space-time co-ordinate x , i.e. a different transformation can be performed in every point. On the classical level, the lagrangian density (2.1) gives rise to Euler-Lagrange equations of motion, usually referred to as the Yang-Mills equations,

$$[D_\mu, F_a^{\mu\nu}] = J_a^\nu \quad (2.7)$$

where J denotes the current $J_\mu^a = \bar{q}\gamma_\mu t^a q$. We will use this equation in chapter 3 to describe the gluon field of an ultrarelativistic nucleus, which can be treated classically due to its large gluonic occupation numbers.

2.2 The running coupling

The QCD lagrangian (2.1) describes the interactions among the colour charged quarks and gluons. We know however that no bare colour charge has ever been seen in nature, instead only composite states appear that are colour neutral; the hadrons. This phenomenon is called confinement, expressing the phenomenological fact that colour charge is confined to spatial regions of roughly the size of hadrons. This is caused by the theory being strongly coupled at the length scale of the hadrons. Conversely, at very small length scales, the coupling becomes increasingly weaker, and vanishes at asymptotically small length scales—or asymptotically large energy scales. This counterpart of confinement is known as asymptotic freedom [4–6]. In this section we will sketch the scale dependence of the coupling constant of QCD.

Classically, QCD is a scale invariant theory, since there is no fundamental parameter to set any scale. Hence, confinement and asymptotic freedom could never emerge. However, subjecting the theory to quantization automatically produces a scale dependence. Consequently, at small length scales quantum corrections to the classical theory occur, which become more important as one goes to smaller scales. Asymptotic freedom and to a certain extent also confinement can be understood in terms of such a quantum effect: the so-called running of the coupling. Running of the coupling in QCD means that the coupling is large at low energies and becomes small at high energies. Technically, this running of the coupling is derived from renormalization.

Renormalization is the way of dealing with ultraviolet divergences that appear in perturbation theory due to quantization of the theory defined by the lagrangian density (2.1). At any given order in perturbation theory, the terms in the expansion can be expressed diagrammatically as Feynman diagrams, which represent momentum integrals. These can yield infinities because there is no restriction on the momenta of virtual particles. Renormalization amounts to subtracting the infinities at an arbitrary energy scale, the so-called renormalization scale, μ say, by a redefinition of the parameters of the theory, so that the theory is rendered finite. Going to higher orders in perturbation theory, more loop diagrams appear causing ever more infinities. Even so, for Yang-Mills gauge theories such as QCD, renormalizability to all orders in the coupling is guaranteed [3, 7, 8]. Of course, as the renormalization scale μ is arbitrary, all observables of the theory must be independent of μ . This requirement leads to the effective coupling that we use in the renormalized perturbation theory acquiring a dependence on the scale μ . The requirement that the theory be independent of μ translates into the following differential equation for the effective coupling $\alpha_s(\mu)$,

$$\mu^2 \frac{\partial \alpha_s}{\partial \mu^2} = \beta(\alpha_s). \quad (2.8)$$

This is known as a renormalization group equation. The behaviour of the coupling is contained in the well known β function, which to one loop order is given by

$$\beta(\alpha_s) = \frac{\alpha_s}{12\pi} (2n_f - 11N) \equiv -b\alpha_s, \quad (2.9)$$

where n_f is the number of flavours, and $N = 3$ is the number of colours. The renormalization group equation (2.8) is readily solved, giving

$$\alpha_s(\mu) = \frac{\alpha_s(\mu_0)}{1 + \alpha_s(\mu_0)b \ln \mu^2 / \mu_0^2}, \quad (2.10)$$

where μ_0 is a constant of integration, which has dimensions of energy. In principle, μ and μ_0 are arbitrary scales, which have no physical interpretation. Usually though, one identifies μ_0 with the energy scale of some scattering process, so that $\alpha_s(\mu_0)$ can be fixed using experimental data. The theory then has predictive power at other energies, at which the value of $\alpha(\mu)$ can be obtained from Eq. (2.10). Further, it is common to introduce the scale Λ , or Λ_{QCD} , instead of μ_0 . One can write

$$\ln \Lambda^2 = \ln \mu_0^2 - \frac{1}{\alpha_s(\mu_0)b}, \quad (2.11)$$

2.2. The running coupling

so that the running coupling can be expressed in terms of only a single unknown parameter, which is of course the new scale Λ ,

$$\alpha_s(\mu) = \frac{1}{b \ln \mu^2 / \Lambda^2}. \quad (2.12)$$

Clearly, the coupling becomes smaller as the energy scale increases, asymptotically approaching zero. This behaviour is illustrated in Fig. 2.1. Thus, the running of α_s provides an explanation of asymptotic freedom. At larger distance scales, at lower energy, the coupling grows, and the concept of confinement appears on the horizon. At the scale Λ , sometimes called the QCD scale, the coupling would diverge, so that Λ is thought of as a measure for the energy scale at which perturbation theory can definitely not be used anymore. Its value, which needs to be extracted from experiment, lies around $\Lambda \approx 200$ GeV. In fact, there are infinitely many possible definitions of Λ , corresponding to different orders in perturbation theory, the choice of factorization scheme and so on. Of course, we cannot actually use Eq. (2.12) at low energies of the order of Λ where the coupling becomes large, i.e. of order 1, since it is a perturbative result.

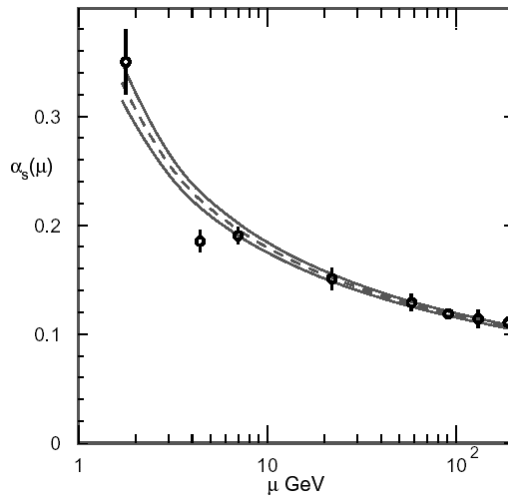


Figure 2.1: The scale dependence of α_s . Plot taken from the particle data group.

Due to confinement, the structure of hadrons cannot be calculated using perturbation theory. Instead, the quark and gluon content of hadrons are parameterized by distribution functions, also known as parton density functions, that are obtained from experiment. Assuming universality of these functions, one can use them to make predictions for other experiments. We will introduce the concept of distribution functions in the context of deep inelastic scattering, which is a process that we will encounter several times in this thesis.

2.3 Deep inelastic scattering

The cleanest way of probing the structure of hadrons is by using an itself structureless probe, like a lepton. The interaction between the lepton and the hadron takes place by the exchange of a virtual photon², which scatters off a constituent of the hadron. If we define the momentum that is transferred from the lepton to the hadron by the virtual photon as Q , the structure of the hadron is probed with a spatial resolution of roughly the De Broglie wavelength of the virtual photon $\lambda \sim 1/Q$. Hence, to resolve the structure of the hadron, a large momentum transfer is required. If the momentum transfer is large, there is a large possibility that the original hadron breaks up into some new hadronic final state, X . The resulting process $e + h \rightarrow e + X$ is called deep inelastic scattering (DIS)—inclusive DIS when this hadronic final state remains undetected, or semi-inclusive or exclusive DIS when respectively some produced hadrons or all final state particles are detected. We will from here on assume that the target hadron is a proton.

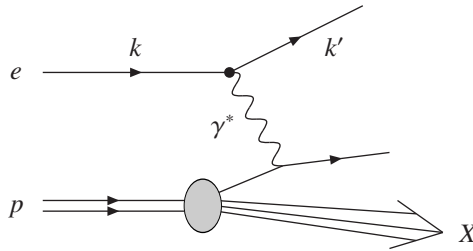


Figure 2.2: Lowest order description of DIS. The lepton (k) interacts with the proton (p) through the exchange of a virtual photon (q).

The DIS process is depicted in Fig.2.2. The momentum of the proton is denoted with p , the lepton momentum with k while k' is the lepton momentum after the emission of the virtual photon, whose momentum is $q = k - k'$. The cross section of the process can depend on the following Lorentz invariant kinematic variables,

$$\begin{aligned}
 Q^2 &= -q^2 \\
 M^2 &= p^2 \\
 \nu &= p \cdot q = M(E' - E) \\
 x_B &= \frac{Q^2}{2\nu} = \frac{Q^2}{2M(E' - E)} \\
 y &= \frac{q \cdot p}{k \cdot p} = 1 - E'/E
 \end{aligned} \tag{2.13}$$

where M is the mass of the proton, and E and E' are given in the rest frame of the proton as $k^0 = E$ and $k'^0 = E'$. The mass of the virtual photon Q^2 is known as the virtuality of the

²Also, a weak gauge boson can be exchanged, especially in neutrino-hadron scattering.

2.3. Deep inelastic scattering

photon, which sets the hard scale at which the proton is probed. The invariant x_B is known as the Bjorken variable. It scales at high centre of mass energy $s \gg Q^2$ as $x_B \sim Q^2/s$. The energy transfer from the lepton to the proton is given by ν . The fraction of the lepton's total energy that this energy transfer ν represents is given by y .

2.3.1 DIS in terms of structure functions

The cross section of the lepton scattering off the proton can be separated in a leptonic part that describes the radiation of the virtual photon by the lepton, and a hadronic part that describes the interaction of the virtual photon with the proton,

$$\frac{d\sigma}{dx_B dy} \propto L_{\mu\nu} W^{\mu\nu}. \quad (2.14)$$

Whereas the leptonic tensor L can be calculated perturbatively in QED, the hadronic tensor W cannot, since it comprises the non-perturbative structure of the proton. However, for scattering off an unpolarized proton its most general Lorentz structure can be parameterized as

$$W^{\mu\nu}(p, q) = \left(g^{\mu\nu} - \frac{q^\mu q^\nu}{q^2} \right) W_1(x_B, Q^2) + \left(p^\mu + \frac{1}{2x_B} q^\mu \right) \left(p^\nu + \frac{1}{2x_B} q^\nu \right) W_2(x_B, Q^2), \quad (2.15)$$

where the W_i 's are functions that contain the non-perturbative information on the proton structure. Usually, the so-called structure functions F_1 and F_2 are used instead,

$$\begin{aligned} F_1(x_B, Q^2) &= W_1(x_B, Q^2) \\ F_2(x_B, Q^2) &= \nu W_2(x_B, Q^2). \end{aligned} \quad (2.16)$$

In the so-called Bjorken limit, i.e. fixed x_B and $Q^2 \rightarrow \infty$, F_1 and F_2 become independent of Q^2 , and are functions of x_B only. This is known as Bjorken scaling. In terms of F_1 and F_2 the cross section is expressed as

$$\frac{d\sigma}{dx_B dy} = \frac{8\pi\alpha^2 ME}{Q^4} \left[(1 + (1-y)^2) x_B F_1 + (1-y)(F_2 - 2x_B F_1) \right], \quad (2.17)$$

where corrections of higher order in the proton mass M^2/Q^2 have been neglected. The first term corresponds to the absorption of a transversely polarized photon, while the second term corresponds to the absorption of a longitudinally polarized photon. For that reason, the combination of the structure functions that appears in the second term is called F_L ,

$$F_L(x_B, Q^2) = \left(1 + \frac{4M^2 x_B^2}{Q^2} \right) F_2(x_B, Q^2) - 2x_B F_1(x_B, Q^2). \quad (2.18)$$

The structure functions are related to the densities of particles that together make up the proton—these constituent particles are called partons, as the picture of DIS in terms of

the virtual photon scattering off such constituent particles was developed by Feynman in 1969 and given the name parton model [9]. In the parton model, the proton is treated as a collection of free point-like partons. After the formulation of QCD, the partons were identified with the quarks and gluons. Since the proton is probed with a resolution that is given by the photon virtuality $1/Q^2$, the scale of the strong interactions within the proton is set by Q^2 . Hence, the parton model is recovered from QCD in the limit $Q^2 \rightarrow \infty$, or equivalently the zeroth order in α_s , in which the proton consists of free quarks due to asymptotic freedom.

In the Bjorken limit, the longitudinal structure function reduces to $F_L = F_2 - 2x_B F_1$, which is known as the Callan-Gross relation, and turns out to vanish to lowest order. In this limit, only transversely polarized photons can be absorbed by the proton. This has a natural interpretation in terms of the partons. Since in the Bjorken limit the strong coupling constant $\alpha_s(Q^2)$ vanishes, the lepton can only scatter off the (free) quarks that are contained in the proton, which are spin 1/2 particles. Hence, they cannot absorb a longitudinally polarized photon due to helicity conservation.

2.3.2 Parton distribution functions

In the parton model approximation, the proton is composed of a number of free constituents that each carry a fraction x of the proton's total momentum. This so-called longitudinal momentum fraction x must be a number between 0 and 1. In this picture, the lepton-proton cross section is simply given by the cross section of the lepton scattering off one of the constituents times the probability that the proton contains such a constituent,

$$\frac{d\sigma^{lh}}{dx_B dy} = \int_0^1 dx \sum_i q_i(x) \frac{d\sigma^{lq}}{dx dy}. \quad (2.19)$$

Here, the sum runs over all partons, which in the parton model approximation are only the quarks and antiquarks. The probability functions $q(x)$ are known as parton distribution functions, or pdf's. To this order, the struck parton is probed at a momentum fraction that is given by the Bjorken variable, i.e. $x = x_B$ —the partonic cross section to this order contains a factor of $\delta(x - x_B)$. The structure functions are expressed as

$$F_2(x_B) = 2x_B F_1(x_B) = \sum_i e_i^2 x_B q_i(x_B), \quad (2.20)$$

where e_i is the electric charge of the parton q_i . F_L vanishes, as we have seen. The Feynman diagram that corresponds to the parton model description of DIS, the so-called handbag diagram, is given in Fig. 2.3.

Since quarks (and gluons) are not free particles, but have interactions whose strength is characterized by $\alpha_s(Q^2)$, beyond the parton model approximation the pdf's acquire a Q^2 dependence through higher order corrections in $\alpha_s(Q^2)$. Also, the structure function F_L is non-zero in higher orders of α_s . The first order contribution is given by

$$F_L(x_B, Q^2) = \sum_i x_B e_i^2 \frac{\alpha_s}{\pi} \int_{x_B}^1 \frac{dy}{y} \frac{x_B}{y} \left[C_F q_i(y, Q^2) + (1 - x_B/y) g(y, Q^2) \right], \quad (2.21)$$

2.3. Deep inelastic scattering

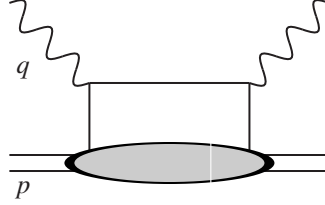


Figure 2.3: The handbag diagram that corresponds to the squared amplitude of DIS in the parton model approximation—QCD at $Q^2 \rightarrow \infty$. The virtual photon interacts with a constituent of the proton, which is represented by a line emerging from the proton.

where $g(y, Q^2)$ denotes the gluon density. As mentioned, the distribution functions, and hence the structure functions³, acquire a dependence on Q^2 at higher orders in α_s . Consider the first order corrections to the process depicted in Fig. 2.3, which are given in Fig. 2.4. The gluon radiation in Fig. 2.4 yields collinear singularities, so called since they

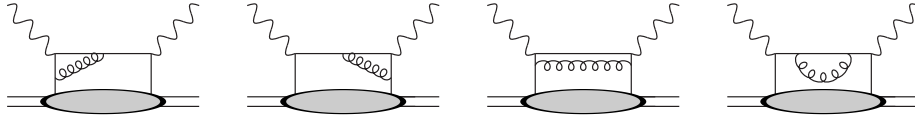


Figure 2.4: First order α_s corrections to the handbag diagram.

arise when a gluon is radiated exactly parallelly with the parent parton, i.e. at zero transverse momentum. Since the probability of gluon emission is proportional to $\alpha_s dk_{\perp}^2/k_{\perp}^2$, one encounters singularities of the form $\alpha_s \ln Q^2/\kappa^2$, where κ is a lower cut off on k_{\perp} . The diagrams in Fig. 2.4 give the following correction to expression (2.20) for the structure function F_2 ,

$$F_2(x_B, Q^2) = \sum_i e_i^2 x_B \int_{x_B}^1 \frac{dy}{y} \left[\delta(1 - x_B/y) + \frac{\alpha_s}{2\pi} \ln \frac{Q^2}{\kappa^2} P_{qq}(x_B/y) \right] q_i(y) \quad (2.22)$$

The function P_{qq} describes the emission of the gluon from the quark in the proton. Since the divergences arise from soft gluon emission, which puts them outside the jurisdiction of perturbation theory, it seems natural to absorb them into the parton distributions. This is called factorization. A so-called factorization scale μ is introduced⁴ so that the ‘renormalized’ parton distributions depend on $\ln Q^2/\mu^2$, and the divergences $\ln \mu^2/\kappa^2$ are absorbed in a ‘bare’ distribution. As an illustration, we can write Eq. (2.22) as

$$F_2(x_B, Q^2) = \sum_i e_i^2 x_B q_i(x_B, Q^2), \quad (2.23)$$

³In fact, the observation of the predicted violation of Bjorken scaling in DIS is seen as one of the most important experimental corroborations of QCD.

⁴There is some freedom in the choice of factorization scheme, like in renormalization, since there is an arbitrariness in the treatment of finite terms.

where

$$q(x_B, Q^2) = q(x) + \frac{\alpha_s}{2\pi} \ln \frac{Q^2}{\kappa^2} P_{qq}(x/y)q(y). \quad (2.24)$$

If we now introduce a factorization scale $\kappa < \mu^2 < Q^2$, we can obviously write

$$q(x_B, \mu^2) = q(x) + \frac{\alpha_s}{2\pi} \ln \frac{\mu^2}{\kappa^2} P_{qq}(x/y)q(y). \quad (2.25)$$

We can now remove the singularity from the ‘renormalized’ density $q(x_B, Q^2)$ by expressing it in the following way,

$$q(x_B, Q^2) = q(x_B, \mu^2) + \frac{\alpha_s}{2\pi} \ln \frac{Q^2}{\mu^2} P_{qq}(x/y)q(x_B, \mu^2), \quad (2.26)$$

where the divergence has been absorbed into $q(x_B, \mu^2)$. This expression is equivalent to Eq. (2.24) to first order in α_s . Since $F_2(x_B, Q^2)$, given in Eq. (2.23), is a measurable quantity it cannot depend on the new scale μ , and hence its derivative with respect to $\ln \mu^2$ must vanish. This gives rise to a ‘renormalization group’ equation that governs the scale dependence of the distribution function. Exploiting the fact that $q(x_B, Q^2)$ depends on Q^2 and μ^2 through $\ln Q^2/\mu^2$ only, we see that because $\partial/\partial \mu^2 q(x_B, Q^2) = -\partial/\partial Q^2 q(x_B, Q^2)$ these equations describe the Q^2 dependence of the parton distributions. Also taking into account the gluon distribution functions leads to the following evolution equations for the Q^2 dependence of the quark (q), gluon (g) and antiquark (\bar{q}) distributions,

$$\begin{aligned} \frac{\partial q(x, Q^2)}{\partial \ln Q^2} &= \frac{\alpha_s}{2\pi} \int_x^1 \frac{dy}{y} \left[P_{qq}(x/y)q(y, Q^2) + P_{qg}(x/y)g(y, Q^2) \right]; \\ \frac{\partial g(x, Q^2)}{\partial \ln Q^2} &= \frac{\alpha_s}{2\pi} \int_x^1 \frac{dy}{y} \left[P_{gq}(x/y)(q(y, Q^2) + \bar{q}(y, Q^2)) + P_{gg}(x/y)g(y, Q^2) \right]; \\ \frac{\partial \bar{q}(x, Q^2)}{\partial \ln Q^2} &= \frac{\alpha_s}{2\pi} \int_x^1 \frac{dy}{y} \left[P_{q\bar{q}}(x/y)\bar{q}(y, Q^2) + P_{qg}(x/y)g(y, Q^2) \right]. \end{aligned} \quad (2.27)$$

These are the Dokshitzer-Gribov-Lipatov-Altarelli-Parisi (DGLAP) equations [10–12]. The P ’s are so-called splitting functions that arise from the various correction diagrams—they describe the various gluon emission and absorption probabilities. Such corrections turn out to have a rather intuitive interpretation. Suppose that a photon with virtuality Q^2 encounters a quark with momentum fraction x . The density of quarks with this momentum fraction x may change due to a quark with momentum fraction $y > x$ radiating off a gluon, thus bringing its momentum fraction down to x , or a gluon that carries a momentum fraction $y > x$ producing a quark-antiquark pair of which the quark has a momentum fraction x . If we denote the probability of the first process with $P_{qq}(x/y)$ and the probability of the second with $P_{qg}(x/y)$, we find exactly Eq. (2.27) for the density of quarks with momentum fraction x . Similarly, the second and third lines of Eq. (2.27) can be interpreted as the gluon and antiquark densities changing due to gluon emission and pair

2.3. Deep inelastic scattering

production. Since the pdf's describe the density of partons that are probed with a spatial resolution $1/Q$, they 'contain' all partons that have transverse momenta that are smaller than Q , but not those with larger transverse momenta, as the latter cannot be resolved. The gluon distribution $g(x, Q^2)$ that is evolved to the scale Q^2 thus contains all gluons that have transverse momenta $k_{\perp}^2 \leq Q^2$, i.e.

$$xg(x, Q^2) \equiv \int^{Q^2} dk_{\perp}^2 \hat{g}(x, k_{\perp}^2), \quad (2.28)$$

where $\hat{g}(x, k_{\perp}^2)$ is known as the unintegrated gluon distribution. The repeated radiation of gluons that is contained in the distribution functions is pictured in Fig. 2.5. Diagrams

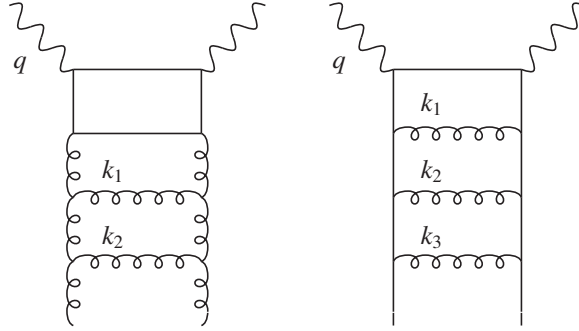


Figure 2.5: Gluon ladder diagrams that are summed into the gluon distribution (left) and the quark distributions (right) by DGLAP evolution.

featuring such consecutive emissions are called ladder diagrams. The dominant contribution to the ladder diagrams in Fig. 2.5 comes from the region of phase space where the transverse momenta of the gluons, i.e. the rungs of the ladder, are strongly ordered; $Q^2 \geq k_{1\perp}^2 \gg k_{2\perp}^2 \gg \dots$. If the transverse momenta are strongly ordered, the diagram yields the leading terms in an $\alpha_s \ln Q^2$ expansion [13]. At large Q^2 these are dominant because every power of α_s is accompanied by the same power of the large logarithm of Q^2 . Instead of considering only terms to some order in the parameter α_s , the perturbation series is restructured in terms of the parameter $\alpha_s \ln Q^2$, which is called ‘‘resummation’’ of the series. Hence, the DGLAP equations are said to resum the perturbation series in terms of $\alpha_s \ln Q^2$.

There exists also a region of phase space where, instead of the transverse momenta, the longitudinal momenta of the radiated gluons are strongly ordered, i.e. $x_1 \gg x_2 \gg \dots$. In this case, the ordering yields the leading terms in a resummation in terms of $\alpha_s \ln 1/x$. Where x becomes so small that $\ln 1/x$ corrections become important with respect to $\ln Q^2$, we enter the region of what is called small- x evolution.

2.4 Small- x evolution

The DGLAP equations describe the evolution with Q^2 of the parton distribution functions. This evolution also changes the behaviour as a function of x . It turns out that as x decreases the gluon density rises especially steeply. This is illustrated in Fig. 2.6, which shows the DGLAP-evolved density of up down and strange quarks as well as the density of gluons in the proton as a function of x , for an arbitrary choice of $Q = 2$ GeV [14]. Apparently, at small x protons consist mainly of gluons.

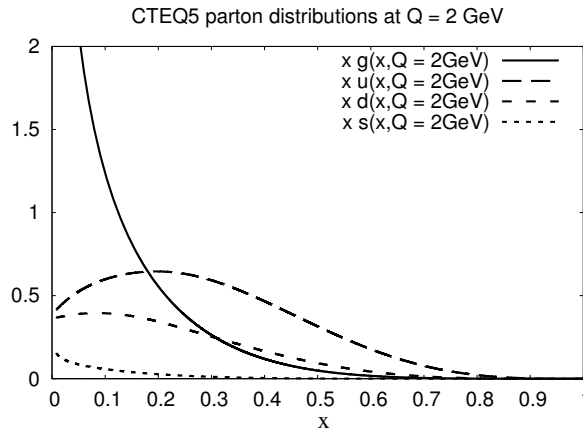


Figure 2.6: Parton distributions of the up, down and strange quarks and the gluon according to the CTEQ5 parameterization [14] at $Q = 2$ GeV. At small values of x the gluon distribution clearly dominates.

Ignoring quark contributions, cf. Fig. 2.6, one can approximate the gluon-to-gluon splitting function P_{gg} at small values of x by $P_{gg} \simeq 6/x$, which simplifies the DGLAP equation (2.27) for $g(x, Q^2)$,

$$\frac{\partial xg(x, Q^2)}{\partial \ln Q^2} = \frac{3}{\pi b} xg(x, Q^2), \quad (2.29)$$

where we have used (2.12). If the initial distribution $xg(x, Q_0^2)$ is slowly varying, a solution can be obtained analytically. The small- x behaviour is then given by [13]

$$xg(x, Q^2) \sim xg(x, Q_0^2) \exp \left[2 \sqrt{\frac{6}{b}} \ln \ln \left(\frac{Q^2}{Q_0^2} \right) \ln \left(\frac{1}{x} \right) \right]. \quad (2.30)$$

This behaviour is recovered by constructing the solution from the summation of gluonic ladders with strong ordering in both transverse momentum and longitudinal momentum fractions. Since it can be shown that this yields the leading logarithms in both Q^2 and

2.4. Small- x evolution

x , this solution is known as the double leading logarithmic approximation (DLA) to the DGLAP equations [15]. In the region where the DLA is applicable, i.e. small x but large Q^2 , we see that the gluon distribution rises quickly with x . However, as we will see, at still smaller values of x with respect to Q^2 , the gluon distribution rises even faster.

As x becomes smaller and smaller, we enter a region where the DGLAP equations lose their applicability. The solutions of the DGLAP equations are valid in a region where the parameter $\alpha_s \ln Q^2$ dominates the perturbation series. However, at sufficiently small x there must be a point where $\alpha_s \ln 1/x$ becomes larger⁵ than $\alpha_s \ln Q^2$, so that one needs to consider evolution driven by the radiation of gluons that are strongly ordered in x . This is achieved by the Balitsky-Fadin-Kuraev-Lipatov (BFKL) equation [17–19], which is the subject of chapter 4. The BFKL equation can be written in terms of the unintegrated gluon density as [20],

$$x \frac{\partial \phi(x, k_\perp^2)}{\partial x} = -\frac{3\alpha_s}{\pi} k_\perp^2 \int_0^\infty \frac{dq_\perp^2}{q_\perp^2} \left[\frac{\phi(x, q_\perp^2) - \phi(x, k_\perp^2)}{|q_\perp^2 - k_\perp^2|} + \frac{\phi(x, k_\perp^2)}{\sqrt{4q_\perp^4 + k_\perp^4}} \right], \quad (2.31)$$

where $\phi(x, k_\perp^2)/k_\perp^2 = \hat{g}(x, k_\perp^2)$, cf. Eq. (2.28). The rise towards small x of the integrated gluon distribution in the DLA limit can be recovered from the BFKL equation⁶. In the pure small- x region the BFKL equation predicts an even steeper rise of the gluon density. As we will see in section 4.2, the BFKL equation can be solved analytically in this region. One finds the following small- x behaviour of $\phi(x, k_\perp^2)$ [20],

$$\phi(x, k_\perp^2) \sim (1/x)^\lambda, \quad (2.32)$$

where $\lambda \approx 0.5$.

The rapid growth of the gluon density following from BFKL evolution leads to theoretical problems. In the DGLAP and BFKL evolution equations, the gluons are treated as independent partons. However, if the gluon density rises fast, the gluons will become so closely packed that they will start interacting. One can estimate the scale at which this will happen in the following way. Since the gluons are probed at a scale Q^2 , their effective transverse size is $1/Q$. At the same time, the cross section depends on the number of gluons $xg(x, Q^2)$, or $Axg(x, Q^2)$ if the target hadron is a nucleus instead of a proton, containing A nucleons. Hence, the transverse area that is occupied by the gluons that are probed at a scale Q^2 is given by $Axg(x, Q^2)/Q^2$. The gluons will then start ‘feeling’ each other if $Axg(x, Q^2)/Q^2$ becomes of the order of the hadron’s transverse area, S_\perp say. For a nuclear target, this transverse area is proportional to $A^{2/3}$, so that we may write $S_\perp = A^{2/3}S_{0\perp}$. Now, as the probability that the gluons interact is proportional to α_s , we can estimate that interactions among the gluons will become important at a scale

$$Q_s^2(x) \sim \alpha_s(Q_s) A^{1/3} \frac{xg(x, Q_s^2)}{S_{0\perp}} \sim A^{1/3} \left(\frac{1}{x}\right)^\lambda, \quad (2.33)$$

⁵A discussion of the energy scale at which this so-called leading logarithmic approximation (in $\alpha_s \ln 1/x$) starts to make sense can be found in Ref. [16].

⁶See section 4.4. The behaviour of xg as a function of x in the DLA limit is recovered from BFKL evolution, but not the Q^2 dependence.

where we have used that according to the BFKL equation $xg(x, Q^2) \sim x^{-\lambda}$ at small x . The scale Q_s is known as the *saturation scale*⁷, since it is expected that the fast rise of the gluon density will be slowed by the gluons interacting with each other⁸.

Saturation of the gluon density is expected not only because the rise of the density makes the gluons overlap. The fast rise of the gluon distribution also leads to inconsistencies with the unitarity of hadronic scattering amplitudes. Like the cross section of DIS (2.19), cross sections of hadronic scattering grow with the density of the partons that are involved in the scattering process. However, from general arguments it follows that in order for the scattering amplitude to be unitary, the total cross section of a hadronic scattering process cannot grow faster than the logarithm squared of the centre of mass energy s ,

$$\sigma_{\text{tot}} \leq \frac{\pi}{m_\pi^2} \ln^2 s/s_0, \quad (2.34)$$

where the pion mass m_π denotes the smallest inverse length scale of the strong force, and s_0 is some unknown scale. The bound (2.34) is known as the Froissart bound⁹ [23, 24]—it is a general result that includes non-perturbative effects, which can be seen from the appearance of m_π . The rise of the gluon density of Eq. (2.32) is such that it must eventually lead to a violation of the Froissart bound. This inconsistency is known as the small- x problem. Hence, it is expected that the gluon density saturates at high energies, or rather, at such small values of x that $Q_s^2(x) > Q^2$. Fig. 2.7 shows the resulting picture of evolution in the x - Q plane. The fact that the BFKL equation does not include any mechanism

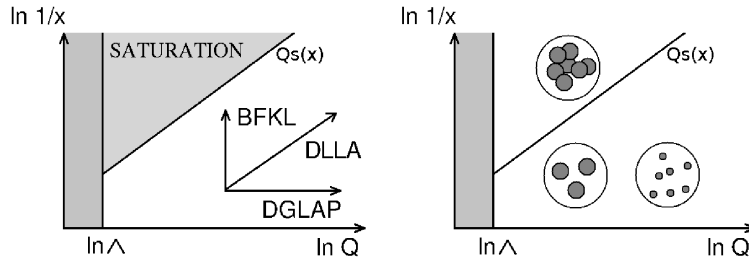


Figure 2.7: Pictorial representation of evolution in x and Q . The resolved partons are represented by circles whose size scales like $1/Q$. At fixed Q , the density increases with $1/x$, while the size of the circles stays the same, leading to saturation when the circles overlap.

that leads to saturation of the gluon density corresponds to the equation being linear in the density. At high energies, where saturation is expected to occur, it should therefore be replaced by a *non-linear* evolution equation, of which the non-linear term accounts for the saturating effect that becomes sizable at large values of the density. The first such equation was proposed by Gribov, Levin and Ryskin (GLR) [25, 26], and describes evolution in Q^2 . It is obtained in the DLA approximation, i.e. it is valid where $\ln 1/x$

⁷The x dependence of x of the saturation scale is derived from the BFKL equation in section 4.5.1.

⁸An alternative view of saturation as arising from instantons is given in Ref. [21].

⁹In Ref. [22] it is observed that also data on the DIS cross section respects the Froissart bound.

2.5. The dipole picture

and $\ln Q^2$ are both important. If the gluon density is small, it reduces to the usual DGLAP equation. Presumably the best known example of a non-linear evolution equation in x that does not assume large Q^2 is the Balitsky-Kovchegov (BK) equation [27–30], which is the subject of chapter 5. The BK equation, which in the weak field limit reduces to the BFKL equation, will play a prominent part in this thesis. As we will see in the next section, the BK equation is not an evolution equation for the unintegrated gluon density.

2.5 The dipole picture

Close to the saturation region, $Q^2 \lesssim Q_s^2$, the gluon density is large and one expects the linear BFKL equation to be supplanted by a non-linear evolution equation. In this regime however, the gluon density starts to lose its meaning. Roughly speaking, the parton density gives the probability of finding a single parton in the target, and consequently, the cross section is given by a convolution of the parton density with the amplitude of the scattering of the probe off such a parton. If however the gluon density is so high that the gluons overlap, scattering off a single gluon becomes unlikely. Instead, one has to consider scattering off multiple gluons, which is not described by the gluon density $xg(x, Q^2)$ anymore. Seen in another way, the (unintegrated) gluon density in a hadronic system is given in terms of the colour field of the hadron by the correlator of two field potentials [31],

$$\hat{g}(x, k_\perp^2) \sim \text{Tr} \langle A(-k_\perp) \cdot A(k_\perp) \rangle. \quad (2.35)$$

If the field becomes strong enough, one needs to take into account also correlators of more than two potentials, so that the description in terms of the ordinary gluon distribution loses its validity.

Hence, at small x , a different description of DIS is needed, that replaces the one based on the scattering of the virtual photon off a single parton from the target. Such a description is provided by the dipole formalism, which was proposed by Mueller in [32]. The corresponding physical picture of DIS is rather intuitive. When the virtual photon probes the hadron at very small x , it probes mainly gluons. Since the photon does not carry colour charge, it does not scatter off the gluon field directly. Instead, it fluctuates into a quark-antiquark pair, a *colour dipole*, that subsequently scatters off the small- x gluon field of the hadron. The gluons are themselves represented by colour dipoles comprising a quark and an antiquark, an approximation which becomes exact in the limit of a large number of colours, $N \rightarrow \infty$. This picture of DIS is depicted to lowest order in Fig. 2.8. The virtual photon fluctuating into a quark-antiquark pair is described by the so-called photon wavefunction ψ , which can be calculated perturbatively in QED. Denoting the cross section of the dipole scattering off the small- x field of the hadron with $\sigma(r_\perp, x)$, the cross section of the scattering process of Fig. 2.8 can be written as (see also [33])

$$\sigma_{T,L}(x_B, Q^2) = \int dz \int d^2 r_\perp |\psi_{T,L}(z, r_\perp, Q^2)|^2 \sigma(r_\perp, x_B), \quad (2.36)$$

for respectively transversely and longitudinally polarized photons. Here, z is the longitudinal momentum fraction of the quark in the dipole, and r_\perp is the size of the dipole in

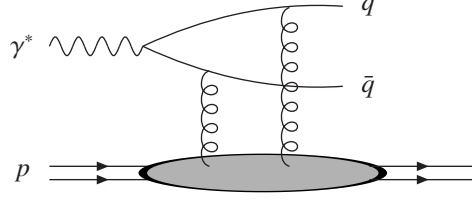


Figure 2.8: DIS in the dipole picture at lowest order.

transverse co-ordinate space. The cross section $\sigma_{T,L}$ is related to the structure functions by (see e.g. [34])

$$F_{T,L}(x_B, Q^2) = \frac{Q^2}{4\pi\alpha_{\text{em}}} \sigma_{T,L}(x_B, Q^2), \quad (2.37)$$

where $F_2 = F_T + F_L$. The dipole cross section itself is given by

$$\sigma(r_{\perp}, x_B) = \sigma_0 N(r_{\perp}, x_B), \quad (2.38)$$

where $N(r_{\perp}, x_B)$ denotes the forward scattering amplitude of the quark-antiquark dipole. Since the dipole scatters off the gluon field of the target, the dipole scattering amplitude is related to the gluon density of the target hadron in a region where the gluon density is still well defined, i.e. for moderate values of r_{\perp} and large x_B . In the case of a nuclear target, rescattering of the dipole off the nucleons of the target then leads to the following relation [35–37],

$$N(r_{\perp}, x_B) = 1 - \exp \left[-\frac{\alpha_s \pi^2}{2NS_{\perp}} r_{\perp}^2 x g_A(x, Q^2 = 1/r_{\perp}^2) \right], \quad (2.39)$$

where $S_{\perp} \sim A^{2/3}$ is the transverse area of the nucleus ‘seen’ by the dipole, and $x g_A \sim A x g$ is the nuclear gluon density¹⁰ at the scale $Q^2 = 1/r_{\perp}^2$. As it generalizes the Glauber model [38] of multiple scattering off a nucleus to QCD, this expression is known as the Glauber-Mueller formula. When r_{\perp}^2 times the density is small (i.e. large Q^2), Eq. (2.39) reduces to [30]

$$N(r_{\perp}, x_B) = \frac{\alpha_s \pi^2}{2NS_{\perp}} r_{\perp}^2 x g_A(x, Q^2 = 1/r_{\perp}^2). \quad (2.40)$$

In the dipole picture, one considers the x evolution of N instead of the gluon density, since the gluon density is ‘contained’ in the dipole amplitude N . It was shown [39] that the dipole amplitude evolves with x according to the following evolution equation,

$$\frac{\partial}{\partial Y} N(r_{10\perp}^2, Y) = N_c \frac{\alpha_s}{\pi} \int \frac{d^2 r_{2\perp}}{2\pi} \frac{r_{10\perp}^2}{r_{20\perp}^2 r_{21\perp}^2} \left[N(r_{21\perp}^2, Y) + N(r_{20\perp}^2, Y) - N(r_{10\perp}^2, Y) \right], \quad (2.41)$$

¹⁰The density in Eq. (2.39) is to be evaluated at an effective value of x , which is not equal to x_B [36].

2.5. The dipole picture

that is equivalent [40] to the BFKL equation (2.31). Here, we use the notation $Y = \ln 1/x$. This equation, known as Mueller's form of the BFKL equation, will be discussed in chapter 4. In the rest frame of the target, it emerges from the emission of gluons that are strongly ordered in their longitudinal momentum fractions by the incoming dipole. If N is described as the probability of finding one such gluon in the dipole convolved with the propagator of a gluon through the target, one obtains Mueller's BFKL equation for N . The corresponding picture of the scattering process is depicted in Fig. 2.9a.

If one takes into account the possibility that more than one gluon from the probe can scatter off the target, the dipole amplitude is defined as the convolution of n dipoles with n propagators, summed over all values of n . One then finds that the dipole amplitude obeys the non-linear BK evolution equation [30, 41], instead of the BFKL equation. As the BK equation arises in this way from the scattering of multiple dipoles off the target instead of the scattering of only a single dipole, it is said to resum so-called fan diagrams, an example of which is given in Fig. 2.9b. Thus, the BK equation describes the evolution of the dipole amplitude, instead of the gluon density. In the DLA, where the density is small enough for Eq. (2.40) to hold, the resummation of fan diagrams reproduces the GLR equation, which is recovered from the BK equation in this limit [30]. Clearly then, in the dipole picture, saturation of the gluon density is equivalent to saturation of the dipole amplitude.

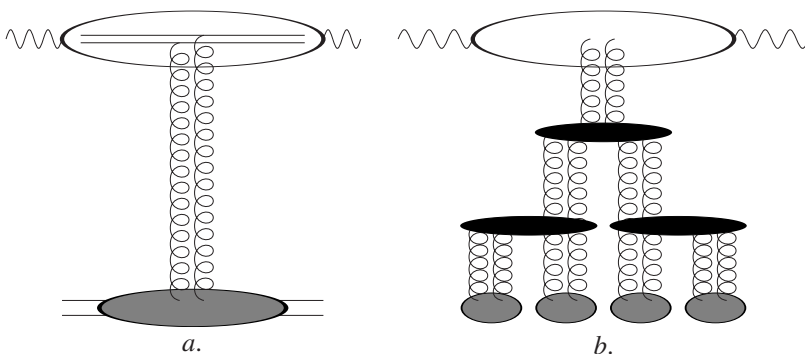


Figure 2.9: Single (a) vs. multiple (b) scattering. The scattering of a single gluon from the dipole leads to linear evolution of the dipole scattering amplitude, described by the BFKL equation. The multiple scattering fan diagram on the right leads to non-linear evolution of the dipole scattering amplitude, described by the BK equation. This picture of evolution replaces the picture of Fig. 2.5 at small x .

As an illustration of how non-linear evolution can lead to saturation, we can write down the BK equation in momentum space, neglecting the dependence on the transverse momenta and keeping only the dependence on x . The kernel is now a constant, and the BK equation reduces to

$$\frac{\partial}{\partial Y} \mathcal{N}(Y) = \chi \left[\mathcal{N}(Y) - \mathcal{N}(Y)^2 \right], \quad (2.42)$$

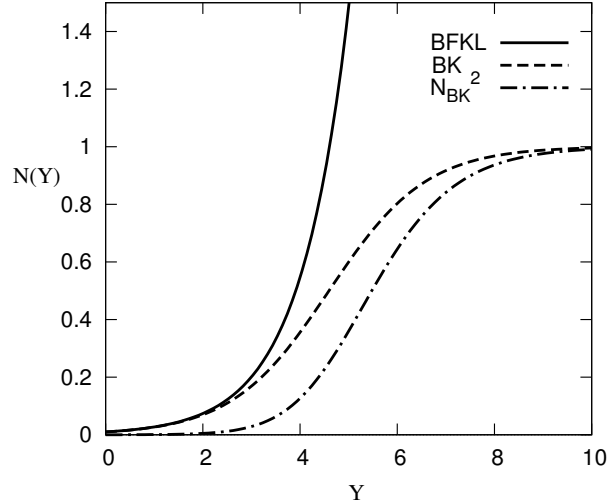


Figure 2.10: Solutions of the BFKL and BK equations in 0+1 dimensions. Also shown is the square of the solution of the BK equation, to indicate where the non-linear term becomes important.

where $Y = \ln 1/x$, and \mathcal{N} is the Fourier transform of $N(r, x)$ defined in Eq. (5.3). This resulting toy model is referred to as the 0+1 dimensional BK equation [41], where Y is thought of as the time variable, and k_{\perp} as space (in this case momentum) variables. In 0+1 dimensions, the BK equation is equivalent to the so-called logistic equation, or Verhulst model, which is used to describe the growth of a biological population that is limited by a supply of food [42, 43]. Even though the 0+1 toy model is heavily simplified, it already exhibits the characteristic saturation property. The BFKL equation corresponds to the linearized version of (2.42). The solution of Eq. (2.42) can be found straightforwardly. It is shown in Fig. 2.10, together with the solution of the linearized equation, i.e. the BFKL equation in 0+1 dimensions. Clearly, the linear equation leads to an exponential rise of the density with Y , consistent with Eq. (2.32), whereas the non-linear equation leads to saturation at large values of Y , so that N approaches unity.

2.6 Geometric scaling

2.6.1 DIS at small x

We have seen how the fast rise of the gluon density at small x leads to the expectation of saturation around a scale $Q_s^2(x) \sim x^{-\lambda}$. At this so-called saturation scale, the dipole amplitude N reaches a value that is large enough so that the non-linear terms in N cannot be neglected anymore, and the BFKL equation breaks down. An expected sign of

2.6. Geometric scaling

saturation is the property of geometric scaling. Geometric scaling means that the dipole amplitude is a function of $r_{\perp} Q_s(x)$ instead of a function of r_{\perp} and x independently. If one approximates the BK equation up to the scale Q_s by the BFKL equation, and imposes a saturation boundary condition (i.e. $N(r_{\perp} = 1/Q_s) = \kappa$, where κ is a constant such that N^2 becomes non-negligible with respect to N), it follows that the dipole amplitude is geometrically scaling at small values of x [44]. From this analysis, which is presented in detail in section 4.5, the scaling property of the dipole amplitude is expected to hold to good approximation in the kinematic region $1 \ll \ln(Q^2/Q_s^2) \ll \ln(Q_s^2/\Lambda^2)$. The same expectation follows from an analysis of the BK equation, cf. section 5.3. As can be seen in chapter 7 numerical solutions of the BK equation indeed show geometric scaling at asymptotic values of $Y = \ln 1/x$.

Experimentally, geometric scaling was established in the total cross section of DIS at small x [34, 45], as measured at HERA. At values of x below 0.01 these data are a function of the single variable $\tau = Q/Q_s(x)$, where $Q_s \sim x^{-\lambda}$ turns out to be identifiable with the saturation scale.

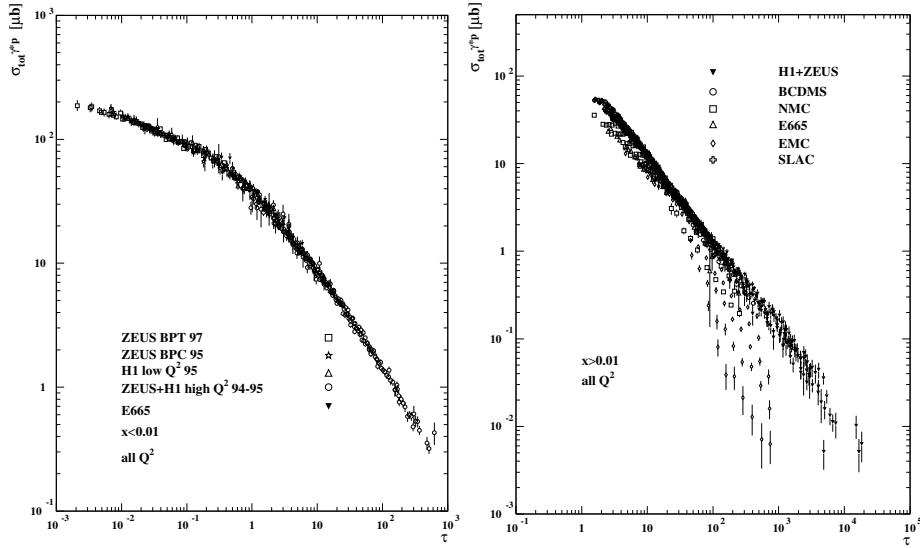


Figure 2.11: The DIS cross section for $x < 0.01$ (left) and $x > 0.01$ (right), as a function of $\tau = Q^2/Q_s^2$, where $0.045 \text{ GeV}^2 < Q^2 < 450 \text{ GeV}^2$. The small- x data show geometric scaling, while the large- x data do not. Plots taken from [45].

Consequently, the property of geometric scaling is often seen as an indication of saturation. The scale Q_s extracted from the DIS data is given by

$$Q_s(x) = 1 \text{ GeV} \left(\frac{x_0}{x} \right)^{1/2}, \quad (2.43)$$

where $x_0 = 3 \cdot 10^{-4}$ and $\lambda = 0.3$. This power-law dependence on x is indeed consistent with the saturation scale that follows from small x evolution, cf. Eq. (2.32), as we will see in more detail in section 4.5. The parameterization (2.43) implies that in DIS for $x < 0.01$, the saturation scale is larger than $Q_s \gtrsim 0.6$, which seems sufficiently large to be in the small coupling regime. The scaling property of the small- x DIS data together with the violation of geometric scaling in the large- x data is depicted in Fig. 2.6.1.

Not only do the small- x DIS data show geometric scaling, the data are well described by models that incorporate saturation. Using the dipole formalism, the small x DIS data from HERA have been successfully described using a phenomenological model for the dipole amplitude that incorporates saturation, the Golec-Biernat-Wüsthoff (GBW) model [34]

$$N_{\text{GBW}}(r_{\perp}, x) = 1 - \exp \left[-\frac{1}{4} r_{\perp}^2 Q_s^2(x) \right], \quad (2.44)$$

where Q_s is given by Eq. (2.43). We can interpret this expression roughly as the Glauber-Mueller rescattering formula (2.39) near the saturation scale, where the gluon density divided by the transverse area is replaced by Q_s according to (2.33). The amplitude (2.44) clearly exhibits saturation, since it approaches unity as $r_{\perp} \sim 1/Q$ becomes large. Even though the GBW model was able to describe the small- x DIS data, as mentioned, it is not clear that the property of geometric scaling is indeed caused by saturation. Firstly, the same data can also be described without saturation, using the partonic DGLAP description of perturbative QCD (pQCD). A next to leading order (NLO) fit to the F_2 data is shown in Fig. 2.13.

Secondly, geometric scaling holds in a much larger region of Q than is expected from small- x evolution. The data seem to scale for $0.045 \text{ GeV}^2 < Q^2 < 450 \text{ GeV}^2$ [45], while theoretically¹¹, geometric scaling is expected to hold approximately in a region above Q_s , $1 \ll \ln(Q^2/Q_s^2) \ll \ln Q_s^2/\Lambda^2$, which would amount to roughly $1 \text{ GeV}^2 < Q^2 < 100 \text{ GeV}^2$ for the optimistic estimate $Q_s \sim 1 \text{ GeV}$ [44]. In this thesis, we will adopt the point of view that geometric scaling may be caused by saturation, and explore the corresponding formalism. To further investigate whether expectations from small- x evolution are corroborated by experiments, one can study other scattering processes.

2.6.2 Nucleon-nucleus scattering at small x .

Hadronic scattering processes at such high energy that one of the colliding hadrons can be considered dense can, like DIS at small x , be described in terms of the dipole scattering amplitude [46, 47]. A description in terms of saturation models requires that the saturation scale, which grows with the atomic number A and $1/x$, is large. This may be the case in for instance hadron production in the scattering of a proton off a large nucleus, $p + A \rightarrow h + X$, or in the production of forward hadrons in proton proton scattering, at high energy. Even though these processes can be described in the dipole formalism, in this case the underlying picture is less intuitive than in DIS. On the partonic level, a quark or gluon from the probe—i.e. the dilute particle—scatters off the small- x field of the target—i.e.

¹¹See section 4.5.2.

2.6. Geometric scaling

the dense particle. The squared amplitude in momentum space of a quark scattering off a small- x field, N_F , turns out to be given by minus the Fourier transform of N . If one writes the analogous object describing the scattering of a gluon off the small- x field as N_A , the total scattering process can be described as [47, 48]

$$\frac{dN_h}{dy_h d^2 p_\perp} \sim f_{q/p} \otimes N_F \otimes D_{h/q} + f_{g/p} \otimes N_A \otimes D_{h/g}. \quad (2.45)$$

We can interpret this expression as a quark or gluon from the probe scattering off the small- x field of the target and consequently fragmenting into hadrons, cf. Fig. 2.12. The fragmentation process is described by the functions D , and the functions f are the parton distributions describing the probe. Due to their non-perturbative nature, both need to be taken from experiment at a given scale. Their evolution to different scales is then given by the DGLAP equations. We note that since the target is described as a colour *field*, instead of as a collection of partons, the kinematics is different from the usual perturbative description [47]. This is further discussed in appendix B.

A theoretical model for the dipole scattering amplitude in proton-nucleus collisions is provided by the so-called McLerran-Venugopalan (MV) model [49–51], which is investigated in chapter 3. In this approach, we distinguish partons of the nucleus that have respectively large and small longitudinal momenta (with respect to some reference scale). The small- x partons, i.e. gluons, are then treated as the colour field that is radiated by the large- x partons—due to the high occupation numbers, this field is treated classically. The high- x partons are described as a configuration of sources that move in the x^+ direction. These configurations, and hence the field that they emit, appear as static to a probe, due to time dilation. The resulting small- x field, obtained for a single source configuration, must then be averaged over all configurations of sources. This picture of the nucleus is known as a *colour glass condensate* (CGC), where the term ‘colour’ is used because of the colour charge of the gluons, the term ‘glass’ refers to the system appearing to a probe as a state of frozen disorder, and the term ‘condensate’ is used because the gluon field has very high occupation numbers. The MV model now consists in modelling the configurations of sources with a Gaussian distribution, which makes that the source-average of the scattering amplitude can be computed analytically. The resulting expression for N_F is formulated in section section 6.2.1, on the basis of a calculation of the quark-CGC scattering amplitude given in chapter 3. In the MV model, there is no evolution in x , i.e. the saturation scale does not depend on x , but is simply a constant. Beyond the MV model, the CGC picture of hadronic scattering has been shown to lead to a complicated set of coupled evolution equations, the JIMWLK equations [52–55], which is equivalent to the BK equation in weak field, or the large- N_c limit (see e.g. [56]).

Thus, nucleon-nucleus collisions at high energy can be described in the same terms as DIS at small x . In the absence of analytical solutions of non-linear evolution equations, a number of phenomenological models for the dipole scattering amplitude have been proposed to describe both the small- x DIS data and hadron production in d - Au collisions at RHIC. The models that are most relevant for the work presented in this thesis are presented in chapter 6.

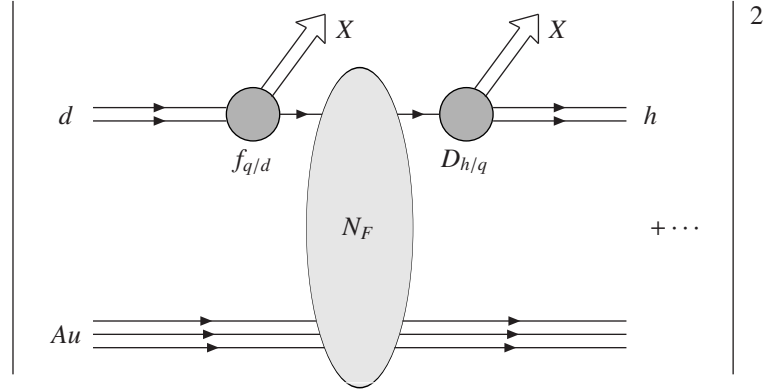


Figure 2.12: Proton-nucleus (d - Au) scattering in the dipole picture—note that the pdf's, the fragmentation functions and the dipole amplitude strictly only appear after squaring the diagram.

2.7 Outline of this thesis

In the following four chapters, 3-6, we will introduce the formalism that is used in the later chapters. The chapters 7-9 are based on published analyses.

- In chapter 3, we introduce the colour glass condensate description of the gluon field of an ultrarelativistic large nucleus. We will calculate the scattering amplitude of a quark off the CGC, using the MV model in which an analytical expression is obtained. The MV model result will be used in chapter 7 as an initial condition at $x = x_0$ for the BK equation, and in chapter 9 to reproduce and extend earlier results of Ref. [57]. The general formalism will be used throughout this thesis for the description of nucleon-nucleus collisions, particularly in chapters 8 and 9 for the description of respectively RHIC $d + A$ data, and the transverse polarization of Λ hyperons that are produced in p - A collisions.
- In chapter 4, the BFKL equation is obtained in the dipole picture. We show how the BFKL equation can be solved in the saddle point approximation. Further, we will see how the solution leads to a fast rise of the dipole scattering amplitude with $1/x$ which compromises unitarity. Next, a number of expectations from BFKL evolution are discussed that play a major role in subsequent chapters. First, we study the dependence of the solution on the initial condition at $x = x_0$, and the behaviour of the saddle point. Second, we investigate the solution of the BFKL equation in the presence of saturation. In this way, the x dependence of the saturation scale is derived. Also, it is shown how this approach leads to the expectation of geometric scaling. These expectations, which are encoded in a number of phenomenological dipole models, will be checked numerically in chapter 7. In chapter 8, we will study to what extent these expectations are confirmed by data on hadron production in d - Au collisions from RHIC.

2.7. Outline of this thesis

- In chapter 5, the non-linear BK equation is introduced. In this chapter, we discuss the results that have been obtained with analytic methods to approximate the solutions. We briefly discuss the travelling wave approximation, which leads to the property of geometric scaling at asymptotically small x . This result is consistent with the expectation from BFKL evolution in the presence of a saturation boundary condition.
- In chapter 6, we introduce a number of phenomenological dipole models that were proposed for the description of both DIS and d -Au collisions. We briefly discuss how they are based on expectations from small- x evolution, i.e. the BFKL and BK equations. These expectations are parameterized in the so-called anomalous dimension of the dipole scattering amplitude, which is closely related to the saddle point of the BFKL equation. The small- x properties of the anomalous dimension will be tested against numerical solutions of the BK equation and RHIC data.
- In chapter 7, we use numerical solutions of the BK equation to investigate whether the small- x features of the phenomenological dipole models that were introduced in chapter 6 are actually consistent with the BK equation. In particular, we demonstrate the effect of BK evolution on the behaviour of the anomalous dimension. This chapter is largely based on Phys. Rev. D75, 094022 (2007).
- In chapter 8, d -Au data from RHIC are investigated to test the small- x features of phenomenological dipole models against experiment. A new phenomenological dipole model is proposed in order to study to what extent the data are sensitive to small- x features of the dipole model, in particular geometric scaling and the dependence of the anomalous dimension on transverse momentum. We show that the RHIC data are inconclusive, and predict that measurements at the LHC will provide a first test of the properties of the anomalous dimension. The analysis presented in this chapter is published in Phys. Rev. D77, 054014 (2008) and arXiv:0810.0113 [hep-ph].
- In chapter 9, the transverse polarization of Λ hyperons that are produced in proton-nucleus collisions is studied in the context of saturation. We first review the results of Ref. [57], where it is shown that the polarization in the presence of saturation is peaked at a value of its transverse momentum that is roughly equal to the saturation scale. The analysis of Ref. [57] is extended with a discussion of more realistic fragmentation functions. These results rely on the MV model for the dipole scattering amplitude. In the second part of the chapter, which is based on Phys. Lett. B671, 91 (2009), we show that also using more realistic dipole models that incorporate evolution in x , the peak of the polarization remains a direct probe of the saturation scale. It is argued how a measurement of this peak can be used to determine the x dependence of the saturation scale. We predict the polarization of Λ 's produced in p -Pb collisions at the LHC, and specify the kinematic range in which a measurement of the peak would provide information on the running of the saturation scale.

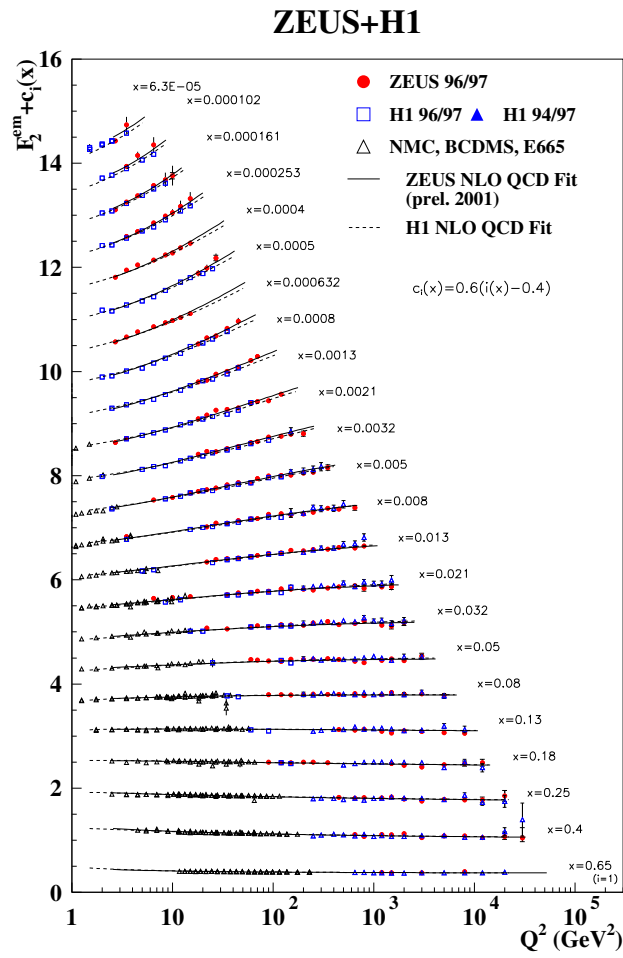


Figure 2.13: DIS data on the structure function F_2 , described with NLO pQCD.

Chapter 3

The colour glass condensate

In the colour glass condensate picture of high energy scattering off a nucleus, the nucleus is represented by an effective colour field at small- x , instead of by parton distribution functions (we refer to e.g. [58–61] for details). In a frame in which the nucleus moves ultrarelativistically, the nucleus consists of partons which each carry a fraction x of its total momentum. In the colour glass condensate description, the partons carrying a large momentum fraction act as sources of the partons, i.e. gluons, that carry a small momentum fraction. Since at small x the gluon density is high, the occupation number is large. Now, since the number of particles is proportional to $N \propto a^\dagger a$, the commutator describing quantum effects $[a^\dagger, a] \approx 1 \ll N$ can be neglected. Hence, the small- x gluons can be described as a *classical field* [49–51]. In electrodynamics, the field that is emitted by an ultrarelativistic charge is known as the Weizsäcker-Williams field [62–65]. In the nucleus, the colour field emitted by the high- x sources forms the non-abelian counterpart of the Weizsäcker-Williams field, and is usually simply referred to with the same name. Since the sources move ultrarelativistically, their distribution, and hence the field that they emit, appears frozen to a probe, due to time dilation. However, the distribution of the sources can vary between collisions. Hence, having calculated the classical colour field that arises from a single configuration of such colour sources, one must subsequently average over all possible distributions of sources. In this scheme, the expectation value of an observable $O[\rho]$, calculated for a particular source distribution ρ , is given by [49–51]

$$\langle O \rangle_\rho = \int \mathcal{D}\rho w[\rho] O[\rho], \quad (3.1)$$

where $w[\rho]$ is a suitable weight functional defining the average. Here, we will use the McLerran-Venugopalan (MV) model [49–51, 66], in which the source configurations have a Gaussian distribution,

$$w[\rho] = \exp \left[- \int dz^- d^2 z_\perp \frac{\rho^a(z^-, z_\perp) \rho^a(z^-, z_\perp)}{2\mu(z^-)^2} \right], \quad (3.2)$$

where μ denotes the width of the distribution. This approximation is considered good for a large number of uncorrelated sources, i.e. for a large nucleus, since corrections to the

3.1. Scattering off the Weizsäcker-Williams field

Gaussian distribution are inversely proportional to the square of the number of sources [49]. Since in the colour glass condensate picture the small- x gluons are described as the field produced by large- x sources, the distribution functional w of the sources depends on a reference scale x_0 that defines the notion of small x . Via w , all observables are in principle x dependent because they are averaged over all source distributions described by w . The evolution of w , and hence all observables, is described by a renormalization group equation, known as the Jalilian-Marian-Weigert-Leonidov-Kovner (JIMWLK) equation [52–55]. The JIMWLK equation is equivalent to the infinite hierarchy of coupled evolution equations for the correlators of Wilson line operators derived in Ref. [27]. In the Gaussian approximation of Eq. (3.2), x -evolution of w would imply that μ depends on x . However, evolution in x in general does not preserve the Gaussian form¹ of w [37], so that the MV model does not incorporate evolution. In particular, in this chapter the saturation scale will be independent of x . In the mean field approximation, the JIMWLK equations and the so-called Balitsky hierarchy of Ref. [27] decouple, and the first equation becomes equivalent to the BK equation. Thus, the BK equation provides a good approximation of the JIMWLK equations. Hence, we will not focus on the JIMWLK equation, but instead on the BK equation, which will be discussed in chapter 5.

In order to build up a description of scattering off a colour glass condensate, we will first derive in section 3.1.1 the form of the Weizsäcker-Williams field in electrodynamics, and calculate the scattering amplitude of an electron propagating through such a background field in section 3.1.2. Then, in section 3.2.1, we will construct the colour glass condensate, i.e. the classical colour field of the light-cone sources of a nucleus. Finding that this field is a non-abelian analogue of the Weizsäcker-Williams field, in section 3.2.2 we will generalize the scattering amplitude found for an electron to the case of a quark scattering off the colour glass condensate, and obtain the scattering cross section. In section 3.2.3 we will sketchily discuss the JIMWLK equation that describes the evolution in x of the weight functional w . We end with a summary of the results that will be most important for the following chapters.

3.1 Scattering off the Weizsäcker-Williams field

3.1.1 The Weizsäcker-Williams field

The Weizsäcker-Williams (WW) field is the classical electromagnetic field radiated by a charged particle moving along the light cone [62–65]. We can derive an expression for the potential of such a field by Lorentz-boosting the known fields in the rest frame of the particle to a frame in which the particle moves with velocity v , and subsequently taking the limit of $v \rightarrow 1$ [67].

In its rest frame S , a particle with charge e emits an electromagnetic field that is

¹See e.g. Fig. 7.3 of chapter 7, which shows that the shape of the MV model is not preserved under BK evolution.

described by a static Coulomb potential²

$$\begin{aligned} A^\mu(x) &= (\varphi(x), \mathbf{0}); \\ \varphi(x) &= \frac{e}{4\pi} \frac{1}{|\mathbf{x}|}. \end{aligned} \quad (3.3)$$

To obtain the potential of a moving charge, we boost to a frame S' that moves with a velocity $-v$ in the $z = x^3$ -direction, say, with respect to S . In S' , the charge moves with velocity v in the z -direction. The potential is given by

$$\begin{aligned} A'^{\perp} &= 0; \\ A'^0 &= \gamma\varphi(x); \\ A'^3 &= v\gamma\varphi(x). \end{aligned} \quad (3.4)$$

Here $\gamma = 1/\sqrt{1-v^2}$, and φ is expressed in terms of the co-ordinates of S' as

$$\varphi(x) = \frac{e}{4\pi} \frac{1}{|\mathbf{x}|} = \frac{e}{4\pi} \frac{1}{\sqrt{\gamma^2(z' - vt')^2 + x'^{\perp 2}}} \quad (3.5)$$

$$= \frac{e}{4\pi} \frac{1}{\gamma \sqrt{(z' - vt')^2 + (1-v^2)x'^{\perp 2}}}. \quad (3.6)$$

We see that in terms of $v^\mu \hat{=} (1, 0, 0, v)$, the potential in the frame S' can be written as

$$A'^\mu(x') = \frac{e}{4\pi} v^\mu \frac{1}{\sqrt{(z' - vt')^2 + (1-v^2)x'^{\perp 2}}}. \quad (3.7)$$

Now, in order to formulate the WW potential, we need to take the limit of $v \rightarrow 1$. In order to do so it is convenient to first write down the physical fields,

$$\begin{aligned} \mathbf{E} &= -\frac{\partial \mathbf{A}}{\partial t} - \nabla\varphi; \\ \mathbf{B} &= \nabla \times \mathbf{A}, \end{aligned} \quad (3.8)$$

and take the limit of the non-zero components using [67]

$$\lim_{v \rightarrow 1} \frac{1-v^2}{[(z \pm vt)^2 + (1-v^2)x^{\perp 2}]^{3/2}} = \frac{2}{x^{\perp 2}} \delta(t \pm z). \quad (3.9)$$

Hence, the fields become proportional to $\delta(t - z)$. Following this procedure, we find that in the limit, the particle produces only transverse fields,

$$\begin{aligned} \lim_{v \rightarrow 1} \mathbf{E}^\perp &= \frac{e\mathbf{x}^\perp}{2\pi x^{\perp 2}} \delta(t - z); \\ \lim_{v \rightarrow 1} B^x &= E^y \\ \lim_{v \rightarrow 1} B^y &= -E^x. \end{aligned} \quad (3.10)$$

²Here we use Heaviside-Lorentz units.

3.1. Scattering off the Weizsäcker-Williams field

From Eq. (3.8) we can see that these fields are equivalent to a potential of the following form,

$$A^\mu(x) = \frac{e}{2\pi} n^\mu \ln(\mu x^\perp) \delta(t - z) \quad (3.11)$$

where $n^\mu \hat{=} (1, 0, 0, 1)$ is the 4-velocity of the charged particle, and μ is some constant scale that is introduced to ensure that the logarithm be dimensionless. Introducing the notation $e/(2\pi) \ln(\mu x^\perp) \equiv \Lambda(x^\perp)$, where $\Lambda(x^\perp)$ is exactly the Coulomb-potential of a point charge in the two-dimensional transverse plane, the WW field can be written as

$$A^\mu(x) = \delta^{\mu+} \delta(x^-) \Lambda(x^\perp). \quad (3.12)$$

Thus, a charged particle that moves along the light cone is described by an electromagnetic potential that is localized at $x^- = 0$ due to Lorentz contraction, and depends on the transverse co-ordinates through the two-dimensional Coulomb potential $\Lambda(x^\perp)$. Hence, it is sometimes referred to as a “shock wave”.

3.1.2 Scattering of electrons off the Weizsäcker-Williams field

In the previous section, we derived an expression for the WW field, of an ultrarelativistic charge that moves in the x^+ direction. Here, we consider the scattering of an electron that moves in the x^- direction off this field (i.e. we consider the scattering of two charges that move along the light cone), following Ref. [68]. Note that this kinematic situation results in a different convention in terms of light cone vectors ($- \leftrightarrow +$) than usual in light front dynamics. Later, we will generalize the resulting scattering amplitude to the case of QCD, as discussed in the introductory section of this chapter, where it will be applied as a description of the colour field of an ultrarelativistic nucleus.

The propagation of an electron through the WW field (3.12), can be thought of as a multiple scattering process off the background field. The propagator in the background field can then be expressed in terms of the free propagator G_0 as

$$\begin{aligned} G(q, p) &= \begin{array}{c} p \longrightarrow q \\ + \quad p \longrightarrow \text{blob} \longrightarrow q \end{array} \quad (3.13) \\ &= (2\pi)^4 \delta(q - p) G_0(p) + G_0(q) T(q, p) G_0(p), \end{aligned}$$

where the “scattering amplitude” T describes the multiple scattering off the background, which is here represented with a blob. This amplitude T consists of a sum of terms that comprise increasingly many couplings of the fermion to the background field, which are described by the vertex $-2\pi i e A$. We can then write the n 'th term of T in the following way [68]

$$\begin{aligned}
 T_n(q, p) &= \begin{array}{c} p \longrightarrow \bullet \xrightarrow{p+k_1} \bullet \cdots \cdots \bullet \longrightarrow q \\ \quad \quad \quad \downarrow \quad \downarrow \quad \quad \quad \downarrow \\ \quad \quad \quad k_1 \quad k_2 \quad \quad \quad k_n \end{array} \\
 &= (-ie)^n \int \frac{d^4 k_1}{(2\pi)^4} 2\pi A(k_1) G_0(p+k_1) \dots \int \frac{d^4 k_n}{(2\pi)^4} \times \quad (3.14)
 \end{aligned}$$

$$2\pi A(p + \sum_{i=1}^n k_i) G_0(p + \sum_{i=1}^{n-1} k_i) (2\pi)^4 \delta^4(p + \sum_{i=1}^n k_i - q), \quad (3.15)$$

where of course the background field is given by the Fourier transform of Eq. (3.12)

$$A^\mu(k) = \delta^{\mu+} \delta(k^-) \Lambda(k_\perp), \quad (3.16)$$

in which Λ is the transverse Coulomb potential in momentum space. The product of integrals can be reduced to a single integral of a product of terms; details of the evaluation of which may be found in [68], and Appendix A.2. We find

$$T_n(q, p) = 2\pi \delta(p^- - q^-) \frac{(-ie)^n \gamma^-}{(2\pi)^n} \frac{1}{n!} \text{sign}^{n-1}(\varepsilon) \int d^2 x_\perp e^{i(p_\perp - q_\perp) \cdot x_\perp} \Lambda^n(x_\perp), \quad (3.17)$$

where ε denotes the small imaginary term in the free fermion propagator, which we will ignore from now on. Now that we know how to systematically write all terms in the expansion of T , we can construct T itself by simply summing all terms,

$$T(q, p) = \sum_{n=1}^{\infty} T_n(q, p) = \sum_{n=0}^{\infty} T_n(q, p) - T_0(q, p) \quad (3.18)$$

$$= 2\pi \delta(p^- - q^-) \gamma^- \int d^2 x_\perp e^{i(p_\perp - q_\perp) \cdot x_\perp} [U(x_\perp) - 1], \quad (3.19)$$

where

$$U(x_\perp) = \exp[-ie\Lambda(x_\perp)]. \quad (3.20)$$

Having calculated the interaction part of the propagator, T , the scattering amplitude \mathcal{M} can be defined as [69]

$$2\pi \delta(p^- - q^-) T(q, p) \equiv \mathcal{M}(q, p), \quad (3.21)$$

so that we can write the scattering amplitude of a charge scattering off the WW field as

$$\mathcal{M}(q, p) = \gamma^- \int d^2 x_\perp e^{i(p_\perp - q_\perp) \cdot x_\perp} [U(x_\perp) - 1], \quad (3.22)$$

with U given by Eq. (3.20).

3.2 Scattering off the colour glass condensate

3.2.1 The classical colour field

Now that we have obtained the electromagnetic field of a charge that moves along the light cone, and the scattering amplitude of another charge off this field, we turn to (Q)CD. Here, we want to calculate the *classical* colour field in the analogous case of a colour charge that moves along the light cone, following the treatments of Refs. [49, 70].

The classical colour field, which is to describe the small- x gluonic content of the nucleus, is found by solving the classical Yang-Mills equations (2.7)

$$[D_\mu, F^{\mu\nu}] = J_a^\nu T^a \equiv J^\nu. \quad (3.23)$$

Here, $F^{\mu\nu} = \partial^\mu A^\nu - \partial^\nu A^\mu - ig[A^\mu, A^\nu]$ is the colour field strength tensor and J is the colour current. Since the sources are highly relativistic we can assume that they move along the light cone, in the x^+ direction, say. Hence the current J runs in the same direction,

$$J^\mu = \delta^{\mu+} J^+. \quad (3.24)$$

From the identity $[D_\mu, [D_\nu, F^{\mu\nu}]] = 0$, it follows that J must be covariantly conserved

$$[D_\mu, J^\mu] = [D^-, J^+] = 0, \quad (3.25)$$

from which we can find its x^+ dependence. We can write the current at a particular point x_0^+ as the product of the colour charge g with the distribution of sources at x_0^+ ,

$$J^+(x^+ = x_0^+) = g\rho(x^-, x^\perp), \quad (3.26)$$

where $\rho = \rho_a T^a$. As the sources move along the light cone in the x^+ -direction, we will assume translational invariance in that direction, i.e. $\partial^- \rho = 0$. The x^+ dependence of the current can then be constructed using the path-ordered exponential

$$W(x^+) = P \exp \left\{ ig \int_{x_0^+}^{x^+} dx'^+ A^-(x'^-) \right\}. \quad (3.27)$$

We see that W has the property $\partial^- W = igA^- W$, and hence $D^- W = D^- W^\dagger = 0$, which means that we can write

$$J^+(x^+, x^-, x^\perp) = gW(x^+) \rho(x^-, x^\perp) W^\dagger(x^+), \quad (3.28)$$

which satisfies the relation (3.25). Using this expression for the current J , the Yang-Mills equations can be written as

$$[D_\mu, F^{\mu\nu}] = g\delta^{\nu+} W\rho W^\dagger. \quad (3.29)$$

In order to solve for the fields, it is convenient to use a specific gauge, the light cone gauge $A^+ = 0$. Later, we will transform the results obtained in this gauge to the light cone gauge

$A^- = 0$, in order to be able to make a comparison with Eq. (3.12). In the gauge $A^+ = 0$, it turns out to be possible to obtain a solution of the Yang-Mills equations with $A^- = 0$ [49, 70]. Hence, we will assume that also in the $A^+ = 0$ gauge we have $A^- = 0$, which will be justified afterward. Since under this assumption $W = 1$ and $F^{-\mu} = 0$, Eq. (3.29) now reads

$$[D_i, F^{ij}] = 0; \quad (3.30)$$

$$[D^\perp, F^{\perp+}] = -[D^\perp, \partial^+ A^\perp] = g\rho, \quad (3.31)$$

From the first expression we see that the transverse potential is a pure gauge, for which the field strength vanishes

$$A^\perp = \frac{i}{g} U \partial^\perp U^\dagger, \quad (3.32)$$

where U denotes some gauge transformation. We can find U in terms of the source ρ by plugging this expression for A^\perp into the second line of Eq. (3.31), however, instead it is more convenient to perform a gauge transformation generated by U itself³ [70],

$$A'^\mu = U^\dagger A^\mu U + \frac{i}{g} U^\dagger \partial^\mu U. \quad (3.33)$$

Since as mentioned, we are interested in the potentials A'^μ in the $A'^- = 0$ gauge, we will transform to this gauge. In other words, since U denotes an arbitrary gauge transformation, we choose it so that it transforms the gauge $A^+ = 0$ into the desired gauge $A'^- = 0$. In the new gauge, the potentials A'^\perp and A'^+ are given by

$$\begin{aligned} A'^\perp &= \frac{i}{g} \partial^\perp U^\dagger U + \frac{i}{g} U^\dagger \partial^\perp U = \frac{i}{g} \partial^\perp (U^\dagger U) = 0; \\ A'^+ &= \frac{i}{g} U^\dagger \partial^+ U. \end{aligned} \quad (3.34)$$

We can now proceed to determine the x^\perp dependence of A'^+ . The equations of motion for A'^+ in this gauge read

$$[D'_\mu, F'^{\mu+}] = [D'_i, F'^{i+}] = -[\partial_i, \partial^i A'^+] = g\rho' \quad (3.35)$$

or in other words,

$$\partial_i \partial^i A'^+ \equiv \nabla_\perp^2 A'^+ = \nabla_\perp^2 \left[\frac{i}{g} U^\dagger \partial^+ U \right] = -g\rho'. \quad (3.36)$$

This is nothing but a two-dimensional Poisson equation dictating how the potential is related to the source configuration. We can write down a formal solution by writing

$$U = P \exp \left[ig^2 \int_{-\infty}^{x^-} dx'^- \frac{1}{\nabla_\perp^2} \rho' (x'^-, x^\perp) \right]. \quad (3.37)$$

³A gauge transformation generated by U^\dagger , to be precise.

3.2. Scattering off the colour glass condensate

Now we see that $A^- = i/g U^\dagger \partial^- U$ in the old gauge vanishes due to translational invariance, $\partial^- U = 0$, justifying our earlier assumption that $A^- = 0$. We see that U has the property

$$\partial^+ U^\dagger = \frac{ig^2}{\nabla_\perp^2} \rho' U^\dagger \quad (3.38)$$

and hence

$$\frac{i}{g} U \partial^+ U^\dagger = -\frac{g}{\nabla_\perp^2} \rho'. \quad (3.39)$$

Therefore, Eq. (3.36) is solved by

$$A'^+ = \frac{i}{g} U \partial^+ U^\dagger, \quad (3.40)$$

which gives us the x^\perp dependence of the potential in terms of ρ .

Since the sources move along the light cone in the x^+ direction, they must be localized at $x^- = 0$. Hence, we can write $\rho(x^-, x^\perp) = \delta(x^-) \rho(x^\perp)$. Moreover, we can see from Eq. (3.38) that $\partial^+ U^\dagger$ is proportional to ρ , so that the potential itself must be proportional to $\delta(x^-)$. We conclude that the classical potential, in the light cone gauge $A^- = 0$, of an ultrarelativistic colour charge g moving in the x^+ direction is given by

$$A^\mu = \frac{i}{g} \delta^{\mu+} \delta(x^-) U \partial^+ U^\dagger, \quad (3.41)$$

where we have dropped the $'$ on the potentials.

Clearly, the potential (3.41) is the non-abelian analogue of the WW potential (3.12), in which Λ denotes the x^\perp dependent part of the potential of the electromagnetic charge. Hence, in the colour glass condensate picture, the nucleus can be represented by a non-abelian WW field.

3.2.2 Cross-section of a quark-colour glass condensate scattering

Having concluded that the colour glass condensate is described by a classical non-abelian WW-field, we can generalize the scattering amplitude of a charged particle off a background WW-field, Eq. (3.22), to the scattering of a quark off the CGC.

The cross section of a quark that scatters off the non-abelian WW-field is given by [46]

$$d\sigma = \int \frac{d^4 q}{(2\pi)^4} (2\pi) \delta(2q^+ q^- - q_\perp^2) \theta(q^+) \frac{1}{2p^-} (2\pi) \delta(p^- - q^-) |\mathcal{M}|^2. \quad (3.42)$$

To calculate the cross section, we first have to evaluate the amplitude \mathcal{M} of a quark scattering off the field (3.41). Writing the transverse field as $(i/g) U \partial^+ U^\dagger$ instead of $\Lambda(x_\perp)$, we can express \mathcal{M} as

$$\mathcal{M} = \bar{u}(q) \gamma^- u(p) \int d^2 x_\perp e^{i(q_\perp - p_\perp) \cdot x_\perp} [U(x_\perp) - 1] \quad (3.43)$$

where U is given by Eq (3.37), and $\bar{u} = u^\dagger \gamma^0$. In order to find the cross section we have to square the amplitude, sum over the spins of the incoming particles, average over the spins of the outgoing particles, and perform the average over the source configurations (3.1). Squaring the amplitude (3.43), we can write $|\mathcal{M}|^2$ in terms of the variables $\mathbf{r}_\perp = \mathbf{x}_\perp - \mathbf{y}_\perp$ and $\mathbf{b}_\perp = (\mathbf{x}_\perp + \mathbf{y}_\perp)/2$ as

$$|\mathcal{M}|^2 = \bar{u}(q)\gamma^- u(p)u^\dagger(p)\gamma^{-\dagger}\gamma^0 u(q) \int d^2 r_\perp d^2 b_\perp e^{i(q_\perp - p_\perp)r_\perp} \left[U\left(b_\perp + \frac{r_\perp}{2}\right) - 1 \right] \left[U^\dagger\left(b_\perp - \frac{r_\perp}{2}\right) - 1 \right]. \quad (3.44)$$

First, we look at the spinor part of $|\mathcal{M}|^2$, which using $u^\dagger(p)\gamma^{-\dagger}\gamma^0 = \bar{u}(p)\gamma^0\gamma^{-\dagger}\gamma^0 = \bar{u}(p)\gamma^-$ can be written as

$$\bar{u}(q)\gamma^- u(p)u^\dagger(p)\gamma^{-\dagger}\gamma^0 u(q) = \bar{u}(q)\gamma^- u(p)\bar{u}(p)\gamma^- u(q). \quad (3.45)$$

Since we know that $\sum_{\text{spins}} u(p)\bar{u}(p) = \not{p} + m$, and we can write $\gamma^- \not{p} \gamma^- = 2p^- \gamma^-$, we can perform the spin summation,

$$\begin{aligned} \frac{1}{2} \sum_{\text{spins}} [\bar{u}(q)\gamma^- u(p)\bar{u}(p)\gamma^- u(q)] &= \frac{1}{2} \sum_{\text{spins}} [2p^- \bar{u}(q)\gamma^- u(q)] \\ &= p^- \text{tr}[(\not{q} + m)\gamma^-] = 4p^- q^-, \end{aligned} \quad (3.46)$$

where the factor of 1/2 accounts for averaging over the spins of the outgoing particle.

Next, we have to calculate the average over all colour source configurations of Eq. (3.44), i.e. we want to know

$$\left\langle \left[\left[U(x_\perp) - 1 \right] \left[U^\dagger(y_\perp) - 1 \right] \right] \right\rangle_\rho = \langle U(x_\perp)U^\dagger(y_\perp) \rangle_\rho - \langle U(x_\perp) \rangle_\rho - \langle U^\dagger(y_\perp) \rangle_\rho + 1, \quad (3.47)$$

where the average is defined by Eq. (3.1). We will assume the Gaussian distribution of sources (3.2) of the McLerran-Venugopalan (MV) model. As argued before, the MV model corresponds to the approximation of a large nucleus, and neglects evolution in x . In Appendix A.1 the calculation of $\langle UU^\dagger \rangle_\rho$ and $\langle U \rangle_\rho$ using the MV-model is performed, the result of which, Eqs. (A.11) and (A.21), leads to

$$\left\langle \left[\left[U(x_\perp) - 1 \right] \left[U^\dagger(y_\perp) - 1 \right] \right] \right\rangle_\rho = e^{-B_2(x_\perp - y_\perp)} - 2e^{-B_1} + 1, \quad (3.48)$$

where the functions B_1 and B_2 are defined in Eqs. (A.14) and (A.24) as

$$B_1 = Q_s^2 \int \frac{d^2 p_\perp}{(2\pi)^2} \frac{1}{p_\perp^4}; \quad B_2(x_\perp) = Q_s^2 \int \frac{d^2 p_\perp}{(2\pi)^2} \frac{2}{p_\perp^4} \left[1 - e^{i\mathbf{p}_\perp \cdot \mathbf{x}_\perp} \right]. \quad (3.49)$$

Both integrals are to be regularized using a lower cut-off, see appendix A.1. The saturation scale Q_s is defined in terms of the distribution of the colour sources as follows,

$$Q_s^2 = \frac{g^4}{2} t^a t^a \int dx^- \mu(x^-)^2. \quad (3.50)$$

3.2. Scattering off the colour glass condensate

which is as mentioned independent of x . In principle we also have to take the average of all possible colours as well as the spins. However, since $t^a t^a \propto 1$, the squared amplitude is diagonal in colour space so that the averaging gives a factor of unity.

Having obtained the scattering amplitude, we can now find an expression for the cross section using Eq. (3.42). After performing the integration over q^+ using the δ -function, Eq. (3.42) can be written as

$$d\sigma = \int \frac{d^2 q_\perp dq^-}{(2\pi)^2} \theta\left(\frac{q_\perp^2}{2q^-}\right) \delta(p^- - q^-) \frac{1}{2p^-} \frac{1}{2q^-} |\mathcal{M}|^2. \quad (3.51)$$

Since the quark moves in the x^- direction, we have $q^- \gg 1$, so that the argument of the θ -function is always positive. Using Eqs. (3.44), (3.48), and (3.46), we obtain the following expression for the cross section of a quark scattering of a colour glass condensate

$$\frac{d\sigma}{dq^- d^2 q_\perp d^2 b_\perp} = \frac{1}{(2\pi)^2} \delta(p^- - q^-) \int d^2 r_\perp e^{i(q_\perp - p_\perp) r_\perp} \left[e^{-B_2(r_\perp)} - 2e^{-B_1} + 1 \right]. \quad (3.52)$$

Defining transverse momenta with respect to the momentum p of the incoming quark, i.e. $p_\perp = 0$, we can write the cross-section in the following way

$$\frac{d\sigma}{dq^- d^2 q_\perp d^2 b_\perp} = \frac{1}{(2\pi)^2} \delta(p^- - q^-) C(q_\perp). \quad (3.53)$$

Here, we have defined

$$C(q_\perp) = \int d^2 r_\perp e^{iq_\perp r_\perp} \left\langle \left[U(r_\perp) - 1 \right] \left[U^\dagger(0) - 1 \right] \right\rangle_\rho, \quad (3.54)$$

which in the MV model is given by

$$C(q_\perp) = \int d^2 r_\perp e^{iq_\perp r_\perp} \left[e^{-B_2(r_\perp)} - 2e^{-B_1} + 1 \right]. \quad (3.55)$$

If we multiply Eq. (3.53) by q^- , and extract $1/P^-$ from the δ -function, where P is the momentum of the proton, say, that harbours the incoming quark, we can write

$$x' \frac{d\sigma^{qA \rightarrow hX}}{dx' d^2 q_t d^2 b} = \frac{1}{(2\pi)^2} x' \delta(x - x') C(q_t), \quad (3.56)$$

where we have defined the longitudinal momentum fraction of the incoming quark as $p^-/P^- \equiv x$, and that of the scattered quark as $q^-/P^- \equiv x'$. We will use this expression in chapters 6 and 9 to calculate the cross section of respectively $p + A \rightarrow h + X$ and the transverse polarization of the Λ hyperons that are produced in $p + A \rightarrow \Lambda + X$.

3.2.3 Evolution in x : the JIMWLK equation

In this section, we will briefly sketch how the description of a nucleus as a colour glass condensate leads to the JIMWLK equations that describe the x evolution of observables

through the weight functional $w[\rho]$. Since the results of this chapter, obtained in the Gaussian approximation of the MV model, do not incorporate x evolution, the JIMWLK equation does not play an important role in this chapter. In the remainder of this thesis, we will focus on the BFKL and BK equations, which are recovered from the JIMWLK equations in the mean field limit.

In section 3.2.1 we have seen that the small- x gluonic content of a nucleus is described in the colour glass condensate model by the classical colour field (3.41). In principle however, this description is valid given a reference momentum scale Λ^+ that separates the high- x partons from the small- x ones. The field (3.41) describes the gluons that have a momentum fraction $x \leq x_0 = \Lambda^+/P^+$, where P is the total momentum of the nucleus. The sources of this field have a momentum fraction that is larger than x_0 . The scale Λ^+ , or equivalently x_0 , denotes the definition of what values of x we consider small. If, given a choice of Λ^+ , we want to use the colour glass condensate description for different values of x , we have to shift x_0 accordingly. Shifting the value of x_0 has no consequence for the form of the fields (3.41)—we do not want to change Λ so drastically that the model assumptions are invalidated. However, the distribution $w[\rho]$ of the colour sources does change as it includes by definition all partons with a momentum fraction larger than Λ^+/P^+ . Shifting the value of x_0 means that slightly more or less partons are now considered sources, so that $w[\rho]$ becomes slightly different. This change of the distribution $w[\rho]$ with x_0 , and hence with x , is described by a renormalization group equation, known as the JIMWLK equation [52–55]. One important consequence of the JIMWLK equation is that the saturation scale (3.50) becomes a function of x , instead of being a constant like in the preceding analysis. Consequently, the (dipole) scattering amplitude (3.55) will gain an x dependence. In Ref. [37] it is argued however that the distribution of sources, which was assumed to be Gaussian in order to calculate the scattering cross section, may change under evolution in x . Hence, in the Gaussian approximation, i.e. the MV model (3.55), no evolution in x is taken into account.

To obtain the JIMWLK renormalization group equation, we need a Lagrangian density that gives rise to the equations of motion (3.23) and the current (3.24). Decomposing the Lagrangian in the kinetic term for the fields, $\mathcal{L}_{YM} = -\frac{1}{4}F_{\mu\nu}^a F_a^{\mu\nu}$ and a term for the sources \mathcal{L}_W , we can write

$$\mathcal{L} = -\frac{1}{4}F_{\mu\nu}^a F_a^{\mu\nu} + \mathcal{L}_W. \quad (3.57)$$

In appendix A.3 it is shown that Eqs. (3.23) and (3.24) are reproduced by the lagrangian density⁴

$$\mathcal{L}_W = \frac{i}{N_c} \rho_a \text{tr} [T^a W(-\infty, \infty)]. \quad (3.58)$$

Armed with this lagrangian, we can define a generating functional for the correlators of the theory in the usual way, but adding the average over the source distributions. This causes the observables of the theory to evolve with x through w . Using the rapidity

⁴An alternative form of the action is derived in Ref. [71].

3.3. Summary

$Y = \ln(1/x)$ rather than x to denote the scale dependence, we can define the generating functional in the following way,

$$Z = \int \mathcal{D}\rho w_Y[\rho] \frac{\int^{\Lambda^+} \mathcal{D}A \delta(A^+) \exp[iS_{YM} + iS_W]}{\int^{\Lambda^+} \mathcal{D}A \delta(A^+) \exp[iS_{YM}]}, \quad (3.59)$$

where we have adopted the notation $w_Y[\rho]$ instead of $w[\rho]$ to indicate the Y dependence of w . The RGE that governs the evolution of $w_Y[\rho]$ as Y is changed is given by

$$\frac{\partial w_Y}{\partial Y} = \alpha_s \left[\frac{1}{2} \frac{\delta^2}{\delta\rho_Y^a(\mathbf{x}_\perp) \delta\rho_Y^b(\mathbf{y}_\perp)} (w_Y \chi^{ab}(\mathbf{x}_\perp, \mathbf{y}_\perp)) - \frac{\delta}{\delta\rho_Y^a(\mathbf{x}_\perp)} (w_Y \sigma^a(\mathbf{x}_\perp)) \right], \quad (3.60)$$

where χ and σ are related to respectively the one and two point functions of the sources. This is the JIMWLK equation that describes the x -evolution of the colour glass condensate⁵

In terms of the correlators of the theory, the JIMWLK equation translates into a tower of coupled equations, relating the evolution of an n -point function to the evolution of a higher order correlator and so on. This system of equations is equivalent to the so-called Balitsky hierarchy of equations [27] that describe the evolution of correlators of increasingly many Wilson line operators. In the mean-field approximation, the JIMWLK and Balitsky equations decouple, and the lowest order equation that describes the evolution of the 2-point function reproduces the BK equation, which is discussed in chapter 5.

3.3 Summary

In the colour glass condensate description of quark-nucleus scattering, the nucleus is represented by a non-abelian Weizsäcker-Williams field that is emitted by sources that move ultrarelativistically with respect to the projectile. Observables are obtained by averaging over all distributions of such sources,

$$\langle O \rangle_\rho = \int \mathcal{D}\rho w[\rho] O[\rho]. \quad (3.61)$$

In the MV model, the weight functional w describing the distribution of sources is taken to be Gaussian. By generalizing the equivalent result calculated in QED, one obtains an expression for the scattering cross section of a quark moving in the x^- direction that scatters off the colour glass condensate (i.e. a nucleus that moves in the x^+ direction),

$$\frac{d\sigma^{qA \rightarrow qX}}{dq^- d^2q_\perp d^2b_\perp} = \frac{1}{(2\pi)^2} \delta(p^- - q^-) C(q_\perp). \quad (3.62)$$

where the scattering amplitude is given by a correlator of Wilson line operators along the quark trajectory

$$C(q_\perp) = \int d^2r_\perp e^{iq_\perp \cdot r_\perp} \langle [U(r_\perp) - 1][U^\dagger(0) - 1] \rangle_\rho. \quad (3.63)$$

⁵The actual calculation is complicated—since we will be concerned with the BK equation rather than the JIMWLK equation, it is not repeated here.

This amplitude can be calculated analytically in the MV model as

$$C(q_{\perp}) = \int d^2 r_{\perp} e^{iq_{\perp} \cdot r_{\perp}} \left[\exp \left(-Q_s^2 \int \frac{d^2 p_{\perp}}{(2\pi)^2} \frac{2}{p_{\perp}^4} [1 - e^{ip_{\perp} \cdot r_{\perp}}] \right) - 2 \exp \left(Q_s^2 \int \frac{d^2 p_{\perp}}{(2\pi)^2} \frac{1}{p_{\perp}^4} \right) + 1 \right]. \quad (3.64)$$

The x dependence of the weight functional w is governed by a renormalization group equation, known as the JIMWLK equation. In terms of the correlators of the Wilson line operators, it leads to an infinite tower of coupled evolution equations that turns out to be equivalent to the Balitsky hierarchy of Ref. [27]. In the mean field approximation, both hierarchies decouple, and the lowest order equation becomes equivalent to the BK equation. The Gaussian distribution of sources is not preserved under JIMWLK evolution; hence the MV model does not incorporate evolution in x . In particular, the saturation scale

$$Q_s^2 = \frac{g^4}{2} t^a t^a \int dx^- \mu(x^-)^2, \quad (3.65)$$

where μ denotes the width of the Gaussian distribution, is a constant.

Chapter 4

BFKL evolution

In this chapter, we give a derivation of the Mueller’s dipole version [39] of the Balitsky-Fadin-Kuraev-Lipatov (BFKL) equation [17–19], cf. section 2.5. The derivation given in section 4.1 draws heavily on the treatment in [13]. In section 4.2 we show how the BFKL equation leads to a rapid rise of the dipole scattering amplitude at small x . The influence of the initial condition on the solution, which will play a role in the analysis of chapter 7, is discussed in section 4.3. The solution of the BFKL equation is calculated in the saddle point approximation, so that the behaviour of the saddle point is crucial to the form of the solution. The saddle point is discussed in section 4.4. Finally, in section 4.5, we discuss the BFKL evolution in the presence of a saturation boundary condition. By thus approximating the evolution of the dipole amplitude near the saturation scale Q_s , the x dependence of Q_s can be derived. Also, we show how the saturation boundary condition leads to approximate geometric scaling in a specific kinematic region above Q_s , the so-called extended geometric scaling (EGS) region. The expectations that are derived in this section for the solution of the BFKL equation in the presence of a saturation boundary condition have been crucial to the formulation of a number of phenomenological dipole models. Some of these models will be discussed in chapter 6. The expectations derived here will be tested for compatibility with the BK equation in chapter 7, and with d -Au data from RHIC in chapter 8. Finally, we summarize the results that are most important for the analysis of the following chapters.

4.1 BFKL equation in the colour dipole formalism

In the dipole picture of DIS, following [72] we approach the scattering of the quark-antiquark pair off the target hadron in the rest frame of the hadron, instead of in the hadron infinite momentum frame of chapter 2. In this frame, we do not study the evolution of the gluon density in the hadron, but rather, the density of gluons *in the quark-antiquark dipole* that scatters off the hadron [72]. This makes the properties of the hadron irrelevant

4.1. BFKL equation in the colour dipole formalism

to the present treatment¹; it will play no role in the following discussion. We will adopt the large- N_c limit, in which the system of gluons can be treated as a collection of dipoles which scatter off the hadron. The dipole scattering amplitude $N_F(r_\perp, x)$, which describes the scattering of the quark-antiquark dipole off a hadron, cf. Eq. (2.38), is then given by the convolution of the probability of finding a gluon, i.e. a dipole, with the propagator of that dipole through the hadron² [30, 39, 41]. This is represented schematically in the left diagram of Fig. 2.9. In this picture, we can construct the evolution of the dipole scattering amplitude by investigating the dipole content of the original quark-antiquark pair.

Following [13], we will construct the BFKL equation in a rather intuitive way³ by studying the radiation of soft gluons by a quark-antiquark pair that moves along the light cone. A gluon radiated by either the quark or the antiquark can be thought of as creating two new colour dipoles. If either of these new dipoles radiates a second gluon, three dipoles are created, and so on. Under the assumption that the radiated gluons are always soft with respect to the parent dipole, such a chain of processes can be treated in a systematic way. Thus, neglecting interference between the dipoles, the gluon content of the quark-antiquark pair emerges from the subsequent eikonal radiation of ever softer gluons. First, we have to uncover the systematics of such gluon radiation.

Consider a heavy quark-antiquark pair⁴ moving along the light cone, its momentum being given by $p = (P, 0, 0, P)$. The radiation of a gluon by either the quark or the antiquark is represented in Fig. 4.1.

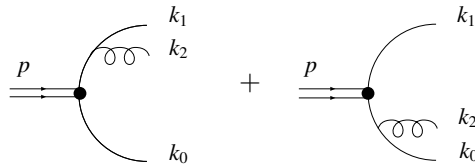


Figure 4.1: Emission of a gluon by a quark-antiquark dipole.

The emission of the gluon in the first diagram of Fig. 4.1 is described by

$$\text{Diagram} = \frac{(\not{k}_1 + \not{k}_2) \gamma \cdot \epsilon_2}{(k_1 + k_2)^2}, \quad (4.1)$$

¹Since the evolution is contained in the wave function of the virtual photon, i.e. the quark-antiquark pair, the way the interaction of the dipoles with the hadron is modelled is not important for the evolution [72].

²If more than a single dipole scatters off the hadron one would obtain a different evolution equation, namely the BK equation, discussed in chapter 5.

³A more rigorous derivation can be found in [39, 73].

⁴In DIS, the mass of the pair is given by the mass of the virtual photon, Q^2 , which must be large enough for perturbation theory to apply.

where ϵ_i is the polarization vector of the gluon with momentum k_i . Since the quarkonium moves along the light cone, the plus components of the momenta k_i are large so that

$$\begin{aligned} (\mathbf{k}_1 + \mathbf{k}_2) \gamma \cdot \epsilon_2 &\approx (k_1^+ + k_2^+) \gamma^- \gamma^+ \epsilon^- \\ &\approx (k_1^+ + k_2^+) (2\eta^{-+} - \gamma^+ \gamma^-) \epsilon^-. \end{aligned} \quad (4.2)$$

It is understood that the gluon will couple to the quark after squaring the diagram, which means that by the Dirac equation $\mathbf{k}_1 \bar{u}(k_1) = 0$ we have $\gamma^- \bar{u}(k_1) = 0$, so that the term containing $\gamma^+ \gamma^-$ must vanish eventually. Since the radiated gluons are assumed to be soft (i.e. x is small) and strongly ordered in their momentum fractions ($k_2^+ \ll k_1^+$) we can write

$$\begin{aligned} \text{Diagram} &\approx \frac{k_1^+ \epsilon_2^-}{k_1 \cdot k_2} \approx \frac{k_1 \cdot \epsilon_2}{k_1 \cdot k_2}. \end{aligned} \quad (4.3)$$

Writing the wave function of a quarkonium state comprising n gluons with momenta k_2, \dots, k_{n+1} as $\psi^{(n)}(k_1, k_2, \dots, k_{n+1})$, where k_1 denotes the momentum of the quark, we can now express the one gluon wave function in terms of the zero gluon wave function,

$$\psi^{(1)}(k_1, k_2) = g t^a \left[\psi^{(0)}(k_1 + k_2) \frac{k_1 \cdot \epsilon_2}{k_1 \cdot k_2} - \psi^{(0)}(k_1) \frac{k_0 \cdot \epsilon_2}{k_0 \cdot k_2} \right]. \quad (4.4)$$

We can simplify this expression by decomposing the k_i and ϵ_i in terms of the light cone vectors p and $n \equiv (1, 0, 0, -1)/(2P)$,

$$\begin{aligned} k_i &= x_i p + \kappa_i n + \mathbf{k}_{i\perp} \\ \epsilon_i &= \varepsilon_i n + \epsilon_{i\perp}. \end{aligned} \quad (4.5)$$

Using respectively the mass shell and transversality conditions, $k_i^2 = k_i \cdot \epsilon_i = 0$, we find $\kappa_i = k_{i\perp}^2/(2x_i)$ and $\varepsilon_i = \mathbf{k}_{i\perp} \cdot \epsilon_{i\perp}/x_i$, which allows us to write

$$\begin{aligned} k_1 \cdot \epsilon_2 &= \frac{x_1}{x_2} \mathbf{k}_{2\perp} \cdot \epsilon_{2\perp} - \mathbf{k}_{1\perp} \cdot \epsilon_{2\perp} \\ k_1 \cdot k_2 &= \frac{1}{2} \frac{x_1}{x_2} k_{2\perp}^2 + \frac{1}{2} \frac{x_2}{x_1} k_{1\perp}^2 - \mathbf{k}_{1\perp} \cdot \mathbf{k}_{2\perp}. \end{aligned} \quad (4.6)$$

Because the gluon is soft, its momentum fraction is small $x_2 \ll x_1$, so that Eq. (4.4) at small x reduces to

$$\psi^{(1)}(k_1, k_2) = 2g t^a \left[\psi^{(0)}(k_1 + k_2) - \psi^{(0)}(k_1) \right] \frac{\mathbf{k}_{2\perp} \cdot \epsilon_{2\perp}}{k_{2\perp}^2}, \quad (4.7)$$

where we leave the x dependence of $\psi^{(n)}$ implicit, $\psi^{(n)}(k_1) = \psi^{(n)}(x_1, \mathbf{k}_{1\perp})$. This expression turns out to be more wieldy in co-ordinate space, where the dependence on $\psi^{(0)}$ factors out. The Fourier transform with respect to the transverse co-ordinates is defined as,

$$\tilde{\psi}^{(1)}(r_1, r_2) = \int \frac{d^2 k_{1\perp}}{(2\pi)^2} \frac{d^2 k_{2\perp}}{(2\pi)^2} e^{-i(\mathbf{k}_{1\perp} \cdot r_{1\perp} + \mathbf{k}_{2\perp} \cdot r_{2\perp})} \psi^{(1)}(k_1, k_2), \quad (4.8)$$

4.1. BFKL equation in the colour dipole formalism

in both terms of which the integration over $\mathbf{k}_{1\perp}$ gives simply the Fourier transform of the one gluon wave function, since

$$\int \frac{d^2 k_{1\perp}}{(2\pi)^2} \frac{d^2 k_{2\perp}}{(2\pi)^2} \psi^{(0)}(k_1) \frac{\mathbf{k}_{2\perp} \cdot \boldsymbol{\epsilon}_{2\perp}}{k_{2\perp}^2} e^{-i(\mathbf{k}_{1\perp} \cdot \mathbf{r}_{1\perp} + \mathbf{k}_{2\perp} \cdot \mathbf{r}_{2\perp})} = \tilde{\psi}^{(0)}(r_1) \int \frac{d^2 k_{2\perp}}{(2\pi)^2} \frac{\mathbf{k}_{2\perp} \cdot \boldsymbol{\epsilon}_{2\perp}}{k_{2\perp}^2} e^{-i\mathbf{k}_{2\perp} \cdot \mathbf{r}_{2\perp}} \quad (4.9)$$

and, with a shift of variables,

$$\int \frac{d^2 k_{1\perp}}{(2\pi)^2} \frac{d^2 k_{2\perp}}{(2\pi)^2} \psi^{(0)}(k_1 + k_2) \frac{\mathbf{k}_{2\perp} \cdot \boldsymbol{\epsilon}_{2\perp}}{k_{2\perp}^2} e^{-i(\mathbf{k}_{1\perp} \cdot \mathbf{r}_{1\perp} + \mathbf{k}_{2\perp} \cdot \mathbf{r}_{2\perp})} = \tilde{\psi}^{(0)}(r_1) \int \frac{d^2 k_{2\perp}}{(2\pi)^2} \frac{\mathbf{k}_{2\perp} \cdot \boldsymbol{\epsilon}_{2\perp}}{k_{2\perp}^2} e^{-i\mathbf{k}_{2\perp} \cdot (\mathbf{r}_{2\perp} - \mathbf{r}_{1\perp})}. \quad (4.10)$$

Hence, denoting $\mathbf{r}_{ij\perp} = \mathbf{r}_{i\perp} - \mathbf{r}_{j\perp}$, we can perform the $k_{2\perp}$ -integration, which gives

$$\int \frac{d^2 k_{\perp}}{(2\pi)^2} \frac{\mathbf{k}_{\perp} \cdot \boldsymbol{\epsilon}_{\perp}}{k_{\perp}^2} e^{-i\mathbf{k}_{\perp} \cdot \mathbf{r}_{\perp}} = \frac{i\boldsymbol{\epsilon}_{\perp} \cdot \mathbf{r}_{\perp}}{2\pi r_{\perp}^2}, \quad (4.11)$$

and write Eq. (4.4) in the following way,

$$\tilde{\psi}^{(1)}(r_1, r_2) = \frac{ig}{\pi} t^a \tilde{\psi}^{(0)}(r_1) \left(\frac{\mathbf{r}_{21\perp}}{r_{21\perp}^2} - \frac{\mathbf{r}_{20\perp}}{r_{20\perp}^2} \right) \cdot \boldsymbol{\epsilon}_{2\perp}, \quad (4.12)$$

where we have taken $\mathbf{r}_{0\perp} = 0$. To find the probability that the quarkonium dipole radiates a gluon, we take the square of this expression and sum over the gluon polarizations and colours. Remembering that $\sum_{\text{pol}} \epsilon_{\mu}^* \epsilon_{\nu} = \eta_{\mu\nu}$ we obtain

$$\sum_{\text{pol}} \left| \left(\frac{\mathbf{r}_{21\perp}}{r_{21\perp}^2} - \frac{\mathbf{r}_{20\perp}}{r_{20\perp}^2} \right) \cdot \boldsymbol{\epsilon}_{2\perp} \right|^2 = \left(\frac{r_{21\perp}}{r_{21\perp}^2} - \frac{r_{20\perp}}{r_{20\perp}^2} \right)^2 = \frac{r_{10\perp}^2}{r_{20\perp}^2 r_{21\perp}^2}. \quad (4.13)$$

It now follows directly from this expression that the one gluon wave function is given by

$$|\tilde{\psi}^{(1)}|^2 = 4C_F \frac{\alpha_s}{\pi} |\tilde{\psi}^{(0)}|^2 \frac{r_{10\perp}^2}{r_{20\perp}^2 r_{21\perp}^2}, \quad (4.14)$$

where $\alpha_s = g^2/(4\pi)$ and $t^a t^a = C_F$.

We can interpret this result in terms of the probability that a dipole (10) emits a *soft* gluon, thus producing two new dipoles (21) and (20). Clearly, this probability is given by $(4C_F \alpha_s / \pi) r_{10\perp}^2 / (r_{20\perp}^2 r_{21\perp}^2)$. We can use this mechanism to obtain the two gluon wave function by describing the second gluon as being emitted from either of the two dipoles (21) and (20), since we have just calculated the probability of such a process. In the same way we can systematically construct the n -gluon wave function for any number of gluons that are strongly ordered in x . However, in doing so we neglect the interference between the emitted gluons, because we only take into account diagrams of the form of

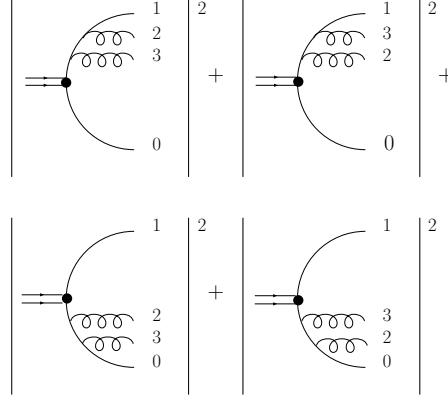


Figure 4.2: Planar contributions to the two gluon wave function.

Fig. 4.1, applied to single dipoles. As an illustration, in this scheme the relation between the two gluon wave function and the one-gluon wave function is depicted in Fig. 4.2. The diagrams of Fig. 4.2 correspond to a two gluon wave function that is given by

$$|\psi^{(2)}|^2 = 4C_F \frac{\alpha_s}{\pi} |\psi^{(1)}|^2 \left(\frac{r_{20\perp}^2}{r_{30\perp}^2 r_{32\perp}^2} + \frac{r_{21\perp}^2}{r_{31\perp}^2 r_{32\perp}^2} \right). \quad (4.15)$$

In this expression, we have ignored such diagrams as Fig. (4.3) that correspond to ‘in-

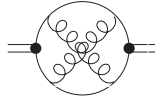


Figure 4.3: Non-planar diagram corresponding to gluon interference.

terference between the gluons’. Technically, we are using the planar approximation, i.e. we neglect diagrams in which gluon lines cross. This approximation becomes exact in the large N_c limit. Non-planar diagrams are suppressed by powers of $1/N_c$ with respect to planar diagrams, since they contain fewer colour loops. A closed colour loop leads to a trace of colour matrices, $t^a t^a = C_F = (N_c^2 - 1)/(2N_c)$ giving roughly a power of N_c . For the two gluon wave function, this implies that the neglected diagrams are suppressed by a factor of $1/N_c^2$, which is on the 10% level for $N_c = 3$. In this approximation, the probability that a dipole (ij) emits a gluon is thus seen to be given by

$$2N_c \frac{\alpha_s}{\pi} \frac{r_{ij\perp}^2}{r_{(i+1)j\perp}^2 r_{(i+1)i\perp}^2}, \quad (4.16)$$

4.1. BFKL equation in the colour dipole formalism

where we have used $C_F = (N_c^2 - 1)/(2N_c) \approx N_c/2$.

On the basis of this mechanism of radiating gluons in the dipole, we can construct the evolution equation that describes the x evolution of the dipole scattering amplitude. We recall that in DIS in the dipole picture, the virtual photon fluctuates into a quark-antiquark pair that subsequently scatters off the hadron. Via the emission of gluons—that are equivalent to colour dipoles—in the quark-antiquark dipole, the scattering of the quark-antiquark pair off the hadron can be thought of as the scattering of one of the dipoles contained in the pair scattering. The total scattering amplitude can then be defined as the convolution of the probability, P say, of finding a dipole in the original quark-antiquark pair with the propagator of such a single dipole through the target hadron [30, 72]. Crucially, the propagator that describes the scattering of a ‘constituent’ dipole off the target does not depend on the dipole’s momentum fraction x [74], so that all the x dependence is contained in P . To find the x dependence of the amplitude N then, we have to construct P .

We consider a quark-antiquark dipole of which the quark is labelled with (1) and the antiquark with (0). We denote the probability of finding a gluon—i.e. a dipole—in the pair with $P(x, r_{10\perp}^2, x_1)$, where x_1 is the longitudinal momentum fraction of the quark and x the longitudinal momentum fraction of the gluon. Increasing x_1 by an infinitesimal amount δx_1 would lead to slightly more phase space being available for the emission of a gluon. The radiation of a gluon is equivalent to the splitting of the original dipole into two new ones. Labelling the gluon that is emitted due to the shift in x_1 with (2), the two new dipoles that are created are (21) and (20), replacing the original dipole (10). The probability that in this way the dipole (10) splits into two new dipoles (21) and (20) is given by Eq. (4.16). Therefore, the change in the probability of finding a gluon, or dipole, $\delta P(x, r_{10\perp}^2, x_1)$, due to the increase in phase space $x_1 \rightarrow x_1 + \delta x_1$ can be written as [13]

$$\begin{aligned} \delta P(x, r_{10\perp}^2, x_1) = \\ 2N_c \frac{\alpha_s}{\pi} \frac{\delta x_1}{2} \int \frac{d^2 r_2}{2\pi} \frac{r_{10\perp}^2}{r_{20\perp}^2 r_{21\perp}^2} \left[P(x, r_{21\perp}^2, x_1) + P(x, r_{20\perp}^2, x_1) - P(x, r_{10\perp}^2, x_1) \right]. \end{aligned} \quad (4.17)$$

Since $P(x, r_{1\perp}^2, x_1)$ must be boost invariant, it can only depend on x/x_1 instead of on both momentum fractions independently. Hence, we can write Eq. (4.17) in terms of x , and forget about the x_1 dependence, because the same mechanism drives the radiation of additional gluons for any value of x_1 and any number of gluons/dipoles that may have been already emitted. The result, written in terms of N , is then

$$x \frac{\partial}{\partial x} N(r_{10\perp}^2, x) = -N_c \frac{\alpha_s}{\pi} \int \frac{d^2 r_{2\perp}}{2\pi} \frac{r_{10\perp}^2}{r_{20\perp}^2 r_{21\perp}^2} \left[N(r_{21\perp}^2, x) + N(r_{20\perp}^2, x) - N(r_{10\perp}^2, x) \right], \quad (4.18)$$

which is the BFKL equation in the dipole picture [13, 39, 41]. We conclude that in the kinematic regime where the emitted gluons are strongly ordered in x (Y), and where interactions among the gluons themselves can be neglected, Eq. (4.18) describes the small- x evolution of the dipole scattering amplitude.

4.2 Solution of the BFKL equation and the small- x problem

The evolution described by the BFKL equation leads to a power-like growth of the dipole scattering amplitude as x becomes very small. To see how this behaviour occurs, we will solve the BFKL equation in the limit of small x , i.e. in the kinematic region where $\ln(1/x) \gg \ln(1/r_\perp^2)$, using the saddle point approximation.

To be able to find the x -behaviour of the dipole amplitude, we follow Ref. [13] by first performing the angular integration in Eq. (4.18)

$$\int \frac{d^2 r_{2\perp}}{r_{21\perp}^2} = \int_0^\infty r_{2\perp} dr_{2\perp} \int_0^{2\pi} \frac{d\theta}{r_{2\perp}^2 + r_{1\perp}^2 - 2r_{2\perp}r_{1\perp} \cos \theta}. \quad (4.19)$$

Defining $z = \exp(i\theta)$, the angular integral can be written as a contour integral over the unit circle, here denoted C ,

$$\int_0^{2\pi} \frac{d\theta}{r_{2\perp}^2 + r_{1\perp}^2 - 2r_{2\perp}r_{1\perp} \cos \theta} = \frac{1}{i} \int_C \frac{dz}{(r_{2\perp}^2 + r_{1\perp}^2)z - r_{2\perp}r_{1\perp}z^2 - r_{2\perp}r_{1\perp}}. \quad (4.20)$$

The integrand is now simply a polynomial of degree two in z . Denoting its roots with α and β , the integral along C gives

$$\int_C \frac{dz}{(z - \alpha)(z - \beta)} \equiv \int_C \frac{dz}{f(z)} = 2\pi i \left[\frac{1}{f'(\alpha)} + \frac{1}{f'(\beta)} \right], \quad (4.21)$$

provided that both roots are enclosed by the contour C , the unit circle. In fact, one of the roots always lies outside of the unit circle, and therefore does not contribute to the integral, whereas the other always lies within the unit circle. Hence, the integral yields

$$\int \frac{d^2 r_{2\perp}}{r_{21\perp}^2} = \pi \int_0^\infty \frac{dr_{20\perp}^2}{|r_{20\perp}^2 - r_{10\perp}^2|} \quad (4.22)$$

The radial integration now splits into two parts, $0 < r_{20\perp}^2 < r_{10\perp}^2$ and $r_{10\perp}^2 < r_{20\perp}^2 < \infty$. Note that the first and second terms in Eq. (4.18) equate to the same integral after a shift of the integration variable. We can unify the two parts of the integral by substituting $r_{20\perp}^2 = ur_{10\perp}^2$ in the region $0 < r_{20\perp}^2 < r_{10\perp}^2$ and $r_{20\perp}^2 = r_{10\perp}^2/u$ in the region $r_{10\perp}^2 < r_{20\perp}^2 < \infty$. Eq. (4.18) then reads

$$x \frac{\partial}{\partial x} N(r_\perp^2, x) = -\bar{\alpha}_s \int_0^1 \frac{du}{1-u} \left[N(ur_\perp^2, x)/u + N(r_\perp^2/u, x) - 2N(r_\perp^2, x) \right], \quad (4.23)$$

where we have written $r_{10\perp}^2 = r_\perp^2$, and introduced the notation $\bar{\alpha}_s = N_c \alpha_s / \pi$. The pole of $1/(1-u)$ at $u = 1$ is regularized by the terms between brackets. This equation can be further simplified by a transformation to Mellin space

$$N(\gamma, x) = \int_0^\infty dr_\perp^2 (r_\perp^2 Q_0^2)^{-\gamma-1} N(r_\perp^2, x), \quad (4.24)$$

4.2. Solution of the BFKL equation and the small- x problem

where Q_0 is an arbitrary momentum scale that we introduce to make the dimension of $N(\gamma, x)$ independent of γ . Defining a function χ

$$\chi(\gamma) = \int_0^1 \frac{du}{1-u} [u^{\gamma-1} + u^{-\gamma} - 2] = 2\psi(1) - \psi(\gamma) - \psi(1-\gamma), \quad (4.25)$$

where ψ is the digamma function,

$$\psi(z) = \frac{d}{dz} \ln \Gamma(z), \quad (4.26)$$

in Mellin space Eq. (4.23) takes the following very simple form

$$x \frac{\partial}{\partial x} N(\gamma, x) = -\bar{\alpha}_s \chi(\gamma) N(\gamma, x). \quad (4.27)$$

The function $\chi(\gamma)$ is depicted in Fig. 4.4. We see that in Mellin space the BFKL equation

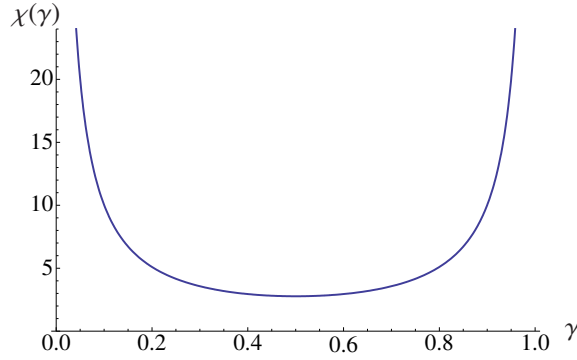


Figure 4.4: The BFKL kernel $\chi(\gamma)$.

can be solved straightforwardly, giving

$$N(\gamma, x) = N(\gamma, x_0) \left(\frac{x_0}{x} \right)^{\bar{\alpha}_s \chi(\gamma)}, \quad (4.28)$$

where x_0 is a constant of integration. The solution of the original equation is found by taking the inverse transformation

$$N(r_\perp^2, x) = \int_M \frac{d\gamma}{2\pi i} (r_\perp^2 Q_0^2)^\gamma N(\gamma, x), \quad (4.29)$$

where the contour M runs parallelly to the imaginary axis, crossing the real axis between 0 and 1/2, and is closed to the right. This transformation yields the following expression for the dipole amplitude in transverse co-ordinate space

$$\begin{aligned} N(r_\perp^2, x) &= \int_M \frac{d\gamma}{2\pi i} N(\gamma, x_0) \exp \left[\gamma \ln(r_\perp^2 Q_0^2) + \bar{\alpha}_s \chi(\gamma) \ln \frac{x_0}{x} \right] \\ &\equiv \int_M \frac{d\gamma}{2\pi i} N(\gamma, x_0) \exp [F(\gamma, r_\perp^2)]. \end{aligned} \quad (4.30)$$

Such a contour integral in general picks up contributions from the poles of the integrand. Here, contributions from the initial condition, which in principle could have poles inside the contour, are ignored, which is usually done when solving the BFKL equation. The role of the initial condition will be discussed in section 4.3.

When x becomes so small that the term containing $\ln(x_0/x)$ is dominant, we can solve the integral in the saddle point approximation⁵. The integrand is then so strongly peaked that this peak, located at the saddle point, completely determines the integral. Expanding the argument of the exponential, which we denote F , to second order around the saddle point γ_{sp} , i.e. the point where $F'(\gamma_{sp}) = 0$, we can solve the remaining contour integral exactly,

$$\begin{aligned} N(r_{\perp}^2, x) &\simeq N(\gamma_{sp}, x_0) e^{F(\gamma_{sp})} \int_M \frac{d\gamma}{2\pi i} \exp \left[\frac{1}{2} F''(\gamma_{sp}) (\gamma - \gamma_{sp})^2 \right] \\ &= \frac{N(\gamma_{sp}, x_0) (r_{\perp}^2 Q_0^2)^{\gamma_{sp}}}{\sqrt{2\pi \bar{\alpha}_s \chi''(\gamma_{sp}) \ln(x_0/x)}} \left(\frac{x_0}{x} \right)^{\bar{\alpha}_s \chi(\gamma_{sp})}. \end{aligned} \quad (4.31)$$

Apparently, in the limit of small- x , the gluon density grows as $(1/x)^\lambda$, where $\lambda = \bar{\alpha}_s \chi(\gamma_{sp})$. The value of λ is determined by the saddle point γ_{sp} , which is in turn found by solving

$$F'(\gamma_{sp}) = \ln(r_{\perp}^2 Q_0^2) + \bar{\alpha}_s \chi'(\gamma_{sp}) \ln \frac{x_0}{x} = 0. \quad (4.32)$$

In the approximation where $\ln(x_0/x)$ dominates the integral, the saddle point corresponds to the minimum of the function χ , which is given by $\chi'(1/2) = 0$. This is the well known BFKL saddle point, $\gamma_{sp} = 1/2$. Thus, as x becomes smaller and smaller, the dipole amplitude increases like $(1/x)^{\bar{\alpha}_s \chi(1/2)} = (1/x)^{4 \ln 2 \bar{\alpha}_s}$, where $4 \ln 2 \bar{\alpha}_s \approx 0.5$ for $\bar{\alpha}_s = 0.2$.

As argued in chapter 2, such a power-like rise of the dipole amplitude must violate unitarity. Hence, it is expected that saturation of the amplitude (or the gluon density) occurs at momenta near the saturation scale $Q_s(x)$, cf. Eq. (2.33). The BFKL equation must then be replaced with a non-linear evolution equation. An example of such a non-linear equation that will play a prominent role in this thesis is the BK equation [27, 30], which reduces to the BFKL equation for $r_{\perp}^2 \ll 1/Q_s^2$. It will be discussed in chapter 5.

4.3 The small- r_{\perp}^2 limit and the initial condition

In the standard treatment of the BFKL equation presented in the previous section, any possible effect of the initial condition is ignored. The reason for this is that the initial condition is assumed to be slowly varying, so that the integral can be performed in the saddle point approximation. However, in some cases the initial condition still gives a non-negligible contribution to the small- r_{\perp}^2 limit of the solution. The reason for this is as follows. The solution of the BFKL equation is formulated as a contour integral, see

⁵The same can be done when the term containing $\ln r_{\perp}^2 Q_0^2$ is dominant. The saddle point will be discussed in different kinematic regimes in section 4.4.

4.3. The small- r_\perp^2 limit and the initial condition

Eq. (4.30), (the contour is closed at $+\infty$),

$$N(r_\perp^2, x) = \int_M \frac{d\gamma}{2\pi i} N(\gamma, x_0) \exp \left[\gamma \ln(r_\perp^2 Q_0^2) + \bar{\alpha}_s \chi(\gamma) \ln \frac{x_0}{x} \right], \quad (4.33)$$

which picks up contributions, the residues of the integrand, from all simple poles that lie inside the contour. Apart from these contributions, the integral can be approximated by the saddle point method, which if we only take into account the contribution from the saddle point γ_{sp} itself simply gives

$$N(r_\perp^2, x) \sim \exp \left[\gamma_{sp} \ln(r_\perp^2 Q_0^2) + \bar{\alpha}_s \chi(\gamma_{sp}) \ln \frac{x_0}{x} \right], \quad (4.34)$$

where the saddle point γ_{sp} is determined by Eq. (4.32). However, the initial condition, or more precisely its Mellin transform $N(\gamma, x_0)$, may have a simple pole enclosed by the contour and therefore contribute to the integral as well. In fact, as discussed in appendix C.2, the dipole amplitude at small r_\perp^2 , equivalently, at large transverse momentum, should be proportional to a power of r_\perp^2 in order to be consistent with the known perturbative results. Any physical initial condition will therefore be proportional to $r_\perp^{2\gamma_0}$ when r_\perp approaches zero, where we expect $\gamma_0 = 1$ but keep it explicitly for generality. This small- r_\perp behaviour makes that the Mellin transform has a simple pole at γ_0 [75]. We can readily convince ourselves of this by considering the Mellin transform of the following example

$$N_0(r_\perp^2) = \begin{cases} (r_\perp^2 Q_0^2)^{\gamma_0} & r_\perp < 1 \\ 1 & r_\perp \geq 1 \end{cases} \quad (4.35)$$

which can be straightforwardly calculated from Eq. (4.24), and is given by

$$N_0(\gamma) = \frac{1}{Q_0^2} \int_0^1 dr^2 (r^2)^{-\gamma-1} r^{2\gamma_0} + \frac{1}{Q_0^2} \int_1^\infty dr^2 (r^2)^{-\gamma-1} = \frac{1}{Q_0^2} \left[\frac{1}{\gamma_0 - \gamma} + \frac{1}{\gamma} \right], \quad (4.36)$$

We see that the simple pole at γ_0 results from the small- r_\perp^2 limit of N_0 , which will show up for any initial condition that has a similar behaviour in this limit. The occurrence of the pole at γ_0 means that there is an additional contribution to the integral (4.33), equal to the residue at γ_0

$$N(r_\perp^2, x) \sim \exp \left[\gamma_0 \ln(r_\perp^2 Q_0^2) + \bar{\alpha}_s \chi(\gamma_0) \ln \frac{x_0}{x} \right]. \quad (4.37)$$

Hence, instead of only by the saddle point contribution, the solution of the BFKL equation is given by the sum of the saddle point contribution and the residue of the integrand at γ_0 . This manifests itself particularly in the limit $r_\perp^2 \rightarrow 0$ and fixed x , where one of the two contributions dominates the other, *depending on which of γ_{sp} and γ_0 is the smallest*. In the limit, when x is kept fixed, the solution is given by $\exp(-\gamma \ln 1/r_\perp^2)$, where γ is the smallest of γ_{sp} and γ_0 , because the other contribution will fall off faster.

From Eq. (4.32) and Fig. 4.4 we see that the limit $r_\perp^2 \rightarrow 0$ and fixed x , the saddle point γ_{sp} approaches 1, since $\chi(\gamma)$ goes to infinity if γ approaches 1. This will be discussed in more detail in the next section BFKL evolution thus preserves the small- r_\perp^2 behaviour of the initial condition, namely $r_\perp^{2\gamma_0}$, if $\gamma_0 < 1$, and replaces it with r_\perp^2 otherwise.

4.4 Behaviour of the saddle point

The saddle point of the BFKL equation plays a role in the construction of the phenomenological dipole models for d - Au collisions that are discussed in chapter 6. Therefore, in this section, which is based on the analysis of Ref. [44], we will inspect the behaviour of the saddle point in more detail.

In solving the BFKL equation in section 4.2, we used the saddle point approximation under the assumption that $x \rightarrow 0$ while r_\perp remains finite, so that the saddle point becomes equal to $1/2$. More generally however, one can distinguish three kinematic regimes in which the saddle point either approaches 0, $1/2$, or 1. Here, we will briefly discuss these cases, and refer to Ref. [44] for more details.

The solution of the BFKL equation can be written as a contour integral in the complex plane, given in Eq. (4.30). In the saddle point approximation, the solution is written as, cf. Eq. 4.31,

$$N(r_\perp^2, x) \simeq \frac{N(\gamma_{sp}, Y_0) \exp[F(\gamma_{sp}, r_\perp, Y)]}{\sqrt{2\pi F''(\gamma_{sp}, r_\perp, Y)}} \quad (4.38)$$

where we denote $Y = \ln x_0/x$, and γ_{sp} is the saddle point of the integrand, which is defined as the point at which the derivative of the function F with respect to γ vanishes,

$$\left. \frac{\partial F}{\partial \gamma} \right|_{\gamma=\gamma_{sp}} = 0. \quad (4.39)$$

We recall that F is defined as

$$F(\gamma, r_\perp, Y) = \gamma \ln r_\perp^2 Q_0^2 + \bar{\alpha}_s \chi(\gamma) Y, \quad (4.40)$$

where Q_0 is an arbitrary scale, so that the saddle point is determined by

$$\chi'(\gamma_{sp}) = \frac{\ln 1/(r_\perp^2 Q_0^2)}{\bar{\alpha}_s Y}. \quad (4.41)$$

Fig 4.5 shows the resulting saddle point as a function of r_\perp for different values of Y .

Inspecting Fig. 4.4, we can distinguish three limits in which Eq. (4.41) makes the saddle point approach an asymptotic value:

1. If $1/(\bar{\alpha}_s Y) \ln r_\perp^2 Q_0^2 \rightarrow \infty$, the saddle point approaches $\gamma_{sp} \rightarrow 0$. This is the case when $r_\perp \gg Y$.
2. If $1/(\bar{\alpha}_s Y) \ln 1/r_\perp^2 Q_0^2 \rightarrow 0$, the saddle point approaches $\gamma_{sp} \rightarrow 1/2$. This is the case when at fixed r_\perp , $Y \rightarrow \infty$, i.e. $x \rightarrow 0$. This is the usual BFKL saddle point in the limit of small x that we encountered in section 4.2.
3. If $1/(\bar{\alpha}_s Y) \ln 1/r_\perp^2 Q_0^2 \rightarrow \infty$, the saddle point approaches $\gamma_{sp} \rightarrow 1$. This is the case when at fixed Y , $r_\perp \rightarrow 0$, or, in momentum space, when $k_\perp \rightarrow \infty$. This corresponds to the double logarithmic approximation (DLA), which is appropriate when both Y and $Q^2 \sim 1/r_\perp^2$ are large.

4.4. Behaviour of the saddle point

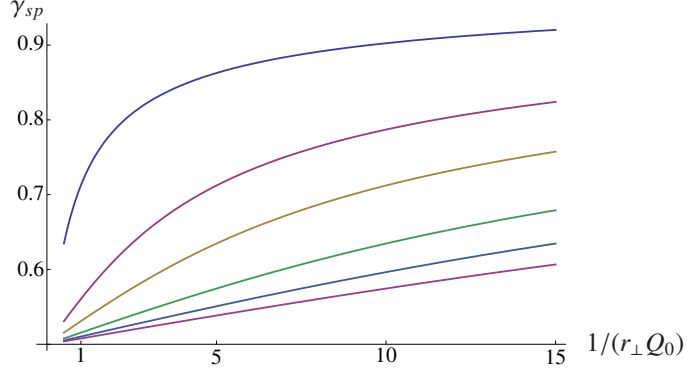


Figure 4.5: The saddle point following from Eq. (4.41) as a function of $1/(r_{\perp} Q_0)$ (with $\bar{\alpha}_s = 0.2$), for $Y = 1, 5, 10, 20, 30, 40$ (from the top down).

To obtain the saddle point in these limits, one can for $0 < \gamma < 1$, use the approximation

$$\chi(\gamma) \approx \frac{1}{\gamma} + \frac{1}{1-\gamma} + 4 \ln 2 - 4, \quad (4.42)$$

which results in the following expressions:

1. If $\gamma_{sp} \rightarrow 0$, we can neglect the contribution from $1/(1-\gamma)$ in Eq. (4.42), so that we find the saddle point

$$\gamma_{sp} \approx \sqrt{\frac{\bar{\alpha}_s Y}{\ln(r_{\perp}^2 Q_0^2)}}. \quad (4.43)$$

2. If we expand Eq. (4.42) around $\gamma = 1/2$, we find the saddle point

$$\gamma_{sp} \approx \frac{1}{2} + \frac{1}{32} \frac{\ln 1/(r_{\perp}^2 Q_0^2)}{\bar{\alpha}_s Y}. \quad (4.44)$$

Additionally, we can make an estimate of the upper limit on the kinematic region where the saddle point is close to $1/2$. Defining, like in Ref. [44], this region as $\gamma_{sp} \ll 3/4$, which is the middle point between region 2. and 3., from Eq. (4.44) it follows that the corresponding kinematic region is bounded by

$$\ln \frac{1}{r_{\perp}^2 Q_0^2} \ll 8 \bar{\alpha}_s Y. \quad (4.45)$$

3. If $\gamma_{sp} \rightarrow 1$, we can neglect the contribution from $1/\gamma$ in Eq. (4.42), so that we find the DLA saddle point

$$\gamma_{DLA} \approx 1 - \sqrt{\frac{\bar{\alpha}_s Y}{\ln 1/(r_{\perp}^2 Q_0^2)}}. \quad (4.46)$$

We note that in case 3, Eq. (4.38) yields the following solution of the BFKL equation,

$$N(r_{\perp}^2, Y) \approx \frac{N(\gamma_{sp}, Y_0)}{\sqrt{2\pi\bar{\alpha}_s Y \chi''(\gamma_{DLA})}} r_{\perp}^2 Q_0^2 \exp \left[\sqrt{\bar{\alpha}_s Y \ln \frac{1}{r_{\perp}^2 Q_0^2}} \right]. \quad (4.47)$$

We can compare this expression with the DLA solution of the DGLAP equation, cf. the discussion leading to Eq. (2.30),

$$xg(x, Q^2) \sim xg(x, Q_0^2) \exp \left[2 \sqrt{\frac{6}{b} \ln \ln \left(\frac{Q^2}{Q_0^2} \right) \ln \left(\frac{1}{x} \right)} \right]. \quad (4.48)$$

Bearing in mind relation (2.40), i.e. $N_F(r_{\perp}, x) \sim r_{\perp}^2 xg(x, Q^2 = 1/r_{\perp}^2)$, we see that both solutions show the same behaviour as a function of x , but differ⁶ in their dependence on Q^2 .

As mentioned, the saddle point of the BFKL equation plays a role in the construction of phenomenological dipole models that are discussed in chapter 6. In that context, especially the value of the saddle point in the presence of a so-called saturation boundary condition, discussed in the next section, is of importance.

4.5 The BFKL equation with a saturation boundary condition

We have seen that the BFKL equation leads to an unreasonable growth of the dipole scattering amplitude at very small x , necessitating some other description that leads to saturation in order to preserve unitarity. One such description is provided by the BK equation, which is a non-linear evolution equation that reduces to the BFKL equation when the amplitude is small enough for the non-linearity to be negligible. Given this property, one can try to approximate the solution of the BK equation outside the saturation region $r_{\perp} \leq 1/Q_s(x)$ by a solution of the BFKL equation, *in the presence of a saturation boundary condition* [44].

4.5.1 The saturation scale

Conceptually, we may expect saturation effects to show up when the transverse size r_{\perp} of the gluons in the incoming dipole becomes so large with respect to the density that the gluons start to overlap in phase space and interactions among them become important. Since more and more gluons are emitted as x becomes smaller, saturation effects will not set in at a fixed scale, but rather at an x dependent scale $r_{\perp} = 1/Q_s(x)$. The saturation momentum scale $Q_s(x)$ will then increase as x becomes smaller. At small r_{\perp} , or more precisely $r_{\perp} \ll 1/Q_s$, the transverse size of the gluons is relatively small and the gluons

⁶In Ref. [44] however, it is claimed that both solutions are identical. Rather, as stated in Ref. [13], the BFKL result is to be seen as a fixed coupling version in co-ordinate space of the DLA solution.

4.5. The BFKL equation with a saturation boundary condition

hardly feel each other. Hence, the dipole amplitude is small. When r_\perp increases, the dipole amplitude becomes larger until at $r_\perp = 1/Q_s$ it reaches a value that is so large that N^2 is not negligible anymore with respect to N itself and the gluons start interacting. This defines the saturation scale. The exact value that we choose for the dipole amplitude at the saturation scale is not important as it only influences the normalization, and not the x dependence of the saturation scale.

For illustrational purposes, we can simply take the value 1, and define the saturation scale thus

$$N(r_\perp^2 = 1/Q_s^2, x) = 1, \quad (4.49)$$

This is the saturation boundary condition that we will impose on the solution of the BFKL equation. From the saddle point approximation to this solution (cf. (4.30)) we know that we can write $N(r_\perp^2, x)$ roughly as

$$N(r_\perp^2, x) = \exp \left[\gamma_{sp} \ln(r_\perp^2 Q_0^2) + \bar{\alpha}_s \chi(\gamma_{sp}) \ln \frac{x_0}{x} \right], \quad (4.50)$$

where we ignore the initial condition $N(\gamma_{sp}, x_0)$ since if slowly varying, it plays a role only in the limit of small r_\perp , as discussed in section 4.3. The saddle point is found by solving Eq. (4.32).

$$\bar{\alpha}_s \chi'(\gamma_{sp}) \ln \frac{x_0}{x} = \ln \frac{1}{r_\perp^2 Q_0^2}. \quad (4.51)$$

The saturation boundary condition (4.49) gives the further constraint

$$\bar{\alpha}_s \chi(\gamma_{sp}) \ln \frac{x_0}{x} = \gamma_{sp} \ln \frac{Q_s^2}{Q_0^2}, \quad (4.52)$$

which dictates the value of the saddle point at the saturation scale, for which will use the common notation γ_s ,

$$\frac{\chi'(\gamma_s)}{\gamma_s} = \chi(\gamma_s). \quad (4.53)$$

Numerically, this implies $\gamma_s = 0.6275\dots$, which is slightly different from the pure BFKL saddle point $\gamma_{sp} = 1/2$. Given the value of γ_s , we can from the same equations find the x dependence of the saturation scale

$$Q_s^2(x) = Q_0^2 \exp [\bar{\alpha}_s \chi'(\gamma_s) \ln(x_0/x)] = Q_0^2 \left(\frac{x_0}{x} \right)^{\bar{\alpha}_s \chi'(\gamma_s)}. \quad (4.54)$$

Thus, assuming that the BFKL equation describes the evolution up to the saturation scale Q_s to good approximation, BFKL evolution⁷ implies that Q_s^2 grows as x^λ as x becomes smaller, where numerically $\lambda \approx 0.9$ for $\bar{\alpha}_s = 0.2$.

⁷BFKL evolution with running coupling leads in this approach to a slower rise of the saturation scale; $Q_s \sim \exp(c\sqrt{Y})$, where $Y = \ln 1/x$ [76].

4.5.2 Geometric scaling window

From Eq. (4.30) we know that the solution of the BFKL equation is written as a contour integral. If we approximate this integral by the saddle point contribution only, i.e. we ignore the initial condition, the dipole amplitude can be written as

$$N(r_{\perp}^2, x) = \exp \left[\gamma_s \ln(r_{\perp}^2 Q_0^2) + \bar{\alpha}_s \chi(\gamma_s) \ln \frac{x_0}{x} \right] \equiv \exp \left[F(\gamma_s, r_{\perp}^2) \right], \quad (4.55)$$

which due to the saturation boundary condition equals 1 at the point $r_{\perp} = 1/Q_s$. We can now construct the solution for values of $1/r_{\perp} > Q_s$ by expanding the integrand F around $\ln r_{\perp}^2 = \ln 1/Q_s^2$, or in terms of the variable $\xi \equiv \ln 1/r_{\perp}^2 Q_0^2$, expanding F around $\xi = \ln Q_s^2/Q_0^2 \equiv \xi_s$. This way, ξ increases as $1/r_{\perp}$ becomes larger than Q_s .

In the region $\xi > \xi_s$, but $\xi - \xi_s \ll \xi_s$ (i.e. $0 < \xi - \xi_s \ll \xi_s$) we can make a Taylor series expansion in powers of $\xi - \xi_s$,

$$F(\gamma_s, \xi) = F(\gamma_s, \xi_s) + \frac{\partial}{\partial \xi} F(\gamma_s, \xi) \Big|_{\xi=\xi_s} (\xi - \xi_s) + \frac{1}{2} \frac{\partial^2}{\partial \xi^2} F(\gamma_s, \xi) \Big|_{\xi=\xi_s} (\xi - \xi_s)^2, \quad (4.56)$$

where the coefficients are derived from F straightforwardly,

$$\frac{\partial}{\partial \xi} F(\gamma_s, \xi) = -\gamma_s \quad (4.57)$$

and

$$\frac{\partial^2}{\partial \xi^2} F(\gamma_s, \xi) = \frac{\partial \gamma}{\partial \xi} = \frac{\partial \gamma}{\partial \chi'(\gamma_s)} \frac{\partial \chi'(\gamma_s)}{\partial \xi} = \frac{1}{\bar{\alpha}_s Y \chi''(\gamma_s)}. \quad (4.58)$$

Here, for convenience we again use the notation $Y = \ln x_0/x$. Note that the saddle point is defined by

$$\chi'(\gamma_s) = \frac{1}{\bar{\alpha}_s Y} \ln \frac{1}{r_{\perp}^2 Q_0^2} \quad (4.59)$$

while at the saturation scale $F = 0$. Plugging these coefficients into Eq. (4.56), we find that F can be written around ξ_s as

$$F(\gamma_s, r_{\perp}^2) = \gamma_s \ln(r_{\perp}^2 Q_s^2) - \frac{\ln^2(1/r_{\perp}^2 Q_s^2)}{2\bar{\alpha}_s Y \chi''(\gamma_s)}. \quad (4.60)$$

The amplitude itself in the presence of a saturation boundary condition is now written as

$$N(r_{\perp}^2, Y) = (r_{\perp}^2 Q_s^2)^{\gamma_s} \exp \left[\frac{-\ln^2(1/r_{\perp}^2 Q_s^2)}{2\bar{\alpha}_s Y \chi''(\gamma_s)} \right]. \quad (4.61)$$

We see that the leading order term in Eq. (4.60) is a function of $r_{\perp} Q_s$ only, instead of a function of r_{\perp} and $Y = \ln x_0/x$ independently. This property is known as geometric scaling⁸. Only in higher orders in the expansion this scaling property is violated.

⁸See section 2.5.

4.6. Summary

Moreover, $\chi''(\gamma_s) \approx 48.5$ so that the parameter of the scaling violating correction is $1/(2\bar{\alpha}_s\chi''(\gamma_s)) \approx 0.05$ for $\bar{\alpha}_s = 0.2$. Hence scaling violations are still suppressed if ξ moves away from ξ_s . This means that geometric scaling is predicted if ξ is close to ξ_s , and expected to hold to good approximation in the region where the expansion (4.56) is valid. From this analysis, the amplitude is expected to retain geometric scaling in the region $0 < \xi - \xi_s \ll \xi_s$, which means

$$1 < \ln 1/r_\perp^2 Q_s^2 \ll \ln Q_s^2/Q_0^2. \quad (4.62)$$

As noted in Ref. [44], (almost) this entire region is situated within the kinematic region (4.45) where⁹ the saddle point lies between 1/2 and roughly 3/4, so that the extent of the scaling window is consistent with the value of $\gamma_s = 0.628$. The region (4.62) is sometimes referred to as the extended geometric scaling (EGS) region. Its upper limit is often denoted as $Q_{gs} = Q_s^2/Q_0$.

4.6 Summary

In this chapter we have given a derivation of the BFKL equation in the dipole picture. We have seen that in the limit of $x \rightarrow 0$, the solution exhibits a power-like rise with $1/x$, i.e. $N(r_\perp, x) \sim (1/x)^\lambda$, where $\lambda \approx 0.5$. This leads to the conclusion that at very small x , the BFKL equation is to be replaced with a non-linear evolution equation, like e.g. the non-linear BK equation, which is discussed in the next chapter.

Further, we showed that in the small- r_\perp limit the solution of the BFKL equation falls off like $N(r_\perp, x) \sim r_\perp^{2\gamma}$, where γ is equal to 1 or γ_0 , if $\gamma_0 < 1$. Here, γ_0 is the power of the small- r_\perp limit of the initial condition, i.e. $N_0 = N(r_\perp, x_0) \sim r_\perp^{2\gamma_0}$. This property of the solution will be recovered from the BK equation in chapter 7.

Finally, the solution of the BFKL equation the presence of a saturation has been discussed. It follows that (for fixed coupling) the saturation scale increases power-like with $1/x$; $Q_s^2(x) \sim (1/x)^\lambda$, where $\lambda \approx 0.9$. We showed that the saddle point takes the value γ_s . Also, we derived the solution of the BFKL equation in the presence of the saturation boundary condition, given by Eq. (4.61). In the so-called EGS region, $1 < \ln 1/r_\perp^2 Q_s^2 \ll \ln Q_s^2/Q_0^2$, this solution exhibits approximate geometric scaling. As explained in chapter 6, these expectations for the properties of the dipole amplitude play an important role in phenomenological models for the dipole amplitude.

⁹The upper limit on the scaling window is equal to $\ln Q_s^2/Q_0^2 = \bar{\alpha}_s Y \chi'(\gamma_s)$.

Chapter 5

BK evolution

In this chapter, we discuss the non-linear BK equation for the x evolution of the dipole scattering amplitude. We briefly sketch how it is derived in Refs. [30, 72], and show some numerical results to illustrate that it leads to saturation and geometric scaling. Further, we discuss a number of analytical expectations for the solution of the BK equation that follow from the so-called travelling wave approximation. We end by summarizing the results that play a role in the analyses of the following chapters.

5.1 Introduction

In section 4.2 the leading order BFKL equation was constructed in the dipole picture of deep inelastic scattering. In the hadron rest frame, the evolution is contained in the density of gluons (which in the large- N_c limit are equivalent to dipoles themselves) in the quark-antiquark pair that scatters off the hadron, instead of in the gluon density in the hadron [72]. It was shown how this leads to a non-physically strong rise of the dipole amplitude N at small x . The dipole amplitude was defined as the convolution of the gluon (dipole) density inside the pair, with the propagator (through the target hadron) of such a dipole [39, 41]. The BFKL equation turns out to predict a rise of the dipole scattering amplitude at very small x that violates unitarity. To solve this problem, a non-linear evolution equation featuring a damping term would be required, to saturate the rise when the amplitude becomes large. Such an equation can be obtained by taking into account not only the scattering of a single gluon (dipole), from the quark-antiquark pair off the hadron, but including the scattering of any number of gluons (dipoles) in the dipole amplitude [30, 72]. The corresponding picture is represented schematically in Fig. 5.1. The dipole amplitude is then expressed as the convolution of the probability of finding i dipoles, P_i , with a propagator, f , that describes the scattering of a single dipole off the nucleus, for each dipole [30, 41, 72]. Schematically, this can be expressed as

$$N(r_{\perp}, x) \sim \sum_{i=1}^{\infty} P_i \otimes f \cdots f, \quad (5.1)$$

5.2. The BK equation

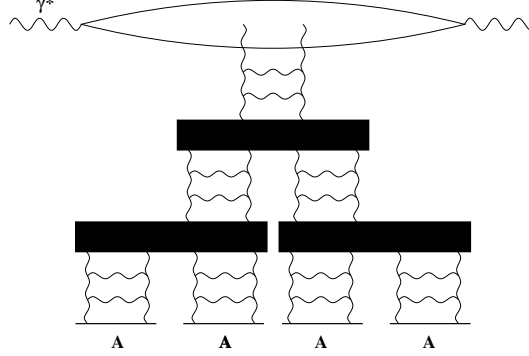


Figure 5.1: Fan diagram corresponding to multiple scattering of gluons (dipoles) off the hadron. Plot taken from [30].

where the number of propagators is equal to i . Differentiation with respect to $Y = \ln 1/x$ then yields a non-linear evolution equation for N , instead of the linear BFKL equation that would be obtained if only the first term of the sum is taken into account [30, 41]. This non-linear evolution equation, which is known as the Balitsky-Kovchegov (BK) equation, can therefore be thought of as a non-linear generalization of the BFKL equation.

5.2 The BK equation

The BK equation for the dipole scattering amplitude $N(x, r_{\perp}^2)$ in co-ordinate space reads [27, 30]

$$\frac{\partial}{\partial Y} N(r_{10\perp}^2, Y) = \bar{\alpha}_s \int \frac{d^2 r_{2\perp}}{2\pi} \frac{r_{10\perp}^2}{r_{20\perp}^2 r_{21\perp}^2} \times [N(r_{21\perp}^2, Y) + N(r_{20\perp}^2, Y) - N(r_{10\perp}^2, Y) - N(r_{21\perp}^2, Y)N(r_{20\perp}^2, Y)], \quad (5.2)$$

where $\bar{\alpha}_s = \alpha_s N_c / \pi$ and $Y = \ln 1/x$. For small values of N , the non-linear term can be neglected, so that the BFKL equation (4.18) is recovered. The BK equation can be much simplified by introducing the following transformation of the dipole amplitude $N(r_{\perp}^2, Y)$,

$$\mathcal{N}(k, Y) \equiv \int \frac{d^2 r}{2\pi} e^{ik \cdot r} \frac{N(r, Y)}{r^2}, \quad (5.3)$$

where we omit the subscript \perp on the transverse vectors. In terms of \mathcal{N} , the BK equation can be very compactly written as

$$\partial_Y \mathcal{N} = \bar{\alpha}_s \chi(-\partial_L) \mathcal{N} - \bar{\alpha}_s \mathcal{N}^2, \quad (5.4)$$

where $L = \ln(k^2/k_0^2)$, for some arbitrary scale k_0 , and χ is the BFKL kernel (4.25)

$$\chi(\gamma) = 2\psi(1) - \psi(\gamma) - \psi(1 - \gamma). \quad (5.5)$$

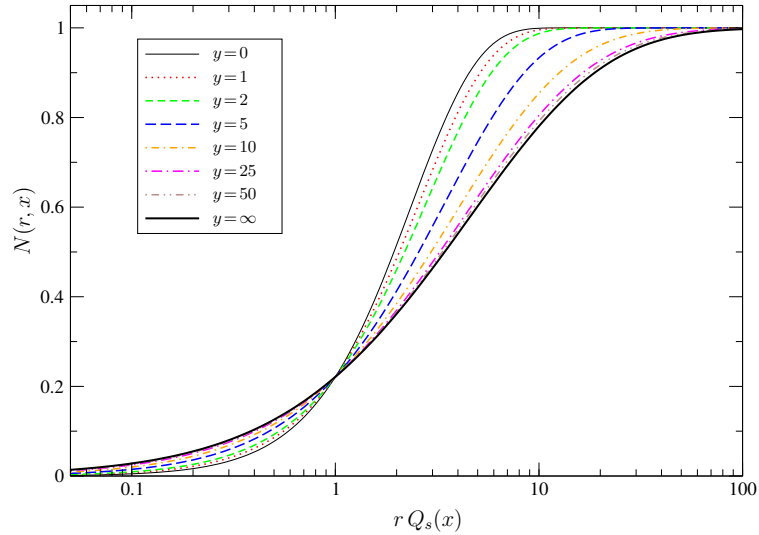


Figure 5.2: The dipole scattering amplitude $N(r, x)$ resulting from the numerical result $N(k, x)$ as a function of $rQ_s(x)$ for various rapidities y . The solution is evolved from the MV model (6.23) at $y = \ln(x_0/x) = Y - Y_0 = 0$.

The BK equation has not been solved analytically, although in some specific cases analytical results have been obtained [72, 75, 77–81]. Numerical solutions however have been obtained for all momenta [82–89], cf. [41]. We will discuss some analytical properties of the solution of the BK equation at large rapidities, obtained in the so-called travelling wave approximation, in section 5.3.

In order to investigate the relation between these analytical results at very large rapidity and the actual solution at finite rapidity, we will make a comparison with numerical solutions of the BK equation in chapter 7. We will use the results of [89], employing the publicly available code [90] to generate numerical solutions of the BK equation, by evolving some starting distribution¹.

As an illustration, Fig. 5.2 shows the solution of the BK equation generated by the code [90] for various values of the rapidity. While the properties of the solutions will be discussed in detail in chapter 7, we want to mention here the important property of geometric scaling. At asymptotically large values of $Y = \ln 1/x$, the dipole amplitude $N(r, x)$ that is plotted in Fig. 5.2 becomes a function of $rQ_s(x)$ only, which is known as geometric scaling. In the figure, this means that the solutions approach a limiting curve, labelled $y = \infty$.

¹Mostly, for this purpose we will use the MV model, discussed in section 6.2.1.

5.3 Travelling waves

In the so-called travelling wave approach, the BK equation is approximated by expanding the kernel $\chi(\gamma)$ around a characteristic value of γ . By doing so, it can be shown that the approximated BK equation belongs to the universality class of the Fisher-Kolmogorov-Petrovsky-Piscounov (FKPP) equation [78]. It is known that under certain circumstances equations of this class admit so-called travelling wave solutions [91]. In the case of the BK equation, this means that for asymptotically large rapidities, it admits geometrically scaling solutions, $\mathcal{N}(k, Y) \rightarrow \mathcal{N}(k/Q_s(Y))$. In this section we will briefly review some results of Refs. [75, 78], focussing only on those results that are relevant to our purposes.

5.3.1 The travelling wave approximation

In section 4.2 we have seen that the solution of the BFKL equation can be written as

$$\mathcal{N}_{\text{BFKL}} = \int \frac{d\gamma}{2\pi i} \mathcal{N}_0 \exp[-\gamma L + \bar{\alpha}_s \chi(\gamma) Y] \quad (5.6)$$

where, ignoring for the moment possible contributions from the initial condition, the integral is dominated by the saddle point γ_{sp} of the exponential. A useful observation is that Eq. (5.6) is a superposition of waves that are eigenfunctions of the operator ∂_L with eigenvalue $-\gamma$. Since the dominant contribution to the integral comes from $\gamma = \gamma_{sp}$, in first approximation $\mathcal{N}_{\text{BFKL}}$ is an eigenfunction of ∂_L with eigenvalue $-\gamma_{sp}$,

$$\partial_L \mathcal{N}_{\text{BFKL}} \approx -\gamma_{sp} \mathcal{N}_{\text{BFKL}}. \quad (5.7)$$

Knowing that the BK equation reduces to the BFKL equation in the dilute region, we can expect that there the solution of the full equation will have the same property. In Ref. [75, 78] the BK equation is then approximated by expanding $\chi(-\partial_L)$ around the BFKL saddle point γ_{sp} . One writes

$$\chi(-\partial_L) \approx \chi(\gamma_{sp}) + \chi'(\gamma_{sp})(-\partial_L - \gamma_{sp}) + \frac{1}{2} \chi''(\gamma_{sp})(-\partial_L - \gamma_{sp})^2. \quad (5.8)$$

We note that it is not clear that this is a good approximation in the non-linear regime, but that the authors of Ref. [78] expect it to remain valid for the full non-linear equation. If the kernel is expanded around the BFKL saddle point², cf. section 4.4, $\gamma_{sp} = 1/2$, the term χ' vanishes. With a change of variables $(k, Y) \rightarrow (x, t)$ [78], where $\bar{\gamma} = 1 - (1/2)\sqrt{1 + 8\chi(1/2)/\chi''(1/2)}$,

$$\begin{aligned} x &= (1 - \bar{\gamma}) \left(L + \frac{\bar{\alpha}_s \chi''(1/2)}{2} Y \right); \\ t &= \frac{\bar{\alpha}_s D}{\chi''(1/2)} (1 - \bar{\gamma})^2 Y, \end{aligned} \quad (5.9)$$

²If the solution is of the form (5.7), this requires roughly $L \ll 8\bar{\alpha}_s Y$, cf. Eq. (4.45).

the BK equation reduces to the Fisher-Kolmogorov-Petrovsky-Piscounov (FKPP) equation [92, 93]

$$\partial_t u(t, x) = \partial_x^2 u(t, x) - u(t, x)(1 - u(t, x)). \quad (5.10)$$

Here $u = 2\mathcal{N}/(D(1 - \bar{\gamma}^2))$. The evolution in the time variable t corresponds to evolution in rapidity Y . This equation was originally proposed to describe the advance of genes through a population [92]. At large times t , the equation admits so-called travelling wave solutions [91],

$$u(t, x) \xrightarrow{t \rightarrow \infty} u(x - ct), \quad (5.11)$$

i.e. solutions whose shape remains the same in time t , but travels in x space with phase velocity c . A condition for travelling wave solutions to occur is that the initial condition $u(t_0, x)$ decreases from 1 at $x = -\infty$ to 0 at $x = +\infty$, where it should approach 0 exponentially; $u(t_0, x) \sim \exp(-\beta x)$. In terms of \mathcal{N} , this condition implies that at large k , the amplitude should fall off like $\mathcal{N}(k, Y = 0) \sim k^{-2\gamma_0}$, for some (positive) value of γ_0 , where $\gamma_0 = (1 - \bar{\gamma})\beta$. For all cases that we will consider, this condition is satisfied, cf. sections 5.3.3 and C.3. Hence, for large t , the solution in terms of x and t , defined in Eq. (5.9), can indeed be written as $u(x - m(t))$, where $m(t) = 2t - (3/2) \ln t$ [78]. Consequently, at asymptotically large t , one obtains

$$u(t, x) \xrightarrow{t \rightarrow \infty} u(x - 2t), \quad (5.12)$$

or, in the original variables,

$$\mathcal{N} \xrightarrow{Y \rightarrow \infty} \mathcal{N}_{\text{TW}}(k^2/Q_s^2(Y)), \quad \text{where} \quad Q_s^2(Y) = k_0^2 \exp\left[\bar{\alpha}_s \chi''\left(\frac{1}{2}\right)\left(\frac{1}{2} - \bar{\gamma}\right)Y\right]. \quad (5.13)$$

Here, k_0^2 absorbs all constants of order 1. Thus, the approximation (5.8) leads to the expectation of geometric scaling at large Y . Since $\chi''(1/2)(1/2 - \bar{\gamma}) \approx 4.8$, the running of the saturation scale is consistent with the prediction from BFKL evolution in the presence of saturation³ (4.54).

In Ref. [75], an explicit solution of the BK equation is constructed using approximation (5.8) to expand the BFKL kernel around the saddle point in the presence of saturation, $\gamma_s \approx 0.628$, cf. Eq. (4.53). This reduces the BK equation to the following partial differential equation,

$$\partial_Y \mathcal{N} = \frac{1}{2} \bar{\alpha} \chi''(\gamma_s) (\partial_L + \gamma_s)^2 \mathcal{N} - \bar{\alpha} \chi'(\gamma_s) \partial_L \mathcal{N} - \bar{\alpha} \mathcal{N}^2, \quad (5.14)$$

which belongs to the universality class of the FKPP equation (5.10) that consists of equations of the form

$$\partial_t u(t, x) = D_x u(t, x) + f(u(t, x)) \quad (5.15)$$

where D_x is some differential operator, and f is a non-linear term. The evolution in the time variable t again corresponds to evolution in rapidity Y . Like the FKPP equation

³We note that in that case, the saddle point is given by $\gamma_s \approx 0.628$ instead of $1/2$.

5.3. Travelling waves

itself, all equations belonging to this universality class admit travelling wave solutions at asymptotically large times, under the discussed criterion for the initial condition.

The solution to the *linear* part of Eq. (5.14), i.e. not too close to the saturation region, is derived in [75], and reads

$$\mathcal{N}_{\text{TW (dilute)}} \propto \sqrt{\frac{2}{\bar{\alpha}} \chi''(\gamma_s)} \ln\left(\frac{k^2}{Q_s^2(Y)}\right) \left(\frac{k^2}{Q_s^2(Y)}\right)^{-\gamma_s} \exp\left(-\frac{1}{2\bar{\alpha}\chi''(\gamma_s)Y} \ln^2\left(\frac{k^2}{Q_s^2(Y)}\right)\right), \quad (5.16)$$

where $Q_s(Y)$, is given by

$$Q_s^2(Y) = Q_0^2 \exp\left[\bar{\alpha}_s \frac{\chi(\gamma_s)}{\gamma_s} Y - \frac{3}{2\gamma_s} \ln Y\right]. \quad (5.17)$$

Here, Q_0 again absorbs all constants. Eq. (5.16) is qualitatively similar to the expectation that follows from BFKL evolution in the presence of saturation, cf. Eq. (4.61). In the limit of $Y \rightarrow \infty$, we see that this travelling wave solution indeed becomes exactly geometrically scaling,

$$\mathcal{N}_{\text{TW (dilute)}} \sim \left(k^2/Q_s^2\right)^{-\gamma_s} \ln\left(\frac{k^2}{Q_s^2}\right), \quad (5.18)$$

where the saturation scale reduces to $Q_s^2 \sim \exp[\bar{\alpha}_s \chi(\gamma_s)/\gamma_s Y]$, which, as $\chi(\gamma_s)/\gamma_s = \chi'(\gamma_s)$, is identical to the BFKL result (4.54).

5.3.2 Travelling wave at subasymptotic rapidity

As pointed out in Ref. [80], the travelling wave results are of limited phenomenological importance due to the fact that they are asymptotic solutions, and hence require very high rapidities in order to arise. Also, analytical expressions for the dipole amplitude, like Eq. (5.16), are known only for relatively large values of k , so that analytical predictions can only be made for the tail of the amplitude, which is essentially determined by the linear regime [80].

In order to derive a solution that has a broader range of applicability, in Ref. [80] a travelling wave solution has been derived by truncating the kernel of the BK equation, where the non-linear term is kept⁴. The BK equation is approximated by writing

$$\partial_Y \mathcal{N} = \bar{\alpha} \chi_{P,\gamma_0}(-\partial_L) \mathcal{N} - \bar{\alpha} \mathcal{N}^2 \quad (5.19)$$

where the truncated kernel is defined as

$$\chi_{P,\gamma_0}(-\partial_L) = \sum_{p=0}^P (-1)^p A_p \partial_L^p; \quad A_p = \sum_{i=0}^{P-p} (-1)^i \frac{\chi^{i+p}(\gamma_0)}{i! p!} \gamma_0^i. \quad (5.20)$$

⁴We recall that Eq. (5.16) is a solution of the *linearized* version of Eq. (5.14).

In Ref. [80], the solution of the approximate equation is derived taking into account the first two terms of this expansion, i.e. $P = 2$. One finds

$$\mathcal{N}(k, Y) = \frac{A_0}{1 + (k^2/Q_s^2)^{\lambda/c}} - \frac{A_0}{c^2} \frac{(k^2/Q_s^2)^{\lambda/c}}{1 + (k^2/Q_s^2)^{\lambda/c}} \ln \frac{\left(1 + (k^2/Q_s^2)^{\lambda/c}\right)^2}{4 (k^2/Q_s^2)^{\lambda/c}} + \mathcal{O}(1/c^3), \quad (5.21)$$

where $\lambda = \sqrt{A_0/A_2}$ and $c = 2$. The saturation scale is defined as $Q_s^2(Y) = k_0^2 \exp(\bar{\alpha}_s v(c)Y)$, where $v(c) = A_1 + c \sqrt{A_0 A_2}$.

There are however several problems which make this solution impossible to use for our purposes. In this thesis, we investigate phenomenological dipole models that are of the form

$$N(r, Y) = 1 - \exp\left[-\frac{1}{4} (r^2 Q_s^2)^\gamma\right], \quad (5.22)$$

where following [48, 94] γ is often taken to be a function of k and Y , with $\gamma(k = Q_s) = \gamma_s$. The value of $\mathcal{N}(k = Q_s)$ is then fixed⁵ by Eq. (5.3). The commonly used value $\gamma(k = Q_s) = \gamma_s$ leads to $\mathcal{N}(k = Q_s) \approx 0.19$, while Eq. (5.21) equals $A_0/2$ at $k = Q_s$, which using $P = 2$, as was done in Ref. [80] equals approximately 4.5. This would require a value of $\gamma(k = Q_s) \approx 0.025$, which is completely inconsistent with the analyses of chapters 7 and 8, which show that $\gamma(k = Q_s)$ of around 0.6 is to be used in expression (5.22) in order to be compatible with RHIC data. We also note that in a non-linear equation, like the BK equation, the normalization of the solution must be fixed. Further, as already pointed out in Ref. [80], the series expansion for the coefficients A_p actually diverges fast as P increases. Hence, the value $\mathcal{N}(k = Q_s) = A_0/2$ is unstable with respect to the expansion (5.20), and even diverges. Also already mentioned in Ref. [80] is that Eq. (5.21) saturates at small k to a constant, equal to A_0 , and thus does not reproduce the proper small- k behaviour of $\mathcal{N} \sim \ln 1/k$. Hence, like the earlier result (5.16), we cannot use Eq. (5.21) in the saturation region $k < Q_s$, or around the saturation scale. Instead, we will focus on phenomenological models for the dipole amplitude in chapter 6, which incorporate some general features that are derived using the travelling wave approach.

5.3.3 The role of the initial condition

From section 4.5 we know that the poles of the initial condition can contribute to the integral (5.6). As explained in that section, an initial condition $\mathcal{N}(Y_0, k)$ with the asymptotic behaviour $\mathcal{N}(Y_0, k \rightarrow \infty) \sim k^{-2\gamma_0}$ will have a pole in Mellin space at $\gamma = \gamma_0$. This pole gives rise to a contribution to Eq. (5.6) that vanishes like $\exp(-\gamma_0 L)$ as $k \rightarrow \infty$, while the travelling wave (5.18), in the large- Y limit, is proportional to $\exp(-\gamma_s L)$. Consequently, when $\gamma_0 < \gamma_s \approx 0.628$ the solution is dominated by the initial condition at large k , whereas in the case of $\gamma_0 > \gamma_s$ the solution is dominated by the travelling wave (5.18).

This may seem at odds with the result of section 4.5, where we argued that in the case where $\gamma_0 > \gamma_{sp}$ the solution vanishes at large k as $k^{-2\gamma_{sp}}$, where the saddle point γ_{sp}

⁵This is made explicit in Eq. (7.14).

5.4. Summary

approaches 1 as $k \rightarrow \infty$, *not* γ_s . The reason for this is that the travelling wave solution only holds in the limit of large Y . As we will show in chapter 7, the limits $k/Q_s(Y) \rightarrow \infty$ and $Y \rightarrow \infty$ (keeping $k/Q_s(Y)$ fixed) *do not commute*. If Y is kept fixed at some finite value and k/Q_s goes to ∞ , one finds $\mathcal{N} \sim k^{-2}$. However, first taking the limit of $Y \rightarrow \infty$ (keeping $k/Q_s(Y)$ fixed) and afterwards increasing k/Q_s , one finds $\mathcal{N} \sim k^{-2\gamma_s}$ even when k/Q_s becomes larger and larger⁶.

5.4 Summary

In the dilute region, where the BK equation is well approximated by the BFKL equation, one can expand the kernel $\chi(-\partial_L)$ around the BFKL saddle point. It is generally assumed that this approximation holds for the full BK equation. This so-called travelling wave approximation brings the BK equation into the universality class of the FKPP equation. At asymptotically large rapidities, equations in this universality class allow travelling wave solutions, which translates into geometric scaling of the dipole amplitude, i.e. $\mathcal{N}(k, x) = \mathcal{N}(k/Q_s(x))$. The saturation scale then depends on $Y = \ln 1/x$ like $Q_s^2 \sim \exp[\bar{\alpha}_s \chi(\gamma_s)/\gamma_s Y]$. This is consistent with the expectation from the BFKL equation in the presence of a saturation boundary condition.

As mentioned, according to Ref. [78], the expansion of the kernel around the saddle point is expected to remain valid for the full BK equation, which would imply that geometric scaling is expected for asymptotic rapidities and all values of k . In chapter 7, we will find that this is indeed the case for the numerical solutions that we consider. In the dilute region, analytic forms of the solution of the travelling wave solution are known, which are of the form

$$\mathcal{N}_{\text{TW (dilute)}} \sim \left(k^2/Q_s^2\right)^{-\gamma_s} \ln\left(\frac{k^2}{Q_s^2}\right), \quad (5.23)$$

In particular, as this expression is valid at asymptotic Y and $k/Q_s \ll 1$, it leads to the expectation that in the limit of $Y \rightarrow \infty$, the large k/Q_s -behaviour of the amplitude is given by $\mathcal{N} \sim k^{-2\gamma_s}$. Since in the limit of $k/Q_s \rightarrow \infty$ and fixed Y , the amplitude is expected to fall off like $\mathcal{N} \sim k^{-2}$, the two limits do not commute. These properties of the solution will be investigated numerically in chapter 7.

⁶To be precise, in chapter 7 \mathcal{N} in the limit of $k/Q_s \rightarrow \infty$ is calculated numerically up to very large but of course not infinite values, and *seems* consistent with $\mathcal{N} \sim (k^2/Q_s^2)^{\gamma_s}$.

Chapter 6

Models for the dipole amplitude

In this chapter, we will present a number of models for the dipole cross section, aimed at describing DIS and nucleon-nucleus collisions. In this thesis, we will focus on the DHJ model that was proposed to describe d -Au collisions at RHIC, which incorporates expectations from small- x evolution.

In chapter 5 we encountered the nonlinear BK evolution equation for the dipole scattering amplitude. This equation describes saturation of the amplitude and leads to the prediction of geometric scaling at asymptotically small x . Unfortunately, the BK equation has not been solved analytically, so that in order to test it against experimental data one needs to resort to either numerical or approximate solutions, or phenomenological models. Numerical solutions have been constructed and will be touched upon in chapter 7, while the approximate solutions mentioned in section 5.3.2 are of little phenomenological use as explained there. Here, we will introduce a number of phenomenological models that have been devised in order to describe DIS and hadron collisions, in particular proton (or deuteron)-nucleus scattering, at small x . More precisely, we give a brief description of the GBW and IIM models that were proposed to describe DIS data, and the KKT and in particular the DHJ model that were constructed for the description of hadron-nucleus scattering (d -Au at RHIC). More models for DIS and RHIC can be found in respectively Ref. [95, 96] and Ref. [97]. The DHJ model plays an important role in this thesis, as it embodies the most important small- x features of the IIM and KKT models. In chapter 7 the compatibility of the DHJ model with the BK equation is tested using a numerical solution of the latter, while in chapter 8 the DHJ model is used to analyse the small- x properties of the deuteron-gold data from RHIC. The conclusions will apply to the IIM and KKT models as well. We will also formulate a model for the dipole amplitude that can be extracted from the MV model for a saturated nucleus in the colour glass condensate approach of chapter 3. This model, which was historically the first saturation model for the forward dipole amplitude, is however of limited phenomenological importance since it does not incorporate evolution in x , and does therefore not allow a study of geometric scaling. In this thesis, it will be used to reproduce and extend the results on Λ polarization of Ref. [57] as an introduction of chapter 9. It will also be used as an initial condition for

6.1. Dipole models for deep inelastic scattering

the numerical solution of the BK equation in chapter 7.

6.1 Dipole models for deep inelastic scattering

Here, we will present a number of models for the dipole amplitude that were proposed to describe the small- x DIS data. To see how these models have originated, we give a brief introduction to the concept of geometric scaling in experiment, which is incorporated in the Golec-Biernat-Wüsthoff (GBW) dipole model, and proceed to illustrate how theoretical expectations from small- x evolution spawned modifications of it.

6.1.1 Geometric scaling

As we have seen in chapter 2, the total cross section the deep inelastic scattering can be expressed as a function of the momentum transfer Q and the Bjorken variable x_B . As x_B becomes smaller than 0.01, the total cross section shows the so-called property of geometric scaling, which means that the cross section becomes a function of a single scaling variable, $Q^2/Q_s^2(x_B)$, instead of remaining a function of Q^2 and x_B independently. More specifically, geometric scaling was found in the data for $x_B \leq 0.01$ and all Q^2 [34, 45, 98]. Fig. 2.6.1, taken from Ref. [45], shows these small- x data as a function of $\tau = Q^2/Q_s^2(x_B)$, where the function $Q_s(x)$ is given by Eq. (6.5).

In the dipole picture, the scaling property of the data is a consequence of scaling of the dipole scattering amplitude, which gives the scattering of the virtual photon—described as a colour dipole—off the proton. The dipole amplitude must be a function of $r_\perp^2 Q_s^2(x)$ in order for the cross section to depend on $Q^2/Q_s^2(x)$. The cross section is written as $\sigma_{\text{tot}} = \sigma_T + \sigma_L$, where

$$\sigma_{T,L}(x_B, Q^2) = \sigma_0 \int d^2 r_\perp \int_0^1 dz |\psi_{T,L}(z, r_\perp, Q^2)|^2 N(r_\perp, x_B). \quad (6.1)$$

Here $N(r_\perp, x)$ denotes the dipole scattering amplitude, and $\psi_{T,L}$ is the photon wavefunction for transversely and longitudinally polarized photons—the probability that the photon fluctuates into a quark–antiquark pair (the colour dipole) of which the quark carries a momentum fraction z . Ignoring the quark masses, $\psi_{T,L}$ is given in first order in α_{em} by [34]

$$\begin{aligned} |\psi_T(z, r_\perp, Q^2)|^2 &= \frac{6\alpha_{\text{em}}}{4\pi^2} \sum_f e_f^2 \left[(z^2 + (1-z)^2) \epsilon^2 K_1^2(\epsilon r_\perp) \right] \\ |\psi_L(z, r_\perp, Q^2)|^2 &= \frac{6\alpha_{\text{em}}}{4\pi^2} \sum_f e_f^2 \left[4Q^2 z^2 (1-z)^2 K_0^2(\epsilon r_\perp) \right], \end{aligned} \quad (6.2)$$

where $\epsilon^2 = z(1-z)Q^2$, and K_i denote modified Bessel function of the second kind¹. Crucially, both $\psi_{T,L}$, and hence their sum, depend only on $r_\perp Q$, and have an overall factor

¹The functions K_i are also referred to (e.g. in Ref [34]) as MacDonald functions.

of Q^2 . If now the dipole amplitude depends only on $r_\perp Q_s$, we see that the total cross section can be schematically written as

$$\sigma_{T,L}(x_B, Q^2) \propto \int du f(u) N\left(u \frac{Q_s(x_B)}{Q}\right), \quad (6.3)$$

where $u = r_\perp Q$. Clearly, if the dipole amplitude is a function of $r_\perp Q_s$, the cross section depends on Q/Q_s only. Hence, geometric scaling in the dipole formalism means $N(r_\perp, x) = N(r_\perp Q_s(x))$. A successful description of the small- x DIS data using a geometric scaling model for the dipole cross section was performed by Golec-Biernat and Wüsthoff [34].

6.1.2 The GBW model

In Ref. [34] it was shown that the HERA data at low x could be well described by a dipole scattering amplitude of the following form,

$$N_{\text{GBW}}(r_\perp, x) = 1 - \exp\left[-\frac{1}{4} r_\perp^2 Q_s^2(x)\right], \quad (6.4)$$

which we will refer to as the Golec-Biernat-Wüsthoff (GBW) model. We can interpret this expression roughly as the Glauber-Mueller rescattering formula (2.39) near the saturation scale, where the gluon density divided by the transverse area is replaced by Q_s according to (2.33). We note that while Eq. (2.39) was obtained for scattering off a nucleus, the GBW model is used for DIS off the proton ($A = 1$). The parameter σ_0 in Eq. (6.1) was fitted to $\sigma_0 \approx 23$ mb, and the saturation scale Q_s is given by

$$Q_s(x) = 1 \text{ GeV} \left(\frac{x_0}{x}\right)^{\lambda/2}, \quad (6.5)$$

where $x_0 = 3 \cdot 10^{-4}$ and the best fit was found for $\lambda = 0.3$. The function $Q_s(x)$ is identified with the saturation scale that marks the onset of saturation of the target gluon density, or equivalently, it marks the region where nonlinear evolution becomes important. In sections 4.5 and 5.3 we saw that the small- x evolution equations, the BFKL and BK equations, predict that at leading order Q_s should have a power law dependence on x , which is consistent with Eq. (6.5) and hence with the DIS data². The dipole amplitude (6.4) approaches unity as r_\perp becomes large, and hence incorporates saturation. Also, it displays geometric scaling; it is a function of the single parameter $r_\perp Q_s(x)$. Even though the model independent analysis performed in [45] shows that the low- x data display geometric scaling for all Q^2 , the GBW model was found to be inconsistent with newer, more accurate data [99] at large Q^2 . In Ref. [99] a modification of the GBW model was proposed which includes DGLAP evolution, as required to fit the $Q^2 > 20 \text{ GeV}^2$ data. Alternatively, in

²We note that at LO and for fixed coupling, small- x evolution would lead to a value of $\lambda \approx 0.9$. However, if running of the coupling is included in the analysis one obtains $Q_s(x) \sim \exp(\lambda \sqrt{\ln 1/x})$, cf. section 7.2.3, which is numerically consistent with Eq. (6.5) in the region where the data is taken [98].

6.1. Dipole models for deep inelastic scattering

Ref. [100] the dipole scattering amplitude from the GBW model was replaced by a numerical solution to the leading order BK equation with running coupling and with the addition of a correction that satisfies DGLAP evolution in order to also describe the short distance behaviour of N correctly. As emphasized in Ref. [101], the solution of the BK equation (with running coupling) by itself only provides a satisfactory fit for relatively low Q^2 , up to a few GeV^2 . However, in Ref. [101] a different model is constructed, referred to as the Iancu-Itakura-Munier (IIM) model, which leads to a satisfactory fit to DIS data *without* the need to include DGLAP evolution at larger Q^2 . We note that the fact that the small- x DIS data can be described using these different approaches suggests that these data do not span a sufficiently large region in Q^2 and x to discriminate between the different types of evolution.

Even though the GBW model is a phenomenological model, and as such not a theoretical prediction of small- x physics, the property of geometric scaling *is* a prediction of small- x evolution (at asymptotically small x). In sections 4.5 and 5.3 we have seen that geometric scaling is expected to hold approximately in the *extended geometric scaling* (EGS) region $1 \lesssim \ln(Q^2/Q_s^2) \ll \ln(Q_s^2/\Lambda^2)$, where Λ is the QCD scale. This region grows when x becomes smaller, and eventually, at asymptotic values of $Y = \ln 1/x$, small- x evolution predicts scaling in the entire kinematic region. The IIM model proposed in Ref. [101] is a modification of the GBW model, constructed to describe the DIS data in the EGS region. We will discuss this model in the next section.

Here we must mention that although geometric scaling springs naturally from small- x evolution, its experimental observation does not necessarily prove the presence of such evolution. In Ref. [102] the impact of DGLAP evolution on a geometric scaling solution has been numerically studied. An initial condition was constructed so that at $Q^2 = Q_s^2(x)$, with $Q_s(x)$ as in Eq. (6.5), the dipole cross section at leading order is a constant, which makes it geometrically scaling. It was found that under DGLAP evolution to higher values of Q^2 geometric scaling is not violated for $\lambda \geq 4N_c\alpha_s/\pi$ in the fixed coupling case and only mildly violated for all values of λ in the running coupling case. In the latter case geometric scaling holds to very good approximation in the region $\ln Q^2/Q_s^2 \ll \ln Q_s^2/\Lambda^2$, which is exactly compatible with the EGS region predicted from small- x evolution. One can conclude that geometric scaling can be preserved to a large extent by DGLAP evolution. Moreover, in Ref. [103] the double asymptotic scaling (DAS) approximation³ to the LO DGLAP equation [15, 104] was used to demonstrate that DGLAP evolution can lead to a geometrically scaling solution, even without imposing a scaling boundary condition. It was estimated that DGLAP evolution may lead to geometric scaling in the kinematic region $Q^2 \gtrsim 10 \text{ GeV}^2$ and $x \lesssim 0.1$, where the DAS approximation is “quite accurate”. Hence the observation of scaling does not per se prove the breakdown of DGLAP evolution.

In fact, the small- x DIS data can be described without problems in the usual perturbative framework, in which the parton distribution functions evolve according to the DGLAP equations cf. Fig. 2.13. A description of the data including non-linear corrections to the DGLAP equations can be found in [105].

³Note that the name DAS implies scaling in the variables $\sqrt{\ln(1/x)\ln\ln Q^2}$ and $\sqrt{\ln(1/x)/\ln\ln Q^2}$, *not* geometric scaling.

6.1.3 The IIM model

From the analysis of section 4.5, cf. Eq. (4.61), it is expected that the dipole amplitude exhibits the following behaviour in the EGS region,

$$N(r_{\perp}, Y) = \left(r_{\perp}^2 Q_s^2\right)^{\gamma_s} \exp\left[-\frac{\ln^2(1/r_{\perp}^2 Q_s^2)}{2\bar{\alpha}_s Y \chi''(\gamma_s)}\right], \quad (6.6)$$

where $\bar{\alpha}_s = N_c \alpha_s / \pi$, $Y = \ln 1/x$, and χ is the BFKL kernel. The number $\gamma_s = 0.628$ is the BFKL saddle point in the presence of a saturation boundary condition, and is obtained by solving the equation $\chi'(\gamma) = \chi(\gamma)/\gamma$. Roughly the same behaviour of the dipole amplitude is expected from a travelling wave approximation of the BK equation, which can be seen by inspecting Eq. (5.16). We can rewrite expression (6.6) in the following way,

$$N(r_{\perp}, Y) = \left(r_{\perp}^2 Q_s^2\right)^{\gamma(r, Y)} \quad (6.7)$$

where we have defined the exponent γ as

$$\gamma(r_{\perp}, Y) = \gamma_s + \frac{c}{Y} \ln\left(\frac{1}{r_{\perp}^2 Q_s^2}\right), \quad (6.8)$$

with $1/c = 2\bar{\alpha}_s \chi''(\gamma_s)$.

In the GBW model the dipole amplitude is given instead by Eq. (6.4). In the EGS region, where $r_{\perp} Q_s < 1$, it can be approximately written as

$$N_{\text{GBW}}(r_{\perp}, Y) \sim r_{\perp}^2 Q_s^2(Y), \quad (6.9)$$

In order to incorporate the behaviour given by Eq. (6.8), in Ref. [101] the term $r_{\perp}^2 Q_s^2$ in Eq. (6.4) is replaced with $(r_{\perp}^2 Q_s^2)^{\gamma(r, Y)}$. As this behaviour is only expected for $r_{\perp} Q_s < 1$, in Ref. [101], in the saturation region $r_{\perp} Q_s > 1$ an extrapolation to $N = 1$ is used, resulting in the following form of the dipole amplitude in the IIM model,

$$\begin{aligned} N_{\text{IIM}}(r_{\perp}, Y) &= N_0 \left(\frac{r_{\perp}^2 Q_s^2}{2}\right)^{\gamma_s + \frac{1}{\kappa Y} \ln 2/r_{\perp} Q_s} && \text{for } r_{\perp} Q_s \leq 2, \\ N_{\text{IIM}}(r_{\perp}, Y) &= 1 - \exp\left[-a \ln^2(br_{\perp} Q_s)\right] && \text{for } r_{\perp} Q_s > 2. \end{aligned} \quad (6.10)$$

Note that the saturation scale, parameterized like in the GBW model as $Q_s^2 \sim (x_0/x)^\lambda$, has been rescaled by a factor of 2 so that $N(r_{\perp} = 2/Q_s, Y) = N_0$. The value of λ that provides the best fit was found to be $\lambda = 0.25 - 0.29$. The coefficients a and b are determined from the demand that the amplitude and its derivative with respect to r_{\perp} be continuous at $r_{\perp} = 2/Q_s$. The parameter κ is set to $\kappa = 2/c = 9.9$, in accordance⁴ with Eq. (6.8). The

⁴Note the difference of a factor of π w.r.t Eq. (6.8), namely $2/(\pi c) \approx 9.9$, since IIM use the BFKL solution without the saturation boundary condition, i.e. Eq. (3.43) of [44] instead of Eq. (3.36). However, in that case one should strictly speaking also use $\gamma_s = 0.5$, since that is the value of the BFKL saddle point in the absence of saturation.

6.2. Dipole models for nucleon-nucleus scattering

IIM model was specifically proposed to describe the small- x DIS data in the kinematic range “where one expects high density effects, namely $x \leq 0.01$ and $Q^2 < 50 \text{ GeV}^2$ ”, so as to test the expectations from BFKL evolution in the EGS region. Indeed, the IIM model was found to offer a better fit to the (newer) small- x DIS data in this region than the GBW model [101].

6.2 Dipole models for nucleon-nucleus scattering

We have seen how the DIS cross section at small x can be expressed in terms of the dipole amplitude. The scattering of nucleons off a nucleus can be described in terms of a parton from the nucleon scattering off the small- x field of the nucleus, which gives rise to (minus) the Fourier transform of the dipole amplitude on the level of the cross section. Thus, also nucleon-nucleus scattering at small x can be described in terms of the dipole amplitude.

In section 3.2.2, we presented a calculation [68] of the cross section of a quark (e.g. inside a proton) moving in the x^- direction that scatters off a nucleus that moves in the x^+ direction, where the nucleus is described as a colour glass condensate. In terms of the scattered quark’s momentum q , it is given in the eikonal approximation by Eq. (3.56),

$$x' \frac{d\sigma^{qA \rightarrow hX}}{dx' d^2q_\perp d^2b} = \frac{1}{(2\pi)^2} x' \delta(x - x') C(q_\perp), \quad (6.11)$$

where x is the longitudinal momentum fraction of the incoming quark (with respect to the momentum of its parent proton), and x' is the longitudinal momentum fraction of the scattered quark. The function $C(q_\perp)$, which will be further discussed in section 6.2.1, gives the squared amplitude of the partonic scattering process, and is expressed in Eq. (3.55) as the correlator of two Wilson line operators along the light-cone, describing the quark and its conjugate that arises from squaring the amplitude,

$$C(q_\perp) = \int d^2r_\perp e^{iq_\perp r_\perp} \langle [U(r_\perp) - 1][U^\dagger(0) - 1] \rangle_\rho. \quad (6.12)$$

Here, $\langle \rangle_\rho$ denotes the average over all configurations of colour sources of the nucleus. The correlator $C(q_\perp)$ is closely related to the dipole amplitude N in DIS. By the optical theorem, N is given by the imaginary part of the forward scattering amplitude, which yields (see e.g. [33, 56]),

$$N(r_\perp, x) = 1 - \langle U(r_\perp)U^\dagger(0) \rangle_\rho. \quad (6.13)$$

As we will see shortly, in section 6.2.1, the correlators of a single Wilson line operator are constant, and hence can be ignored in the Fourier transform in Eq. (6.12). Therefore, $C(q_\perp \neq 0)$ is equal to the Fourier transform of $\langle U(r_\perp)U^\dagger(0) \rangle_\rho$ so that, up to terms that are proportional to a δ -function, we have the following relation between the scattering

amplitude $C(q_\perp)$ and the dipole amplitude⁵ $N(r_\perp, x)$,

$$C(q_\perp) = - \int d^2 r_\perp e^{iq_\perp \cdot r_\perp} N(r_\perp, x). \quad (6.14)$$

This leads us to the following definition of the Fourier transform of the dipole amplitude, which enters the description of the cross section of p - A collisions,

$$N_F(q_\perp, x) = - \int d^2 r_\perp e^{iq_\perp \cdot r_\perp} N(r_\perp, x), \quad (6.15)$$

which makes sure that $N_F(q_\perp, x)$, and hence the cross section, is positive definite. Henceforth, will use the notation N for the dipole amplitude in co-ordinate space, which is used in the description of DIS, and the notation N_F for its Fourier transform defined in Eq. (6.15), which enters the description of p - A scattering.

The single inclusive cross section of hadron production in the total scattering process $p + A \rightarrow h + X$ can be obtained by convolving the partonic cross section (6.11) with the parton distribution functions ($f_{q/p}$) of the proton and the appropriate fragmentation functions ($D_{h/q}$) [46], yielding

$$x_F \frac{d\sigma^{pA \rightarrow hX}}{dx_F d^2 p_\perp d^2 b} = \int_{x_F}^1 dx' \int_{x_F}^1 \frac{dz}{z^2} f_{q/p}(x, Q^2) x' \frac{d\sigma^{qA \rightarrow hX}}{dx' d^2 q_\perp d^2 b} D_{h/q}(z, Q^2), \quad (6.16)$$

where a summation over quark flavours is understood. Here, x_F is the longitudinal momentum fraction of the produced hadron, whose momentum p is defined with respect to the fragmenting quark as $p = zq$. Hence, we have $q_\perp = p_\perp/z$ and $x_F = xz$, cf. appendix B, so that we can write

$$\begin{aligned} x_F \frac{d\sigma^{pA \rightarrow hX}}{dx_F d^2 p_\perp d^2 b} &= \frac{1}{(2\pi)^2} \int_{x_F}^1 \frac{dz}{z^2} f_{q/p}(x_F/z, Q^2) \frac{x_F}{z} C(p_\perp/z) D_{h/q}(z, Q^2) \\ &= \frac{1}{(2\pi)^2} \int_{x_F}^1 dx \frac{x}{x_F} f_{q/p}(x, Q^2) C(xp_\perp/x_F) D_{h/q}(x_F/x, Q^2). \end{aligned} \quad (6.17)$$

In this expression, contributions from gluons scattering off the nucleus are ignored. Taking into account also these contributions, one finds⁶ [47]

$$\begin{aligned} \frac{dN_h}{dy_h d^2 p_\perp} &= \frac{K(y_h)}{(2\pi)^2} \int_{x_F}^1 dx_1 \frac{x_1}{x_F} \left[f_{q/p}(x_1, Q^2) N_F \left(\frac{x_1}{x_F} p_\perp, x_2 \right) D_{h/q} \left(\frac{x_F}{x_1}, Q^2 \right) \right. \\ &\quad \left. + f_{g/p}(x_1, Q^2) N_A \left(\frac{x_1}{x_F} p_\perp, x_2 \right) D_{h/g} \left(\frac{x_F}{x_1}, Q^2 \right) \right], \end{aligned} \quad (6.18)$$

where N_F is the dipole amplitude in momentum space, defined in Eq. (6.15), which in the MV model is written as C , and N_A is the corresponding expression that applies to gluons.

⁵More precisely, $C(q_\perp)$ is the Fourier transform of $-N(r_\perp, x, b_\perp)$. However, we will not consider impact parameter dependence of the dipole amplitude in this thesis, cf. the discussion in section 6.2.3.

⁶Note that Eq. (6.18) is an expression for the (minimum bias) invariant yield, $dN_h \simeq d\sigma/d^2 b$, since we do not consider the impact parameter dependence of N .

6.2. Dipole models for nucleon-nucleus scattering

We emphasize again that our notation is such that N_{FA} are amplitudes in momentum space, which are related to the corresponding amplitude in co-ordinate space N (as used in DIS) by Eq. (6.15).

Eq. (6.18) is written in terms of the rapidity y_h of the produced hadrons. Ignoring the masses, it is related to the longitudinal momentum fraction by $x_F = p_\perp \exp(y_h) / \sqrt{s}$. The momentum fraction of the target gluons is given by $x_2 = x_1 \exp(-2y_h)$. Details on the kinematics of the scattering process can be found in appendix B. The parton distribution functions and fragmentation functions are evaluated at the scale $Q^2 = p_\perp^2$, and evolve according to the DGLAP equations. In Ref. [47] it is shown that this accounts for LO radiative corrections. Finally, there is an overall K -factor that effectively accounts for resummed NLO corrections. As it is expected [48] that these corrections are more important at small y_h , the K -factor is allowed to be y_h dependent. NLO pQCD analyses show that at RHIC energies such K -factors are indeed relatively constant with p_\perp [106–108].

Eq. (6.18) is represented schematically in Fig. 2.12. By means of Eq. (6.18), hadron production in proton-nucleus collisions at very high energies can be described in terms of the same dipole scattering amplitude as the small- x DIS data⁷.

A number of models have been constructed to describe the p_\perp distribution of produced hadrons in d - Au collisions at the relativistic heavy ion collider (RHIC). The GBW and IIM models that have been proposed to describe the small- x DIS data are not suitable for this purpose, due to the fact that it is the Fourier transform of the dipole amplitude that enters the cross section. The GBW model has a Gaussian dependence on r_\perp , and hence so does its Fourier transform, which turns out to be unable to describe the d - Au data⁸. The IIM model on the other hand leads to unphysical oscillations in the Fourier transform of the dipole amplitude, caused by the fact that the exponent γ depends on r_\perp . In the following, we will discuss the KKT and DHJ models, which were proposed to describe the RHIC data. However, first we extract a parameterization of the dipole amplitude from the MV model, by translating $C(q_\perp)$, defined in Eq. (3.55), into a dipole amplitude N_F using Eq. (6.15).

6.2.1 The MV model

The squared amplitude—in momentum space—of a quark scattering off the colour glass condensate, the small- x gluon field of an ultrarelativistic nucleus, was calculated in section 3.2.2, and denoted with $C(k_\perp)$.

In the MV model, the distribution of sources, ρ , is Gaussian, and the average over the source configurations can be computed analytically [70]. We note that a numerical code for the calculation of $C(k_\perp)$ was written by François Gelis and made publicly available [109]. The analytic result is given in Eq. 3.55, which reads

$$\langle (U(0) - 1)(U^\dagger(r_\perp) - 1) \rangle_\rho = e^{-2\pi B_2(r_\perp)} - 2e^{-2\pi B_1} + 1, \quad (6.19)$$

⁷Since in DIS, a quark-antiquark dipole scatters off the target hadron, the scattering of the dipole is there given by N_F .

⁸Data for hadron production in d - Au collisions at RHIC will be shown in chapter 8.

where B_1 and B_2 are given by⁹

$$\begin{aligned} B_1 &= Q_s^2 \int \frac{d^2 k_\perp}{(2\pi)^2} \frac{1}{k_\perp^4}; \\ B_2(r_\perp) &= Q_s^2 \int \frac{d^2 k_\perp}{(2\pi)^2} \frac{2}{k_\perp^4} [1 - e^{i k_\perp \cdot r_\perp}]. \end{aligned} \quad (6.20)$$

Both integrals can be performed directly using a lower cut-off on the transverse momenta, for which we will take the QCD scale Λ . Since present data do not probe the deep saturation region $r_\perp \geq 1/Q_s$, but rather the region $r_\perp \leq 1/Q_s$, we can approximate B_2 for small r_\perp , in order to obtain an expression that is appropriate in this kinematic regime. Using Eqs. (A.15) and (A.28) from appendix A.1, we can write for small values of r_\perp ,

$$\begin{aligned} B_1 &\simeq \frac{Q_s^2}{4\pi\Lambda^2}; \\ B_2(r_\perp) &\simeq \frac{r_\perp^2 Q_s^2}{4\pi} \ln \frac{1}{r_\perp \Lambda}. \end{aligned} \quad (6.21)$$

In the MV model, the saturation scale Q_s is a constant, which we will assume to be considerably larger than Λ , so that $B_1 \gg 1$. Hence, we can neglect the term $\exp(-2\pi B_1)$ in Eq. (6.19), which only contributes to $C(k_\perp = 0)$ anyway, and write

$$\begin{aligned} C(k_\perp) &= \int d^2 r_\perp e^{i k_\perp \cdot r_\perp} \langle U(r_\perp) U^\dagger(0) \rangle_\rho \\ &= \int d^2 r_\perp e^{i k_\perp \cdot r_\perp} \left[\exp\left(-\frac{1}{4} r_\perp^2 Q_s^2 \ln \frac{1}{r_\perp^2 \Lambda^2}\right) \right], \end{aligned} \quad (6.22)$$

where we ignore all constant contributions, as they vanish for $k_\perp \neq 0$. Since $C(k_\perp)$ is minus the Fourier transform of the dipole scattering amplitude in co-ordinate space, cf. Eq. (6.15), $N(r_\perp, x)$, we can see that the expression for N that corresponds to $C(q_\perp)$ is

$$N(r_\perp, x) = 1 - \exp\left[-\frac{1}{4} r_\perp^2 Q_s^2 \ln \frac{1}{r_\perp^2 \Lambda^2}\right]. \quad (6.23)$$

This is the amplitude, for small r_\perp , i.e. $r_\perp < 1/Q_s$, in the MV model, which we will for convenience refer to as the MV model from now on. We again emphasize that in the MV model, the saturation scale is a constant, so that there is no x dependence in Eq. (6.23). We also note the occurrence of an ultraviolet divergence in Eq. (6.23), which needs to be regularized. In Ref. [110] it is shown that the model does not depend much on the details of the regularization. Hence, we will simply choose the common regularization consisting of the replacement $\ln(1/(r_\perp^2 \Lambda^2)) \rightarrow \ln(e + 1/(r_\perp^2 \Lambda^2))$, and use

$$N_{\text{MV}}(r_\perp, x) = 1 - \exp\left[-\frac{1}{4} r_\perp^2 Q_s^2 \ln\left(e + \frac{1}{r_\perp^2 \Lambda^2}\right)\right]. \quad (6.24)$$

⁹Note that we have rescaled Q_s by a factor of 2π for consistency with the convention for $N_{\text{MV}}(r_\perp, x)$ in the literature.

6.2. Dipole models for nucleon-nucleus scattering

as the MV model expression for the dipole amplitude N . We note that Eq. (6.19) was derived by generalizing the scattering amplitude of an electron off a background field, so that it does not offer an equivalent expression for the description of the scattering of a gluon.

From Eq. (6.24) the behaviour of $C(k_\perp)$ at large values of $k_\perp \gg Q_s$ can be estimated. At such large k_\perp , the dominant contribution to the integral comes from $r_\perp \sim 1/k_\perp$. Ignoring the constant term, which only contributes at $k_\perp = 0$, one obtains by expanding the exponential [57, 70]

$$C(k_\perp, x) \sim 2 \frac{Q_s^2}{k_\perp^4} \left[1 + \frac{4}{\pi} \frac{Q_s^2}{k_\perp^2} \ln \left(\frac{k_\perp^2}{\Lambda^2} \right) + \mathcal{O} \left(\frac{Q_s^4}{k_\perp^4} \right) \right]. \quad (6.25)$$

Clearly, unlike the GBW model, the MV model reproduces the expected perturbative tail at large k_\perp , cf. section C.3.

Since the Gaussian distribution of sources is not preserved under x evolution, the MV model does not incorporate evolution [37]. In particular, it has a constant saturation scale. In experiments however, the concept of geometric scaling, which is intrinsically related to the x dependence of the saturation scale, plays an important role. Hence, in the absence of analytical solutions of the nonlinear evolution equations, a number of phenomenological models have been constructed in order to describe data.

6.2.2 The KKT model

In Ref. [94] a model was put forward in order to perform a quantitative analysis of hadron production in deuteron-gold (d -Au) collisions as measured at RHIC, based on the same philosophy as the model of IIM. In this model, which we will call the Kharzeev-Kovchegov-Tuchin (KKT) model, the dipole scattering amplitude has the following form,

$$N_{A \text{ KKT}}(k_\perp, y_h) = \int d^2 r_\perp e^{ik_\perp r_\perp} \left\{ \exp \left[-\frac{1}{4} (r_\perp^2 Q_s^2)^{\gamma_{\text{KKT}}(r_\perp, y_h)} \right] - 1 \right\}. \quad (6.26)$$

This N_A describes the scattering of a gluon, while the corresponding expression that describes the scattering of a quark, N_F , is obtained from N_A by the substitution $Q_s^2 \rightarrow (C_F/C_A)Q_s^2 = (4/9)Q_s^2$. The saturation scale is given by

$$Q_s(y_h) = Q_0 \exp(\lambda(y_h - y_0)), \quad (6.27)$$

where $\lambda = 0.3$, y_h is the rapidity of the produced hadron and y_0 denotes the “lowest value of the rapidity at which the low- x quantum evolution effects are essential”, which is taken as a free parameter. KKT fix it to $y_0 = 0.6$. The exponent γ_{KKT} , which in Ref. [94] is called the anomalous dimension, is like in the model of IIM inspired by properties that are predicted by the BFKL equation. It is written as

$$\gamma_{\text{KKT}}(r_\perp, y_h) = \frac{1}{2} \left[1 + \frac{\xi(r_\perp, y_h)}{\xi(r, y_h) + \sqrt{2\xi(r_\perp, y_h) + 7\zeta(3)c}} \right] \quad (6.28)$$

where c is a parameter to be fitted, and the function ξ is given by

$$\xi(r_{\perp}, y_h) = \frac{\ln 1/(r_{\perp}^2 Q_s^2(y_h = y_0))}{(\lambda/2)(y_h - y_0)}. \quad (6.29)$$

We note that the value of γ_{KKT} at the saturation scale is equal to the BFKL saddle point $1/2$, instead of the value in the presence of a saturation boundary condition, 0.628 . The parameterization is chosen in this way since it reproduces the BFKL saddle point in both the double logarithmic approximation (DLA) and the leading logarithmic approximation. In the former limit of fixed y_h and $r_{\perp} \rightarrow 0$ it reduces to $\gamma_{\text{KKT}} \rightarrow 1 - \sqrt{1/(2\xi)}$, cf. Eq. (4.46), while in the latter limit of fixed r_{\perp} and $y_h \rightarrow \infty$ it reduces to $\gamma_{\text{KKT}} \rightarrow 1/2 + \xi/(14c\zeta(3))$, cf. Eq. (4.44). An important difference with the parameterization (6.10) of IIM is that $\gamma_{\text{KKT}} \rightarrow 1$ for $r_{\perp} \ll 1/Q_s$, so that¹⁰

$$N(r_{\perp} \ll 1/Q_s) \sim r_{\perp}^2. \quad (6.30)$$

Note that the dipole amplitude in momentum space is needed to obtain the p_{\perp} spectrum, in order to calculate which, the authors of Ref. [94] performed the substitution $\gamma_{\text{KKT}}(r_{\perp}, y_h) \rightarrow \gamma_{\text{KKT}}(1/(2k_{\perp}), y_h)$, where $r_{\perp} \approx 1/(2k_{\perp})$ is taken as a characteristic value of the dipole size.

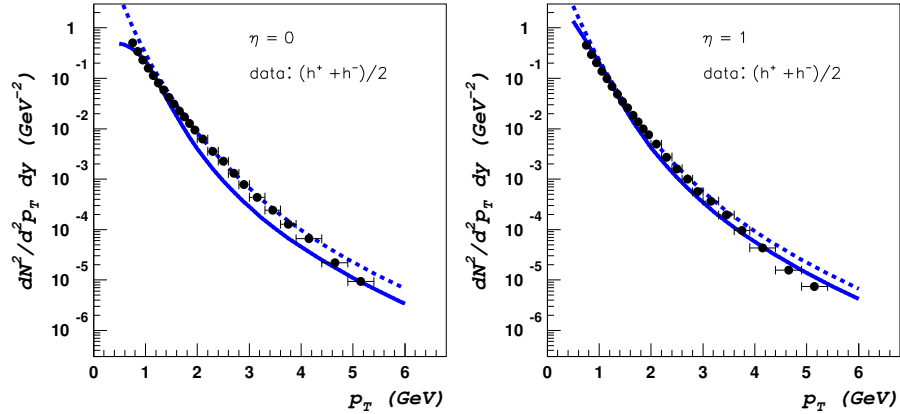


Figure 6.1: KKT model results for the p_{\perp} distribution of charged particles $((h^+ + h^-)/2)$ with $\eta = 0, 1$ at RHIC. The solid line corresponds to $\kappa = 0$, the dashed line to $\kappa = 1$, where $\kappa^2 A^{1/3}$ is a non-perturbative scale that is added to Q_s . Plots taken from [94].

Although the KKT model offers a reasonable agreement with the data on the transverse momentum distribution of charged hadrons produced in the d - Au collisions, in

¹⁰As discussed in appendix C, at small r_{\perp} one expects $N \sim r_{\perp}^2$.

6.2. Dipole models for nucleon-nucleus scattering

Fig. 6.2.2 we see that for $\eta = 0, 1$, where $\eta \approx y_h$ is the pseudo-rapidity of the produced particles, the slope of the p_\perp distribution becomes too shallow as p_\perp increases, while the forward data (not shown) are well described. This feature, which is shared by the IIM and DHJ models, will be discussed in detail in chapter 8.

6.2.3 The DHJ model

In Ref. [48] it was recognized that in the KKT model (6.28) for the dipole amplitude even at $y_h = 0$ remains within approximately 20% of 0.6 which causes the slope of the resulting p_\perp distribution to be too shallow at central rapidities. In the words of [48], the EGS region, where γ is still close to its value at Q_s , extends to too large values of $1/r_\perp$. Instead, “at mid-rapidity and $p_\perp \sim 4$ GeV, the data require a rapid approach to the DGLAP regime”, which means $\gamma \approx 1$. According to Ref. [48], this means that substantial scaling violations are needed to describe the data. We note however that γ not being constant does not necessarily imply scaling violations, since γ could rise as a function of $r_\perp Q_s$ and thus preserve geometric scaling. In chapter 8 we will in fact show that the RHIC data require no scaling violations.

In Ref. [48], the following requirements for the anomalous dimension γ were formulated,

1. At any fixed value of x , γ should approach 1 as $r_\perp \rightarrow 0$.
2. At any value of x , $\gamma(r_\perp = 1/Q_s)$ should equal γ_s .
3. At fixed values of $r_\perp Q_s$, γ should decrease towards γ_s as $x \rightarrow 0$.
4. At small but fixed x , the upper limit on the EGS region must be consistent with the BFKL expectation $Q_{gs}^2 = Q_s^4/Q_0^2$, cf. section 4.5.2.

Requirement 1. makes sure that the correct perturbative limit Eq. (6.30) is reproduced. We note however that, as discussed in chapter 7, also if the BFKL equation governs the large- q_\perp region, one can find that $\gamma \rightarrow 1$ at large q_\perp . Requirements 2-4. are expected from BFKL evolution, which can be seen from Eq. (6.8) and section 4.5.2. The anomalous dimension γ is parameterized according to these requirements as follows,

$$\gamma_{\text{DHJ}}(r_\perp, Y) = \gamma_s + (1 - \gamma_s) \frac{|\ln 1/(r_\perp^2 Q_s^2(Y))|}{\lambda Y + d\sqrt{Y} + |\ln 1/(r_\perp^2 Q_s^2(Y))|}, \quad (6.31)$$

where d is a free parameter that is fitted to $d = 1.2$, and $Y = \ln 1/x$. The parameter $\lambda = 0.3$ is fixed via requirement 4. by the saturation scale, which is parameterized like in the GBW model (6.5) as

$$Q_s^2(x) = Q_0^2 A^{1/3} \left(\frac{x_0}{x}\right)^\lambda, \quad (6.32)$$

where $Q_0 = 1$ GeV and $x_0 = 3 \cdot 10^{-4}$. The factor of A takes into account the size of the Au nucleus. Instead of $A = 197$, which is the number of nucleons of the gold nucleus,

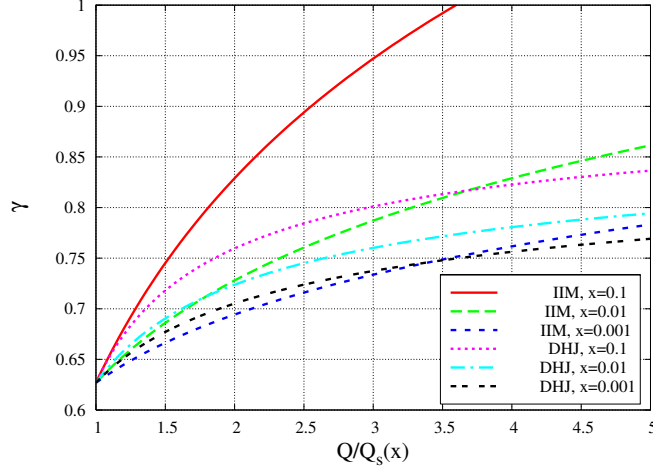


Figure 6.2: $\gamma(1/Q, x)$ as a function of $Q/Q_s(x)$ in the DHJ model, compared with the IIM model, for various values of x . Plot taken from Ref. [48].

an effective value of $A_{\text{eff}} = 18.5$ is used, to account for impact parameter dependence. Fig. 6.2 shows $\gamma_{\text{DHJ}}(k_{\perp}, x)$ as a function of $k_{\perp}/Q_s(x)$, together with $\gamma_{\text{IIM}}(k_{\perp}, x)$.

The parameterization (6.31) is approximately geometrically scaling—i.e. the dipole amplitude depends on $r_{\perp}Q_s(x)$ instead of on r_{\perp} and x separately—if $\Delta\gamma$ is small with respect to γ_s . The region where geometric scaling holds approximately is known as the extended geometric scaling (EGS) region. Hence, the parameterization (6.31) satisfies requirement 4, since for large (but fixed) rapidity $Y \gg (d/\lambda)^2$, the EGS region roughly extends to $\ln Q_{gs}^2/Q_s^2 \sim \lambda Y$, which implies that numerically $Q_{gs} \approx Q_s^2/\Lambda$. We note however that the scale $Q_{gs} = Q_s^2/\Lambda$ as a function of $r_{\perp}Q_s$ will depend on x , so that the EGS region $1 \leq 1/(r_{\perp}Q_s) \leq Q_{gs}$ does not correspond to any fixed region if different values of x are considered. The scale Q_{gs} simply parameterizes where the anomalous dimension becomes close to 1.

In Ref. [48], the substitution $r_{\perp} \rightarrow 1/k_{\perp}$ has been made in Eq. (6.31) in order to facilitate the calculation of the Fourier transform (6.15) of the dipole amplitude, i.e.

$$N_{A \text{ DHJ}}(k_{\perp}, Y) = \int d^2r_{\perp} e^{ik_{\perp}r_{\perp}} \left\{ \exp \left[-\frac{1}{4} (r_{\perp}^2 Q_s^2)^{\gamma_{\text{DHJ}}(r_{\perp}=1/k_{\perp}, Y)} \right] - 1 \right\}, \quad (6.33)$$

that is needed to calculate the p_{\perp} distribution of produced hadrons using Eq. (6.18). The amplitude for quark scattering, N_F , is, similarly to the KKT model, obtained from the substitution $(r_{\perp}^2 Q_s^2)^{\gamma} \rightarrow ((C_F/C_A)r_{\perp}^2 Q_s^2)^{\gamma}$, with $C_F/C_A = 4/9$ in Eq. (6.33). Plots of the resulting p_{\perp} distributions will be given in chapter 8. The DHJ model offers a good description of forward hadron production in deuteron gold collisions at RHIC, but does not completely solve the problem diagnosed in the KKT model, namely the too shallow

6.2. Dipole models for nucleon-nucleus scattering

slope of the p_{\perp} distribution at larger p_{\perp} at central rapidities¹¹.

We will take the DHJ model as the archetype of small- x dipole models, since it incorporates all features of the EGS region expected from BFKL/BK evolution, cf. Eq. (6.8), which are shared by the IIM and KKT models. In chapter 7 we will investigate numerically whether these BFKL/BK inspired properties are corroborated by the full BK equation. In chapter 8 we will test whether these properties, especially the geometric scaling violations and the logarithmic dependence of γ on r_{\perp} , are actually confirmed by the RHIC data.

¹¹The analysis of [48] turns out to contain an artificial cut-off on the x_2 -integration in the numerical code, which caused the central rapidity data to be well describable by the model (6.31).

Chapter 7

Compatibility of phenomenological models with the BK equation

In chapter 6 we have encountered a number of phenomenological models for the dipole scattering amplitude that are inspired by small- x evolution as described by the BK equation. They incorporate features that are expected from analyses based on approximating the BK equation either with the BFKL equation in the presence of a saturation boundary condition, which is mentioned in section 4.5, or with the travelling wave approximation, which is described in section 5.3. Since in both these approaches the BK equation is approximated *above* the saturation scale, i.e. for $r_{\perp} < 1/Q_s(x)$, it is a priori unclear that all expectations following from these approximations are consistent with the full BK equation. In this chapter, we will investigate whether this is the case by making a comparison between the DHJ model and the numerical solutions of the BK equation of [89]. We take the DHJ model as the typical representative of the small- x dipole models, since it incorporates all expectations from the mentioned theoretical approaches, most of which are shared by the IIM and KKT models.

In section 7.1 numerical solutions of the BK equation are briefly reviewed. In section 7.2 we use these numerical solutions of the BK equation, in combination with the general parameterization of the dipole amplitude employed in the DHJ model, to study whether the properties of the DHJ model are compatible with BK evolution. We also study the x dependence of the saturation scale with and without running coupling and consider the dependence of the results on the initial conditions. Finally, we summarize the main conclusions that can be drawn from the comparisons we have performed.

7.1 Numerical solution of the BK equation

The BK equation has been solved numerically by many people [82–89], even including impact parameter dependence [111–114]. Here, we will use the solutions obtained in Ref. [89], since a program called ‘BKSolver’ that generates these solutions is made publicly available [90]. The BKSolver program yields a numerical result for the dipole amplitude in momentum space, $\mathcal{N}(k, x)$, which is related to the amplitude in co-ordinate space by Eq. (5.3),

$$\mathcal{N}(k, x) \equiv \int \frac{d^2r}{2\pi} e^{ik \cdot r} \frac{N(r, x)}{r^2}. \quad (7.1)$$

In this expression, and in the remainder of this chapter, we neglect writing the subscript \perp with the transverse vectors for convenience. We recall that in the DHJ model, like in most models that were discussed in chapter 6, the dipole amplitude in co-ordinate space is written as

$$N(r, x) = 1 - \exp\left[-\frac{1}{4} \left(r^2 Q_s^2(x)\right)^{\gamma(r, x)}\right], \quad (7.2)$$

where the so-called anomalous dimension γ of the DHJ model is given in Eq. (6.31), and the saturation scale is given by

$$Q_s^2(x) = Q_0^2 \left(\frac{x_0}{x}\right)^{\lambda/2}, \quad (7.3)$$

with $Q_0 = 1$ GeV, $x_0 \simeq 3 \times 10^{-4}$ and $\lambda \simeq 0.3$. In terms of \mathcal{N} , the BK equation takes the particularly simple form

$$\partial_Y \mathcal{N} = \bar{\alpha}_s \chi(-\partial_L) \mathcal{N} - \bar{\alpha}_s \mathcal{N}^2, \quad (7.4)$$

where $\chi(\gamma) = 2\psi(1) - \psi(\gamma) - \psi(1 - \gamma)$ is the BFKL kernel (4.25), $\bar{\alpha}_s = N_c/\pi \alpha_s$, and $L = \ln(k^2/k_0^2)$, for some arbitrary scale k_0 . We will not consider the impact parameter dependence of the dipole amplitude in the present analysis. As an illustration of the general properties of the solution, Fig. 7.1 shows the dipole amplitude in co-ordinate space after several steps of evolution¹ in the rapidity variable $y = \ln(x_0/x) \propto Y$, where x_0 is the—irrelevant—value of x from which the evolution starts. Clearly, as expected from the $0 + 1$ dimensional case, Eq. (2.42), cf. Fig. 2.10, $N(r, x)$ vanishes for small r and approaches 1 in the saturation region $rQ_s > 1$. We see from the figure that geometric scaling is found at asymptotically large rapidities, where the solution approaches a limiting curve. To quantify the amount of scaling violation at finite rapidities, Fig. 7.2 shows the solution for $\mathcal{N}(k, x)$ relative to the limiting curve at $y \rightarrow \infty$, denoted by $\mathcal{N}_\infty(k/Q_s)$. Unless stated otherwise, all results of this section have been obtained using a fixed coupling constant $\bar{\alpha} = 0.2$.

The numerical solutions of the BK equation require the input of a starting distribution $\mathcal{N}(k, x = x_0)$. The starting distribution should be appropriate to the choice of x_0 , which itself should be small enough for BK evolution to be applicable. If x_0 is sufficiently

¹ Q_s is defined as the point where $N(r = 1/Q_s(x), x)$ equals a fixed value $\simeq 0.2$, cf. Eq. (7.8).

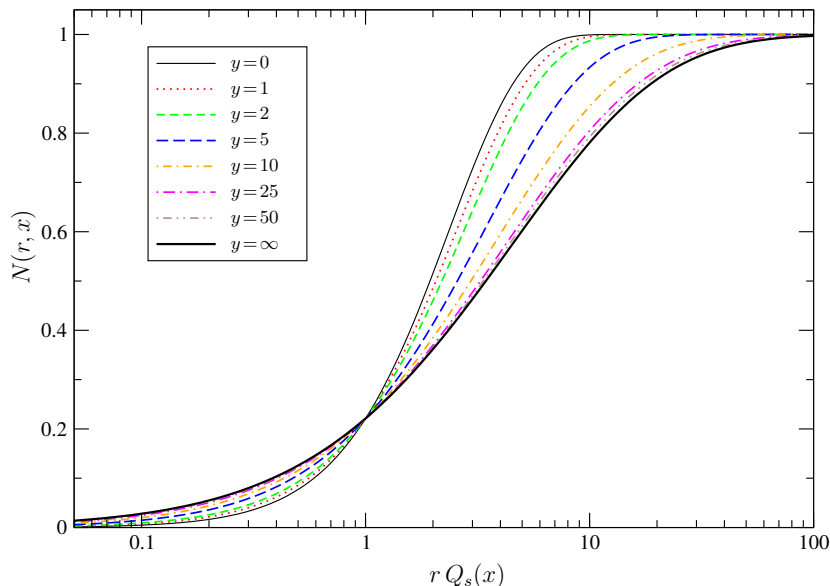


Figure 7.1: The dipole scattering amplitude $N(r, x)$ resulting from a Fourier transformation (7.6) of $\mathcal{N}(k, x)$ as a function of $rQ_s(x)$ for various rapidities $y = \ln x_0/x$. Note that Q_s is defined as $N(r = 1/Q_s(x), x) \approx 0.22$, cf. Eq. (7.8). Hence, $N(r = 1/Q_s, x)$ is by definition geometrically scaling.

small, or alternatively, if A is sufficiently large, one can obtain $\mathcal{N}(k, x = x_0)$ for instance from the McLerran-Venugopalan (MV) model [49–51, 66]. The DHJ model for $N(r, x)$ itself is unsuitable as a starting distribution as its continuation to the saturation region is ambiguous². Unless stated otherwise, we have used as a starting distribution the MV model, given by Eq. (6.24),

$$N(r, x_0) = 1 - \exp \left[-\frac{1}{4} r^2 Q_s^2(x_0) \ln \left(e + 1/(r^2 \Lambda^2) \right) \right], \quad (7.5)$$

from which $\mathcal{N}(k, x = x_0)$ is obtained using Eq. (7.1), which is one of the starting distributions considered in Ref. [89]. The influence of the choice of starting distribution on our results is discussed in section 7.2.4. The dependence of the numerical results on the starting distribution has also been investigated in Ref. [89], to which we refer for additional information. Note that the specific value of x_0 is unimportant for the present analysis, since only the evolution in $y = \ln(x_0/x)$ plays a role.

²The anomalous dimension of DHJ (Eq. (6.31)) is usually defined in the saturation region by substituting $\ln 1/rQ_s \rightarrow |\ln 1/rQ_s|$, but this leads to unphysical oscillations in the Fourier transform, so that it is still unsuitable as a starting distribution.

7.2. Anomalous dimension from the numerical solution

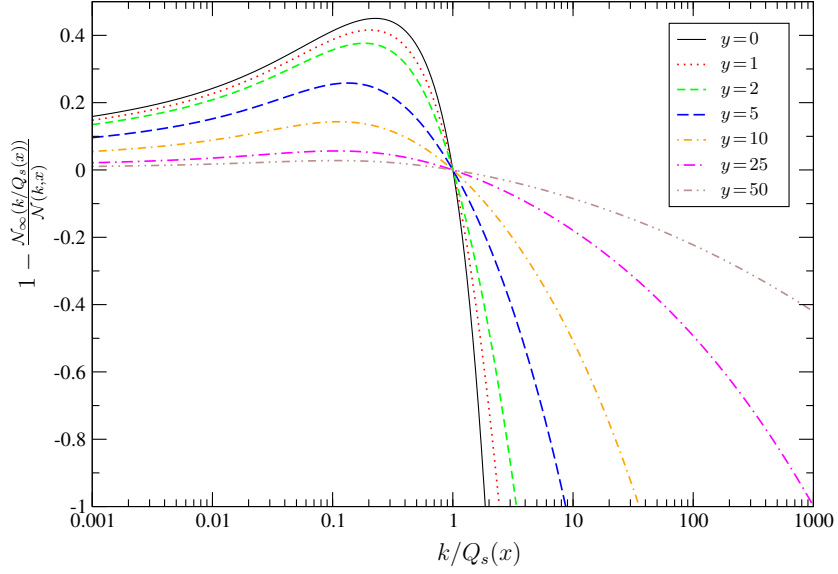


Figure 7.2: The relative difference $1 - N_\infty(k/Q_s(x))/N(k/Q_s(x), x)$ between the function $N(k, x)$ (7.1) following from the BK equation and its geometrically scaling asymptotic $N(k/Q_s(x), x \rightarrow 0) = N_\infty(k/Q_s(x))$ for various rapidities $y = \ln x_0/x$.

7.2 Anomalous dimension from the numerical solution

Now, we will reconstruct the anomalous dimension, as defined in Eq. (7.2), from the numerical solution of the BK equation to see whether the features of the DHJ model, which are given in section 6.2.3, arise from the evolution. The BKSolver program [90] provides numerical values for the amplitude $\mathcal{N}(k, x)$ as a function in momentum space. On the other hand, the DHJ model is formulated in co-ordinate space³. Hence, to compare the two, we have to transform the solution of the BK equation to co-ordinate space. We will distinguish two scenarios, namely the general case in which the anomalous dimension depends on r , and the case where the anomalous dimension depends directly on k , as was assumed in the DHJ model to facilitate the calculation of the Fourier transform.

7.2.1 Anomalous dimension as a function of r

Given the solution of the BK equation in terms of \mathcal{N} , we have to use the inverse transformation of Eq. (7.1) to find the corresponding function in co-ordinate space,

$$N(r, x) = r^2 \int \frac{d^2k}{2\pi} e^{-ik \cdot r} N(k, x) = r^2 \int_0^\infty dk k J_0(kr) N(k, x). \quad (7.6)$$

³The DHJ model is actually used with the substitution $\gamma(r, x) \rightarrow \gamma(r = 1/k, x)$ in Eq. (6.31), so that it is a function of both r and k .

Thus having found the solution in co-ordinate space, we can reconstruct the anomalous dimension by simply equating the result to the general form (7.2). Solving the resulting equation in terms of γ straightforwardly gives

$$\gamma(r, x) = \frac{\ln \left[\ln \left[(1 - N(r, x))^{-4} \right] \right]}{\ln[r^2 Q_s^2(x)]}. \quad (7.7)$$

Still, this equation requires the value of $Q_s(x)$ as separate input. In co-ordinate space the DHJ parameterization (7.2) requires that at the point $r = 1/Q_s$, the amplitude is independent of γ ; it is simply a constant. Therefore, we can define Q_s as the point where the numerical result equals this constant,

$$N(r = 1/Q_s, x) = 1 - \exp[-1/4] \approx 0.22. \quad (7.8)$$

Equating this fixed value to the general relation (7.6) allows one to calculate the saturation scale $Q_s(x)$ by solving the following equation,

$$\frac{1}{Q_s^2(x)} \int_0^\infty dk k J_0(k/Q_s(x)) N(k, x) = 1 - \exp[-1/4]. \quad (7.9)$$

Combining the resulting values of the saturation scale with Eq. (7.7), we obtain a numerical result for $\gamma(r, x)$, which is shown in Fig. 7.3 as a function of $1/(rQ_s(x))$. This means that the saturation region is located to the left of 1 on the horizontal axis, for easier comparison with plots in terms of k/Q_s . From the numerical results (see also Fig. 7.3) we see that the anomalous dimension $\gamma(r, x)$ has the following features:

1. For $r \rightarrow 0$, $\gamma(r, x)$ asymptotically approaches 1.
2. At the saturation scale, $\gamma(r, x)$ is not a constant.
3. For decreasing x , $\gamma(r, x)$ approaches a limiting curve, indicated in Fig. 7.3 by $y = \infty$. Hence, after sufficiently long evolution one indeed recovers geometric scaling.

Since γ is not constant at the saturation scale, instead of writing $\gamma(r, x) = \gamma_s + \Delta\gamma(r, x)$, which is the form of γ in the DHJ model, it seems more natural to consider the following expression

$$\gamma(r, x) = \gamma_\infty(rQ_s(x)) + \Delta\gamma(r, x), \quad (7.10)$$

where it turns out that, similarly to the DHJ model, $\Delta\gamma(r, x)$ decreases as $1/y$ for $y \rightarrow \infty$ and fixed $rQ_s(x)$. We find that in the small- x limit γ at the saturation scale is given by

$$\lim_{x \rightarrow 0} \gamma(r = 1/Q_s(x), x) \equiv \gamma_\infty(1) \approx 0.44, \quad (7.11)$$

a value that is significantly below $\gamma_s = 0.628$.

A word of caution has to be added about the results for small values of y (below $y = 5$, say): the numerical solutions are obtained for a specific starting distribution at $y = 0$ ($x = x_0$). For ‘‘short’’ evolutions (small y -values), the properties of the starting distribution are still visible in the result. Nevertheless, we will be able to draw some qualitative conclusions also for lower y -values from our results in section 7.2.2.

7.2. Anomalous dimension from the numerical solution

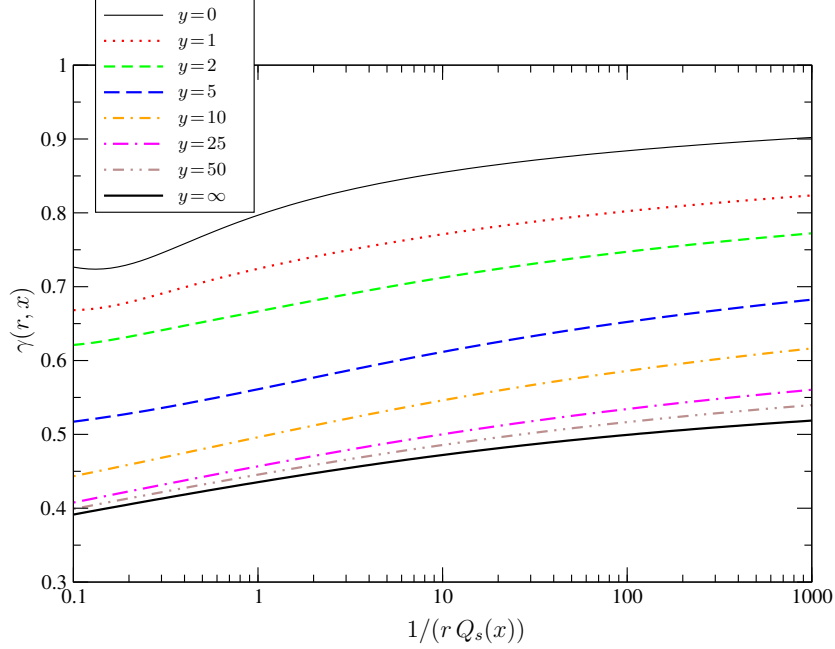


Figure 7.3: $\gamma(r, x)$ resulting from the relations (7.6) and (7.7) as a function of $1/(rQ_s(x))$ and $y = \ln x_0/x$. The curve for $y = 0$ is the anomalous dimension that corresponds to the MV model.

7.2.2 Anomalous dimension as a function of k

As mentioned, in the analysis of DHJ the anomalous dimension was taken to be a function of k rather than of r . That way, $\gamma(k, x)$ does not need to be specified in the saturation region, where it is not clear from the BFKL or BK expectations of sections 4.5 and 5.3 how to continue it below Q_s . Here, we will show what behaviour of γ as a function of k is necessary to comply with BK evolution. This approach requires a different procedure of extracting γ from the numerical solution. If we replace $\gamma(r, x)$ in Eq. (7.2) with $\gamma(k, x)$, the amplitudes in momentum space and co-ordinate space are not related anymore by the straightforward Fourier transform (7.6). Instead, we have the relation

$$\mathcal{N}(k, x) \equiv \int_0^\infty \frac{dr}{r} J_0(kr) \left(1 - \exp \left[-\frac{1}{4} (r^2 Q_s^2(x))^{\gamma(k, x)} \right] \right), \quad (7.12)$$

which we cannot invert to find γ as we did before. Instead, we fix γ at the saturation scale, thereby also determining Q_s itself, after which we can solve Eq. (7.12) numerically. In order to test the DHJ model, we choose the value $\gamma_s \approx 0.628$ at the saturation scale

$$\gamma(Q_s(x), x) = \gamma_s \approx 0.628. \quad (7.13)$$

Since $\gamma(k = Q_s, x)$ is now known, Q_s itself can be determined by setting $k = Q_s$ in Eq. (7.12), which gives the following equation,

$$\mathcal{N}(Q_s(x), x) = \int_0^\infty \frac{dz}{z} J_0(z) \left(1 - \exp \left[-\frac{1}{4}(z^2)^{\gamma_s} \right] \right) \approx 0.19. \quad (7.14)$$

Now we can extract γ from relation (7.12) for any given value of x and k . Fig. 7.4 shows the results for $\gamma(k, x)$ as a function of k/Q_s for a large range of rapidities, outside the saturation region. For small rapidities the resulting γ looks very similar to the one of DHJ (cf. Fig. 4 of Ref. [48]). However, for large rapidities the resulting γ is not compatible with the DHJ parameterization (6.31) anymore (cf. Fig. 6.2); it first decreases ($\Delta\gamma < 0$) before it rises towards 1 asymptotically.

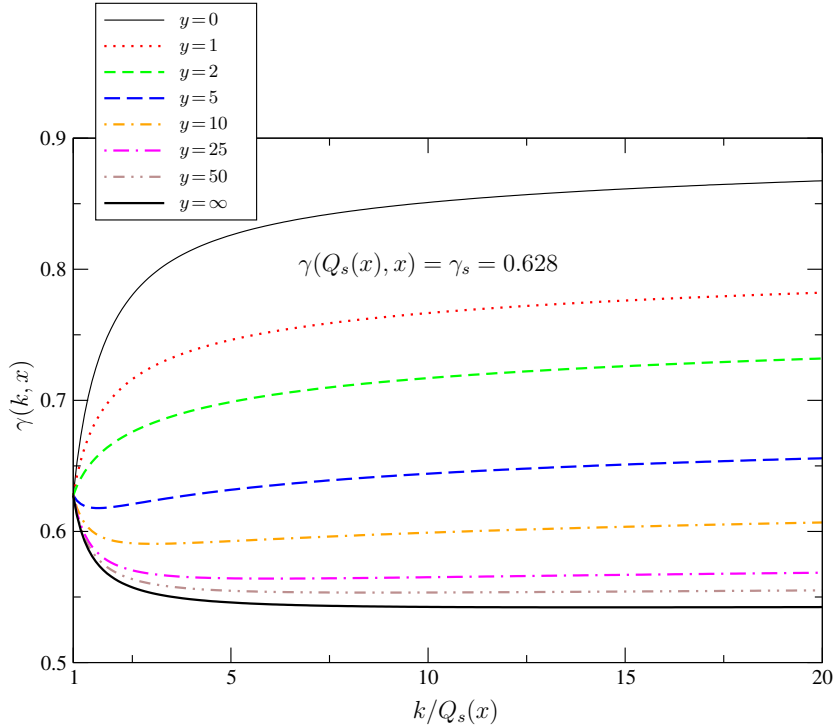


Figure 7.4: $\gamma(k, x)$ as a function of $k/Q_s(x)$ for various rapidities $y = \ln x_0/x$.

As the evolution seems to push the value of γ down, leading to a negative $\Delta\gamma$, we perform the same procedure with a smaller value for γ at the saturation scale. Instead of $\gamma_s = 0.628$ we now choose the value $\gamma(k = Q_s, x) = 0.44$, which is the large- y limit of $\gamma(r = 1/Q_s, x)$ that was calculated previously. Fig. 7.5 shows the result, which is now qualitatively very similar to γ_{DHJ} , cf. Fig. 6.2. Indeed, for the smaller value of $\gamma(k = Q_s, x)$, $\Delta\gamma$ remains positive for all rapidities, in agreement with the DHJ parameterization

7.2. Anomalous dimension from the numerical solution

(6.31). A fit of γ as given in Eq. (6.31) to the numerical results for $k/Q_s = 1, 2, \dots, 5$ and rapidities $y = 1, 2, \dots, 5$ (in order to allow for a comparison to DHJ's results) yields $\lambda \approx 1$ and $d \approx 3$, although it must be emphasized that the shapes of the curves are not exactly of the form (6.31).

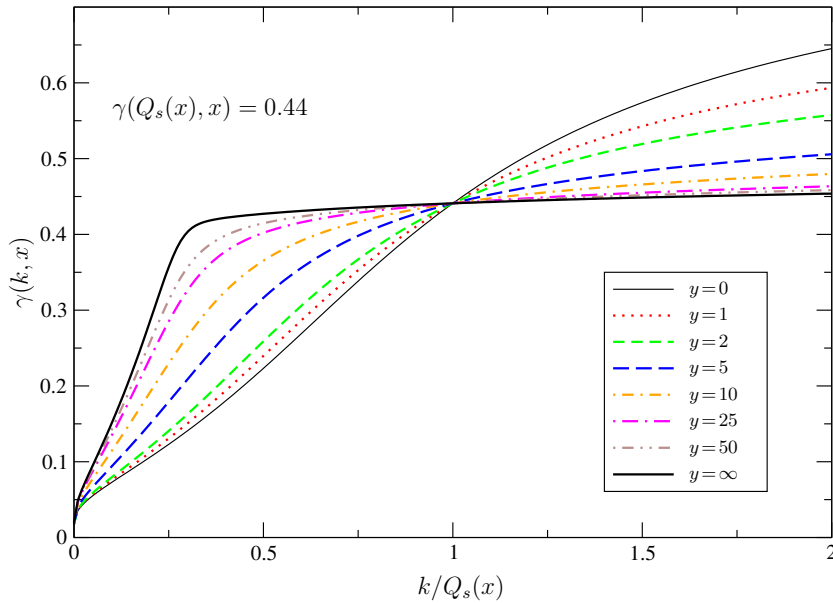


Figure 7.5: $\gamma(k, x)$ as a function of $k/Q_s(x)$ for various rapidities $y = \ln x_0/x$.

A different problem with the choice $\gamma(k = Q_s, x) = \gamma_s$ presents itself in the saturation region $k < Q_s$. In the interval $0.2 \lesssim k/Q_s \lesssim 0.4$ there exists no solution of Eq. (7.12) for γ , i.e. the general parameterization (7.2) is incompatible with the BK equation. We note however that the parameterization (7.2) was intended to describe the dipole amplitude for $rQ_s \leq 1$, and that the parameterization has not been tested phenomenologically for $rQ_s \ll 1$. Still, with the choice $\gamma(k = Q_s, x) = 0.44$, a solution γ exists for all values of k/Q_s . In this case, also in the saturation region geometric scaling is recovered at asymptotic rapidities, where $\gamma(k, x)$ approaches a limiting curve. From Fig. 7.5 we see that for large rapidities, $\gamma(k, x)$ is rather constant down to $k/Q_s \approx 0.3$, where it drops to a small but non-vanishing value. In this region of very small k/Q_s however, the exact value of γ becomes irrelevant, since the amplitude is already approximately equal to 1, and hardly depends on γ .

7.2.3 The saturation scale

The analyses of sections 4.5 and 5.3 lead to a power law behaviour of the saturation scale as a function of x , $Q_s(x) \sim x^{-\lambda/2}$. To check that our approach is consistent with these

results, in Fig. 7.6 we display the values of $Q_s(x)$ for a fixed coupling $\bar{\alpha}_s = 0.2$ as a function of $y = \ln x_0/x$. The figure shows that, at least for larger rapidities, $y > 10$ say, the power law behaviour of $Q_s(x) \sim x^{-\lambda/2}$ is recovered in all scenarios considered here. The value of λ that follows from our analysis, $\lambda \approx 0.9$ is in agreement with the asymptotic result $\lambda \approx \bar{\alpha}_s \chi(\gamma_s)/\gamma_s \approx \bar{\alpha}_s 4.88$ from sections 4.5 and 5.3.

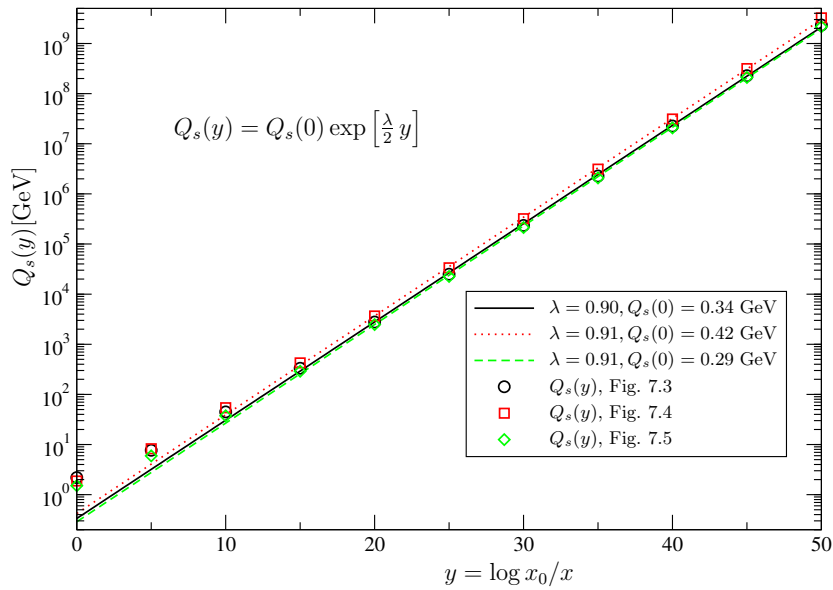


Figure 7.6: The saturation scale from the various approaches for $y = \ln x_0/x = 0, 5, 10, \dots, 50$ (symbols) and the related fits of the form $Q_s(y) = Q_s(0) \exp[\lambda y/2]$ in the fixed coupling case, where $\bar{\alpha}_s = 0.2$.

We have also investigated the running coupling case, where the scale at which the coupling constant is evaluated is given by the reciprocal of the relevant dipole size. For details on this particular choice of scale, we refer to [89, 90]. The energy scale turns out to be effectively of the order of the resulting saturation scale Q_s . The running of the coupling results in a change in the dependence of $Q_s(x)$ on x , for which we now find approximately $Q_s(y) = Q_s(0) \exp[c \sqrt{y}/2]$. While this seems rather different from the GBW result (6.5), it is in fact equally well supported by all relevant DIS data [98]. Since we have plotted every result for the anomalous dimension as a function of dimensionless quantities, i.e. $rQ_s(x)$ or $k/Q_s(x)$, none of those results is significantly affected by including running in the coupling constant. It has to be mentioned that since the BK equation is of leading order in α_s , including the running coupling is not a consistent treatment of higher order effects [115]. For that reason we focus our analysis on the fixed coupling case.

7.2.4 The initial condition

The numerical results generated by the BKsolver program depend on which starting distribution $N(k, x_0)$ is chosen to evolve from. In principle, the program requires the starting distribution to be specified for all values of k . As mentioned, this means that we cannot use the DHJ model, which is not defined in the saturation region, as a starting distribution to see whether BK evolution preserves its characteristics. Instead, throughout this section we have used the MV model (7.5). Here, we illustrate the dependence of our previous results on the choice of this starting distribution, and check whether the theoretical expectations on the dependence on the initial condition that were derived in sections 5.3.3 and 4.3 are recovered. This can be done by generating the numerical solutions using the following starting distribution instead of the MV distribution,

$$N(r, x = x_0) = 1 - \exp \left[-\frac{1}{4} (r^2 Q_s^2(x = x_0))^{\gamma_0} \right], \quad (7.15)$$

where γ_0 is constant. The resulting amplitude⁴ is shown in Fig. 7.7 for three initial condi-

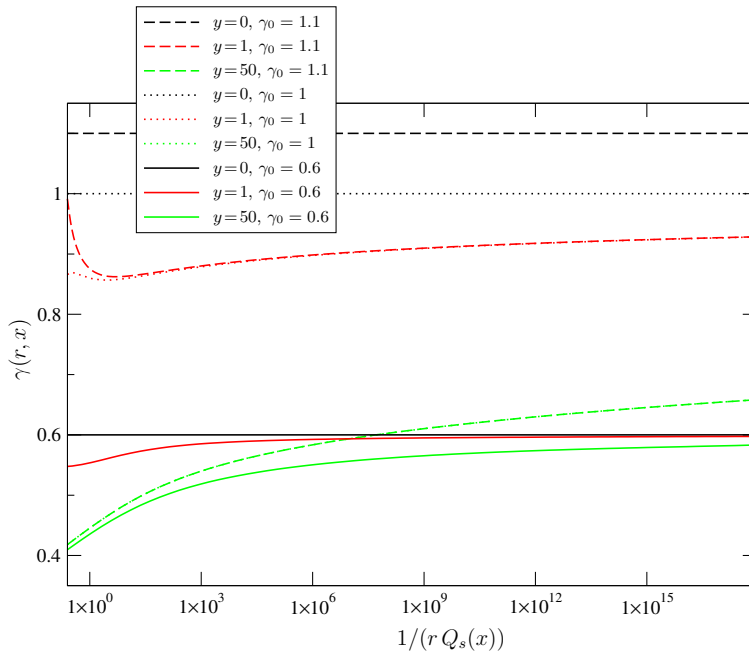


Figure 7.7: $\gamma(r, x)$ for three different rapidities and initial conditions $\gamma_0 = 0.6, 1, 1.1$. To illustrate the small r asymptotics, we show $\gamma(r, x)$ over a very large range. Note that the curves with $\gamma_0 = 1$ and 1.1 for $y = 50$ are hard to distinguish.

tions, $\gamma_0 = 0.6, 1$ and 1.1 , at rapidities of $y = 0, 1$ and 50 . To show the small- r behaviour

⁴We note that the integral in Eq. (7.1) with $N(r, x_0)$ taken as in Eq. (7.15) does not converge for $\gamma_0 < 0.5$.

of the resulting amplitudes, they are shown in a very large range of rQ_s . We see that the curves with $\gamma_0 = 0.6$ approach 0.6 at small r , while the curves with $\gamma_0 = 1$ and 1.1 approach 1. This agrees with the expectation that at fixed y , the small- r limit of γ is given by γ_0 when $\gamma_0 < 1$, and by 1 otherwise⁵.

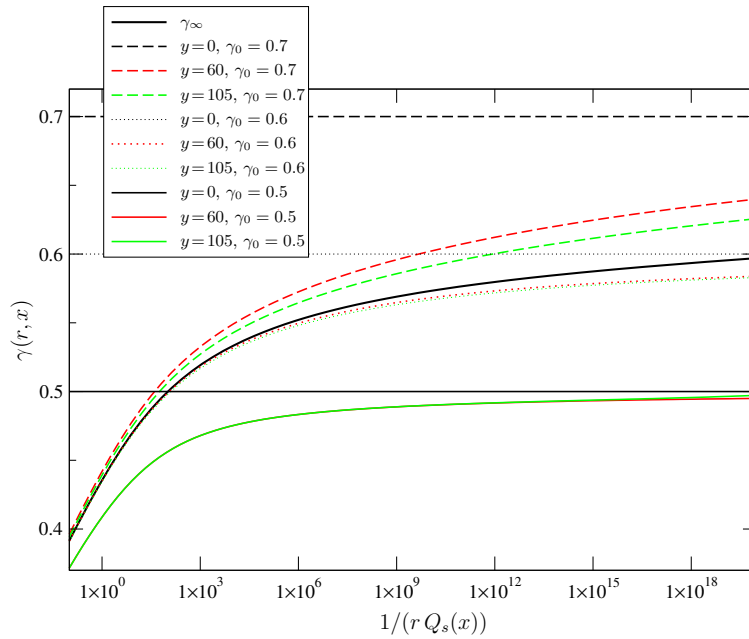


Figure 7.8: $\gamma(r, x)$ as a function of $1/(rQ_s(x))$ and initial conditions $\gamma_0 = 0.5, 0.6$ and 0.7 for large rapidities $y = \ln x_0/x$. Here, the curves for $y = 60$ and $y = 105$ largely coincide for both $\gamma_0 = 0.5$ and 0.6 .

Similarly, Fig. 7.8 shows the amplitudes following from initial conditions $\gamma_0 = 0.5, 0.6$ and 0.7 in a large range of rQ_s . However, in this figure the results are shown for much larger rapidities, namely $y = 0, 60$ and 105 . The limiting curve that is reached at $y \rightarrow \infty$ using the MV distribution, γ_∞ , is also shown. For all initial conditions, a limiting curve is reached, but not always the same one. Let us list the systematics. For $\gamma_0 = 0.5$, at large y , γ reaches a limiting curve that monotonically rises towards 0.5 at small rQ_s . The same happens for $\gamma_0 = 0.6$, but now at small rQ_s the value of 0.6 is approached. We note that in a large range, this limiting curve is very close to the MV one γ_∞ , but slightly undershoots it as rQ_s becomes very small. For $\gamma_0 = 0.7$ however, the limiting curve is equal to γ_∞ in the entire investigated range of rQ_s . We conclude that if $\gamma_0(rQ_s)$ is sufficiently large, γ always reaches the same universal limiting function $\gamma_\infty(rQ_s)$. This function equals approximately 0.44 at the saturation scale and approaches a value $\gamma_\infty(rQ_s \rightarrow 0)$ which

⁵To be precise, γ approaches either γ_0 or the saddle point γ_{sp} (whichever is the smallest), but the latter becomes equal to 1 for small r .

7.3. Conclusions

seems to be slightly larger than 0.6. This latter limit seems consistent with the expectation (see section 5.3) of 0.628. In the specific case of a constant γ_0 , the universal limiting curve is reached if γ_0 is larger than $\gamma_\infty(rQ_s \rightarrow 0)$. If γ_0 is not large enough for the universal curve γ_∞ to be reached, the limiting curve at large y will approach γ_0 as rQ_s becomes very small. If γ_0 is constant, this will happen when γ_0 is smaller than $\gamma_\infty(rQ_s \rightarrow 0)$, which is also consistent with the theoretical expectations. The results of this section are depicted schematically in Fig. 7.9.

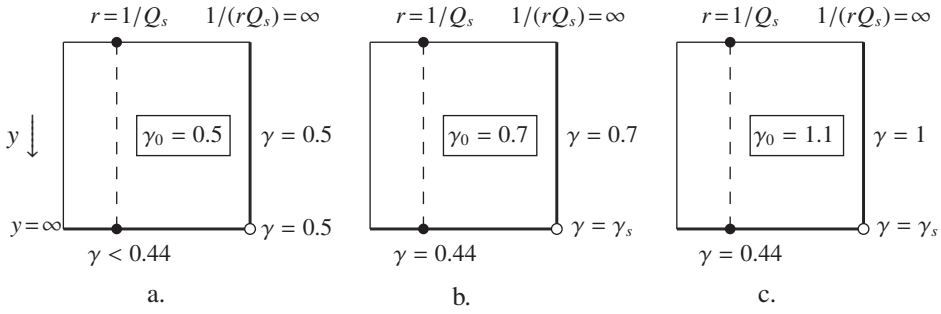


Figure 7.9: The limits of the anomalous dimension γ , according to BK evolution, in the $1/(rQ_s)$ - y plane in the three cases $\gamma_0 = 0.5 < \gamma_s$, $\gamma_s < \gamma_0 = 0.7 < 1$ and $1 < \gamma_0 = 1.1$. In each plot $1/(rQ_s)$ increases from 0 on the left to ∞ on the right while y increases from 0 at the top to ∞ at the bottom.

Finally, we compare our results to those of Ref. [113], especially Fig. 4, which for comparison is given here as Fig. 7.10. There it is found that for small rQ_s the scattering amplitude can be described by

$$N(r) = a(rQ_s)^{2\gamma}(\ln(rQ_s) + \delta), \quad (7.16)$$

where γ approaches approximately 0.65 for large y , regardless of the initial condition, as can be seen in Fig. 7.10. We find that the particular value of 0.65 is consistent with our result for γ_∞ , if we take into account the different functional form for $N(r, x)$ and the specific range of r and y in which γ was calculated. However, even for $\gamma_0 = 0.42$, which means $c = 2\gamma_0 = 0.84$ in Fig. 7.10, Ref. [113] find no dependence of γ on the initial condition, which seems to disagree with our results and the theoretical expectations (see Ref. [75]).

7.3 Conclusions

The numerical solutions of the BK equation do not display exact geometric scaling, although they approach a scaling solution asymptotically small x . Assuming the solutions to be of the form (7.2), therefore leads to the conclusion that the ‘‘anomalous dimension’’ $\gamma(r, x)$ is not a function of $rQ_s(x)$ exclusively. In particular, it is never simply a constant

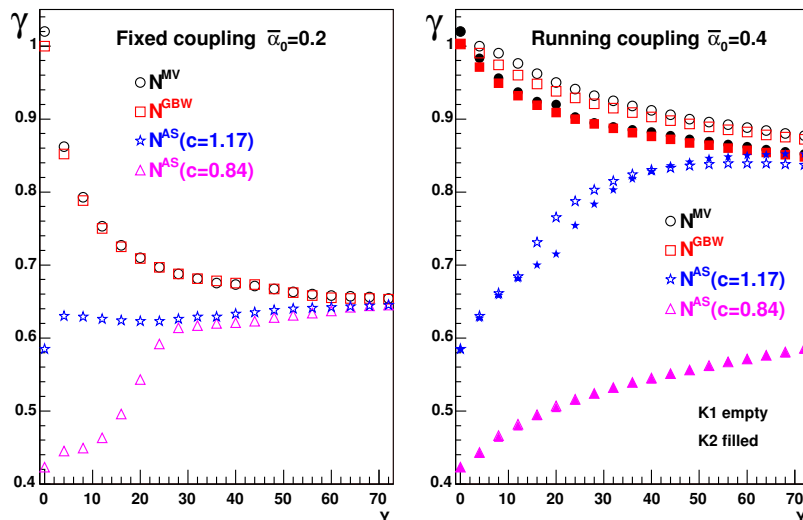


Figure 7.10: The large- y limit of γ according to Ref. [113]. The initial condition N^{AS} is given as $N^{\text{AS}}(r) = 1 - \exp(-(rQ_s)^c)$, so that $c = 2\gamma_0$.

at the saturation scale ($r = 1/Q_s$). At asymptotically large rapidities, γ reaches a limiting function $\gamma_\infty(rQ_s(x))$. This function is universal for a large range of initial conditions. At the saturation scale, this function equals approximately 0.44, which is considerably smaller than the corresponding values of γ in the phenomenological models [48, 94, 101]. For very small values of rQ_s the limiting function seems to reach γ_s , while in the limit of $rQ_s(x) \rightarrow 0$ at fixed x , it is determined by the starting distribution or the BFKL saddle point. This is in accordance with the theoretical expectations given in sections 5.3.3 and 4.3. We note that, as expected, the two limits $rQ_s(x) \rightarrow 0$ and $x \rightarrow 0$ do not commute.

Performing the replacement of $\gamma(r, x) \rightarrow \gamma(1/k, x)$ does allow one to find a solution for which $\gamma(k = Q_s, x)$ is fixed. The behaviour of $\gamma(1/k, x)$ is then qualitatively similar to the DHJ parameterization for small rapidities. However, the usually considered choice $\gamma(k = Q_s, x) = \gamma_s = 0.628$ is incompatible with the BK equation, as $\Delta\gamma$ first becomes negative as k exceeds Q_s for rapidities of $y_h \gtrsim 5$. Also, there is no solution for γ in the saturation region. It must be noted however that the general parameterization (7.2) of N was not intended for the latter region. Keeping $\gamma(k = Q_s, x)$ fixed at a smaller value, e.g. at $\gamma_\infty(rQ_s = 1) \approx 0.44$, seems more suitable.

The resulting saturation scales in the various approaches we adopted, evolve quite similarly with decreasing x , namely approximately as $Q_s(x) = Q_s(x_0)(x_0/x)^{\lambda/2}$, albeit with somewhat different normalizations $Q_s(x_0)$. This is consistent with theoretical expectations, which can be found in sections 4.5.1 and 5.3. In the case of a running coupling constant, the dependence on y changes from $\exp(\lambda y/2)$ to $\exp(c\sqrt{y}/2)$, which is equally well supported by all relevant DIS data [98].

Chapter 8

Compatibility of phenomenological models with RHIC data

We have seen in chapter 6 how expectations from small- x evolution prompted the formulation of a number of dipole models. These models, which have been used to describe small- x DIS and deuteron-gold data, all incorporate to some extent a number of properties that follow from analyses of the BFKL and BK equations. In chapter 7 we have investigated whether these features are truly compatible with the full BK equation. Here, we want to study whether these small- x properties are actually visible in the data on hadron production in deuteron-gold collisions from the Relativistic Heavy Ion Collider (RHIC). In other words, we want to investigate whether such small- x properties are necessary to describe these data. Like in chapter 7, we focus on the DHJ model, since it incorporates all small- x properties that are shared with the IIM and KKT models. Hence, our conclusions extend to those models. Most notably, we find that the RHIC data are compatible with geometric scaling, and hence that no scaling violations can be resolved. Also, the logarithmic rise of the anomalous dimension, which is characteristic for small- x evolution, cannot be established in the RHIC data at small x . We show that data on the transverse momentum distribution of hadrons produced in proton-proton and proton-lead collision at the Large Hadron Collider LHC will provide a test of the latter property.

We will start with a brief description of nucleon-nucleus collisions in section 8.1, more details of which can be found in section 6.2. In section 8.1.1, we will discuss the small- x properties of the DHJ model that will be tested against the data. Next, we will propose a new model, *without* the small- x inspired features of the DHJ model, and show that it is able to describe all the d -Au data from RHIC. We also check for consistency with the small- x DIS data. In section 8.2 we will give predictions from both models for LHC, particularly for the transverse momentum distribution of produced hadrons. We end with conclusions.

8.1 Hadron collisions in the dipole formalism

In chapter 6 we have seen how a number of phenomenological dipole models have been constructed around the observed property of geometric scaling in the small- x DIS cross section. Geometric scaling means that the total cross section depends on x and Q^2 through the combination $Q^2/Q_s^2(x)$ only, where $Q_s(x)$ is the saturation scale. Even though this property appears in a natural way in the (asymptotic) solutions of non-linear evolution equations, such as the GLR equation [25, 26] or the BK equation [27, 30], that are expected to become relevant at small x , the question remains whether the observed DIS data are obtained at sufficiently small x values for such evolution equations to be applicable. In section 6.1.2, we have remarked that the fact that the small- x DIS data can be described using different approaches suggests that the small- x DIS data do not span a sufficiently large region in Q^2 and x to discriminate between different types of evolution. We note that the same is true for the RHIC d - Au data, which can also be described using the perturbative DGLAP description [116]. The question we want to address in this chapter is whether or not the RHIC and future LHC data do span a sufficiently large region to test small- x evolution. In particular we want to investigate the geometric scaling properties of the RHIC data.

Like the DIS cross section, the hadron production cross sections in nucleon-nucleus scattering at high energies have been expressed in terms of the scattering of a colour dipole off small- x partons, which are predominantly gluons [35, 69]. In this approach, geometric scaling means that the dipole scattering amplitude depends on r_\perp and x through the combination $r_\perp^2 Q_s^2(x)$ only, where r_\perp is the transverse size of the dipole¹. For earlier works about d - Au collisions and saturation physics we refer to Refs. [117–121] and the review [37].

In order to investigate whether the geometric scaling violations that are expected from small- x physics are present in the RHIC data, in Refs. [47, 48] the so-called DHJ model has been put forward, which offers a good description of the p_\perp distribution of hadrons produced in d - Au collisions at RHIC in the forward region, and even in p - p collisions in the very forward rapidity region [122].

In terms of the dipole scattering amplitude, the cross section of single-inclusive forward hadron production in high energy nucleon-nucleus collisions is described in the following way [47, 48] (see also section 6.2),

$$\begin{aligned} \frac{dN_h}{dy_h d^2 p_\perp} &= \frac{K(y_h)}{(2\pi)^2} \int_{x_F}^1 dx_1 \frac{x_1}{x_F} \left[f_{q/p}(x_1, p_\perp^2) N_F \left(\frac{x_1}{x_F} p_\perp, x_2 \right) D_{h/q} \left(\frac{x_F}{x_1}, p_\perp^2 \right) \right. \\ &\quad \left. + f_{g/p}(x_1, p_\perp^2) N_A \left(\frac{x_1}{x_F} p_\perp, x_2 \right) D_{h/g} \left(\frac{x_F}{x_1}, p_\perp^2 \right) \right], \end{aligned} \quad (8.1)$$

where x_F is the longitudinal momentum fraction of the produced hadrons, and y_h is their rapidity, i.e. $x_F = p_\perp / \sqrt{s} \exp(y_h)$. In appendix B the kinematics are discussed in more detail. A summation over quark flavours q is understood. Here N_F describes a quark

¹See Eq. (6.3). In momentum space k_\perp^2 times the scattering amplitude $N(k_\perp^2, x)$ is the scaling dimensionless quantity.

scattering off the nucleus, while N_A applies to a gluon. The parton distribution functions $f_{q/p}$ and the fragmentation functions $D_{h/q}$ are evaluated at the scale $Q^2 = p_\perp^2$, which we will always take to be larger than 1 GeV^2 . The momentum fraction of the target partons equals $x_2 = x_1 \exp(-2y_h)$. Finally, there is an overall (p_\perp independent) K -factor that effectively accounts for NLO corrections.

In DIS a scaling behaviour of the dipole scattering amplitude $N(r_\perp Q_s)$ maps directly into a scaling of the DIS cross section with Q^2/Q_s^2 , cf. Eq. (6.3), which is clearly observable in the data at small x ($x \lesssim 0.01$). Due to the convolution in Eq. (8.1) the situation is more involved in hadron-hadron collisions where no such scaling of the cross section in terms of the observed kinematic variables (y_h and p_\perp) can be expected. Therefore, we have to focus on the question whether hadron production in d - Au collisions is describable in terms of scaling dipole amplitudes N_A and N_F , for which we will resort to phenomenological models.

8.1.1 DHJ models versus new model

The dipole scattering amplitude of the DHJ model [47, 48], is given by Eq. (6.33), in which the anomalous dimension is parameterized as (see section 6.2.3)

$$\gamma(q_\perp, x_2) = \gamma_s + (1 - \gamma_s) \frac{|\ln(q_\perp^2/Q_s^2(x_2))|}{\lambda Y + d\sqrt{Y} + |\ln(q_\perp^2/Q_s^2(x_2))|}, \quad (8.2)$$

where $Y = \ln 1/x_2$, and $\gamma_s = 0.628$. The saturation scale $Q_s(x_2)$ and the parameter λ are taken from the GBW model Eq. (6.5),

$$Q_s^2(x_2) = A^{1/3} Q_0^2 \left(\frac{x_0}{x_2} \right)^\lambda, \quad (8.3)$$

where $Q_0 = 1 \text{ GeV}$, $x_0 = 3 \cdot 10^{-4}$ and $\lambda = 0.3$. Unlike in the GBW model, which describes DIS off the proton, here Q_s includes the additional factor $A^{1/3}$, where A is the number of nucleons in the target nucleus. To account for impact parameter dependence DHJ use $A_{\text{eff}} = 18.5$ for d - Au collisions. The parameter d was fitted to the data and set to $d = 1.2$.

For very large $q_\perp \gg Q_s$, or equivalently for small r_\perp , one can use to good approximation

$$N(r_\perp, x_2) \approx \frac{1}{4} (r_\perp^2 Q_s^2(x_2))^{\gamma(q_\perp, x_2)}, \quad (8.4)$$

where γ_{DHJ} can be approximated as

$$\gamma_{\text{DHJ}}(q_\perp, x_2) \approx 1 - \frac{(1 - \gamma_s)(\lambda Y + d\sqrt{Y})}{\ln(q_\perp^2/Q_s^2(x_2))}, \quad (8.5)$$

which approaches unity logarithmically. The way in which γ approaches 1 directly determines how fast the cross section will fall off with increasing p_\perp , as we will discuss in the

8.1. Hadron collisions in the dipole formalism

next section. The logarithmic rise of γ of the DHJ model is directly related to BFKL/BK evolution, which can be seen from Eq. (6.6).

In the DHJ model the dipole amplitude is approximately geometrically scaling when $\Delta\gamma$ is small with respect to γ_s . In general though, it is not simply the variation of γ that determines the scaling violations.

Given expression (6.33) for the dipole amplitude, an anomalous dimension γ leads to a geometric scaling dipole amplitude if it depends on $q_\perp/Q_s(x_2) \equiv w$, but not separately on q_\perp or rapidity $Y = \ln 1/x_2$. We will construct such a model in order to investigate the scaling properties of the data. We will choose the value of γ at the saturation scale, $\gamma(w = 1) \equiv \gamma_1$, to equal γ_s and take a power-like rise towards 1 for large w . The parameterization that we adopt reads

$$\gamma(w) = \gamma_1 + (1 - \gamma_1) \frac{(w^a - 1)}{(w^a - 1) + b}. \quad (8.6)$$

The two free parameters a and b will be fitted to the RHIC data. The parameterizations (8.2) and (8.6) differ not only in the scaling behaviour, but also in the way the large q_\perp limit of $\gamma \rightarrow 1$ is approached, which is much faster in the latter case. This will lead to different large momentum slopes of the dipole amplitude (6.33) and therefore to different predictions for the large p_\perp slope using Eq. (8.1). This can be seen by expanding the exponent for large $w = q_\perp/Q_s$, which simplifies the dipole amplitude (6.33), cf. Eqs. (8.4 and 8.5),

$$N_A(q_\perp) \approx \frac{2\pi}{q_\perp^2} \frac{1}{w^{2\gamma(w)}} \frac{1}{4} \int_0^\infty dz z J_0(z) (-z^{2\gamma(w)}) = \frac{2\pi 2^{2\gamma(w)-1} Q_s^{2\gamma(w)} \Gamma(1 + \gamma(w))}{q_\perp^{2\gamma(w)+2} -\Gamma(-\gamma(w))} \quad (8.7)$$

$$\stackrel{\gamma(w) \rightarrow 1}{\approx} \frac{4\pi Q_s^2}{q_\perp^4} (1 - \gamma(w)) \propto \begin{cases} \frac{Q_s^2}{q_\perp^4 \ln(q_\perp^2/Q_s^2)} & \text{for } \gamma \text{ of Eq. (8.2)} \\ \frac{Q_s^{2+a}}{q_\perp^{4+a}} & \text{for } \gamma \text{ of Eq. (8.6)} \end{cases}.$$

Here, we have suppressed the possible x dependence for clarity. For a constant $\gamma < 1$ the amplitude will drop even more slowly than in either of these models, namely $\propto Q_s^{2\gamma}/q_\perp^{2\gamma+2}$. For $\gamma = 1$ (i.e. the GBW model) one finds on the other hand an unrealistic exponential fall-off $\propto \exp(-q_\perp^2/Q_s^2)/Q_s^2$, which can however be corrected by including a logarithmic term like in the MV model [49, 50, 66, 123], cf. Eq (6.24). Due to the convolution in Eq. (8.1) with the parton distributions and fragmentation functions, the slope of the p_\perp distribution is not so simple to estimate. Empirically we find that the power of the p_\perp distribution is roughly a factor of one to two larger than the power of the dipole scattering amplitude. Below we are going to determine this power. We emphasize that the fall-off with p_\perp is not a measure of the size of the scaling violations². In order to observe such violations one has to study both the y_h and p_\perp dependence over a significantly large range. Moreover, we have to keep in mind that the scaling properties of the dipole scattering amplitude are not directly visible in the hadron production data, due to the parton distributions and fragmentation functions.

²In the DHJ model, γ is smaller in the forward region than in the central region due to the terms $\sim 1/(\lambda Y + d\sqrt{Y})$, where $Y = \ln 1/x_2 \neq y_h$, which in principle leads to a steeper slope of the resulting p_\perp distribution. Such explicit dependence on Y will however turn out not to be necessary to describe the data.

8.1.2 Comparison with RHIC data

In Fig. 8.1 we show our estimate for $dN_h/(dy_h d^2 p_\perp)$ that follows from the integral in Eq. (8.1) with our parameterization (8.6) for $\gamma(w)$, in combination with the dipole scattering amplitude (6.33). All p_\perp distributions of produced hadrons measured at RHIC in d -Au collisions [124–126] are well described. Like in the DHJ model, we have taken for γ at the saturation scale, $\gamma(w = 1) = \gamma_1$, the value $\gamma_1 = \gamma_s = 0.628$, and use $A_{\text{eff}} = 18.5$. We obtain the best fit of the data for

$$a = 2.82 \quad \text{and} \quad b = 168. \quad (8.8)$$

As mentioned, this LO analysis requires the inclusion of a K -factor to account for NLO corrections, which are expected to become more relevant towards central rapidity. Following DHJ, the K -factor is allowed to vary with y_h , but is demanded to be p_\perp -independent. The K -factors we obtain are for our new model equal to $K = 3.4, 2.9, 2.0, 1.6, 0.7$ for respectively $y_h = 0, 1, 2.2, 3.2, 4$, while the equivalent values for the DHJ model are $K = 4.3, 3.3, 2.3, 1.7, 0.7$. We have assumed isospin invariance to obtain the parton distributions for the deuteron from the CTEQ5-LO for the proton [14]. Furthermore, we use the KKP fragmentation functions of Ref. [127].

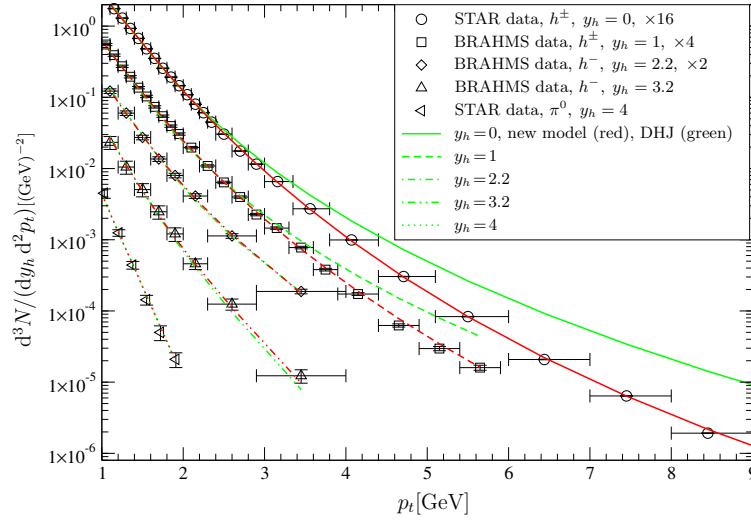


Figure 8.1: Transverse momentum distribution of produced hadrons in d -Au collisions as measured at RHIC (black symbols) for various rapidities y_h . Using the scaling parameterization (8.6) the data are well described by the expression (8.1) with an appropriate K -factor (red/dark curves). The DHJ model (8.2) works well only for smaller p_\perp (green/light curves). To make the plot clearer, the data and the curves for $y_h = 0, 1$ and 2.2 are multiplied with arbitrary factors, namely 16, 4 and 2, respectively. The STAR data at $y_h = 0$ are taken from Ref. [124] and $y_h = 4$ from [126]. The BRAHMS results for $y_h = 1 - 3.2$ can be found in [125].

8.1. Hadron collisions in the dipole formalism

From this analysis we can conclude that a geometrically scaling dipole scattering amplitude is completely compatible with the data. Therefore, the conclusion that scaling violations are observed at RHIC cannot be drawn. Of course, a scaling violating amplitude, i.e. a γ that depends not only on w but on the rapidity $Y = \ln 1/x_2$ explicitly, is not ruled out by the data either. What can be concluded further is that the logarithmic rise of γ in the DHJ model, which is expected from BFKL evolution, is ruled out in the central region, see Fig. 8.1. This may simply indicate that x_2 is already so large that one is in the DGLAP region. In Fig. 8.2, the kinematic region where x_2 is small is indicated in terms of the observables p_\perp and y_h . Indeed, where the DHJ model starts to deviate from the data, x_2 becomes larger than 0.01, although Q_s is still larger than in DIS at $x_B = 0.01$ due to the factor of $A_{\text{eff}}^{1/3}$. If one were to exclude the central rapidity RHIC data in the model fit, one could also obtain a scaling model with a logarithmically rising, or even constant, γ .

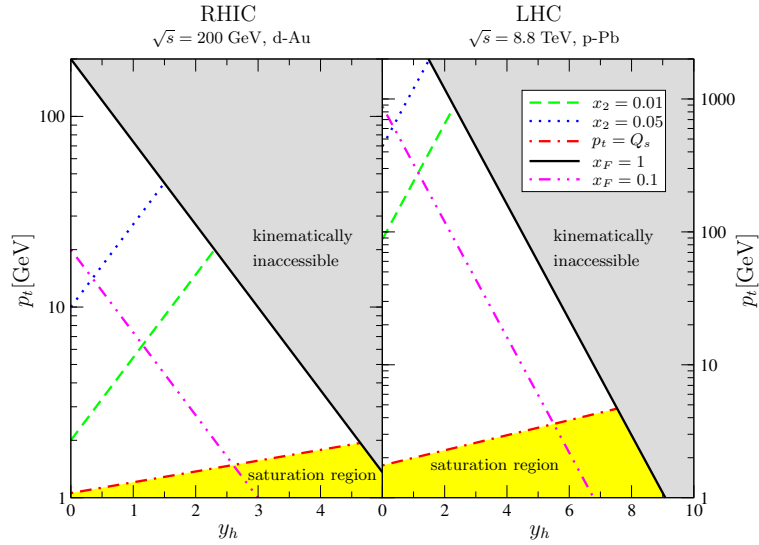
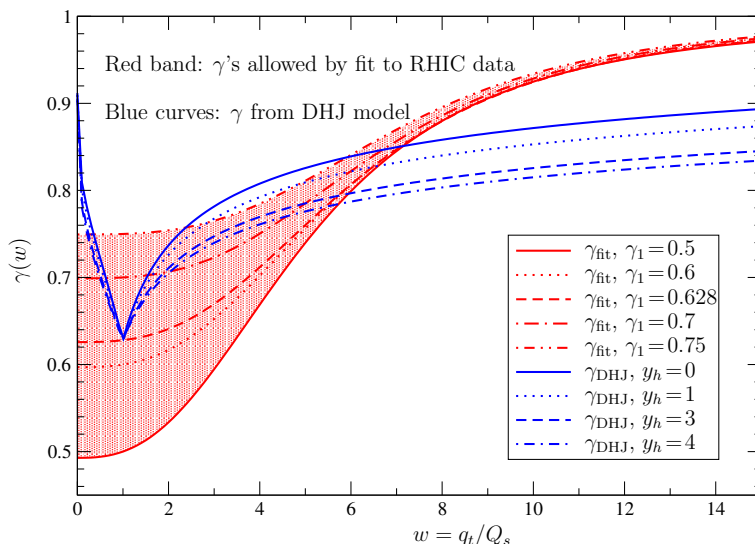


Figure 8.2: Illustration of the kinematic ranges relevant for RHIC and LHC. The saturation region is set by the line $q_\perp = x_1/x_F p_\perp = Q_s(x_2)$. Since the dominant contribution to (8.1) comes from the region x_1 close to $x_F = p_\perp/\sqrt{s} \exp(y_h)$, we used for this plot $x_2 = x_1 \exp(-2y_h) \approx p_\perp/\sqrt{s} \exp(-y_h)$ and $x_1 \approx x_F$. For d -Au we have taken $A_{\text{eff}} = 18.5$ and for p -Pb $A_{\text{eff}} = 20$. The curves of constant x_2 indicate the regions where small- x physics may become relevant.

To indicate how much γ is constrained by the RHIC data, Fig. 8.3 shows various $\gamma(w)$'s that describe the available data equally well. They are all parameterized as in Eq. (8.6) with different a and b values, but require different K -factors. The parameters that define the edges of the allowed region are $\gamma_1 = 0.75$, $a = 3.10$ and $b = 451$ for the upper curve, and $\gamma_1 = 0.50$, $a = 2.60$ and $b = 70.2$ for the lower curve. All γ 's inside the band have $\sqrt{\chi^2} = 0.4 - 0.5$, while outside the band the obtained values of $\sqrt{\chi^2}$ rises quickly


 Figure 8.3: ‘Allowed band’ of γ ’s that describe the RHIC data in combination with γ_{DHJ} .

(it is already roughly twice as big for $\gamma_1 = 0.8$). Clearly, γ is much less well determined close to the saturation scale than in the dilute region. This is so because the integrand in expression (6.33) for the dipole scattering amplitude is only weakly dependent on γ around the saturation scale, and even completely independent of it at $r_\perp = 1/Q_s$. In addition, the forward data ($y_h = 3.2$ and 4) are essentially sensitive only to γ_1 ; because y_h is larger and the p_\perp range smaller, these data probe the region where w is close to 1 only³. Therefore, the rise of γ with w is effectively constrained only by the data for $y_h = 0, 1$. Also, since the RHIC data are not very sensitive to γ around Q_s , the exact value of $\gamma(w = 1) = \gamma_s$, while lying inside the allowed range, remains unconfirmed by the data.

To clarify what we can conclude from this analysis about the study of geometric scaling in the RHIC data, it is useful to realize that given any non-scaling $\gamma(w, y)$ that fits the data for some *single* value of y_h , one can always find a scaling $\tilde{\gamma}(w)$ that leads to *exactly the same* p_\perp distribution. This may not be obvious a priori since even if y_h is fixed, still a range of values of the rapidity Y is probed in the convolution integral (8.1). However, the scaling parameter w can always be expressed as a function of Y and y_h ,

$$w = \frac{x_1}{x_F} \frac{p_\perp}{Q_s(x_2)} = x_2 \exp[y_h] \frac{\sqrt{s}}{Q_s(x_2)} = \exp[-Y + y_h] \frac{\sqrt{s}}{Q_s(Y)} = w(Y, y_h). \quad (8.9)$$

Hence, if y_h is kept fixed one can express the rapidity Y in terms of w and define a scaling $\tilde{\gamma}(w) \equiv \gamma(w, Y = Y(w))$ that leads to the same results as $\gamma(w, Y)$. Clearly, data taken at a

³Assuming $x_1 \approx x_F$, which gives the dominant contribution to the integral in (8.1), we see that the probed values of Y are roughly given by $Y \approx y_h - \ln(p_\perp / \sqrt{s})$. Hence, at large y_h and moderate p_\perp , the probed values of $w = p_\perp / Q_s(Y)$ will remain small.

8.1. Hadron collisions in the dipole formalism

single value of y_h tell us absolutely nothing about the scaling properties of the underlying dipole amplitude. Therefore, scaling violations can be established only by probing a sufficiently large range of y_h .

As mentioned before, like in Ref. [48], γ is chosen to be a function of q_\perp rather than r_\perp . For completeness it should be mentioned that it is possible to describe the data equally well with a scaling γ that depends on $r_\perp Q_s$. In general, this will be a different function than one would obtain by simply replacing q_\perp with $1/r_\perp$ in γ , which would lead to unphysical oscillations in the dipole amplitude and hence in the hadron production cross section⁴.

8.1.3 Compatibility with deep inelastic scattering

Since the parameterization (6.33) of the dipole scattering amplitude uses an anomalous dimension $\gamma \neq 1$, the resulting amplitude is quite different from the GBW model. Therefore, it is important to check whether our anomalous dimension $\gamma(w)$ is still compatible with the small- x DIS data. To do so we use the following expression for the dipole scattering amplitude

$$N(r_\perp, Q, x) = 1 - \exp \left[-\frac{1}{4} (r_\perp^2 Q_s^2(x))^\gamma \left(w = \sqrt{Q^2/Q_s^2(x)} \right) \right], \quad (8.10)$$

where Q_s is given by Eq. (8.3) and for γ we use our model, Eqs. (8.6) and (8.8).

Following the procedure in [34], we predict the total cross section $\sigma_{\gamma^*p} = \sigma_T + \sigma_L$ that follows from the dipole cross section $\sigma = \sigma_0 N_\gamma$ via Eq. (6.1), using the (perturbatively calculable) photon wave function (6.2),

$$\sigma_{T,L}(x, Q^2) = \int dz \int d^2 r_\perp |\psi_{T,L}(z, r_\perp, Q^2)|^2 \sigma(r_\perp, x), \quad (8.11)$$

where z is the longitudinal momentum fraction of the quark in the dipole and x denotes x_B .

In Fig. 8.4 we show the small- x HERA data [128–130] in a large kinematic range as a function of $\tau = Q^2/Q_s^2(x)$. Following Ref. [99], we scale the H1 data [128] by a factor 1.05, which is consistent with the normalization uncertainty. As can be seen, the data for $x < 0.01$ depend on x and Q^2 only through the variable τ . In Fig. 8.4 we compare these data with the original GBW model and the prediction following from our modified γ obtained from a fit to RHIC data. For both models we have neglected effects from finite quark masses in the photon wave function, which become relevant at small Q^2 and break geometric scaling. As a result, the cross section of the GBW model overshoots the data at small τ , i.e. at small Q^2 . Using the modified γ this effect and therefore the fitted quark mass is smaller since the smaller value of γ in the saturation region suppresses the cross section. Further details of the small- τ behaviour can be found in e.g. [131]. In addition, we use a somewhat smaller value of σ_0 in order to obtain a better description of the data, namely 21 mb instead of 23 mb for the GBW model. No parameters of γ are tuned. The

⁴That $\gamma(r_\perp)$ is in general a different function than $\gamma(q_\perp)$ is illustrated by the analysis in sections 7.2 and 7.2.2.

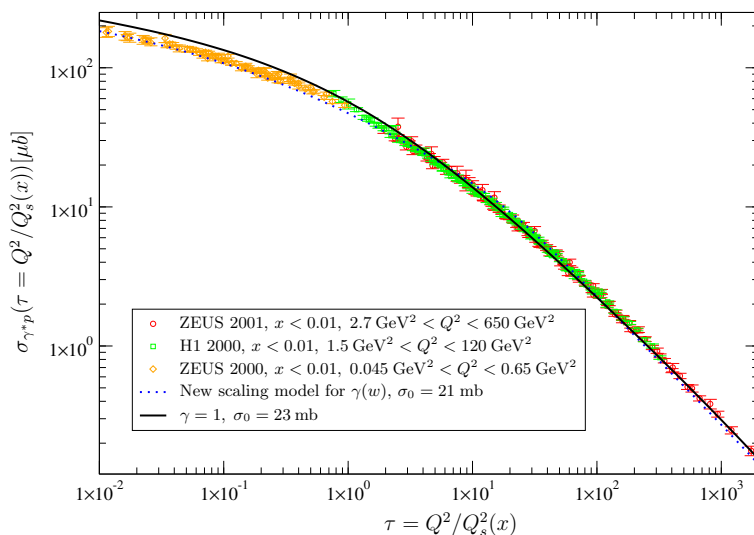


Figure 8.4: The γ^*p cross section as a function of the scaling variable τ measured at HERA [128–130]. We compare the data with the predictions following from the original GBW model, where $\gamma = 1$, and the modified version fitted to RHIC data, where γ depends on $Q^2/Q_s^2(x)$.

smaller value of σ_0 is forced by the region $\tau \approx 10 \dots 100$ where γ is not yet close to one but the effective value of $r_\perp Q_s$ is already large. Given the normalization uncertainty of our model, we do not consider the smaller value of σ_0 a problem. Of course, it would be possible to obtain an optimized parameterization of γ by a simultaneous fit to the RHIC and DIS data, but this is not the purpose of the present analysis. We conclude that the model that we constructed to study the scaling properties of the RHIC data is compatible with the small- x DIS data, since it is able to describe these data equally well as the GBW model, given a slight adjustment of the parameter σ_0 .

We end this section with a comment on whether or not the factor (C_F/C_A) should have been included in N of Eq. (8.10), as was done for N_F earlier. In order to compare the DHJ model or our new model with the GBW model, it would indeed be better to use Eq. (6.33) as a model for N_F and scale $(r_\perp^2 Q_s^2)^\gamma \rightarrow ((C_A/C_F)r_\perp^2 Q_s^2)^\gamma$ to obtain N_A . A fit to RHIC data would then result in a slightly different γ . Since this is not done by DHJ and we are specifically interested in a comparison with the DHJ model, we follow DHJ's approach. This does however obscure the comparison with the GBW model somewhat, since that is a model for (minus) the Fourier transform of N_F without the factor C_F/C_A . Note that for models with $\gamma \neq 1$ this cannot be accounted for by rescaling Q_0 , because one does not rescale Q_s in the anomalous dimension γ . In a future combined fit to RHIC and DIS data one would of course like to avoid this slight conceptual discrepancy. For the present analysis we do not consider it a problem, since the aim is not to obtain a best fit to all available data, but rather to study the small- x properties of the RHIC data.

8.2 LHC predictions

8.2.1 Hadron production

We have seen that where the DHJ model curves deviate from the RHIC data, the probed x_2 -values are not very small. However, at LHC, due to the much higher energies, the region of small x_2 extends to a much larger range of p_\perp , so that the predictions of the DHJ model and the new model will be different even at very small x_2 . In Fig. 8.2 the region of small x_2 is depicted in terms of p_\perp and y_h for p - Pb collisions at LHC, as compared with d - Au collisions at RHIC. For a discussion of experimental possibilities of probing small x values at LHC, see e.g. [132]. In this section we discuss the predictions following from the DHJ model and our new scaling model for the hadron production cross section for p - p collisions at $\sqrt{s} = 14$ TeV and for p - Pb collisions at $\sqrt{s} = 8.8$ TeV.

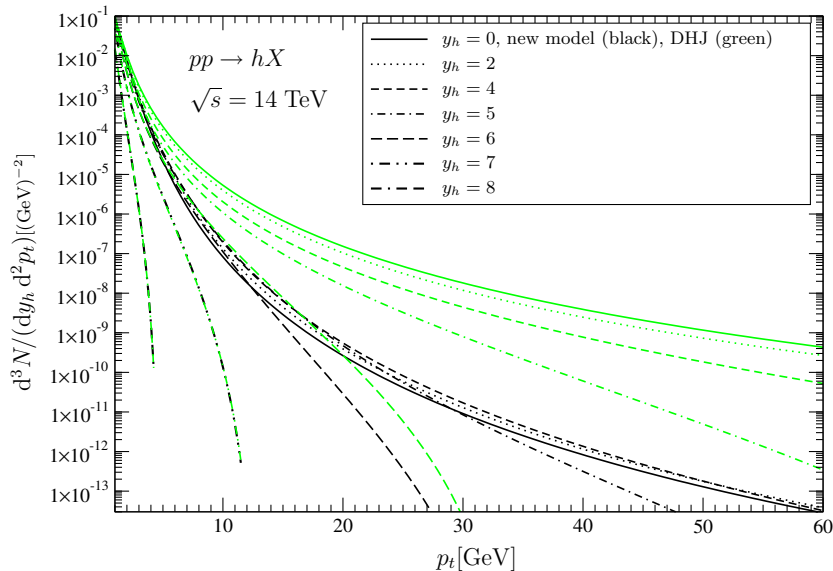


Figure 8.5: Predictions of the transverse momentum distributions of produced hadrons in p - p collisions at the LHC energy of $\sqrt{s} = 14$ TeV and various rapidities $y_h = 0 - 8$. The distributions from the scaling model are represented by the black lines and those from the DHJ model by the green/light ones.

In Fig. 8.5 we show the predictions for the p - p collisions at $\sqrt{s} = 14$ TeV. For small p_\perp the predictions of the DHJ model and the new model are comparable, like in d - Au collisions at RHIC. For large rapidities, i.e. $y_h \approx 7 - 8$, the predictions are indistinguishable since the reachable momenta $q_\perp \leq \sqrt{s} \exp(-y_h)$ are so small that the ratios $w = q_\perp/Q_s$ are always close to one, where the dipole amplitude hardly depends on γ (and moreover, γ is effectively equal to γ_s in both models). However, there is quite a large range where the probed values of $x_2 \sim p_\perp / \sqrt{s} \exp(-y_h)$ are small but the predictions are clearly dif-

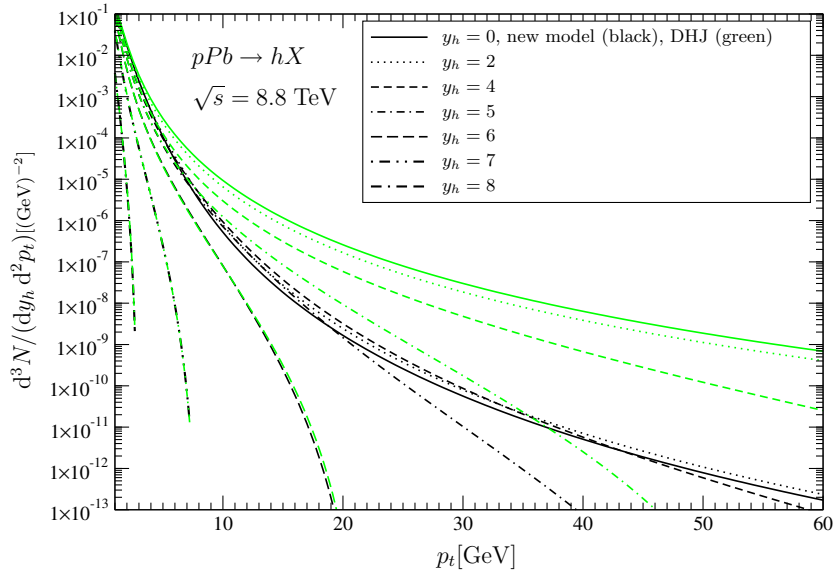


Figure 8.6: Same as Fig. 8.5 but for p - Pb collisions at the LHC energy of $\sqrt{s} = 8.8 \text{ TeV}$. We have used $A_{\text{eff}} = 20$. The black lines represent the scaling model, while the green/light lines represent the DHJ model.

ferent. The slope of the cross section is much larger when described in our model than in the DHJ model, since γ rises towards 1 much faster. Hence, a measurement of the slopes at moderate rapidities y_h at LHC would allow a discrimination between the DHJ model and our model in a region where small- x physics may be expected to be applicable. Since a logarithmic rise of γ , like in the DHJ model, is a generic signature of BFKL evolution, these measurements offer the possibility of testing whether such small- x evolution is actually relevant at present-day hadron colliders.

The p - Pb predictions for LHC are very similar. However, due to the smaller energy of $\sqrt{s} = 8.8 \text{ TeV}$ (see below), the predictions are already comparable for smaller rapidities, i.e. for $y_h \approx 6$, cf. Fig. 8.6. Since protons are accelerated to an energy of 7 TeV, the lead nucleus carries roughly $7Z/A \approx 2.75 \text{ TeV}$ per nucleon, where $A = 208$ and $Z = 82$ are respectively the number of nucleons and the number of protons of Pb . One then finds that p - Pb collisions at LHC take place at a centre of mass energy of $\sqrt{s} \approx 8.8 \text{ TeV}$. Further, we give the rapidities in the nucleon-nucleon centre of mass frame, which for LHC, in contrast to RHIC, is not the lab frame. We saw that at LHC, the proton and the Pb nucleons carry respectively 7 TeV and 2.75 TeV, while in the nucleon-nucleon centre of mass frame, both carry $\sqrt{s}/2 \approx 4.4 \text{ TeV}$. Since the rapidity is proportional to the logarithm of the large light cone component of the momentum, cf. Ref. [133], the rapidity difference between the lab frame and the centre of mass frame is given by $\Delta y_h = y_h^{\text{lab}} - y_h^{\text{cm}} \approx \ln(7/4.4) \approx 0.47$.

8.2. LHC predictions

Note that for the whole kinematic range depicted in Figs. 8.5 and 8.6 the x_2 values⁵ are well below 0.01.

8.2.2 Nuclear modification factor

In the previous section we saw that the slope of the transverse momentum distribution of produced hadrons in p - p and p - Pb collisions at LHC is sensitive to the rise of the anomalous dimension γ . From this point of view, the nuclear modification factor, R_{pA} , which corresponds to the ratio of proton-proton and proton-nucleus scattering at the same centre of mass energy, may be of interest. The nuclear modification ratio is defined as

$$R_{pA} = \frac{1}{N_{\text{collisions}}} \left(\frac{dN^{pA}}{dy_h d^2 p_\perp} \bigg/ \frac{dN^{pp}}{dy_h d^2 p_\perp} \right). \quad (8.12)$$

where the factor of $1/N_{\text{collisions}}$ corrects for the larger number of partonic collisions in p - A . If nuclear scattering would be nothing but proton-proton scattering involving more partons, this ratio would be equal to 1. If it is not, it is a measure of nuclear effects. Also, R_{pA} is sensitive to the nuclear dependence of saturation: since $Q_s^2 \sim A_{\text{eff}}^{1/3}$, saturation effects will show up earlier in proton-nucleus scattering than in proton-proton scattering at the same energy, which makes the observable of interest for saturation models. For details on the nuclear modification factor and saturation physics, we refer to Ref. [94, 134] and references therein.

In Ref. [135], R_{dAu} is calculated using both the DHJ model and the scaling model (R_{dAu} according to the KKT model can be found in [136]). The result is shown in Fig. 8.7. The results of both models are comparable at $y_h = 4$, but turn out to be different, surprisingly, already at $y_h = 3.2$ and lower, where the slopes resulting from the DHJ model are too flat compared with the data, even where x_s is still below 0.01. One can conclude that the nuclear modification factor is a rather sensitive probe of the rise of γ as a function of p_\perp . Unfortunately, at LHC, p - p and p - Pb collisions will take place at different centre of mass energies, namely 14 TeV and 8.8 TeV respectively. Hence, the nuclear modification factor is at LHC not a direct observable.

8.2.3 Geometric scaling in jet production

While the slope of the transverse momentum distribution of produced hadrons (or possibly the nuclear modification ratio) offers a test of the rise of γ , geometric scaling cannot be tested straightforwardly. As mentioned, geometric scaling of the dipole amplitude does not directly lead to scaling of the hadron production cross section at RHIC or LHC, unlike in the case of the DIS cross section, because of the convolution of the amplitude with the non-scaling parton distributions and fragmentation functions. This effect can be reduced by considering jet production. The description of the jet cross section does not involve

⁵The probed values of x_2 in the formalism of Eq. (8.1) are smaller than in the usual perturbative description, due to the different kinematics, see appendix B.

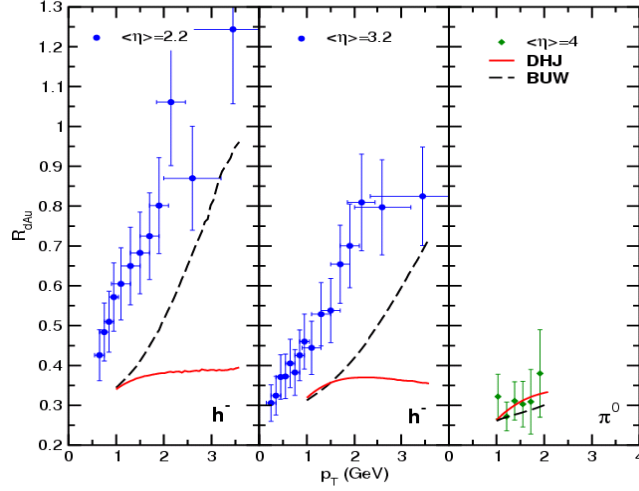


Figure 8.7: Nuclear modification ratio at RHIC, compared with curves calculated using the DHJ model and the new scaling model (indicated with BUW). Plot taken from Ref. [135].

any fragmentation functions, but reduces to just a sum over products of dipole amplitudes and parton distribution functions,

$$\frac{dN_h}{dy_h d^2 p_\perp} = \frac{K(y_h)}{(2\pi)^2} \left[\sum_q f_{q/p}(x_F, p_\perp^2) N_F(p_\perp, x_2) + f_{g/p}(x_F, p_\perp^2) N_A(p_\perp, x_2) \right], \quad (8.13)$$

where $x_F = p_\perp / \sqrt{s} \exp(y_h)$ and $x_2 = x_F \exp(-2y_h) = p_\perp / \sqrt{s} \exp(-y_h)$. This means that in the kinematic regions where either the gluon contribution or the quark contribution is dominant (in general these will be small kinematic regions), the corresponding distribution function can be divided out, so that one obtains the dipole amplitude directly from the data. Of course, if the dipole amplitude is only mildly scaling violating, the kinematic region where this can be done may be too small to observe the violations in this way. At LHC, the gluon contribution to the jet cross section (8.13) is reasonably dominant for transverse momenta $p_\perp \lesssim 15$ GeV and hadron rapidities $y_h = 0 - 2$. In this region, the scaling violations of the ratio $(p_\perp^2 dN_h/dy_h d^2 p_\perp) / f_{g/p}(x_F, p_\perp^2)$ are in the DHJ model about 30%, while the violations for the exactly scaling model are, due to quark contributions, still about 10%. We conclude that it may be difficult to attribute any observed violations directly to N_A . A similar conclusion holds for N_F in the region where quarks dominate (8.13) (when $x_F \gtrsim 0.1$, see Fig. 8.2 where this region is located in the $p_\perp - y_h$ plane).

In summary, even for jet production, where there are no complications from the fragmentation functions, it may not be possible to establish geometric scaling violations conclusively due to the mixture of quark and gluon contributions. The kinematic range at LHC where either quark or gluons dominate is probably too small to reach a definite conclusion about scaling violations.

8.3 Conclusions

In this chapter, we have presented a new phenomenological model of the dipole scattering amplitude to demonstrate that the RHIC data for hadron production in d - Au collisions for all available rapidities are compatible with geometric scaling. We emphasize that geometric scaling cannot be directly observed in the RHIC data, unlike for DIS. Moreover, the new model also provides a reasonable description of the small- x DIS data. On the other hand, in a region of y_h and p_\perp for which the probed values of x are sufficiently small, the RHIC data are also compatible with geometric scaling violating models, such as the DHJ model. The fact that the DHJ model, which to some extent incorporates scaling violations from BFKL (or more generally BK) evolution, also describes the forward RHIC data suggests that the data simply do not span a sufficiently large region in p_\perp and y_h to demonstrate possible violations of geometric scaling. Hence, contrary to statements made in Refs. [47, 48] and Ref. [137], it cannot be concluded whether scaling violations of the dipole scattering amplitude play a role at RHIC. An important difference between the DHJ model and the new model is the way in which the anomalous dimension approaches unity with increasing transverse momentum. In the new model this rise is power-like, while it is logarithmic in the DHJ model, as expected from BFKL/BK evolution. In Ref. [135] it was shown that the slope of the nuclear modification ratio R_{dAu} , is in agreement with the new model, while the slope according to the DHJ model is too shallow for rapidities of $y_h \leq 3.2$.

The breakdown of the DHJ model at mid-rapidity might simply be due to the probed values of x being not sufficiently small. The situation is different at LHC in p - p and p - Pb collisions. For moderate rapidities, but still within the region where the small- x description is expected to be applicable, the DHJ model and the new scaling model lead to different, distinguishable predictions for the p_\perp fall-off of the cross section. This fall-off is determined by the way in which the anomalous dimension γ approaches 1 for large transverse momentum. As mentioned, BFKL/BK evolution typically leads to a logarithmic rise of γ and therefore implies a fall-off that is much slower than one finds for the new scaling model, the slope of which is compatible with both the RHIC and the DIS data. The nuclear modification ratio, which seems an even more sensitive probe of the slope of the cross section, is not a direct observable due to the different energies of p - p and p - Pb collisions. Therefore, at LHC in both p - p and p - Pb collisions the transverse momentum distribution will probe for the first time the rise of the anomalous dimension γ at sufficiently small x , and will thus provide an important test of the expectations from small- x evolution.

Further, we conclude that geometric scaling can presumably not be tested very reliably in a model independent way at LHC. In a kinematic range where either gluons or quarks dominate the cross section for jet production, one can divide out the corresponding parton distribution function to obtain the dipole amplitude directly. However, these kinematic regions are most likely too small to establish scaling violations. Hence, the best test of small- x properties of the dipole amplitude is the transverse momentum distribution of produced hadrons.

Chapter 9

Polarization of Λ hyperons and the saturation scale

In this chapter, we will analyse the polarization of Λ hyperons that are produced in *unpolarized* proton-nucleus collisions at small x , using the framework developed in Refs. [138–140]. In Ref. [57] it was shown that such a description predicts that the polarization of the produced Λ 's shows a peak at transverse momenta that are roughly equal to the saturation scale, which would make it a direct probe of saturation and even the saturation scale itself. To describe the scattering of the partons from the proton off the target nucleus, in the analysis of Ref. [57] the McLerran-Venugopalan (MV) model [49, 50, 66, 123], was used, in which the saturation scale is constant. The MV model is described in section 6.2.1. In this chapter, the analysis is extended to the more realistic case where the saturation scale depends on x . Instead of the MV model, we will focus on the geometric scaling model, introduced in section 8.1.1, and the DHJ model, which is described in section 6.2.3. The geometric scaling model was introduced in chapter 8 to investigate the small- x properties of the d - Au data from RHIC, which it is able to describe at all rapidities, while the DHJ model, which incorporates expectations from BFKL/BK evolution, describes the RHIC data at forward rapidities. As discussed in chapter 8, future LHC data will be able to distinguish these models at small x , but lacking such data we will use both models to investigate the polarization of Λ 's produced in p - A collisions. We demonstrate that using both the geometric scaling model and the DHJ model, the peak in the polarization remains, and is still related to the saturation scale. Moreover, the dependence of the peak position on x_F can be used to determine the x dependence of the saturation scale.

As an introduction, in section 9.2 we briefly review the results of Ref. [57], and inspect some approximations made in that analysis in section 9.3. Section 9.4 is devoted to discussion of the possibility of measuring Λ polarization in hadron colliders. In section 9.5, we will present our analysis of the polarization using the geometric scaling and DHJ dipole models. In section 9.6 we discuss model results for the polarization observable, for LHC kinematics mainly, and point out the generic qualitative features. Achieving re-

9.1. Introduction

alistic quantitative predictions for the degree of Λ polarization will not be our aim, due to the large normalization uncertainty in the polarization dependent fragmentation functions. Nevertheless, an estimate can be given of the range of x_F values required to observe the x dependence of the saturation scale, as the p_\perp dependence of the Λ polarization is found to be less model dependent than its absolute value. Prospects for RHIC are also briefly discussed, but no results will be shown, since, according to our analysis, at RHIC the peak is most likely situated at transverse momenta below 1 GeV, where the considered theoretical description would not be appropriate. We end with conclusions.

9.1 Introduction

It is well-known that Λ hyperons produced in collisions of unpolarized hadrons are to a large degree polarized perpendicularly to the production plane. Even though the origin of this phenomenon has not been clarified fully yet, for sufficiently large transverse momentum p_\perp of the Λ , one expects that a parton description must be applicable.

In order to describe the transverse Λ polarization in unpolarized hadron collisions within such an approach, the possibility has been considered that unpolarized quarks can fragment into transversely polarized hadrons, for instance Λ hyperons. The fragmentation process is described by a so-called polarizing fragmentation function [138, 139] that is *transverse momentum dependent*. This function is an odd function of the transverse momentum \mathbf{k}_\perp of the produced hadron relative to the quark and describes the production of a hadron that is polarized orthogonally to \mathbf{k}_\perp because of parity invariance. It is defined as the difference between the densities $\hat{D}_{h^\uparrow/q}$ and $\hat{D}_{h^\downarrow/q}$ of spin-1/2 hadrons h carrying transverse polarization in the opposite directions (\uparrow) and (\downarrow) that are produced by the fragmentation of an unpolarized parton q [139],

$$\Delta^N D_{h^\uparrow/q}(z, \mathbf{k}_\perp) \equiv \hat{D}_{h^\uparrow/q}(z, \mathbf{k}_\perp) - \hat{D}_{h^\downarrow/q}(z, \mathbf{k}_\perp) = \hat{D}_{h^\uparrow/q}(z, \mathbf{k}_\perp) - \hat{D}_{h^\uparrow/q}(z, -\mathbf{k}_\perp). \quad (9.1)$$

Here, z is the hadron's longitudinal momentum fraction and \mathbf{k}_\perp its transverse momentum, both defined with respect to the fragmenting quark. Clearly, this k_\perp -odd function vanishes when integrated over transverse momentum and also when the transverse momentum and the transverse spin are parallel. The sign convention for the polarization is defined as

$$\Delta^N D_{h^\uparrow/q}(z, \mathbf{k}_\perp) \equiv \Delta^N D_{h^\uparrow/q}(z, k_\perp) \frac{\mathbf{P}_h \cdot (\mathbf{q} \times \mathbf{k}_\perp)}{|\mathbf{q} \times \mathbf{k}_\perp|} \equiv \sin \phi \Delta^N D_{h^\uparrow/q}(z, k_\perp), \quad (9.2)$$

where \mathbf{q} is the momentum of the unpolarized fragmenting quark and \mathbf{P}_h denotes the direction of the polarization vector of the hadron h (the \uparrow direction). Fig. 9.1 shows the kinematics of the process under consideration and indicates the direction of positive Λ polarization for each quadrant in the Λ production plane.

In Refs. [57, 139], it is assumed that the polarized fragmentation function describing the production of Λ hyperons, $\Delta^N D_{\Lambda^\uparrow/q}$, is strongly peaked around some average transverse momentum k_\perp^0 in the production plane (i.e. $\phi = \pm\pi/2$), so that one can use the

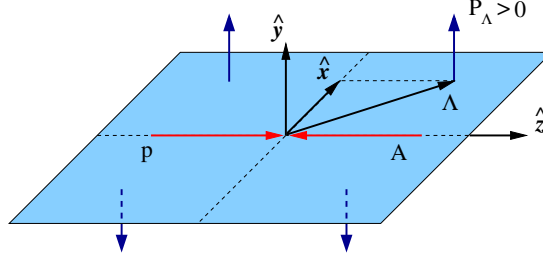


Figure 9.1: Kinematics of the $pA \rightarrow \Lambda X$ process. The sign convention for the Λ polarization is indicated with an arrow in each quadrant of the Λ production plane. Plot taken from Ref. [57].

approximation

$$\int d^2k_{\perp} \Delta^N D_{\Lambda^{\uparrow}/q}(z, Q^2, \mathbf{k}_{\perp}) F(\mathbf{k}_{\perp}) \simeq \Delta^N D_{\Lambda^{\uparrow}/q}(z, Q^2) [F(k_{\perp}^0) - F(-k_{\perp}^0)], \quad (9.3)$$

where $F(\pm k_{\perp}^0) = F(k_{\perp} = k_{\perp}^0, \phi = \pm\pi/2)$, and the average transverse momentum of the produced Λ 's is parameterized as

$$k_{\perp}^0 = 0.66 z^{0.37} (1-z)^{0.50} \text{ GeV}. \quad (9.4)$$

The function $\Delta^N D_{\Lambda^{\uparrow}/q}(z, Q^2)$ is parameterized in terms of the unpolarized fragmentation function, see Ref. [141], as

$$\Delta^N D_{\Lambda^{\uparrow}/q}(z, Q^2) \equiv N_q z^{c_q} (1-z)^{d_q} \frac{D_{\Lambda/q}(z, Q^2)}{2}, \quad (9.5)$$

where

$$N_u = N_d = -28.13, \quad N_s = 57.53, \quad c_q = 11.64, \quad d_q = 1.23. \quad (9.6)$$

Alternatively, one can go beyond the approximation (9.3) and consider Gaussian distributions in k_{\perp} [140]. We will adopt the approximation (9.3) in the present analysis, and show in section 9.3 that the simplification of Eq. (9.3) suffices for qualitative purposes. In fact, the fits of the polarized fragmentation functions were made to $p + A \rightarrow \Lambda^{\uparrow} + X$ data for light nuclei, at moderate centre of mass energies and in a limited range of transverse momenta of the produced Λ 's, where it is not entirely beyond doubt that a factorized approach can be employed. However, as noted in Refs.[57, 139], the resulting fragmentation functions exhibit reasonable features. Hence, the present analysis is to be considered a qualitative study of the general features of Λ polarization rather than an exact quantitative prediction. Still, the general result, namely the relation between the location of the peak of the polarization and the saturation scale does not depend on the details of the parameterization of the polarized fragmentation function—it arises from the odd dependence on k_{\perp} , peaked around k_{\perp}^0 [57].

9.2. Λ polarization in $p + A \rightarrow \Lambda + X$

9.2 Λ polarization in $p + A \rightarrow \Lambda + X$

Armed with the fragmentation functions that describe the production of polarized Λ 's in unpolarized p - A scattering, we proceed to derive an expression for the cross section of p - A scattering in the kinematic regime where the target nucleus can be described as a colour glass condensate.

In section 3.2.2, we calculated the cross section of a quark (e.g. from a proton) moving along the negative light cone that scatters off a nucleus that moves along the positive light cone, where the nucleus is described as a colour glass condensate. The single inclusive cross section of the total scattering process $p + A \rightarrow h + X$ is obtained by convolving the partonic cross section (6.11) with the parton distribution functions ($f_{q/p}$) of the proton and the appropriate fragmentation functions (generically written as $D_{\Lambda/q}$) [46], yielding¹

$$\begin{aligned} x_F \frac{d\sigma^{pA \rightarrow hX}}{dx_F d^2 p_\perp d^2 b} &= \int dx' \int \frac{dz}{z^2} f_{q/p}(x, Q^2) \int d^2 k_\perp x' \frac{d\sigma^{qA \rightarrow hX}}{dx' d^2 q_\perp d^2 b} D_{\Lambda/q}(z, Q^2, \mathbf{k}_\perp) \\ &= \frac{1}{(2\pi)^2} \int dx \int \frac{dz}{z^2} f_{q/p}(x, Q^2) \int d^2 k_\perp x C(q_\perp) D_{\Lambda/q}(z, Q^2, \mathbf{k}_\perp), \end{aligned} \quad (9.7)$$

where x_F and z are the longitudinal momentum fractions of the produced hadron with respect to the incoming proton and the fragmenting quark respectively, and \mathbf{k}_\perp is the hadron's momentum transverse to the fragmenting quark's momentum (i.e. the momentum of the produced hadron is defined as $\mathbf{p} = (p^-, \mathbf{p}_\perp) \equiv z\mathbf{q} + \mathbf{k}_\perp$, where $\mathbf{k}_\perp \perp \mathbf{q}$). The transverse momentum of the produced hadron is denoted with p_\perp , while Q^2 denotes the scale at which the distribution and fragmentation functions are evaluated. In Ref. [57], this scale is put equal to the saturation scale, $Q^2 = Q_s^2$. Further, a summation over the quark flavours is understood²

The function $C(q_\perp)$, which is essentially the squared amplitude of the partonic scattering process, is given in Eq. (3.55). To reproduce the results of Ref. [57], in this section we will use the MV model for $C(q_\perp)$ given in Eq. (3.55), which we evaluate numerically using the code of [109].

The polarization of the Λ particles that are produced in p - A collisions, \mathcal{P}_Λ , is defined as the relative difference of the cross sections of the produced Λ 's with polarization \uparrow and polarization \downarrow ,

$$\mathcal{P}_\Lambda = \frac{d\sigma^{pA \rightarrow \Lambda^\uparrow X} - d\sigma^{pA \rightarrow \Lambda^\downarrow X}}{d\sigma^{pA \rightarrow \Lambda^\uparrow X} + d\sigma^{pA \rightarrow \Lambda^\downarrow X}} \quad (9.8)$$

We can now use Eq. (9.7) to calculate this polarization in the small- x region. The momentum of the produced hadron is defined relative to the momentum q of the fragmenting

¹This expression can be compared with Eq. (6.17). Note that the fragmentation functions considered there are independent of transverse momentum.

²In principle, also contributions from gluons scattering off the nucleus are taken into account, even though this amounts to only a small correction for $x_F \geq 0.1$ [57]. Usually, the scattering amplitude for gluons is obtained from the expression for quarks by replacing Q_s^2 by $(C_F/C_A)Q_s^2 = (4/9)Q_s^2$. However, we will use $C(q_\perp)$ for both quarks and gluons as was done in [57].

quark as $\mathbf{p} = z\mathbf{q} + \mathbf{k}_\perp$, where we assume that only the component of \mathbf{k}_\perp that lies in the production plane contributes to the polarization [57, 139], cf. Eq. (9.3). Since the incoming partons move in the x^- direction, we have $q^- \gg q_\perp$, because the longitudinal momentum of the scattered partons is conserved, cf. Eq. (3.56). Hence, we can write³ $p_\perp \approx zq_\perp + k_\perp$, and for the same reason $x_F \approx zx$. Using these approximations together with Eqs. (9.7) and (9.3), the polarization can be written as

$$\mathcal{P}_\Lambda(p_\perp, x_F) = \frac{\int_{x_F}^1 dx x f_{q/p}(x, Q^2) \Delta^N D_{\Lambda/q}\left(\frac{x_F}{x}, Q^2\right) \left[C\left(\frac{x}{x_F}(p_\perp - k_\perp^0)\right) - C\left(\frac{x}{x_F}(p_\perp + k_\perp^0)\right) \right]}{\int_{x_F}^1 dx x f_{q/p}(x, Q^2) D_{\Lambda/q}\left(\frac{x_F}{x}, Q^2\right) C\left(\frac{x}{x_F} p_\perp\right)} \quad (9.9)$$

In Figs. 9.2 and 9.3 the polarization is depicted following from a numerical evaluation of Eq. (9.9) for d - A collisions. Isospin invariance was used to obtain the parton distribution functions of the deuteron from the leading order (LO) parton distributions of [14]. As mentioned, the factorization scale Q^2 is chosen equal to the saturation scale Q_s , which in the MV model is a constant that is to be specified for the numerical evaluation.

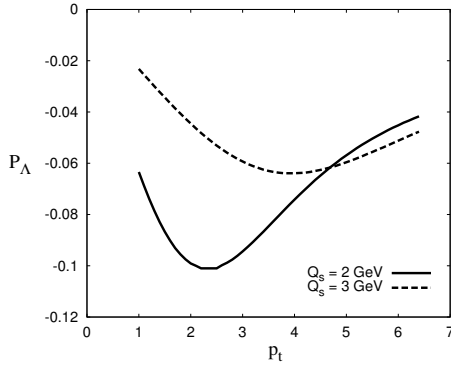


Figure 9.2: Λ polarization in d - Au collisions from Eq. (9.9), for $x_F = 0.5$ and $Q_s = 2, 3$ GeV, as obtained in [57].

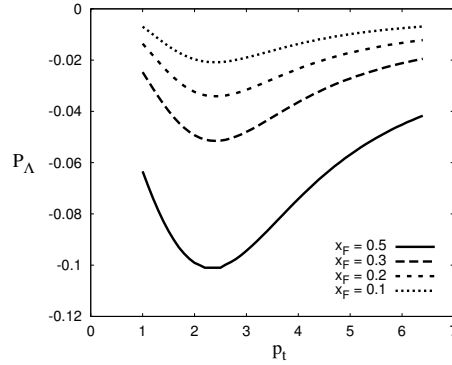


Figure 9.3: Λ polarization in d - Au collisions from Eq. (9.9), from Eq. (9.9) for $Q_s = 2$ GeV and various values of x_F , as obtained in [57].

The most crucial property of the polarization is that it peaks⁴ at transverse momenta around the saturation scale, $p_\perp \sim Q_s$. This property arises due to the k_\perp -odd nature of the polarized fragmentation function, and the fact that this function is peaked around an average $k_\perp^0 \lesssim 0.4$ GeV that is small with respect to $q_\perp \geq p_\perp$. Therefore, the polarization probes essentially the derivative of the partonic cross section, i.e. $C(q_\perp)$, with respect to q_\perp , which varies most rapidly around the saturation scale. In fact, by approximating

³If collinear fragmentation is considered, these approximations are exact, cf. appendix B.

⁴Since the polarized part of the fragmentation function is negative for the u and d quarks that constitute the dominating contributions, \mathcal{P}_Λ will have a negative valued minimum, which for convenience will sometimes also simply be referred to as a peak.

9.3. Gaussian fragmentation functions

$C(q_\perp)$ at $q_\perp \sim Q_s$ (by putting $\ln 1/r_\perp^2 \Lambda^2 \rightarrow \ln Q_s^2/\Lambda^2$ in Eq. (6.22)) as a regularization and substituting the result in Eq. (9.9), it follows [57] that at the peak \mathcal{P}_Λ scales roughly with $1/(Q_s \ln Q_s/\Lambda)$, which can indeed be seen in Fig. 9.2. In Fig. 9.3 the polarization is shown for $Q_s = 2$ GeV, and a number of values of x_F , showing that the amount of polarization scales roughly linearly with x_F .

9.3 Gaussian fragmentation functions

As mentioned in the introduction, the polarized fragmentation function $\Delta^N D(z, \mathbf{k}_\perp)$ is an odd function of \mathbf{k}_\perp , and is peaked around an average value of k_\perp that lies in the production plane. In Eq. (9.3), this k_\perp dependence is approximated with a δ -function. In this section, we consider the more realistic Gaussian distributions in \mathbf{k}_\perp of [140], while still assuming that \mathbf{k}_\perp lies in the production plane. According to Ref. [140], the fragmentation functions can be expressed as

$$\begin{aligned} \hat{D}_{\Lambda/q}(z, \mathbf{k}_\perp) &= \hat{D}_{\Lambda/q}(z, k_\perp) = \frac{D_{\Lambda/q}(z)}{\pi \langle k_\perp^2(z) \rangle} \exp \left[-\frac{k_\perp^2}{\langle k_\perp^2(z) \rangle} \right]; \\ \Delta^N D_{\Lambda/q}(z, \mathbf{k}_\perp) &= \sin \phi \Delta^N D_{\Lambda/q}(z, k_\perp) = \sin \phi \frac{\Delta(z)}{M^2} \frac{k_\perp}{M} \exp \left[-\frac{k_\perp^2}{r \langle k_\perp^2(z) \rangle} \right], \end{aligned} \quad (9.10)$$

where the angle ϕ is defined in Eq. (9.2). Further,

$$\begin{aligned} \frac{\Delta(z)}{M^3} &= N_q D_{\Lambda/q}(z) z^{0.53} (1-z)^{-0.27}; \\ \langle k_\perp^2(z) \rangle &= 2 \left(k_\perp^0(z) \right)^2 \end{aligned} \quad (9.11)$$

where $k_\perp^0(z)$ is defined in Eq. (9.4), and $N_u = N_d = -55.2$, $N_s = 112.9$. The values of these parameters are obtained from matching the peaks of the approximated fragmentation functions (9.5) with the peaks of the Gaussian parameterizations (9.10), as done in Ref. [142]. We use the parameters of Ref. [139] that are fitted to the unpolarized fragmentation functions of Ref. [141].

Using these expressions for the fragmentation functions, we now have to perform the integral over \mathbf{k}_\perp explicitly. We can write $\int d^2 k_\perp = \int d\phi \int dk_\perp k_\perp$, where the assumption that \mathbf{k}_\perp lies in the production plane means that $\phi = \pm\pi/2$. Since $\Delta^N D(\mathbf{k}_\perp) \sim \sin \phi \Delta^N D(k_\perp)$, and $\hat{D}(\mathbf{k}_\perp) = \hat{D}(k_\perp)$, we then obtain instead of Eq. (9.3)

$$\begin{aligned} \int d^2 k_\perp \Delta^N D_{\Lambda/q}(z, \mathbf{k}_\perp) F(\mathbf{k}_\perp) &= \int dk_\perp k_\perp \Delta^N D_{\Lambda/q}(z, k_\perp) [F(k_\perp) - F(-k_\perp)] \\ \int d^2 k_\perp \hat{D}_{\Lambda/q}(z, \mathbf{k}_\perp) F(\mathbf{k}_\perp) &= \int dk_\perp k_\perp \hat{D}_{\Lambda/q}(z, k_\perp) [F(k_\perp) + F(-k_\perp)], \end{aligned} \quad (9.12)$$

where again $F(\pm k_\perp^0) = F(k_\perp = k_\perp^0, \phi = \pm\pi/2)$.

Using Eqs. (9.7) and (9.8), we now find the following expression for the transverse polarization,

$$\mathcal{P}_\Lambda(p_\perp, x_F) = \frac{\int_{x_F}^1 dx \int dk_\perp k_\perp x f_{q/p}(x) \Delta^N D_{\Lambda^+ / q} \left(\frac{x_F}{x}, k_\perp \right) \left[C \left(\frac{x}{x_F} (p_\perp - k_\perp) \right) - C \left(\frac{x}{x_F} (p_\perp + k_\perp) \right) \right]}{\int_{x_F}^1 dx \int dk_\perp k_\perp x f_{q/p}(x) \hat{D}_{\Lambda / q} \left(\frac{x_F}{x}, k_\perp \right) \left[C \left(\frac{x}{x_F} (p_\perp - k_\perp) \right) + C \left(\frac{x}{x_F} (p_\perp + k_\perp) \right) \right]}, \quad (9.13)$$

where we have suppressed the dependence on the fragmentation scale Q^2 for brevity.

In Figs. 9.4 and 9.5 we show the polarization as it follows from a numerical evaluation of Eq. (9.13) for d - Au collisions. Again, we use isospin invariance to obtain the parton distributions of the deuteron from the LO parton distributions of [14], and choose the factorization scale as $Q^2 = Q_s^2$ in order to compare with Ref. [57]. Figs. 9.4 and 9.5 are to be compared with Figs. 9.2 and 9.3 that are obtained using the approximated fragmentation functions. Clearly, the qualitative features are the same. While the normalization is now a bit larger (due to the matching procedure), the position of the peak remains the same. We note that the normalization of the fragmentation functions is subject to uncertainty anyway. We conclude that the approximation (9.3) is sufficient for our purposes, capturing all the qualitative features of the polarization observable.

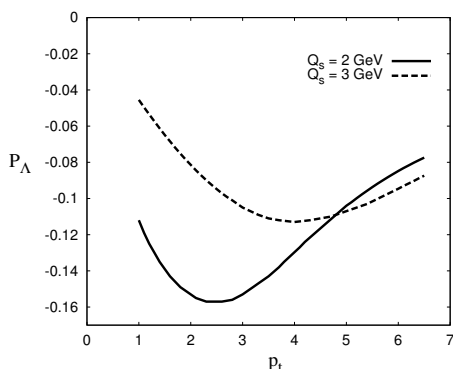


Figure 9.4: Λ polarization from Eq. (9.13) for d - Au collisions, using the Gaussian fragmentation functions (9.10), for $x_F = 0.5$ and $Q_s = 2, 3$ GeV.

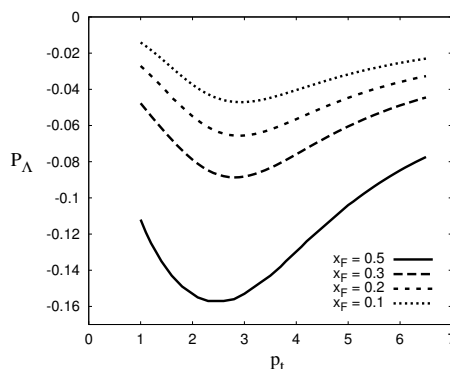


Figure 9.5: Λ polarization from Eq. (9.13) for d - Au collisions, using the Gaussian fragmentation functions (9.10), for $Q_s = 2$ GeV and various values of x_F .

9.4 Measuring \mathcal{P}_Λ

Having discussed this promising use of Λ polarization, let us now address the possibilities of measuring it in the small- x region. In high energy scattering the polarization of a spin-1/2 final state hadron can usually only be measured through self-analysing parity

9.4. Measuring \mathcal{P}_Λ

violating decays. Exploiting this property it was demonstrated already more than 30 years ago [143, 144] that Λ hyperons emerging from unpolarized p - A collisions are polarized perpendicularly to the production plane (cf. Ref. [145] for an extensive review of data). In the fixed target experiments performed at typical centre of mass energies $\sqrt{s} \sim 20$ GeV, the transverse momentum dependence of the degree of polarization shows the characteristic feature that after a linear rise until $p_\perp \sim 1$ GeV, it stays remarkably constant up to the highest measured values $p_\perp \sim 4$ GeV. This behaviour was found to be independent of the specific values of \sqrt{s} and atomic number A . For larger p_\perp values one expects the asymmetry to fall off as $1/p_\perp$, but this has not yet been observed. None of the measurements performed thus far cover a kinematic region where the target could be considered dense, i.e. in the saturation region. In sections 9.2 and 9.3 we saw that the characteristic flat behaviour observed for transverse momenta of a few GeV, would in that case no longer be present, but rather an extremum should be visible, located at $p_\perp \sim Q_s$. In other words, the observed plateau should turn into a peak as saturation effects set in and Q_s becomes a relevant scale. Since Q_s grows with $1/x$ and A , one expects this to happen when \sqrt{s} or A (or both) are increased significantly. Also, the probed values of x become smaller as the rapidity of the produced particles increases, so that in addition, one can focus on forward Λ production. In the colour glass description employed in this chapter, forward Λ 's at RHIC with rapidities of around 4 would begin to probe the small- x region [46], cf. appendix B. The possibilities of probing small x values are of course greater at LHC, where due to the much higher \sqrt{s} much less forward Λ 's are required. In Fig. 8.2 of chapter 8, the small- x regions at RHIC and LHC are depicted in terms of the kinematic variables p_\perp and y_h . For completeness, we recall that at RHIC d - Au collisions have been studied at energies of 200 GeV/ A in the nucleon-nucleon centre of mass frame. At LHC p - Pb collisions will be performed at $\sqrt{s} = 8.8$ TeV, but, as mentioned in chapter 8, these do not take place in the nucleon-nucleon centre of mass frame which leads to a rapidity shift from the lab frame to centre of rapidity frame of about half a unit. In principle also the p - p collisions at LHC are of interest here, due to the very large energy: $\sqrt{s} = 14$ TeV.

Experimentally the measurement of forward Λ 's and their polarization may be hampered by the often restricted particle identification capabilities in the forward region. Two-thirds of the time Λ 's decay into protons and negatively charged pions: $\Lambda \rightarrow p\pi^-$. The angular distribution of the decay in the rest frame of the Λ is used to determine the polarization of the Λ . Unfortunately, protons are usually hard to identify in the forward region. In that case the only alternative may be to exploit that the Λ 's decay one third of the time into neutrons and neutral pions (and subsequently, two photons): $\Lambda \rightarrow n\pi^0 \rightarrow n\gamma\gamma$. Neutrons, π^0 's and photons have been identified in the forward region at RHIC, hence this alternative may be feasible [146] and may in fact be the only way of measuring Λ polarization in the forward region at RHIC, LHC or a future electron-ion collider (EIC) (see e.g. [147]). We will proceed with our investigation under the assumption that forward Λ polarization will be measurable in the future.

9.5 Transverse Λ polarization in phenomenological dipole models

In section 9.2 we showed the results of Ref. [57], where the partonic amplitude is described using the MV model, leading to a peak in the transverse Λ polarization at $p_\perp \sim Q_s$. Since in the MV model the saturation scale is constant, we now want to investigate the more realistic case in which the saturation scale is x dependent [76, 148, 149]. It may be expected that, since now instead of a single value a range of Q_s -values is probed, the minimum of the polarization is smeared out, possibly even beyond recognition. However, we will demonstrate that this is not the case for not too large values of x_F . In fact, the polarization still has a pronounced minimum, which can even be used to probe the x dependence of the saturation scale. This makes the observable of potential interest for collider experiments at RHIC, LHC and a future electron-ion collider, the EIC.

The transverse polarization of forward Λ 's that are produced in unpolarized p - A collisions is obtained from Eq. (9.9) by replacing the scattering amplitude $C(q_\perp)$ from the MV model with the dipole scattering amplitude $N_F(q_\perp, x)$. We now write the gluon contribution to the unpolarized scattering explicitly, since the gluons scattering off the nucleus are described by a different amplitude, $N_A(q_\perp, x)$. The polarization is then given by

$$\mathcal{P}_\Lambda(p_\perp, x_F) = \frac{\int_{x_F}^1 dx x f_{q/p}(x, Q^2) \Delta^N D_{\Lambda^*/q}\left(\frac{x_F}{x}, Q^2\right) \left[N_F(q_\perp^{(-)}, x_2) - N_F(q_\perp^{(+)}, x_2) \right]}{\int_{x_F}^1 dx x \left[f_{q/p}(x, Q^2) D_{\Lambda^*/q}\left(\frac{x_F}{x}, Q^2\right) N_F(q_\perp, x_2) + f_{g/p}(x, Q^2) D_{\Lambda^*/g}\left(\frac{x_F}{x}, Q^2\right) N_A(q_\perp, x_2) \right]}, \quad (9.14)$$

where $q_\perp^{(\pm)} = (p_\perp \pm k_\perp^0)x/x_F$, $q_\perp = p_\perp x/x_F$, and a summation over the quark flavours is understood. As before, x_F and p_\perp are the Feynman x and the transverse momentum of the produced Λ . The rapidity y_h is related to x_F by $x_F = p_\perp/\sqrt{s} \exp[y_h]$ (see appendix B). Further, x and $x_2 = q_\perp^2/(xs)$ are respectively the momentum fractions of the parton in the proton and the target nucleus. Note that the polarization depends on three different values of x_2 , in conjunction with the three different transverse momenta $q_\perp^{(\pm)}$ and q_\perp .

We emphasize that there is a large uncertainty in the parameterization of $\Delta^N D_{\Lambda^*/q}$, as mentioned in section 9.4, so that the numerical results presented below should only be viewed as qualitative, not as quantitative predictions. Future collider data from LHC could be used to obtain a more trustworthy parameterization, for instance through the Λ +jet observable recently pointed out in Ref. [150], which deals with Λ 's at mid-rapidity where particle identification does not pose a problem.

Instead of describing the dipole amplitude $N_{F/A}$ with the MV model, we will analyse \mathcal{P}_Λ using more realistic models. We will focus on the DHJ model (6.31) [47, 48] and the geometric scaling (GS) model (8.6) introduced in chapter 8.

To shed light on the peak in the p_\perp distribution, we will separate \mathcal{P}_Λ into a p_\perp dependent part and an x_F dependent part in the following way. To good approximation the integrals in (9.14) are dominated by a value of $x_F/x \equiv z$ that is independent of p_\perp and only moderately dependent on x_F . Due to the large power c_q in $\Delta^N D$, cf. Eq. 9.6, which

9.5. Transverse Λ polarization in phenomenological dipole models

suppresses small ratios z in the numerator, the values of z that are effectively probed in the numerator and the denominator are different. We will denote the value that dominates the numerator with z and the smaller one that dominates the denominator with z' . Of course in the kinematic limit $x_F \rightarrow 1$, both z and z' must become equal to 1. In the following analysis we will stay away from this limit and assume that x_F stays smaller than roughly 0.5. Ignoring the gluonic contributions, which is a good approximation when x_F is not too small, we can approximate (9.14) in the following way

$$\begin{aligned} \mathcal{P}_\Lambda(p_\perp, x_F) &\approx \frac{D_{\Lambda/q}(z)(x_F/z) f_{q/p}(x_F/z, Q^2) f_q^\Lambda(z)}{D_{\Lambda/q}(z')(x_F/z') f_{q/p}(x_F/z', Q^2)} \\ &\times \frac{N_F\left(\frac{1}{z}(p_\perp - k_\perp^0), \frac{1}{x_F z} \frac{(p_\perp - k_\perp^0)^2}{s}\right) - N_F\left(\frac{1}{z}(p_\perp + k_\perp^0), \frac{1}{x_F z} \frac{(p_\perp + k_\perp^0)^2}{s}\right)}{N_F\left(\frac{1}{z'} p_\perp, \frac{1}{x_F z'} \frac{p_\perp^2}{s}\right)}. \end{aligned} \quad (9.15)$$

Since z and z' are considered constant, Eq. (9.15) now depends on p_\perp through the function N_F only. This is true assuming the factorization scale Q^2 to be constant. Still, in the following analysis we will mostly choose $Q^2 = p_\perp^2$, but this will turn out not to make much difference. The value of k_\perp^0 is only around 0.3 GeV or smaller for all relevant values of z , so that we can expand $N_F\left(\frac{1}{z}(p_\perp - k_\perp^0)\right) - N_F\left(\frac{1}{z}(p_\perp + k_\perp^0)\right)$ in terms of k_\perp^0/p_\perp . Thus, we can write

$$N_F\left(\frac{1}{z}(p_\perp - k_\perp^0)\right) - N_F\left(\frac{1}{z}(p_\perp + k_\perp^0)\right) \approx -2 \frac{k_\perp^0}{z} \frac{dN_F}{dq_\perp}. \quad (9.16)$$

Here we have suppressed the explicit dependence on x_2 for convenience, which we will do frequently below. Writing the dipole scattering amplitude in terms of a dimensionless function \tilde{N}_F ,

$$N_F(q_\perp, x_2) \equiv \frac{2\pi}{q_\perp^2} \tilde{N}_F(q_\perp/Q_s(x_2) \equiv w, x_2), \quad (9.17)$$

we can express Eq. (9.16) in the following way,

$$N_F\left(\frac{1}{z}(p_\perp - k_\perp^0)\right) - N_F\left(\frac{1}{z}(p_\perp + k_\perp^0)\right) \approx 2 \frac{k_\perp^0}{p_\perp} \frac{2\pi}{q_\perp^2} (2\tilde{N}_F(w) - w\tilde{N}'_F(w)). \quad (9.18)$$

Using this result, we can split off the p_\perp dependence (which is now contained in $w = p_\perp/Q_s$) of the transverse polarization and write

$$\mathcal{P}_\Lambda(p_\perp, x_F) \approx \frac{D_{\Lambda/q}(z)(x_F/z) f_{q/p}(x_F/z, Q^2) f_q^\Lambda(z)/z k_\perp^0}{D_{\Lambda/q}(z')(x_F/z') f_{q/p}(x_F/z', Q^2) Q_s z'^2} \frac{z^2}{z'^2} F(w, w'), \quad (9.19)$$

where we have defined the p_\perp dependent part of \mathcal{P}_Λ as a separate function $F(w, w')$,

$$F(w, w') = \frac{2}{w} \frac{2\tilde{N}_F(w) - w\tilde{N}'_F(w)}{\tilde{N}_F(w')}. \quad (9.20)$$

From the asymptotic behaviour of F it can now be seen that it must have an extremum. From Eq. (6.33) for the dipole amplitude in combination with Eq. (9.17), it follows that $\tilde{N}_F \propto 1/w^{2\gamma}$ for large w , and hence that $F(w, w')$ will approach $2(1 + \gamma)/w$. On the other hand, in the deep saturation regime the function (9.17) is proportional to w^2 , so that $F(w, w')$ vanishes as $w \rightarrow 0$. Therefore, the function $F(w, w')$, and consequently \mathcal{P}_Λ , must have a peak as it connects these two asymptotic behaviours. Without saturation there could also be a peak in \mathcal{P}_Λ , but one would in that case not expect the extremum to be rather sharply peaked around a perturbative scale of a few GeV. Therefore, the occurrence of such a peak would be a sign of saturation, especially—when the peak is located at transverse momenta that are proportional to Q_s —i.e. if its location shifts towards larger transverse momenta with increasing energy. Of course, the presence of a sharp peak is not guaranteed; there could be a plateau-like extremum, like at low energies. However, calculation of Ref. [57] using the MV model clearly shows a pronounced peak, the position of which is proportional to the (in that model constant) saturation scale Q_s . If this proportionality holds when Q_s evolves with x , the location of the peak in p_\perp would be a direct probe of the running of Q_s through its dependence on x_F . If however the peak position depends also *explicitly* on x_F , i.e. not only through Q_s , the running of Q_s cannot be reconstructed from the peak position. Because the probed values of $z'/z = w/w'$ depend on x_F , this means that we have to check that they do not influence the position of the peak. Fig. 9.6 shows $F(w, w')$ for various values of $w/w' = z'/z$ ranging from 0.25 to 1, using a dipole scattering amplitude with a constant $\gamma = 0.6275$. The curves indeed have a clear maximum⁵ as a function of w . The position of the peak hardly depends on w'/w if w'/w is not too close to 1, i.e. away from the kinematic limit $x_F \rightarrow 1$. Hence, we conclude that the peak of F is located at an approximately constant value of w . As mentioned, this means that the minimum of \mathcal{P}_Λ does not explicitly depend on x_F , but only through the saturation scale Q_s .

We find that all this remains true not only for different constant γ 's, but also for the DHJ and GS models. The GS model actually leads to the same peak position as a constant $\gamma = \gamma_s$, because it differs only little from $\gamma_{\text{GS}}(w = 1) = \gamma_s$ in the saturation region $w \leq 1$, where the peak of F is located. The DHJ model gives a slightly different peak position, which depends on the continuation of γ_{DHJ} into the saturation region $q_\perp < Q_s$, as will be discussed further below.

The x_F dependence of the peak of the resulting p_\perp -distribution can be estimated as follows. Since the peak of F is located at a constant value of $w = zp_\perp/Q_s$, where z is roughly constant as well, the peak in p_\perp is directly proportional to $Q_s(x_2)$. Because the dominant value of x_2 depends on both p_\perp and x_F , the peak position p_\perp^{peak} will depend on x_F . As the probed value of $z = x_F/x$ in the integrals in Eq. (9.14) is to good approximation constant, the target momentum fraction x_2 , which sets the saturation scale $Q_s(x_2)$, is given by

$$x_2 = x \exp(-2y_h) = \frac{x}{x_F^2} \frac{p_\perp^2}{s} \propto \frac{1}{x_F} \frac{p_\perp^2}{s}. \quad (9.21)$$

⁵As the polarized part of the fragmentation function is negative for the dominant contribution from the u and d quarks, \mathcal{P}_Λ has a negative valued minimum, which we often simply refer to as a peak.

9.5. Transverse Λ polarization in phenomenological dipole models

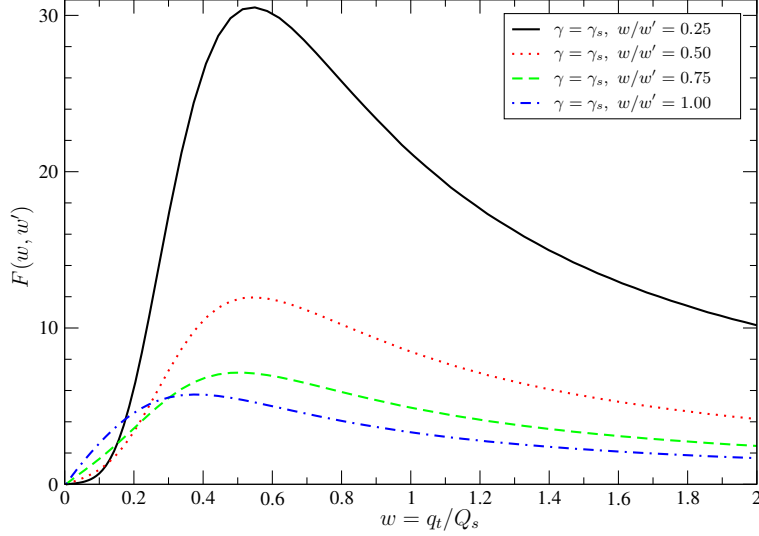


Figure 9.6: The function $F(w, w')$ for $\gamma = 0.6275$ and various ratios w/w'

Using this relation, we can estimate the x_F dependence of the peak position p_{\perp}^{peak} of \mathcal{P}_{Λ} . Assuming that the saturation scale depends on x_2 through a power law in $1/x_2$, cf. Eq. (6.32), we see that

$$p_{\perp}^{\text{peak}} \propto Q_s(x_F, p_{\perp}^{\text{peak}}) \propto Q_0 \left(\frac{x_F x_0 s}{(p_{\perp}^{\text{peak}})^2} \right)^{\lambda/2} \quad (9.22)$$

$$\Rightarrow p_{\perp}^{\text{peak}}(x_F) \propto Q_0 x_F^{\lambda'/2} \left(\frac{x_0 s}{Q_0^2} \right)^{\lambda'/2}, \quad \lambda' = \frac{\lambda}{1 + \lambda} \quad (9.23)$$

Hence, we conclude that the running of the peak position with x_F is a clear indication of the running of the saturation scale $Q_s(x_2)$. Moreover, the power λ can be reconstructed from the behaviour of the peak position as a function of x_F .

The power $\lambda = 0.3$ follows from a fit to the DIS data, using a power law dependence on $1/x$, which is expected from small- x evolution equations in the fixed coupling case. With a running coupling, small- x evolution predicts a different x dependence of Q_s , which over the limited range of experimentally accessible values of x can still be approximated by a power law in $1/x$, and is consistent with $\lambda = 0.3$. This implies however, that in p - A collisions, where a different kinematic range is probed, λ may be different from 0.3. A measurement of the position of the peak in the polarization would provide a test of the running of Q_s in p - A collisions.

In the discussion above we have expanded N_F in terms of k_{\perp}^0/p_{\perp} , which means that we should take care that $p_{\perp} \gtrsim 1$ GeV. We note that given the dipole description and the choice of factorization scale $Q^2 = p_{\perp}^2$, this is a sensible lower bound. Therefore, below

we will only discuss results for which p_{\perp}^{peak} is in the perturbative regime.

9.6 Transverse Λ polarization results

Here we will present our numerical estimates of the transverse polarization (9.14). We use the CTEQ5 LO parton distributions of Ref. [14], and the unpolarized LO fragmentation function of Ref. [141], cf. Eq. (9.5). Unless stated otherwise, we will therefore set the factorization scale to $Q^2 = p_{\perp}^2$. We will return to the Q^2 dependence of the results later on.

We first discuss the p_{\perp} distribution of \mathcal{P}_{Λ} for constant values of x_F . Here we will first give the results for p - Pb collisions at LHC at $\sqrt{s} = 8.8$ TeV explicitly and later point out how they compare with p - p collisions at LHC and d - Au collisions at RHIC. In Eq. (6.32) for the saturation scale we use $A_{\text{eff}} = 20$ to describe the Pb nucleus. Fig. 9.7 shows the resulting \mathcal{P}_{Λ} , calculated for dipole scattering amplitudes with various constant values of γ from 0.5 to 0.9. The increasing magnitude of the polarization with increasing x_F is due to the polarized part of the fragmentation function (for larger x_F , larger values of z are probed). The anticipated rise of the peak position with x_F can be clearly observed. Furthermore, we see that the peak position rises approximately linearly with γ for all considered values of x_F .

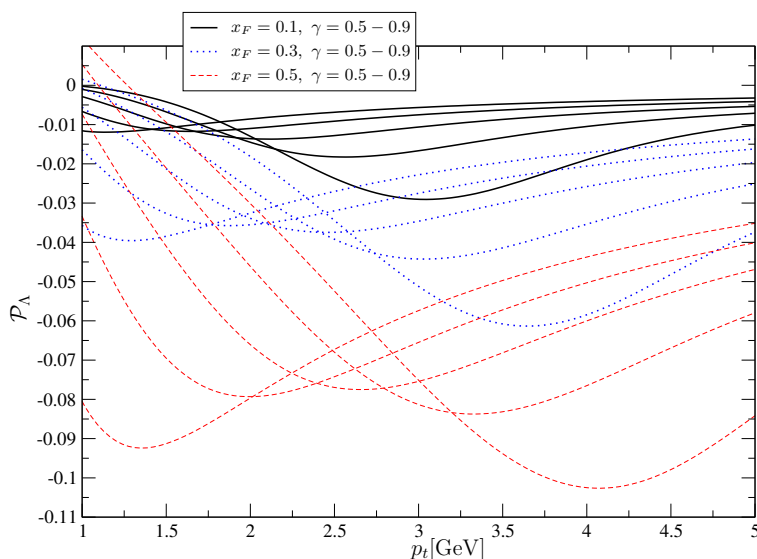


Figure 9.7: \mathcal{P}_{Λ} for various constant γ for p - Pb collisions at $\sqrt{s} = 8.8$ TeV. Curves for smaller γ have their minimum at smaller p_{\perp} .

Figure 9.8 shows the polarization for various values of x_F , as a function of p_{\perp} , but now for three γ 's that are all equal at the saturation scale: a constant γ_s , γ_{DHJ} and γ_{GS} . As expected, the difference between the polarization for γ_s and γ_{GS} is very small because in

9.6. Transverse Λ polarization results

the saturation region γ_{GS} differs only mildly from the value $\gamma_{\text{GS}}(q_{\perp} = Q_s) = \gamma_s$. Because of the uncertainty in the continuation of the DHJ parameterization in the saturation region, the estimate of \mathcal{P}_{Λ} around the peak is ambiguous. If we would for instance continue γ_{DHJ} by keeping it constant for $q_{\perp} < Q_s$, we would obtain roughly the same result as for γ_{GS} . The fact that the DHJ and GS models yield similar results for the behaviour of the peak indicates that our findings are rather robust and to a certain extent (qualitatively) model independent. In contrast, the magnitude of the polarization is subject to considerable uncertainty, mostly due to the parameterization of $\Delta^N D$, but also somewhat due to the choice of the factorization scale.

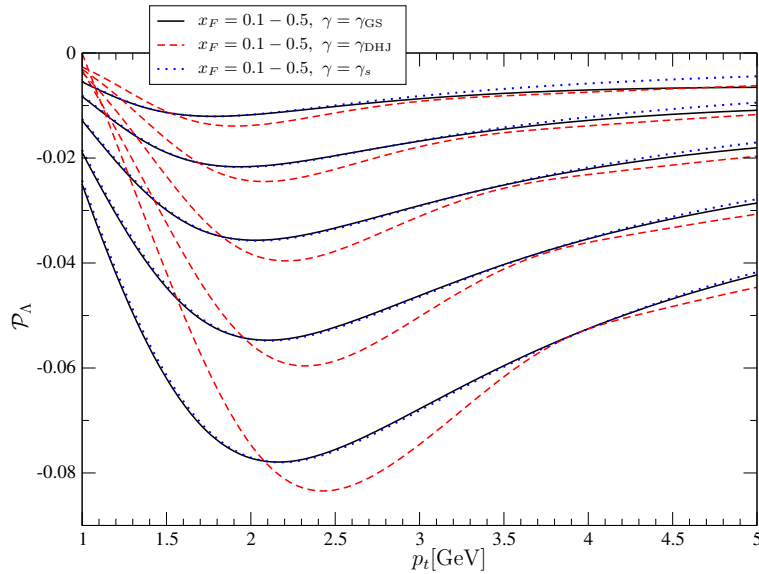


Figure 9.8: \mathcal{P}_{Λ} in p - Pb collisions at $\sqrt{s} = 8.8$ TeV, for γ_{DHJ} , γ_{GS} and a constant γ_s . The top lines correspond to $x_F = 0.1$, the lowest to $x_F = 0.5$.

Thus far, following the argument of Ref. [47], we have used a factorization scale $Q^2 = p_{\perp}^2$. However, in Ref. [57], and hence also in sections 9.2 and 9.3 the scale $Q^2 = Q_s^2$ was adopted, which may also be a natural choice. In the present analysis that choice would lead to an x dependent factorization scale. To illustrate the dependence of our results on the choice of factorization scale, Fig. 9.9 shows \mathcal{P}_{Λ} with γ_{GS} for three different factorization scales, $Q^2 = p_{\perp}^2$, $Q^2 = Q_s^2$, and a constant scale $Q^2 = 1$ GeV. As can be seen, for constant x_F the shape of the p_{\perp} distributions is rather independent of the factorization scale. The normalization however does depend on the choice of Q^2 , but still only moderately. We note once more that the normalization is subject to uncertainty already in the first place due to the parameterization of the polarized fragmentation functions. Therefore, choosing $Q^2 = p_{\perp}^2$ does not noticeably affect our observation that the x_F dependence of the peak momentum directly probes the x dependence of the saturation scale.

Fig. 9.10 shows the x_F dependence of the position of the peak in the p_{\perp} distribution

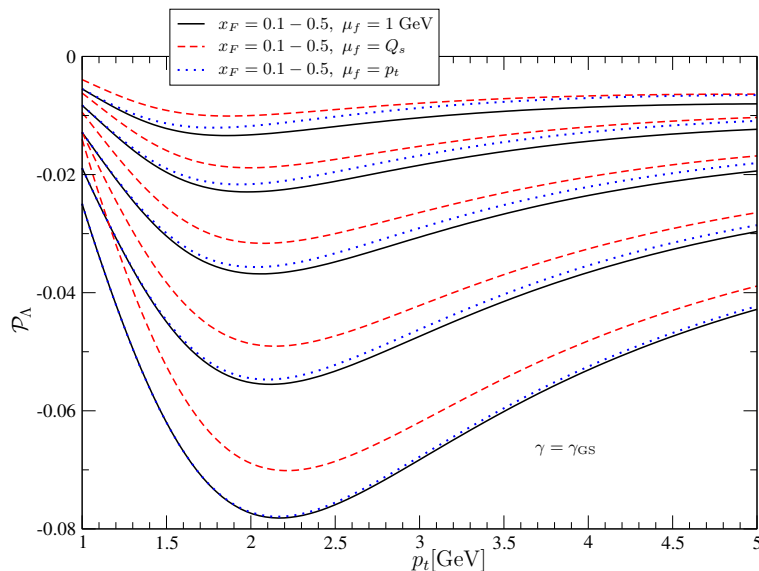


Figure 9.9: \mathcal{P}_Λ in p - Pb collisions at LHC for the scaling γ_{GS} and three different choices of the factorization scale $Q = p_\perp, Q_s$ and 1 GeV. The top lines correspond to $x_F = 0.1$, the lowest to $x_F = 0.5$.

for various choices of γ . The lines for constant γ confirm that the peak position scales linearly with γ . Moreover, for not too large x_F , the power law rise of p_\perp^{peak} with x_F is consistent with the result we obtained in Eq. (9.23), including the fact that the power is independent of γ . As expected, the results for $\gamma_{GS}(w)$ and the constant $\gamma = \gamma_s$ are very close to each other. The curve for γ_{DHJ} is similar to that of a constant γ that is slightly larger than γ_s . This is the case because γ_{DHJ} rises rather quickly in the saturation region as q_\perp decreases.

As can be seen from Fig. 9.10, all slopes are numerically consistent with the power $\lambda'/2$ in Eq. (9.23) for $\lambda = 0.3$, which was used to produce the figure. This implies that an increase in x_F by a factor of 5 would lead to a shift in the peak position of approximately 20%. This can be seen directly in Fig. 9.9 as well, by comparing the peak position at $x_F = 0.1$ and 0.5. Unfortunately, this is not a particularly large shift, but it does give an estimate for the precision with which the peak position needs to be determined. It should be mentioned that, as discussed before, the value of λ may be different in p - A collisions than in DIS. A larger value of λ would result in a stronger x dependence of Q_s and therefore in a larger x_F dependence of the peak position—which would consequently be easier to observe. At small x_F , where the position of the peak is less pronounced, it will be harder to determine than at large x_F . The value of p_\perp/Q_s at which the peak is situated depends—too good approximation linearly—on γ in the saturation region $q_\perp \leq Q_s$. As can be seen in Fig. 9.8, the peak is located for γ_{GS} and $\gamma = \gamma_s$ at almost the same position. We find empirically that in these cases the minimum in the p_\perp distribution shows up at

9.6. Transverse Λ polarization results

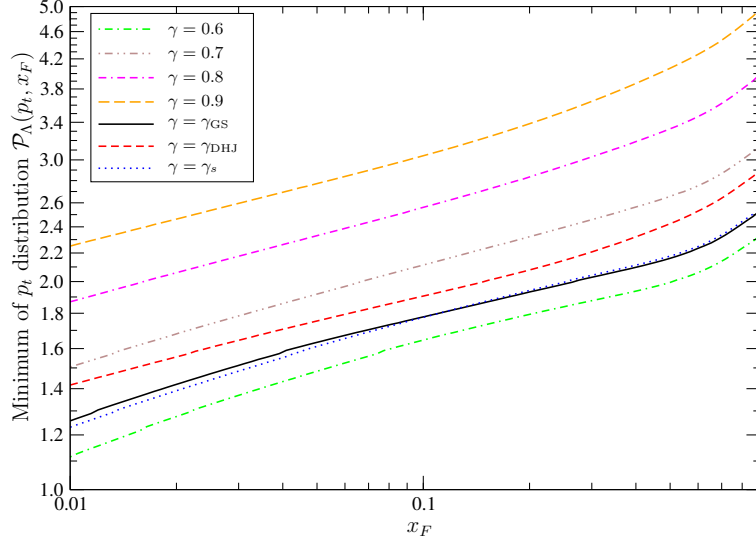


Figure 9.10: The peak position of the p_{\perp} distribution $\mathcal{P}_{\Lambda}(p_{\perp}, x_F)$ as a function of x_F in double logarithmic representation for various choices of γ .

$w \approx 0.55$, i.e. $p_{\perp} \approx 0.55 z Q_s$, where z rises slightly with x_F from 0.7 to 1 in the limit $x_F \rightarrow 1$. In the DHJ model the location of the peak is situated at a value of w that depends on the continuation of γ_{DHJ} to the saturation region. For the continuation of Eq. (6.31) the peak shows up at $p_{\perp} \approx 0.60 z Q_s$. This value is slightly larger than for γ_{GS} since γ_{DHJ} rises again towards smaller q_{\perp} in the saturation region.

Similar results for \mathcal{P}_{Λ} are obtained for p - p collisions at LHC and d - Au collisions at RHIC. Again an extremum is found around one half times the saturation scale with the same x_F dependence as in p - Pb scattering at LHC. However, due to the different energies and targets, Q_s and hence the position of the peak p_{\perp}^{peak} is in both cases smaller. Following the same line of arguments that lead to the x_F dependence of p_{\perp}^{peak} (9.23), one can estimate its \sqrt{s} and Q_0 dependence,

$$p_{\perp}^{\text{peak}}(x_F, \sqrt{s'}, Q_0') = p_{\perp}^{\text{peak}}(x_F, \sqrt{s}, Q_0) \left(\frac{Q_0' \sqrt{s'}^{\lambda}}{Q_0 \sqrt{s}^{\lambda}} \right)^{1/(1+\lambda)}, \quad (9.24)$$

where we have absorbed the factor of $A^{1/6}$ into Q_0 . For p - p at LHC, we take as before $Q_0 = 1$ GeV and $\sqrt{s} = 14$ TeV. Hence, the peak position is expected to be reduced by a factor of 1.3 with respect to p - Pb collisions at $\sqrt{s} = 8.8$ TeV. An explicit calculation confirms that this estimate works very well, i.e. the x_F dependent extremum is expected to show up approximately between 1.5 and 2.0 GeV for $x_F \sim 0.1 - 0.5$. For d - Au collisions at RHIC the probed values of x_2 are less small due to the smaller energy of $\sqrt{s} = 200$ GeV. Hence, in spite of the factor of $A_{\text{eff}} = 18.5$, the probed values of Q_s and hence p_{\perp}^{peak} are reduced even more, namely by a factor of 2.4 compared with p - Pb collisions at LHC.

Hence, the peak is presumably situated below the perturbative regime $p_{\perp} \gtrsim 1$ GeV, for constant values of $x_F = 0.1 - 0.5$. However, given the uncertainties in e.g. the values of Q_0 and λ , a peak in the perturbative region is not ruled out, especially for larger x_F . From this perspective it may still be worthwhile to investigate this observable at RHIC. We note that even if no peak is to be expected in the perturbative regime, a measurement of \mathcal{P}_{Λ} at RHIC may provide valuable input for improving the parameterization of the polarized fragmentation function (9.1).

Up to now we focused on the calculation of \mathcal{P}_{Λ} at constant x_F , where the dependence on \sqrt{s} is not very strong—in the MV model, where Q_s is constant, x_2 and hence \sqrt{s} plays no role at all. However, from an experimental point of view it might be more convenient to measure \mathcal{P}_{Λ} for constant rapidities y_h . As demonstrated before, there is a clear peak in the p_{\perp} distribution at fixed x_F , which is situated at different locations for different values of x_F . Therefore, since at fixed y_h a range of values of x_F contributes, the peak will be smeared out to some extent (this can also be observed for the DHJ model predictions for single spin asymmetries in forward pion production in the collisions of transversely polarized protons with unpolarized protons [122]). Hence, it is not clear a priori whether the peak remains observable and whether the peak position is still a clear probe of the saturation scale.

For LHC kinematics, we know from the previous analysis that a peak at transverse momenta larger than 1 GeV requires $x_F = p_{\perp} / \sqrt{s} \exp[y_h] \gtrsim 0.01$. At LHC such a peak is thus only expected in the forward region $y_h \gtrsim 4$. Fig. 9.11 shows \mathcal{P}_{Λ} for p - Pb scattering at LHC at $\sqrt{s} = 8.8$ TeV, for values of $y_h = 4, 5, 6$. Indeed, the extremum is in these cases located at a p_{\perp} larger than 1 GeV. It is however much less pronounced than at fixed x_F and less recognizable in the GS model than in the DHJ model. We also note that the magnitude of the asymmetry is considerably reduced for fixed x_F .

At RHIC the saturation scale becomes roughly of the order $Q_s \gtrsim 1$ GeV for forward Λ 's with rapidities of around 4. However, unlike for the MV model, the peak position is located at a transverse momentum that is up to a factor of two smaller than Q_s when described in the DHJ and GS models. Hence, even if $Q_s \sim 1$ the peak will probably be situated below $p_{\perp} = 1$ GeV. An explicit calculation of \mathcal{P}_{Λ} for RHIC confirms that even for $y_h = 4$ no peak is expected at transverse momenta larger than 1 GeV. In other words, $Q_s(x)$ can presumably not be extracted in a trustworthy manner from an analysis of RHIC data at fixed $y_h = 4$, unless either Q_0 or λ (or both) turn out to be larger than currently expected.

9.7 Conclusions

The transverse polarization of Λ particles displays a peak at the saturation scale when described using the MV model for the dipole scattering amplitude. We find that in the more realistic case where the dipole amplitude depends on x , such a peak in the p_{\perp} distribution remains. The position of the peak, p_{\perp}^{peak} , is still proportional to Q_s , and therefore offers a direct experimental probe of this scale. For fixed values of x_F , the x dependence of Q_s can be reconstructed from the x_F dependence of p_{\perp}^{peak} . This offers the possibility of comparing

9.7. Conclusions

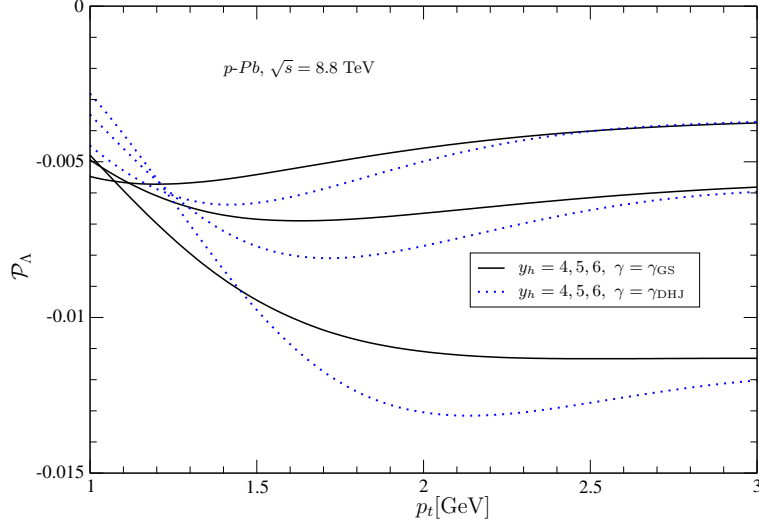


Figure 9.11: \mathcal{P}_Λ in p - Pb collisions at $\sqrt{s} = 8.8$ TeV for constant y_h , using γ_{GS} and γ_{DHJ} . The top lines correspond to $y_h = 4$, the lowest to $y_h = 6$.

the function $Q_s(x)$ obtained in this way from p - A collisions with the well-known GBW parameterization of Q_s that was obtained from DIS data, in order to establish consistency among the descriptions of all available data. The power λ in $Q_s^2 \sim (1/x)^\lambda$ determines how strongly the location of the peak in the polarization varies with x_F . Using the value of $\lambda = 0.3$ from DIS, which is compatible with d - Au data from RHIC (cf. chapter 8), we have obtained the following results. In p - Pb collisions at LHC, for values of x_F that lie between 0.1 and 0.5, the position of the peak is expected between $p_\perp = 1.5$ and 2.5 GeV. This result is obtained for a range of dipole models that includes the DHJ and GS models. In p - p collisions at LHC, the position of the peak is reduced by a factor of 1.3, but is still in the perturbative regime. In d - Au collisions at RHIC, the position of the peak is reduced by a factor of 2.4 with respect to p - Pb at LHC, due to the much smaller energy. Hence, an observation of the peak in the perturbative regime at RHIC seems unlikely, except perhaps at even larger x_F values.

For fixed values of the rapidity instead of x_F , the peak in the p_\perp distribution is smeared out and reduced in size. Moreover, in this case the polarization features a peak in the perturbative regime $p_\perp \gtrsim 1$ GeV only for Λ rapidities of 4 or larger in p - Pb collisions at LHC. Therefore, Λ polarization LHC data at fixed x_F are best suited to the purpose of establishing the x dependence of Q_s in p - A collisions.

Even though the presented quantitative estimates are to some extent model dependent, the qualitative features of the Λ polarization, i.e. the position of the peak with respect to Q_s and its running with x_F , are expected to be generic for the small- x region. This offers a unique possibility of probing Q_s directly in p - A collisions.

Chapter 10

Summary

In high energy scattering off a hadron, the scattered particle probes gluons in the hadron that have a longitudinal momentum fraction x , which decreases as the centre of mass energy becomes larger. As x becomes smaller, the gluon density rises quickly. At very small values of x , the gluon density is expected to saturate in order to preserve unitarity. The physical picture behind this gluon saturation is that the gluon density increases so fast that the gluons start to overlap within the hadron with a probability of the order of unity, so that interactions among the gluons prevent the fast rise to continue.

Deep inelastic scattering at such small values of x can be described in the dipole formalism [32]. The virtual photon fluctuates into a quark-antiquark pair, i.e. a colour dipole, that subsequently scatters off the proton. The scattering of the dipole off the proton is given by the so-called dipole scattering amplitude $N(r_{\perp}, x)$, in which r_{\perp} is the transverse size of the dipole. In the dipole picture, gluon saturation implies that the linear BFKL equation [17–19], which describes the evolution of the dipole scattering amplitude at small x , is expected to be supplanted by a non-linear evolution equation, such as the BK equation [27–30]. These equations are discussed in chapters 4 and 5.

An important consequence of saturation is geometric scaling [44], which means that the dipole amplitude becomes a function of a single parameter, $r_{\perp} Q_s(x)$, where $Q_s(x)$ is the so-called saturation scale. The total cross section of deep inelastic scattering then becomes a function of the single parameter $Q^2/Q_s^2(x)$, where Q^2 is the photon virtuality. This scaling behaviour of the cross section has been observed experimentally for values of x below 0.01 [34, 45, 98]. Here, we address the question whether geometric scaling is also visible in deuteron-gold collision data taken at the Relativistic Heavy Ion Collider (RHIC). Geometric scaling of the dipole amplitude, unlike in DIS, does not lead to a scaling property of the hadron production cross section in nucleon-nucleus collisions, since the dipole amplitude is convolved with parton distribution functions of the nucleon. Hence, one has to study the scaling properties of such data using specific models.

In the usual perturbative picture of nucleon-nucleus (and d - Au) scattering, a parton from the nucleon scatters off a parton from the nucleus. At very high energies however, when the gluon density in the nucleus becomes large enough, the nucleus can be de-

scribed as a so-called colour glass condensate [47, 49–51]. This formalism is discussed in chapter 3. Instead of scattering off a single gluon at small x , the incoming parton scatters off an effective colour field, the non-abelian analogue Weizsäcker-Williams field in electrodynamics, the sources of which are the partons of the nucleus at large x . In the McLerran-Venugopalan (MV) model [49–51, 66], the distribution of these sources is assumed to be Gaussian, and an analytic result can be obtained for the amplitude, N_F , of a quark scattering off the nucleus. The amplitude N_F turns out to be equal to (minus) the Fourier transform of the dipole amplitude N that is used to describe deep inelastic scattering at small x . While the dipole amplitude that corresponds to the MV model shows saturation, it does not incorporate evolution in x . Hence, it cannot be used to investigate geometric scaling.

In principle, one can try to find a dipole amplitude that incorporates x evolution by solving the BK equation. However, presently no analytic solutions are known. Still, one can derive a couple of properties of the solution by considering the BFKL equation in the presence of a saturation boundary condition as an approximation to the BK equation [44], which is discussed in chapter 4. Alternatively, one can approximate the BK equation by expanding its kernel χ . This leads to the so-called travelling wave approximation [75, 78], which is discussed in chapter 5. Both approaches lead to the following two expectations for the dipole amplitude at $r_\perp \leq Q_s(x)$. Firstly, at asymptotically small x , the dipole amplitude becomes geometrically scaling. Secondly, in the kinematic region $1 < \ln 1/r_\perp^2 Q_s^2 \ll \bar{\alpha}_s \chi'(\gamma_s) \ln 1/x$, where $\gamma_s = 0.628$, the amplitude shows approximate geometric scaling, and can be written as $N(r_\perp, x) = (r_\perp^2 Q_s(x)^2)^\gamma$. Here, $\gamma = \gamma_s + \Delta\gamma$ with $\Delta\gamma \sim \ln(1/r_\perp^2 Q_s^2)/Y$, so that the exponent γ rises logarithmically with $1/r_\perp$ and violates geometric scaling at finite values of $Y = \ln 1/x$. The exponent γ is often referred to as the anomalous dimension.

In the absence of analytic solutions of the BK equation, phenomenological models for the dipole amplitude, which share some properties of the MV model, have been constructed, both for the description of small- x DIS data and d - Au collision data. A number of such models that incorporate to some extent the expectations from BFKL/BK evolution are discussed in chapter 6. We focus on the Dumitru-Hayashigaki-Jalilian-Marian (DHJ) model [48], which incorporates both the logarithmic rise and the scaling violations in the anomalous dimension γ . We study in chapter 7 whether these properties are actually consistent with numerical solutions of the BK equation. To do so, we employ the code of Ref. [90] to generate the numerical solutions, and combine them with the DHJ expression for the dipole amplitude to obtain a numerical result for the anomalous dimension γ . From this analysis we recover some expected properties of the anomalous dimension, the most important difference being its behaviour at the saturation scale. Instead of $\gamma(r_\perp = 1/Q_s) = 0.628$, we find that $\gamma(r_\perp = 1/Q_s)$ is in general a function of x , which approaches a value of 0.44 in the limit of $x \rightarrow 0$.

In chapter 8, we investigate whether the small- x properties of the anomalous dimension that are incorporated in the DHJ model are necessary to describe the RHIC data on hadron production in d - Au collisions. While the DHJ model is able to describe the forward data, i.e. at hadron rapidities of more than 2, it turns out that the same data can also be described by a new model whose anomalous dimension has neither the logarithmic

rise, nor the scaling violations that are expected from small- x evolution. In fact, this exactly geometrically scaling model is able to describe the data at all rapidities. Where the DHJ model deviates from the data, the probed values of x in the gold nucleus become larger than 0.01, so that one cannot expect to find small- x effects in the first place. Since at rapidities of 2 and larger both models work, the data are not restrictive enough to discern the exact properties of the anomalous dimension. Hence, we conclude that while the RHIC data turn out to be compatible with geometric scaling, no signatures of small- x evolution are found. Further, we show that at the new Large Hadron Collider (LHC), the DHJ model and the geometrically scaling model are clearly distinguishable at small x , due to the much higher energies. Hence, the LHC will provide a first test of the expected small- x properties of the anomalous dimension of phenomenological dipole models.

Another observable that is sensitive to saturation is the transverse polarization of Λ hyperons that are produced in high energy nucleon-nucleus collisions. As discussed in chapter 9, due to the odd dependence on transverse momentum of the polarized fragmentation functions that are used in the description of this observable [138–140], the polarization is sensitive to the derivative of the dipole scattering amplitude with respect to transverse momentum. In Ref. [57] it was shown that in the MV model this derivative, and hence Λ polarization, peaks around the saturation scale. Extending this analysis, in chapter 9 we find that also using more realistic models that include x -evolution, the polarization displays a peak at transverse momenta that are proportional to the saturation scale. We show that the x dependence of the saturation scale can in principle be reconstructed from the running of the peak position with x_F . Even though this result is to some extent model dependent, the appearance of the peak and its relation to the saturation scale are expected to be generic for dipole models that incorporate saturation. We show that the peak in the polarization is expected to show up at transverse momenta above 1 GeV for LHC kinematics. Hence, the polarization of Λ particles offers a unique way of directly probing the saturation scale in nucleon-nucleus collisions.

In conclusion, the small- x inspired properties of existing phenomenological dipole models are neither completely compatible with the BK equation, nor with presently available RHIC data. We have proposed a model that is compatible with both the RHIC and DIS data, but does not have the small- x properties of previous models—in particular it does not incorporate a logarithmic rise of the anomalous dimension or violations of geometric scaling. Rather, it is exactly geometrically scaling like the DIS data. Hence, neither the scaling violations nor the logarithmic rise that are expected from small- x evolution can be established using present data. We have shown that this may be different at LHC. The transverse momentum distribution of produced hadrons is sensitive to the rise of the anomalous dimension, so that by measuring the slope of this distribution it will be possible to distinguish the logarithmic rise expected from small- x evolution and the faster rise of the new model that follows from the RHIC data. Further, we have shown how the polarization of Λ hyperons provides a direct probe of the saturation scale, so that a measurement of this polarization may, especially at LHC, offer the possibility of probing the x dependence of the saturation scale in nucleon-nucleus collisions.

Appendix A

Colour glass condensate

This appendix contains a number of calculations that are used in chapter 3. As noted there, we use a different convention in terms of light cone vectors ($- \leftrightarrow +$) than usual in light front dynamics, due to the specific kinematics.

A.1 Average of U and $U^\dagger U$.

Here, we want to calculate the average over all colour source configurations of U and $U^\dagger U$, which are needed in section 3.2.2 to evaluate the scattering amplitude and hence the cross section of a quark that scatters off the colour glass condensate. We use the Gaussian approximation of the MV model [49–51, 66]. The results presented in this appendix are those of Ref. [70].

The definition of $\langle O \rangle_\rho$ is, cf. Eq. (3.1),

$$\langle O \rangle_\rho = \int \mathcal{D}\rho w[\rho] O[\rho]. \quad (\text{A.1})$$

The weight functional w is of the form (3.2), i.e. a Gaussian distribution

$$w[\rho] = \exp \left[- \int dz^- d^2 z_\perp \frac{\rho^a(z^-, z_\perp) \rho^a(z^-, z_\perp)}{2\mu(z^-)^2} \right], \quad (\text{A.2})$$

where the ‘width’ μ of the distribution is such that

$$\int \mathcal{D}\rho w[\rho] = 1. \quad (\text{A.3})$$

A.1.1 $\langle U \rangle_\rho$

We want to calculate the average of

$$U(x_\perp) = P \exp \left[-ig^2 \int dz^- \frac{1}{\nabla_\perp^2} \rho^a(z^-, x_\perp) t^a \right]. \quad (\text{A.4})$$

A.1. Average of U and $U^\dagger U$.

First, we write the integrand of the exponential in terms of the free quark propagator G_0 , which satisfies the relation

$$\nabla_\perp^2 G_0(x_\perp - z_\perp) = \delta(x_\perp - z_\perp). \quad (\text{A.5})$$

From this relation we see that we can write

$$\frac{1}{\nabla_\perp^2} \rho^a(z^-, x_\perp) = \int d^2 z_\perp G_0(x_\perp - z_\perp) \rho^a(z^-, z_\perp), \quad (\text{A.6})$$

and hence express U in the following way

$$U(x_\perp) = P \exp \left[-ig^2 \int dz^- d^2 z_\perp G_0(x_\perp - z_\perp) \rho^a(z^-, z_\perp) t^a \right]. \quad (\text{A.7})$$

Having thus got rid of the unwieldy formal operator $(\nabla_\perp^2)^{-1}$, we can write the average $\langle U \rangle_\rho$ as

$$\begin{aligned} \langle U(x_\perp) \rangle_\rho &= \int \mathcal{D}\rho \exp \left[- \int dz^- d^2 z_\perp \frac{\rho^a(z^-, z_\perp) \rho^a(z^-, z_\perp)}{2\mu(z^-)^2} \right. \\ &\quad \left. + ig^2 G_0(x_\perp - z_\perp) \rho^a(z^-, z_\perp) t^a \right] \\ &= \int \mathcal{D}\rho \exp \left[- \int dz^- d^2 z_\perp \left(\frac{\rho^a(z^-, z_\perp)}{\mu(z^-) \sqrt{2}} + \frac{ig^2}{\sqrt{2}} t^a \mu(z^-) G_0(x_\perp - z_\perp) \right)^2 \right. \\ &\quad \left. + \frac{g^4}{2} t^a t^a \mu(z^-)^2 G_0(x_\perp - z_\perp)^2 \right] \\ &= \exp \left\{ - \frac{g^4}{2} t^a t^a \int dz^- \mu(z^-)^2 \int d^2 z_\perp G_0(x_\perp - z_\perp)^2 \right\} \\ &\quad \times \int \mathcal{D}\rho \exp \left[- \int dz^- d^2 z_\perp \left(\frac{\rho^a(z^-, z_\perp)}{\mu(z^-) \sqrt{2}} + \frac{ig^2}{\sqrt{2}} t^a \mu(z^-) G_0(x_\perp - z_\perp) \right)^2 \right] \end{aligned} \quad (\text{A.8})$$

If we define

$$Q_s^2 = \frac{g^4}{2} t^a t^a \int dx^- \mu(x^-)^2; \quad (\text{A.9})$$

$$B_1(x_\perp) = Q_s^2 \int d^2 z_\perp G_0(x_\perp - z_\perp)^2, \quad (\text{A.10})$$

where Q_s is the saturation scale¹, and perform the following substitution, $\rho'^a = \sqrt{2} \rho^a + ig^2 \mu^2 t^a G_0$, we can write the average of U as

$$\begin{aligned} \langle U(x_\perp) \rangle_\rho &= \exp[-B_1(x_\perp)] \int \mathcal{D}\rho' \exp \left[- \int dz^- d^2 z_\perp \frac{\rho'^a(z^-, z_\perp) \rho'^a(z^-, z_\perp)}{2\mu(z^-)^2} \right] \\ &= \exp[-B_1(x_\perp)] \int \mathcal{D}\rho' w[\rho'] \\ &= \exp[-B_1(x_\perp)]. \end{aligned} \quad (\text{A.11})$$

¹Note that Q_s is independent of x in the MV model.

The function B_1 can be expressed in rather a simpler way when we recall that the quark propagator G_0 satisfies Eq. (A.5), and may consequently be written as

$$G_0(x_\perp) = - \int \frac{d^2 p_\perp}{(2\pi)^2} \frac{e^{i p_\perp \cdot x_\perp}}{p_\perp^2}. \quad (\text{A.12})$$

In terms of B_1 , this implies

$$B_1(x_\perp) = Q_s^2 \int \frac{d^2 p_\perp}{(2\pi)^2} \frac{d^2 k_\perp}{(2\pi)^2} d^2 z_\perp \frac{e^{i(p_\perp + k_\perp) \cdot (x_\perp - z_\perp)}}{p_\perp^2 k_\perp^2}. \quad (\text{A.13})$$

The integration over z_\perp yields a δ -function, which can be used to perform one of the momentum integrations

$$B_1(x_\perp) = Q_s^2 \int \frac{d^2 p_\perp}{(2\pi)^2} \frac{1}{p_\perp^4}. \quad (\text{A.14})$$

Clearly, B_1 is independent of x_\perp , and will therefore only contribute to $C(k_\perp)$ via a δ -function in k_\perp . As it stands, this integral is divergent; imposing a lower cut-off, Λ say we may write B_1 more appropriately as

$$B_1 = \frac{Q_s^2}{4\pi\Lambda^2}. \quad (\text{A.15})$$

However, in practice this divergence is unproblematic, as in the quark-colour glass condensate scattering cross section it contributes a terms $\exp(-B_1)$, which will vanish if $\Lambda \rightarrow \infty$.

A.1.2 $\langle U^\dagger U \rangle_\rho$

Now we want to calculate $\langle U^\dagger(x_\perp)U(y_\perp) \rangle_\rho$. Since from Eq. (A.7) we have

$$U(x_\perp) = \exp \left[-ig^2 \int dz^- d^2 z_\perp G_0(x_\perp - z_\perp) \rho^a(z^-, z_\perp) t^a \right], \quad (\text{A.16})$$

and hence, since $t^\dagger = t$,

$$U^\dagger(x_\perp) = \exp \left[ig^2 \int dz^- d^2 z_\perp G_0(x_\perp - z_\perp) \rho^a(z^-, z_\perp) t^a \right]. \quad (\text{A.17})$$

Following the same procedure as in Eq. (A.8), we can write

$$\begin{aligned} \langle U^\dagger(x_\perp)U(y_\perp) \rangle_\rho &= \int \mathcal{D}\rho \exp \left[- \int dz^- d^2 z_\perp \frac{\rho^a(z^-, z_\perp) \rho^a(z^-, z_\perp)}{2\mu(z^-)^2} \right. \\ &\quad \left. + ig^2 [G_0(y_\perp - z_\perp) - G_0(x_\perp - z_\perp)] \rho^a(z^-, z_\perp) t^a \right] \\ &= \int \mathcal{D}\rho \exp \left[- \int dz^- d^2 z_\perp \left(\frac{\rho^a(z^-, z_\perp)}{\sqrt{2}\mu(z^-)} + \frac{ig^2}{\sqrt{2}} \mu(z^-) \right) \right. \\ &\quad \left. \times [G_0(y_\perp - z_\perp) - G_0(x_\perp - z_\perp)] \rho^a(z^-, z_\perp) t^a \right]^2 \\ &\quad \left. + \frac{g^4}{2} \mu(z^-)^2 t^a t^a [G_0(y_\perp - z_\perp) - G_0(x_\perp - z_\perp)]^2 \right]. \quad (\text{A.18}) \end{aligned}$$

A.1. Average of U and $U^\dagger U$.

We now perform the substitution $\rho'^a = \rho^a + \sqrt{2}ig^2\mu^2 t^a [G_0(y_\perp - z_\perp) - G_0(x_\perp - z_\perp)]$, from which we find

$$\begin{aligned} \langle U^\dagger(x_\perp)U(y_\perp) \rangle_\rho &= \exp\left\{-\frac{g^4}{2}t^a t^a \int dz^- \mu(z^-)^2 \int d^2 z_\perp [G_0(y_\perp - z_\perp) - G_0(x_\perp - z_\perp)]^2\right\} \\ &\quad \times \int \mathcal{D}\rho' \exp\left[-\int dz^- d^2 z_\perp \frac{\rho'^a(z^-, z_\perp)\rho'^a(z^-, z_\perp)}{2\mu(z^-)^2}\right] \\ &= \exp\left\{-Q_s^2 \int d^2 z_\perp [G_0(y_\perp - z_\perp) - G_0(x_\perp - z_\perp)]^2\right\}. \end{aligned} \quad (\text{A.19})$$

Defining a function B_2 ,

$$B_2(y_\perp, x_\perp) = Q_s^2 \int d^2 z_\perp [G_0(y_\perp - z_\perp) - G_0(x_\perp - z_\perp)]^2, \quad (\text{A.20})$$

We can write the average of $U^\dagger U$ simply as

$$\langle U^\dagger(x_\perp)U(y_\perp) \rangle_\rho = e^{-B_2(x_\perp, y_\perp)} \quad (\text{A.21})$$

Given Eq. (A.12) we see that we can write B_2 in the following way,

$$\begin{aligned} B_2(y_\perp, x_\perp) &= Q_s^2 \int d^2 z_\perp \frac{d^2 p_\perp}{(2\pi)^2} \frac{d^2 k_\perp}{(2\pi)^2} \frac{1}{p_\perp^2 k_\perp^2} \left[e^{i(p_\perp + k_\perp) \cdot (y_\perp - z_\perp)} \right. \\ &\quad \left. + e^{i(p_\perp + k_\perp) \cdot (x_\perp - z_\perp)} - 2e^{ip_\perp \cdot (y_\perp - z_\perp)} e^{ik_\perp \cdot (x_\perp - z_\perp)} \right]. \end{aligned} \quad (\text{A.22})$$

Again, the integration over z_\perp gives a δ -function which we can use to perform one of the remaining integrations. Thus we find

$$B_2(y_\perp, x_\perp) = Q_s^2 \int \frac{d^2 p_\perp}{(2\pi)^2} \frac{2}{p_\perp^4} \left[1 - e^{ip_\perp \cdot (y_\perp - x_\perp)} \right]. \quad (\text{A.23})$$

Clearly, since $B_2(y_\perp, x_\perp) = B_2(y_\perp - x_\perp)$, we obtain

$$B_2(x_\perp) = Q_s^2 \int \frac{d^2 p_\perp}{(2\pi)^2} \frac{2}{p_\perp^4} \left[1 - e^{ip_\perp \cdot x_\perp} \right]. \quad (\text{A.24})$$

Also this integral is formally divergent.

We can regularize Eq. (A.24) in the following way. Using Eq. (A.15), the first term of B_2 is taken care of. Next we introduce the regulator Λ in the second term by replacing the denominator of the integrand by

$$\int d^2 p_\perp \frac{e^{ip_\perp \cdot x_\perp}}{(p_\perp^2 + \Lambda^2)^2}. \quad (\text{A.25})$$

Note that even though Eq. (A.15) was obtained by imposing a lower cut-off, the same result would follow from this way of regularizing. Decomposing the integration over p_\perp

in Cartesian co-ordinates, p and k say, and choosing the p -axis along the direction of x_\perp , we find

$$\begin{aligned} \int dpdk \frac{e^{ipx}}{(p^2 + k^2 + \Lambda^2)^2} &= \int dp e^{ipx} \int \frac{dk}{(p^2 + \Lambda^2)^2 \left(\frac{k^2}{p^2 + \Lambda^2} + 1\right)^2} \\ &= \int dp \frac{e^{ipx}}{(p^2 + \Lambda^2)^{3/2}} \int \frac{d\xi}{(\xi^2 + 1)^2} \\ &= \frac{\pi x_\perp^2}{\Lambda} K_1(x_\perp \Lambda), \end{aligned} \quad (\text{A.26})$$

where K_1 is the modified Bessel function of the second kind, and we have written $|x_\perp| = x$. In terms of Λ , we can now express B_2 as

$$B_2(x_\perp) = \frac{Q_s^2}{2\pi\Lambda^2} [1 - x_\perp \Lambda K_1(x_\perp \Lambda)] \quad (\text{A.27})$$

which reduces to

$$B_2(x_\perp) = \frac{Q_s^2 x_\perp^2}{4\pi} \ln\left(\frac{1}{x_\perp \Lambda}\right) \quad (\text{A.28})$$

when x_\perp is small.

A.2 Scattering off the WW-field

In this section, we present the calculation of the electron propagator in the presence of a background field A_μ , following Ref. [68]. As noted in chapter 3, we use a different convention in terms of light cone vectors than usual in light front dynamics, due to the specific kinematics.

The interaction part of the propagator can be written as in Eq. (3.15)

$$T_n(q, p) = (-ie)^n \int \frac{d^4 k_1}{(2\pi)^4} 2\pi A(k_1) G_0(p + k_1) \dots \int \frac{d^4 k_n}{(2\pi)^4} \times \quad (\text{A.29})$$

$$2\pi A(p + \sum_{i=1}^n k_i) G_0(p + \sum_{i=1}^{n-1} k_i) (2\pi)^4 \delta(p + \sum_{i=1}^n k_i - q), \quad (\text{A.30})$$

where

$$A^\mu(k) = \delta(k^-) \delta^{\mu-} \Lambda(k_\perp) \quad (\text{A.31})$$

is the Fourier transform of Eq. (3.12). Given this form of A_μ , we can perform the integration over k^- . Keeping in mind $\gamma^- \not{k} \gamma^- = 2k^- \gamma^-$ and using

$$G_0(p) = i \frac{\not{p} - m}{p^2 - m^2 + i\epsilon}. \quad (\text{A.32})$$

A.2. Scattering off the WW-field

we see that the integration over k^- reduces to a product of terms of the following form,

$$\begin{aligned}
\int dk^- \delta(k^-) \gamma^- G_0(p+k) \gamma^- &= \int dk^- \delta(k^-) \frac{\gamma^- (\not{p} + \not{k} + m) \gamma^-}{(p+k)^2 - m^2 + i\varepsilon} \\
&= \frac{2p^- \gamma^-}{2p^- p^+ + 2p^- k^+ - (p_\perp + k_\perp)^2 - m^2 + i\varepsilon} \\
&= \frac{\gamma^-}{p^+ + k^+ - \frac{(p_\perp + k_\perp)^2 - m^2}{2p^-} + \frac{i\varepsilon}{2p^-}}.
\end{aligned} \tag{A.33}$$

We introduce the following definitions for ease of notation

$$\begin{aligned}
\omega_a^2 &= m^2 + (p_\perp + \sum_{i=1}^a k_{i\perp})^2; \\
\omega_0^2 &= 2p^+ p^-; \\
\frac{\varepsilon}{2p^-} &= \varepsilon_p,
\end{aligned} \tag{A.34}$$

but continue to write ε instead of ε_p , we see that the integrations over the remaining components of k split;

$$\begin{aligned}
T_n(q, p) &= (-ie)^n 2\pi \delta(p^- - q^-) \frac{\gamma^-}{(2\pi)^n} \int \frac{d^2 k_{1\perp}}{(2\pi)^2} 2\pi \Lambda(k_{1\perp}) \dots \times \\
&\quad \int \frac{d^2 k_{n\perp}}{(2\pi)^2} 2\pi \Lambda(k_{n\perp}) (2\pi)^2 \delta(p_\perp + \sum_{i=1}^n k_{i\perp} - q_\perp) \times \\
&\quad \int \frac{dk_1^+}{2\pi} \dots \int \frac{dk_n^+}{2\pi} 2\pi \delta(p^+ + \sum_{i=1}^n k_i^+ - q^+) \times \\
&\quad \frac{i}{p^+ + k_1^+ - \frac{\omega_1^2}{2p^-} + i\varepsilon} \dots \frac{i}{p^+ + \sum_{i=1}^{n-1} k_i^+ - \frac{\omega_{n-1}^2}{2p^-} + i\varepsilon} \\
&\equiv (-ie)^n 2\pi \delta(p^- - q^-) \gamma^- I_n^+ I_n^+.
\end{aligned} \tag{A.35}$$

First, we will calculate I_n^\perp . We start with writing $\Lambda(k_\perp)$ as a Fourier transform of $\Lambda(x_\perp)$, so that I_n^\perp becomes

$$I_n^\perp = \left[\prod_{i=1}^n \int \frac{d^2 k_{i\perp}}{(2\pi)^2} \int d^2 x_{i\perp} e^{ix_{i\perp} \cdot k_{i\perp}} \Lambda(x_{i\perp}) \right] (2\pi)^2 \delta(p_\perp + \sum_{i=1}^n k_{i\perp} - q_\perp). \tag{A.36}$$

We then write the δ -function in the following way

$$\delta(p_\perp + \sum_{i=1}^n k_{i\perp} - q_\perp) = \int \frac{d^2 \xi_\perp}{(2\pi)^2} e^{i(p_\perp - q_\perp) \cdot \xi_\perp} \prod_{i=1}^n e^{ik_{i\perp} \cdot \xi_\perp}, \tag{A.37}$$

which enables us to perform the k_\perp -integration;

$$\begin{aligned}
 I_n^\perp &= (2\pi)^2 \int \frac{d^2\xi_\perp}{(2\pi)^2} \prod_{i=1}^n \int \frac{d^2k_{i\perp}}{(2\pi)^2} \int d^2x_{i\perp} e^{-i(\xi_\perp - x_{i\perp})\cdot k_{i\perp}} e^{i(p_\perp - q_\perp)\cdot \xi_\perp} \Lambda(x_{i\perp}) \\
 &= \int d^2\xi_\perp e^{i(p_\perp - q_\perp)\cdot \xi_\perp} \prod_{i=1}^n \int d^2x_{i\perp} \delta(\xi_\perp - x_{i\perp}) \Lambda(x_{i\perp}) \\
 &= \int d^2x_\perp e^{i(p_\perp - q_\perp)\cdot x_\perp} \Lambda^n(x_\perp)
 \end{aligned} \tag{A.38}$$

Next we tackle I_n^+ , which is given by

$$I_n^+ = \int \frac{dk_1^+}{2\pi} \dots \int \frac{dk_n^+}{2\pi} 2\pi\delta(p^+ + \sum_{i=1}^n k_i^+ - q^+) \times \tag{A.39}$$

$$\frac{i}{p^+ + k_1^+ - \frac{\omega_1^2}{2p^-} + i\varepsilon} \dots \frac{i}{p^+ + \sum_{i=1}^{n-1} k_i^+ - \frac{\omega_{n-1}^2}{2p^-} + i\varepsilon}. \tag{A.40}$$

If we define the more convenient variables $a_i = k_i^+ + (\omega_{i-1}^2 - \omega_i^2)/2p^-$, where we note that $\omega_0^2 = 2p^+p^-$, we have $dk_i^+ = da_i$, which enables us to write I_n^+ as

$$I_n^+ = \int \frac{da_1}{2\pi} \dots \int \frac{da_n}{2\pi} 2\pi\delta(\sum_{i=1}^n a_i + \frac{\omega_n}{2p^-} - q^+) \times \tag{A.41}$$

$$\frac{i}{a_1 + i\varepsilon} \dots \frac{i}{\sum_{i=1}^{n-1} a_i + i\varepsilon}. \tag{A.42}$$

Now let us use a trick. Since the indices of the a 's are interchangeable, they are integration variables after all, I_n^+ satisfies the relation

$$I_n^+ = \frac{1}{n!} \sum_{\sigma} I_n^+, \tag{A.43}$$

where the summation runs over all permutations σ of the indices of the a 's. If we momentarily use the notation $a'_i = a_i + i\varepsilon$, we see that Eq. (A.42) can be simplified using the following identity,

$$\sum_{\sigma} \frac{i}{a_1} \dots \frac{i}{\sum_{i=1}^{n-1} a_i} = (i)^{n-1} \frac{a_1 + \dots + a_n}{a_1 a_2 \dots a_n}. \tag{A.44}$$

If we use this identity and write $x = \frac{\omega_n}{2p^-} - q^+$, we can express Eq. (A.42) as

$$I_n^+ = \frac{2\pi}{n!} \int \frac{da_1}{2\pi} \dots \int \frac{da_n}{2\pi} \delta(\sum_{i=1}^n a_i + x) (i)^{n-1} \frac{a'_1 + \dots + a_n}{a'_1 a_2 \dots a_n}. \tag{A.45}$$

A.2. Scattering off the WW-field

To be able to evaluate this integral we temporarily assign to a_2, \dots, a_n an imaginary part ϵ , with the same sign as ε , that we will put to zero afterwards. However, we will *not* add an imaginary part to the a 's in the δ -function! In this way we obtain

$$\begin{aligned}
I_n^+ &= \frac{2\pi(i)^{n-1}}{n!} \lim_{\epsilon \rightarrow 0} \int \frac{da_1}{2\pi} \dots \int \frac{da_n}{2\pi} \delta\left(\sum^n a + x\right) \times \\
&\quad \frac{a_1 + \dots + a_n + i\varepsilon + i(n-1)\epsilon}{(a_1 + i\varepsilon)(a_2 + i\varepsilon)\dots(a_n + i\varepsilon)} \\
&= \frac{(i)^{n-1}}{n!} \lim_{\epsilon \rightarrow 0} \int \frac{da_1}{2\pi} \dots \int \frac{da_{n-1}}{2\pi} \times \\
&\quad \frac{x - i\varepsilon - i(n-1)\epsilon}{(a_1 + i\varepsilon)(a_2 + i\varepsilon)\dots(a_1 + \dots + a_{n-1} + x - i\varepsilon)}. \tag{A.46}
\end{aligned}$$

To perform the integration over a_1 , which of course runs from $-\infty$ to ∞ , we close the integration contour in the ‘southern hemisphere’, say—closing the contour at $+i\infty$ is also possible, and leads to the same result. The poles of the integrand are at $-i\varepsilon$ and $\dots + i\varepsilon$, so that if $\varepsilon > 0$, we enclose the pole at $-i\varepsilon$, whereas if $\varepsilon < 0$, we enclose the other pole at $i\varepsilon$. Hence, we ignore² the sign of ε . Thus we find

$$I_n^+ = \frac{(i)^n}{n!} \lim_{\epsilon \rightarrow 0} \int \frac{da_2}{2\pi} \dots \int \frac{da_{n-1}}{2\pi} \times \tag{A.47}$$

$$\frac{x - i\varepsilon - i(n-1)\epsilon}{(a_2 + i\varepsilon)\dots(a_2 + \dots + a_{n-1} + x - i\varepsilon - i\varepsilon)} \tag{A.48}$$

In this way, we can do all integrations, each of which will produce a term $-i\varepsilon$ in the denominator, and an overall factor of $2\pi i \operatorname{sign}(\varepsilon)$. The result of doing all integrations is therefore given by

$$I_n^+ = \frac{1}{n!} \lim_{\epsilon \rightarrow 0} \frac{x - i\varepsilon - i(n-1)\epsilon}{x - i\varepsilon - i(n-1)\epsilon} = \frac{1}{n!} \operatorname{sign}^{n-1}(\varepsilon). \tag{A.49}$$

Combining I_\perp and I^+ , i.e. Eqs. (A.38) and (A.49), we find for T_n the following expression

$$T_n(q, p) = 2\pi\delta(p^- - q^-) \frac{(-ie)^n \gamma^-}{(2\pi)^n} \frac{1}{n!} \int d^2 x_\perp e^{i(p_\perp - q_\perp) \cdot x_\perp} \Lambda^n(x_\perp), \tag{A.50}$$

from which $T(q, p)$ is found by summing all terms,

$$\begin{aligned}
T(q, p) &= \sum_{n=1}^{\infty} T_n(q, p) = \sum_{n=0}^{\infty} T_n(q, p) - T_0(q, p) \\
&= 2\pi\delta(p^- - q^-) \gamma^- \int d^2 x_\perp e^{i(p_\perp - q_\perp) \cdot x_\perp} [U(x_\perp) - 1],
\end{aligned} \tag{A.51}$$

and

$$U(x_\perp) = e^{-ie\Lambda(x_\perp)}. \tag{A.52}$$

²The sign of ε can play a role if the electron scatters off more than one nucleus, see Ref. [68]

A.3 Lagrangian density for CGC

We want to find a lagrangian density that reproduces Eqs. (3.23) and (3.24). The setup given here is taken from Ref. [31]. We write

$$\mathcal{L} = -\frac{1}{4}F_{\mu\nu}^a F_a^{\mu\nu} + \mathcal{L}_W, \quad (\text{A.53})$$

where

$$F_{\mu\nu}^a = \partial_\mu A_\nu^a - \partial_\nu A_\mu^a + g f^{abc} A_\mu^b A_\nu^c. \quad (\text{A.54})$$

The Euler-Lagrange equations then dictate

$$\frac{\partial \mathcal{L}}{\partial A_\mu^a} = \partial_\nu \frac{\partial \mathcal{L}}{\partial \partial_\nu A_\mu^a}. \quad (\text{A.55})$$

Since

$$\frac{\partial \mathcal{L}}{\partial A_\mu^b} = -\frac{1}{4} \frac{\partial F_{\mu\nu}^a F_a^{\mu\nu}}{\partial A_\mu^b} + \frac{\partial \mathcal{L}_W}{\partial A_\mu^b} = -g f^{abc} A_\nu^c F_a^{\mu\nu} + \frac{\partial \mathcal{L}_W}{\partial A_\mu^b} \quad (\text{A.56})$$

and we see from Eq. (A.53) directly that

$$\frac{\partial \mathcal{L}}{\partial \partial_\nu A_\mu^b} = F_b^{\mu\nu}, \quad (\text{A.57})$$

the Euler-Lagrange equations can be written as

$$\partial_\nu F_b^{\mu\nu} = -g f^{abc} A_\nu^c F_a^{\mu\nu} + \frac{\partial \mathcal{L}_W}{\partial A_\mu^b}. \quad (\text{A.58})$$

Contracting with the group matrices, we have

$$\partial_\nu F^{\mu\nu} = -g f^{abc} A_\nu^c F_a^{\mu\nu} T^b + \frac{\partial \mathcal{L}_W}{\partial A_\mu^b} T^b \quad (\text{A.59})$$

$$= -ig[T^a, T^c] A_\nu^c F_a^{\mu\nu} T^b + \frac{\partial \mathcal{L}_W}{\partial A_\mu^b} T^b \quad (\text{A.60})$$

$$= -ig[F^{\mu\nu}, A_\nu] + \frac{\partial \mathcal{L}_W}{\partial A_\mu^b} T^b \quad (\text{A.61})$$

and finally

$$\partial_\nu F^{\mu\nu} - ig[A_\nu, F^{\mu\nu}] = [D_\nu, F^{\mu\nu}] = \frac{\partial \mathcal{L}_W}{\partial A_\mu^b} T^b. \quad (\text{A.62})$$

Suppose we would make the following choice for \mathcal{L}_W ,

$$\mathcal{L}_W = g A_a^- \rho^a \quad (\text{A.63})$$

A.3. Lagrangian density for CGC

in other words,

$$\frac{\partial \mathcal{L}_W}{\partial A_\mu^b} = \delta^{\mu+} g \rho^b. \quad (\text{A.64})$$

The Euler-Lagrange equations would then read

$$[D_\nu, F^{\mu\nu}] = \delta^{\mu+} g \rho \quad (\text{A.65})$$

which is exactly Eq. (3.23) for the current (3.24), since $J^+ = g\rho$.

However, this expression, which is valid in the light cone gauge $A^+ = 0$, does not preserve the residual gauge symmetry, which consists of transformations that do not depend on x^- [31]. Following Ref. [31] we can construct an \mathcal{L}_W that reproduces Eq. (A.65) in this particular gauge, but which still preserve this residual symmetry. Consider the following choice

$$\mathcal{L}_W = \frac{i}{N_c} \text{tr} \{ \rho_a T^a W(-\infty, \infty) \} \quad (\text{A.66})$$

where

$$W(x^+, y^+) = P \exp \left\{ -ig \int_{x^+}^{y^+} dx'^+ A^-(x') \right\}. \quad (\text{A.67})$$

In this case we have

$$\frac{\partial \mathcal{L}_W}{\partial A_\mu^b} = -\frac{i}{N_c} \text{tr} \left\{ \rho^a T^a \frac{\partial W(-\infty, \infty)}{\partial A_\mu^b} \right\}, \quad (\text{A.68})$$

so that $W(-\infty, \infty)$ is explicitly gauge invariant under gauge transformation that are independent of x^- , provided that the gauge functions vanish at $x^+ \rightarrow \pm\infty$ [31]. The functional differentiation is defined by

$$\frac{\partial F[A(x)]}{\partial A(y)} = \lim_{\epsilon \rightarrow 0} \frac{1}{\epsilon} [F[A(x) + \epsilon \delta(x-y)] - F[A(x)]]. \quad (\text{A.69})$$

Also, we can write

$$W(-\infty, \infty) = \lim_{\epsilon \rightarrow 0} W(-\infty, x^+ - \epsilon) W(x^+ - \epsilon, \infty). \quad (\text{A.70})$$

Keeping in mind that

$$\frac{\partial}{\partial A_\mu^a} = \frac{\partial A_\nu}{\partial A_\mu^a} \frac{\partial}{\partial A_\nu} = T_a \frac{\partial}{\partial A_\mu} \quad (\text{A.71})$$

We first determine the derivatives of $W(-\infty, x^+ - \epsilon)$ en $W(x^+ - \epsilon, \infty)$;

$$\begin{aligned}
 \frac{\partial W(x^+ - \epsilon, \infty)}{\partial A_\mu(y^+)} &= -W(x^+ - \epsilon, \infty) ig \frac{\partial \int_{x^+ - \epsilon}^{\infty} dx^+ A^-(x)}{\partial A_\mu(y^+)} \\
 &= -W(x^+ - \epsilon, \infty) ig \delta^{\mu+} \lim_{\epsilon \rightarrow 0} \frac{1}{\epsilon} \left[\int_{x^+ - \epsilon}^{\infty} dx^+ (A^-(x) + \epsilon \delta(x^+ - y^+)) \right. \\
 &\quad \left. + \int_{x^+ - \epsilon}^{\infty} dx^+ A^-(x) \right] \\
 &= -ig W(x^+ - \epsilon, \infty) \delta^{\mu+}, \tag{A.72}
 \end{aligned}$$

and, since the support of the δ -function lies outside the region of integration,

$$\frac{\partial W(-\infty, x^+ - \epsilon)}{\partial A_\mu(y^+)} = 0. \tag{A.73}$$

Hence, we find for the full differential

$$\begin{aligned}
 \frac{\partial W(-\infty, \infty)}{\partial A_\mu^a} &= \lim_{\epsilon \rightarrow 0} W(-\infty, x^+ - \epsilon) \frac{\partial W(x^+ - \epsilon, \infty)}{\partial A_\mu^a} \\
 &= -ig \delta^{\mu+} \lim_{\epsilon \rightarrow 0} W(-\infty, x^+ - \epsilon) T_a W(x^+ - \epsilon, \infty) \\
 &= -ig \delta^{\mu+} W(-\infty, x^+) T_a W(x^+, \infty), \tag{A.74}
 \end{aligned}$$

so that we can finally write

$$\frac{\partial \mathcal{L}_W}{\partial A_\mu^b} = \delta^{\mu+} \frac{g}{N_c} \text{tr} \left\{ \rho^a W(-\infty, x^+) T_a W(x^+, \infty) \right\}. \tag{A.75}$$

The Euler-Lagrange equation of motion now reduce to

$$[D_\nu, F^{\mu\nu}] = \delta^{\mu+} \frac{g}{N_c} \text{tr} \left\{ \rho^a W(-\infty, x^+) T_a W(x^+, \infty) \right\}, \tag{A.76}$$

which for $A^- = 0$ indeed reduces to $\delta^{\mu+} g \rho$, as required by Eq. (A.65). Hence, the colour glass condensate is described by the lagrangian density specified by Eqs. (A.53) and (A.66).

Appendix B

CGC and DGLAP descriptions

B.1 Cross section in CGC and DGLAP

Here, we briefly compare the description of hadron production in nucleon-nucleus scattering in the colour glass formalism and the perturbative DGLAP formalism. In the colour glass picture, the cross section is expressed as a convolution of a parton distribution function of the nucleon with the dipola amplitude and a fragmentation function, cf. Eq (2.45),

$$\frac{dN_h}{dy_h d^2 p_\perp} \sim f \otimes N \otimes D. \quad (\text{B.1})$$

Note that N is the dipole amplitude in momentum space, defined in Eq. (6.15). The scattering partons, described by f , can be either quarks or gluons. This expression is to be compared with the perturbative description, in which the cross section can be schematically written as

$$\frac{dN_h}{dy_h d^2 p_\perp} \sim f \otimes g \otimes H \otimes D, \quad (\text{B.2})$$

where H denotes the partonic scattering amplitude. We see that the dipole amplitude N corresponds to a convolution of the gluon distribution with the perturbative partonic scattering amplitude (in a kinematic region where the gluon distribution is well defined). As we will see shortly though, the values of x (and hence the partonic momenta) that enter the gluon distribution are not equal to those probed by N , due to the different kinematics. We note that from this correspondence one expects that in the limit of $p_\perp \rightarrow \infty$, where the partonic amplitude is dominated by single-gluon exchange, i.e. it is proportional to the gluon propagator squared: $H \sim 1/q_\perp^4$, the dipole amplitude $N(q_\perp, x)$ behaves as $N \sim 1/q_\perp^4$ (up to logarithmic corrections). This is consistent with the expected limit of $r_\perp \rightarrow 0$ of $N(r_\perp, x)$ given in appendix C.3 (see also [151]). Further, the dipole amplitude $N(r_\perp, x)$ is in this thesis parameterized in terms of an anomalous dimension, γ , cf. Eq. (6.33). This anomalous dimension should approach unity in the limit of $r_\perp \rightarrow 0$, to reproduce the behaviour $N(r_\perp \rightarrow 0, x) \sim r_\perp^2$. Given the correspondence $N(q_\perp, x) \sim g \otimes H$ in the

B.2. Kinematics: average values of x

DGLAP region, one may expect that it is possible to extract an expression for γ , γ_{DGLAP} say, from the perturbative description. However, since the kinematics of both descriptions are different, and due to the convolution integral, the correspondence is not one to one except in the extreme limit, so that no such DGLAP limit of γ can be straightforwardly derived.

B.2 Kinematics: average values of x

Now, we will calculate the probed values of x in the colour glass description, i.e. $2 \rightarrow 2$ kinematics, following Ref. [47]. Most importantly, the momentum fractions that are probed in the target are much smaller than in the $2 \rightarrow 2$ kinematics of leading-twist perturbative computations (see e.g. [116]). We consider nucleon-nucleus scattering in the centre of mass frame, where the nucleon moves in the x^- direction, while the nucleus moves along the x^+ direction—we will neglect the masses of the particles. The momenta of the particles are defined in Fig. B.1. The momentum of the incoming parton is denoted

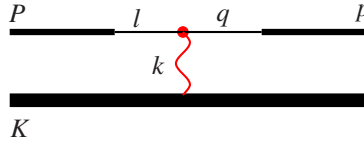


Figure B.1: The $2 \rightarrow 1$ kinematics. Plot taken from Ref. [47].

with l while that of the projectile nucleons is labelled P ; the momentum of the scattered parton is q while that of the produced hadron is p . The momentum of the constituents of the incoming nucleus is K , and k is the momentum that is exchanged between the incoming parton and the nucleus. In other words,

$$\begin{aligned}
 P^\mu &= (P^- = \sqrt{s/2}, P^+ = 0, \mathbf{P}_\perp = 0) \\
 l^\mu &= (l^- = x_1 P^-, l^+ = 0, \mathbf{l}_\perp = 0) \\
 q^\mu &= (q^- = l^-, q^+ = \frac{q_\perp^2}{2q^-}, \mathbf{q}_\perp) \\
 p^\mu &= (p^- = z q^-, p^+ = \frac{p_\perp^2}{2p^-}, \mathbf{p}_\perp = z \mathbf{q}_\perp) \\
 k^\mu &= (k^- = 0, k^+ = x_2 K^+, \mathbf{k}_\perp) \\
 K^\mu &= (K^- = 0, K^+ = P^- = \sqrt{s/2}, \mathbf{K}_\perp = 0),
 \end{aligned} \tag{B.3}$$

where \sqrt{s} is the centre of mass energy, and where we have

$$q = l + k \tag{B.4}$$

from energy-momentum conservation. Apart from neglecting the masses, the only approximation made in (B.3) is setting $k^- \approx 0$, which corresponds to the eikonal approxima-

Appendix B. CGC and DGLAP descriptions

tion. Using (B.4), we have $\mathbf{k}_\perp = \mathbf{q}_\perp$, $x_1 P^- = q^-$ and $k^+ = q^+$. Following [47, 48], we define the Feynman x of the produced hadrons as the longitudinal momentum fraction of the produced hadron $x_F \equiv p^-/P^-$, which is invariant under longitudinal boosts. We note that the conventional (fixed target) definition of the Feynman x is $x_F \equiv 2p_z/\sqrt{s}$, which is approximately equal to the longitudinal momentum fraction p^-/P^- when $\exp y_h \gg \exp -y_h$. It follows that $x_F = zx_1$, so that we obtain

$$x_2 = \frac{x_1 p_\perp^2}{x_F^2 s}, \quad (\text{B.5})$$

This relation can be rewritten in terms of the rapidity y_h of the produced hadron, which is defined¹ as [133]

$$p^- \equiv \sqrt{\frac{p_\perp^2 + m^2}{2}} e^{y_h} \approx p_\perp e^{y_h} / \sqrt{2}. \quad (\text{B.6})$$

Using this expression, we finally obtain

$$x_2 = x_1 e^{-2y_h}; \quad x_F = \frac{p_\perp}{\sqrt{s}} e^{y_h}. \quad (\text{B.7})$$

The average values of x_2 that are probed according to this formalism (using Eq. (6.18) for the cross section) in d - Au collisions at RHIC at a centre of mass energy $\sqrt{s} = 200$ GeV are depicted in Fig. B.2.

In the $2 \rightarrow 1$ kinematics, the average x_2 is roughly two orders of magnitude smaller [47] than in the $2 \rightarrow 2$ kinematics of the perturbative DGLAP description. In the latter formalism, the lower limits on x_1 and x_2 are given by [116]

$$\begin{aligned} x_2^{\min} &= \frac{x_\perp e^{-\eta}}{2 - x_\perp e^\eta}; \\ x_1^{\min} &= \frac{x_2 x_\perp e^\eta}{2x_2 - x_\perp e^{-\eta}}. \end{aligned} \quad (\text{B.8})$$

Here, $x_\perp = 2p_\perp/\sqrt{s}$, and η is the pseudorapidity, which is approximately equal to the rapidity y_h if $m \ll p_\perp$ [133]. These lower limits however hardly contribute to the cross section, as they are suppressed by the distribution and fragmentation functions [116]. Fig. B.3 shows the distribution of the contributing values of x_1 and x_2 in the colour glass description (6.18) in d - Au collisions at RHIC ($\sqrt{s} = 200$ GeV), while the corresponding plot in the perturbative description of [116] is depicted in Fig. B.4.

¹Note that as the produced hadron moves in the x^- direction, the sign convention for the rapidity is opposite to Ref. [133].

B.2. Kinematics: average values of x

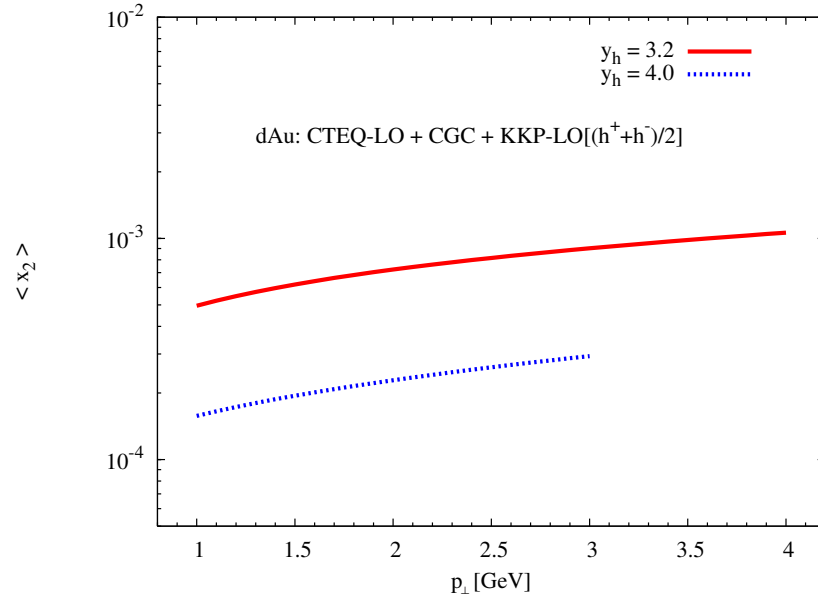


Figure B.2: Average x_2 in the colour glass description d -Au collisions at RHIC. Plot taken from [47].

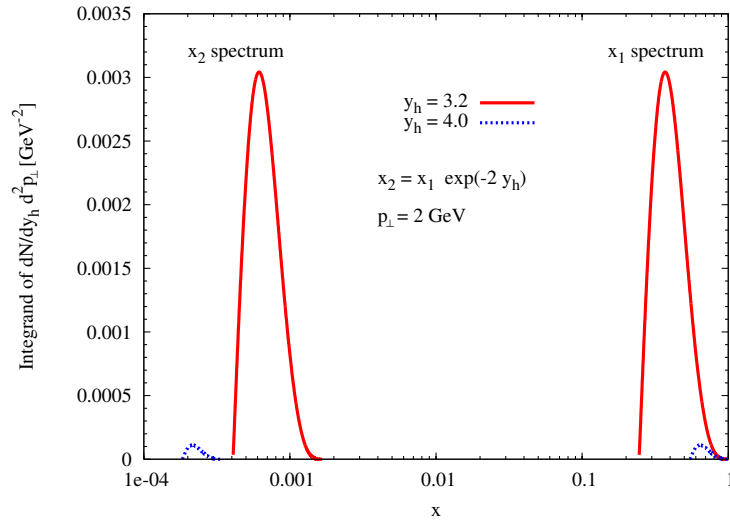


Figure B.3: Distribution of values of x_1 and x_2 in the colour glass description of d -Au collisions at RHIC ($\sqrt{s} = 200$ GeV), at $p_{\perp} = 2$ GeV and $y_h = 3, 4$. Plot taken from [47].

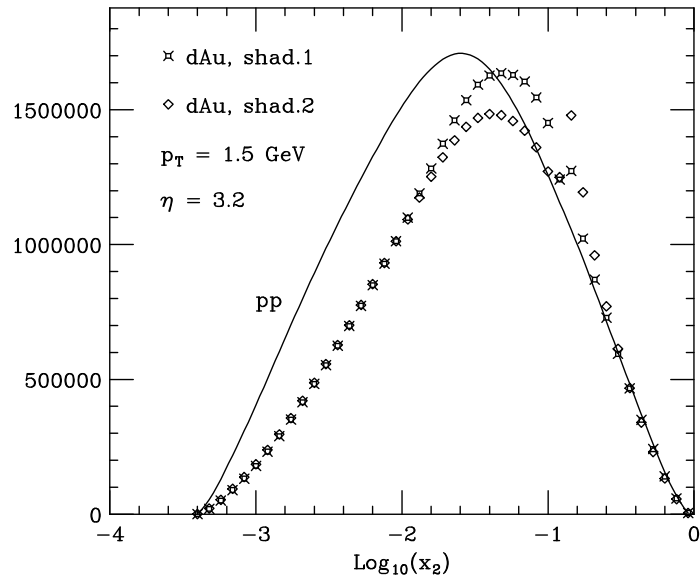


Figure B.4: Distribution of x_2 values in d -Au collisions at RHIC, in the perturbative framework of Ref. [116]. The solid line corresponds to p - p , shad. 1 and shad. 2 denote two different ways of obtaining the parton distributions of the Au nucleus. Plot taken from [116].

Appendix C

Definitions of gluon distributions

Here, we will give the relations between the unintegrated gluon densities in momentum space and co-ordinate space that are used in this thesis, and relate them to the dipole scattering amplitude $N(r_\perp, x)$. We will define these objects with respect to the integrated gluon distribution of section 2.3.2, $g(x, Q^2)$. We will not discuss the operator definitions of the gluon distributions, nor related issues such as their renormalization.

C.1 Unintegrated gluon distributions

In chapter 2 we have defined the unintegrated gluon distribution $\hat{g}(x, k_\perp^2)$ as follows,

$$xg(x, Q^2) \equiv \int^{Q^2} dk_\perp^2 \hat{g}(x, k_\perp^2). \quad (\text{C.1})$$

We then define the unintegrated gluon density in co-ordinate space, $\tilde{g}(x, r_\perp^2)$, as the Fourier transform of $\hat{g}(x, k_\perp^2)$,

$$\hat{g}(x, k_\perp^2) = \int d^2 r_\perp e^{ik_\perp \cdot r_\perp} \tilde{g}(x, r_\perp^2). \quad (\text{C.2})$$

We note that often the dimensionless unintegrated gluon distribution $\phi(x, k_\perp^2)/k_\perp^2 = \hat{g}(x, k_\perp^2)$ is used in the literature.

Further, from definition (C.1), we can find by differentiating with respect to Q^2 the following relation between the unintegrated and integrated gluon distributions,

$$\hat{g}(x, k_\perp^2) = \left. \frac{\partial xg(x, Q^2)}{\partial Q^2} \right|_{Q^2=k_\perp^2}. \quad (\text{C.3})$$

C.2. Limit of small r_\perp

C.2 Limit of small r_\perp

Using expression (C.3), we can find the relation between $g(x, Q^2)$ and $\tilde{g}(x, r_\perp^2)$ for small values of r_\perp^2 . We write the inverse transformation of (C.2),

$$\begin{aligned}\tilde{g}(x, r_\perp^2) &= \int \frac{d^2 k_\perp}{(2\pi)^2} e^{-ik_\perp r_\perp} \hat{g}(x, k_\perp^2) \\ &= \int \frac{d^2 k_\perp}{(2\pi)^2} e^{-ik_\perp r_\perp} \frac{\partial}{\partial k_\perp^2} xg(x, k_\perp^2),\end{aligned}\quad (\text{C.4})$$

where $g(x, k_\perp^2)$ means $g(x, Q^2 = k_\perp^2)$. Partial integration yields

$$\begin{aligned}\tilde{g}(x, r_\perp^2) &= \int \frac{dk_\perp^2}{4\pi} J_0(k_\perp r_\perp) \frac{\partial}{\partial k_\perp^2} xg(x, k_\perp^2) \\ &= - \int \frac{dk_\perp^2}{4\pi} \left(\frac{\partial}{\partial k_\perp^2} J_0(xk_\perp r_\perp) \right) xg(x, k_\perp^2),\end{aligned}\quad (\text{C.5})$$

where J_0 is the Bessel function of the first kind. For small values of r_\perp , we can now use [152] (the limit of $z \rightarrow \infty$ is equivalent to the limit of $x \rightarrow 0$)

$$J_0(\sqrt{zx}) \xrightarrow{z \gg 1} \theta(1/z - x), \quad (\text{C.6})$$

which gives

$$\begin{aligned}\tilde{g}(x, r_\perp^2) &\approx - \int \frac{dk_\perp^2}{4\pi} \left(\frac{\partial}{\partial k_\perp^2} \theta(1/k_\perp^2 - r_\perp^2) \right) xg(x, k_\perp^2) \\ &= \int \frac{dk_\perp^2}{4\pi} \delta(k_\perp^2 - 1/r_\perp^2) \frac{1}{r_\perp^2 k_\perp^2} xg(x, k_\perp^2) \\ &= \frac{1}{4\pi} xg(x, 1/r_\perp^2).\end{aligned}\quad (\text{C.7})$$

Thus, for small values of r_\perp , we have

$$\tilde{g}(x, r_\perp^2) \sim xg(x, Q^2 = 1/r_\perp^2). \quad (\text{C.8})$$

C.3 Relation with the dipole scattering amplitude

From Eq. (2.40), we know that for moderate values of $r_\perp^2 g$, the dipole amplitude N is related to the gluon density by

$$N(r_\perp, x_B) \sim \frac{r_\perp^2}{S_\perp} xg(x, Q^2 = 1/r_\perp^2), \quad (\text{C.9})$$

Appendix C. Definitions of gluon distributions

where S_\perp is the transverse size of the target hadron and x is an effective value of the longitudinal momentum fraction, cf. [36]. If r_\perp is not too large, Eqs. (C.8) and (C.9) imply that the dipole amplitude is also related to the unintegrated gluon density,

$$N(r_\perp, x_B) \sim \frac{r_\perp^2}{S_\perp} x \tilde{g}(x, r_\perp^2). \quad (\text{C.10})$$

Hence, up to logarithmic corrections, the dipole amplitude behaves in the limit of $r_\perp \rightarrow 0$ like

$$N(r_\perp, x) \sim r_\perp^2, \quad (\text{C.11})$$

where a factor of S_\perp that makes N dimensionless is left implicit, and we have dropped the subscript on x_B .

From Eq. (C.11), we can also find the large- k_\perp^2 tail of the dipole amplitude in momentum space. The regular Fourier transform of N is defined as

$$N(k_\perp, x) = \int d^2 r_\perp e^{ik_\perp \cdot r_\perp} N(r_\perp, x) = \pi \int_0^\infty dr_\perp^2 J_0(k_\perp r_\perp) N(r_\perp). \quad (\text{C.12})$$

If $k_\perp^2 \gg 1$, we can again use the approximation of Eq. (C.6) for the Bessel function, so that

$$\begin{aligned} N(k_\perp, x) &\xrightarrow{k_\perp \gg 1} \pi \int_0^{1/k_\perp^2} dr_\perp^2 N(r_\perp, x) \sim \int_0^{1/k_\perp^2} dr_\perp^2 r_\perp^2 \\ &\sim \frac{1}{k_\perp^4} \end{aligned} \quad (\text{C.13})$$

Likewise, the transform \mathcal{N} of chapter 7, cf. Eq. (7.1)

$$\mathcal{N}(k_\perp, x) = \int \frac{d^2 r_\perp}{2\pi} e^{ik_\perp \cdot r_\perp} \frac{N(r_\perp, x)}{r_\perp^2}, \quad (\text{C.14})$$

in the limit of large k_\perp^2 behaves like

$$\mathcal{N}(k_\perp, x) \sim \frac{1}{k_\perp^2}. \quad (\text{C.15})$$

Samenvatting

Dit proefschrift handelt over de structuur van materie bij zeer hoge energieën. Naar huidig inzicht is alle materie opgebouwd uit zogenaamde elementaire deeltjes, dat wil zeggen, deeltjes die zelf geen inwendige structuur hebben. De precieze samenstelling van materie in termen van deze elementaire deeltjes volgt uit de wisselwerkingen die tussen de elementaire deeltjes bestaan.

Materie blijkt te zijn opgebouwd uit atomen, welke bestaan uit een kern met daaromheen als het ware een wolk van elektronen. De negatief geladen elektronen zijn door de elektromagnetische wisselwerking aan de positief geladen kern gebonden. De atoomkern, waarin zich overigens vrijwel alle massa van het atoom bevindt, bestaat uit protonen, die de positieve lading van de kern dragen, en ongeladen neutronen. De protonen en neutronen zijn op hun beurt opgetrokken uit quarks en gluonen. De quarks dragen naast elektrische lading ook een zogenaamde kleurlading, die maakt dat ze onderhevig zijn aan de sterke wisselwerking. Deze sterke wisselwerking, die kan worden beschouwd als een analogon van de elektromagnetische wisselwerking, zorgt dat de quarks worden samengebonden tot deeltjes als bijvoorbeeld de protonen en neutronen, wat indirect ook tot gevolg heeft dat deze kerndeeltjes samen een atoomkern kunnen vormen. Naast de elektromagnetische en sterke wisselwerking kennen we de zwakke wisselwerking en de zwaartekracht. De zwaartekracht speelt doorgaans geen rol van betekenis bij de beschrijving van elementaire deeltjes, en wordt hier dan ook buiten beschouwing gelaten. De theoretische beschrijving van de elektromagnetische, de zwakke, en de sterke wisselwerking wordt gegeven door een quantumveldentheorie die bekend staat onder de naam “standaardmodel der elementaire deeltjes”. In een quantumveldentheorie bestaan deeltjes uit aangeslagen toestanden van een fundamenteel veld. De interactie tussen de deeltjes wordt gedragen door een ander veld, waarvan de aangeslagen toestanden ook deeltjes vormen. Zo wordt de elektromagnetische wisselwerking tussen geladen deeltjes overgebracht via het elektromagnetische veld, dat wil zeggen, door fotonen. Licht bestaat bijvoorbeeld uit dezelfde fotonen. Het deel van het standaardmodel dat de elektromagnetische wisselwerking beschrijft heet quantumelektrodynamica, ofwel QED. In dit proefschrift richten we ons met name op de structuur van de kerndeeltjes, en derhalve op de beschrijving van de sterke wisselwerking—de quantumchromodynamica, afgekort tot QCD. In QCD wordt de sterke wisselwerking gedragen door de zogenaamde gluonen. Deze kunnen worden beschouwd als familieleden van de fotonen uit QED, met als belangrijk verschil dat de gluonen zelf net als de quarks kleurlading dragen, terwijl de fotonen elektrisch ongeladen zijn. De

Samenvatting

gluonen interacteren dus niet slechts met de quarks, maar ook met elkaar. Dit maakt dat de wisselwerking tussen quarks en gluonen danig ingewikkelder is dan de wisselwerking tussen bijvoorbeeld elektronen.

QCD heeft de interessante eigenschap dat de interactie in kracht afneemt naarmate de wisselwerkende deeltjes dichter bij elkaar zitten, en juist sterker wordt wanneer deze verder van elkaar verwijderd zijn. Zodoende zitten quarks altijd samengebonden in zogenaamde hadronen, waarvan de kerndeeltjes een voorbeeld zijn. Ook zorgt deze eigenschap ervoor dat een bepaling van de precieze samenstelling van hadronen in termen van quarks en gluonen buiten de macht ligt van gebruikelijke rekenmethodes, die uitsluitend toepasbaar zijn wanneer de wisselwerking vrij zwak is. Dat is namelijk pas het geval op afstandsschalen die fors kleiner zijn dan de typische afmetingen van de hadronen zelf. De structuur van hadronen op dergelijke kleine afstandschalen kan worden bestudeerd in verstrooiingsexperimenten bij hoge energie. Een deeltje dat in botsing komt met een hadron verstrooit dan aan een quark of een gluon binnen het hadron. Om een dergelijk proces te kunnen beschrijven moeten we dus de dichtheid van quarks en gluonen binnen het hadron kennen. Hoewel we deze dichtheden niet direct uit de theorie kunnen bepalen, valt wel te berekenen hoe ze veranderen als de energie van de botsing verandert. De vergelijkingen die dit gedrag beschrijven worden wel evolutievergelijkingen genoemd. Als we dus uit een experiment hebben bepaald wat de dichtheden van de quarks en gluonen zijn, dan kunnen we met deze evolutievergelijkingen uitrekenen wat de dichtheden zullen zijn bij andere energieën.

Hierbij stuiten we echter op een theoretisch probleem. De evolutievergelijking die beschrijft hoe de gluondichtheid afhangt van de energie, de zogenaamde BFKL vergelijking, voorspelt namelijk dat bij zeer hoge energieën deze dichtheid zo snel stijgt dat de unitariteit van de theorie in het geding komt. Dat wil zeggen dat de kans om een gluon in het hadron aan te treffen groter kan worden dan 100%. Nu is een kans die groter is dan 100% absurd, dus moeten we wel concluderen dat bij dergelijke energieën effecten een rol gaan spelen die bij het opstellen van de BFKL vergelijking over het hoofd zijn gezien. We verwachten dat als de gluondichtheid eenmaal een kritieke waarde heeft bereikt de groei zal worden afgeremd, en wel zodanig dat unitariteit behouden blijft. Dit verschijnsel wordt gluonverzadiging genoemd, en de karakteristieke energieschaal waarbij dit gebeurt heet derhalve de verzadigingsschaal. In dit proefschrift wordt nader ingegaan op de vraag of gluonverzadiging een rol speelt bij energieën die kunnen worden bereikt in huidige deeltjesversnellers. Om dit te kunnen doen nemen we eerst de theoretische beschrijving van gluonverzadiging onder de loep.

Een evolutievergelijking die mogelijk een beschrijving van gluonverzadiging biedt is de zogenaamde BK vergelijking. Wanneer de gluondichtheid klein is, is deze vrijwel gelijk aan de BFKL vergelijking, maar als de dichtheid groot wordt voorspelt de BK vergelijking een tragere groei van de dichtheid dan de BFKL vergelijking. Nu wil het geval dat er vooralsnog geen exacte oplossingen van de BK vergelijking zijn gevonden. Wel zijn enige eigenschappen van de oplossing bepaald door deze te benaderen met verscheidene theoretische technieken. Vervolgens is er in de literatuur een aantal modellen opgesteld waarin deze theoretische eigenschappen zijn verwerkt, met als doel om deze te vergelijken met experimentele resultaten.

In dit proefschrift wordt bepaald in welke mate deze semi-theoretische eigenschappen nu eigenlijk in overeenstemming zijn met de BK vergelijking in onbenaderde vorm. Om dit te doen is gebruik gemaakt van numerieke oplossingen van de BK vergelijking, die kunnen worden vergeleken met bestaande modellen. Aldus is gebleken dat niet alle verwachte eigenschappen daadwerkelijk consistent zijn met de BK vergelijking.

Daarnaast wordt geanalyseerd of de eigenschappen van de oplossing van de BK vergelijking onderscheidbaar zijn in experimentele resultaten afkomstig van de deeltjesversneller RHIC, de Relativistic Heavy Ion Collider. In tegenstelling tot eerder gemaakte beweringen in de literatuur blijkt dit niet het geval te zijn. Dit wordt gedemonstreerd aan de hand van een nieuw model dat een belangrijke eigenschap heeft die voortvloeit uit gluonverzadiging, maar toch geen van de eigenschappen bezit die worden verwacht van BK evolutie. Dit model blijkt evenwel in staat tot het beschrijven van alle experimentele gegevens van RHIC die ons ter beschikking staan. We voorspellen echter dat de nieuwe versneller LHC, de Large Hadron Collider, dermate hoge energieën kan bereiken dat deze onderscheid zou kunnen maken tussen de bestaande modellen die zijn gebaseerd op BK evolutie en het nieuwe model. Zodoende kan worden bepaald of BK evolutie, en daarmee verzadiging van de gluondichtheid, mogelijk een rol speelt bij die energieën.

Tot slot volgt een analyse van de polarisatie van zogenaamde Λ -deeltjes, deeltjes die bestaan uit drie verschillende soorten quarks, welke kunnen worden geproduceerd in hadronische botsingsexperimenten. We laten zien dat deze polarisatie gevoelig is voor de verzadigingsschaal van de gluondichtheid in de botsende hadronen, zodanig dat deze schaal direct uit metingen zou kunnen worden gereconstrueerd. Uit onze analyse blijkt dat de verzadigingsschaal bij LHC naar verwachting groot genoeg is om op deze manier te worden waargenomen, mits de experimentele gegevens voldoende nauwkeurig zijn. Derhalve vormt de polarisatie van Λ -deeltjes een uitzonderlijk directe proef van het optreden van verzadiging in hadronische botsingen.

Dankwoord

Vanzelfsprekend zou dit proefschrift nooit kunnen zijn voltooid zonder de hulp van de talrijke personen die bij de totstandkoming van het geheel een rol hebben gespeeld. Van hen wil ik allereerst mijn copromotor Daniël Boer hartelijk bedanken voor zijn begeleiding. Met name vanwege je nooit aflatende enthousiasme en bereidheid tot het voeren van discussies—al dan niet gerelateerd aan het onderzoek, het feit dat je altijd aandacht had voor mij, en niet uitsluitend voor de resultaten, en je vermogen om me de motivatie te doen vinden om door te zetten heb ik onze samenwerking altijd als zeer prettig ervaren. Ik hoop dat het gemuggenzift over komma's hier en daar tijdens het schrijven van onze artikelen niet al te vermoeiend is geweest. Daarnaast gaat mijn dank natuurlijk ook uit naar mijn promotor Piet Mulders, voor de geboden ondersteuning en enthousiasme, en de plezierige momenten tijdens het geven van het vak quantummechanica.

To Andre Utermann I am greatly indebted for the pleasant collaboration that has led to the main results that are presented in this thesis, and also to results that are less suitable for being presented here, such as the distinction between Feuchtnasensaffen and Trockenasensaffen to name just one example. Without your help and the fun that I had working with you this thesis would not have been completed.

Of course, I would also like to thank the members of the reading committee, Ben Bakker, Adrian Dumitru, Eric Laenen, Ronald Kleiss and Andre Utermann for taking the time and effort to read the manuscript and providing me with valuable suggestions.

Wat verder van cruciaal belang is geweest voor de goede sfeer en het sociale leven op de universiteit is het in het gezelschap van collegae nuttigen van wat met enige neiging tot het eufemisme als een zwart bocht van beklagenswaardige kwaliteit kan worden omschreven. Gedurende deze koffiepauzes zijn, naast de onkunde van de componist des bochts, de meest uiteenlopende onderwerpen de revue gepasseerd, aldus de vastgelopen en vermoeide geesten der deelnemers weer van nieuwe krachten voorzienend. Voor het tot stand brengen van deze plezierige sfeer gaat mijn dank uit naar Klaas Allaart, Ben Bakker (met dank voor enige hulp van technische aard), Federica Bazzocchi, Henk Blok, Mathieu Blom, Cedran Bomhof (die met zijn encyclopedische kennis van muziek het niveau nog wat op peil wist te houden), Jorn Boomsma (alias de Hazesfan—mijn wereldbeeld zal nimmer nog hetzelfde zijn), Thomas van Dijk (hallo!), Jeroen Dreschler, Wilco den Dunnen, Hartmut Erzgräber, Kirk Green, Philipp Hägler, Marja Herronen, Miranda van Iersel, Christiaan Mantz, Sonia May, Fetze Pijlman, Cristian Pisano (grazie (rsv) mille), Ted Rogers, Hugo Schouten, Thijs Stegeman, Andre Utermann (again? Unacceptable!),

Dankwoord

Taco Visser en Harmen Warringa.

During my stay in Amsterdam I have been a member of a fine rock band that bears the name On Leaf of Absynthe (although Woolly Badger would have been a first class name as well). Many thanks to Alexis Gillett, Patrick Motylinski, Menelaos Tsiakiris, Wouter Vijvers and Chris White for lots of fun, craziness (maybe I should have added Marco to the list after all) and good times. And gentlemen, I apologize once more for failing to think through the consequences of hitting “reply all”.

Tot slot wil ik mijn familie en vrienden bedanken voor hun steun waarop ik altijd heb kunnen rekenen. Met name ben ik natuurlijk mijn dank verschuldigd aan Ashley.

Bibliography

- [1] C.-N. Yang and R. L. Mills, *Conservation of isotopic spin and isotopic gauge invariance*, Phys. Rev. **96**, 191 (1954)
- [2] L. D. Faddeev and V. N. Popov, *Feynman diagrams for the Yang-Mills field*, Phys. Lett. **B25**, 29 (1967)
- [3] G. 't Hooft and M. J. G. Veltman, *Combinatorics of gauge fields*, Nucl. Phys. **B50**, 318 (1972)
- [4] D. J. Gross and F. Wilczek, *Asymptotically Free Gauge Theories. 1*, Phys. Rev. **D8**, 3633 (1973)
- [5] D. J. Gross and F. Wilczek, *Asymptotically Free Gauge Theories. 2*, Phys. Rev. **D9**, 980 (1974)
- [6] H. D. Politzer, *Asymptotic Freedom: An Approach to Strong Interactions*, Phys. Rept. **14**, 129 (1974)
- [7] G. 't Hooft, *Renormalizable Lagrangians for massive Yang-Mills Fields*, Nucl. Phys. **B35**, 167 (1971)
- [8] G. 't Hooft and M. J. G. Veltman, *Regularization and Renormalization of Gauge Fields*, Nucl. Phys. **B44**, 189 (1972)
- [9] R. P. Feynman, *Very high-energy collisions of hadrons*, Phys. Rev. Lett. **23**, 1415 (1969)
- [10] V. N. Gribov and L. N. Lipatov, *Deep inelastic $e p$ scattering in perturbation theory*, Sov. J. Nucl. Phys. **15**, 438 (1972)
- [11] G. Altarelli and G. Parisi, *Asymptotic Freedom in Parton Language*, Nucl. Phys. **B126**, 298 (1977)
- [12] Y. L. Dokshitzer, *Calculation of the Structure Functions for Deep Inelastic Scattering and $e^+ e^-$ Annihilation by Perturbation Theory in Quantum Chromodynamics. (In Russian)*, Sov. Phys. JETP **46**, 641 (1977)
- [13] R. K. Ellis, W. J. Stirling and B. R. Webber, *QCD and Collider Physics* (Cambridge University Press)
- [14] H. L. Lai et al., *Global QCD analysis of parton structure of the nucleon: CTEQ5 parton distributions*, Eur. Phys. J. **C12**, 375 (2000), hep-ph/9903282
- [15] A. De Rujula et al., *Possible NonRegge Behavior of Electroproduction Structure Functions*, Phys. Rev. **D10**, 1649 (1974)

Bibliography

- [16] A. Babansky and I. Balitsky, *Scattering of color dipoles: From low to high energies*, Phys. Rev. **D67**, 054026 (2003), hep-ph/0212075
- [17] V. S. Fadin, E. A. Kuraev and L. N. Lipatov, *On the Pomeron Singularity in Asymptotically Free Theories*, Phys. Lett. **B60**, 50 (1975)
- [18] E. A. Kuraev, L. N. Lipatov and V. S. Fadin, *The Pomeron Singularity in Nonabelian Gauge Theories*, Sov. Phys. JETP **45**, 199 (1977)
- [19] I. I. Balitsky and L. N. Lipatov, *The Pomeron Singularity in Quantum Chromodynamics*, Sov. J. Nucl. Phys. **28**, 822 (1978)
- [20] J. Kwiecinski, *QCD expectations for deep inelastic scattering at small x* , J. Phys. **G19**, 1443 (1993)
- [21] F. Schrempp and A. Utermann, *QCD instantons and high-energy diffractive scattering*, Phys. Lett. **B543**, 197 (2002), hep-ph/0207300
- [22] M. M. Block, E. L. Berger and C.-I. Tan, *Small x behavior of parton distributions from the observed Froissart energy dependence of the deep inelastic scattering cross section*, Phys. Rev. Lett. **97**, 252003 (2006), hep-ph/0610296
- [23] M. Froissart, *Asymptotic behavior and subtractions in the Mandelstam representation*, Phys. Rev. **123**, 1053 (1961)
- [24] A. Martin, *Unitarity and high-energy behavior of scattering amplitudes*, Phys. Rev. **129**, 1432 (1963)
- [25] L. V. Gribov, E. M. Levin and M. G. Ryskin, *Semihard Processes in QCD*, Phys. Rept. **100**, 1 (1983)
- [26] E. Laenen and E. Levin, *A New evolution equation*, Nucl. Phys. **B451**, 207 (1995), hep-ph/9503381
- [27] I. Balitsky, *Operator expansion for high-energy scattering*, Nucl. Phys. **B463**, 99 (1996), hep-ph/9509348
- [28] I. Balitsky, *Factorization for high-energy scattering*, Phys. Rev. Lett. **81**, 2024 (1998), hep-ph/9807434
- [29] I. Balitsky, *Factorization and high-energy effective action*, Phys. Rev. **D60**, 014020 (1999), hep-ph/9812311
- [30] Y. V. Kovchegov, *Small- x F_2 structure function of a nucleus including multiple pomeron exchanges*, Phys. Rev. **D60**, 034008 (1999), hep-ph/9901281
- [31] J. Jalilian-Marian, A. Kovner and H. Weigert, *The Wilson renormalization group for low x physics: Gluon evolution at finite parton density*, Phys. Rev. **D59**, 014015 (1999), hep-ph/9709432
- [32] A. H. Mueller and B. Patel, *Single and double BFKL pomeron exchange and a dipole picture of high-energy hard processes*, Nucl. Phys. **B425**, 471 (1994), hep-ph/9403256
- [33] F. Gelis and J. Jalilian-Marian, *From DIS to proton nucleus collisions in the color glass condensate model*, Phys. Rev. **D67**, 074019 (2003), hep-ph/0211363
- [34] K. J. Golec-Biernat and M. Wüsthoff, *Saturation effects in deep inelastic scattering at low Q^2 and its implications on diffraction*, Phys. Rev. **D59**, 014017 (1999), hep-ph/9807513
- [35] A. H. Mueller, *Small x Behavior and Parton Saturation: A QCD Model*, Nucl. Phys. **B335**, 115 (1990)

Bibliography

- [36] Y. V. Kovchegov and A. H. Mueller, *Gluon production in current nucleus and nucleon nucleus collisions in a quasi-classical approximation*, Nucl. Phys. **B529**, 451 (1998), hep-ph/9802440
- [37] J. Jalilian-Marian and Y. V. Kovchegov, *Saturation physics and deuteron gold collisions at RHIC*, Prog. Part. Nucl. Phys. **56**, 104 (2006), hep-ph/0505052
- [38] R. J. Glauber, *Cross-sections in deuterium at high-energies*, Phys. Rev. **100**, 242 (1955)
- [39] A. H. Mueller, *Soft gluons in the infinite momentum wave function and the BFKL pomeron*, Nucl. Phys. **B415**, 373 (1994)
- [40] Z. Chen and A. H. Mueller, *The Dipole picture of high-energy scattering, the BFKL equation and many gluon compound states*, Nucl. Phys. **B451**, 579 (1995)
- [41] A. M. Stasto, *Nonlinear evolution equations in QCD*, Acta Phys. Polon. **B35**, 3069 (2004), hep-ph/0412084
- [42] P. F. Verhulst, *Recherches mathématiques sur la loi d'accroissement de la population*, Nouv. mm. de l'Academie Royale des Sci. et Belles-Lettres de Bruxelles **18** (1845)
- [43] P. F. Verhulst, *Recherches mathématiques sur la loi d'accroissement de la population*, Mém. de l'Academie Royale des Sci. des Lettres et des Beaux-Arts de Belgique **20** (1847)
- [44] E. Iancu, K. Itakura and L. McLerran, *Geometric scaling above the saturation scale*, Nucl. Phys. **A708**, 327 (2002), hep-ph/0203137
- [45] A. M. Stasto, K. J. Golec-Biernat and J. Kwiecinski, *Geometric scaling for the total $\gamma^* p$ cross-section in the low x region*, Phys. Rev. Lett. **86**, 596 (2001), hep-ph/0007192
- [46] A. Dumitru and J. Jalilian-Marian, *Forward quark jets from protons shattering the colored glass*, Phys. Rev. Lett. **89**, 022301 (2002), hep-ph/0204028
- [47] A. Dumitru, A. Hayashigaki and J. Jalilian-Marian, *The color glass condensate and hadron production in the forward region*, Nucl. Phys. **A765**, 464 (2006), hep-ph/0506308
- [48] A. Dumitru, A. Hayashigaki and J. Jalilian-Marian, *Geometric scaling violations in the central rapidity region of $d + Au$ collisions at RHIC*, Nucl. Phys. **A770**, 57 (2006), hep-ph/0512129
- [49] L. D. McLerran and R. Venugopalan, *Computing quark and gluon distribution functions for very large nuclei*, Phys. Rev. **D49**, 2233 (1994), hep-ph/9309289
- [50] L. D. McLerran and R. Venugopalan, *Gluon distribution functions for very large nuclei at small transverse momentum*, Phys. Rev. **D49**, 3352 (1994), hep-ph/9311205
- [51] L. D. McLerran and R. Venugopalan, *Green's functions in the color field of a large nucleus*, Phys. Rev. **D50**, 2225 (1994), hep-ph/9402335
- [52] J. Jalilian-Marian, A. Kovner, A. Leonidov and H. Weigert, *The BFKL equation from the Wilson renormalization group*, Nucl. Phys. **B504**, 415 (1997), hep-ph/9701284
- [53] J. Jalilian-Marian, A. Kovner, A. Leonidov and H. Weigert, *The Wilson renormalization group for low x physics: Towards the high density regime*, Phys. Rev. **D59**, 014014 (1999), hep-ph/9706377
- [54] E. Iancu, A. Leonidov and L. D. McLerran, *Nonlinear gluon evolution in the color glass condensate. I*, Nucl. Phys. **A692**, 583 (2001), hep-ph/0011241
- [55] E. Ferreiro, E. Iancu, A. Leonidov and L. McLerran, *Nonlinear gluon evolution in the color glass condensate. II*, Nucl. Phys. **A703**, 489 (2002), hep-ph/0109115

Bibliography

- [56] K. Rummukainen and H. Weigert, *Universal features of JIMWLK and BK evolution at small x* , Nucl. Phys. **A739**, 183 (2004), hep-ph/0309306
- [57] D. Boer and A. Dumitru, *Polarized hyperons from p A scattering in the gluon saturation regime*, Phys. Lett. **B556**, 33 (2003), hep-ph/0212260
- [58] E. Iancu, A. Leonidov and L. McLerran, *The colour glass condensate: An introduction* (2002), hep-ph/0202270
- [59] E. Iancu and R. Venugopalan, *The color glass condensate and high energy scattering in QCD* (2003), hep-ph/0303204
- [60] E. Iancu, *Cronin effect and high- p_T suppression from the color glass condensate*, AIP Conf. Proc. **739**, 362 (2005), hep-ph/0408228
- [61] H. Weigert, *Evolution at small x_{bj} : The color glass condensate*, Prog. Part. Nucl. Phys. **55**, 461 (2005), hep-ph/0501087
- [62] E. Fermi, *On the Theory of the impact between atoms and electrically charged particles*, Z. Phys. **29**, 315 (1924)
- [63] C. F. von Weizsacker, *Radiation emitted in collisions of very fast electrons*, Z. Phys. **88**, 612 (1934)
- [64] E. J. Williams, Proc. Roy. Soc. **A139**, 163 (1933)
- [65] E. J. Williams, Kgl. Dansk. Vid. Selsk. **13** (1935)
- [66] Y. V. Kovchegov, *Non-Abelian Weizsaecker-Williams field and a two- dimensional effective color charge density for a very large nucleus*, Phys. Rev. **D54**, 5463 (1996), hep-ph/9605446
- [67] R. Jackiw, D. N. Kabat and M. Ortiz, *Electromagnetic fields of a massless particle and the eikonal*, Phys. Lett. **B277**, 148 (1992), hep-th/9112020
- [68] A. J. Baltz, F. Gelis, L. D. McLerran and A. Peshier, *Coulomb corrections to $e^+ e^-$ production in ultra- relativistic nuclear collisions*, Nucl. Phys. **A695**, 395 (2001), nucl-th/0101024
- [69] A. Dumitru and J. Jalilian-Marian, *Forward quark jets from protons shattering the colored glass*, Phys. Rev. Lett. **89**, 022301 (2002), hep-ph/0204028
- [70] F. Gelis and A. Peshier, *Probing colored glass via q anti- q photoproduction*, Nucl. Phys. **A697**, 879 (2002), hep-ph/0107142
- [71] J. Jalilian-Marian, S. Jeon and R. Venugopalan, *Wong's equations and the small x effective action in QCD*, Phys. Rev. **D63**, 036004 (2001), hep-ph/0003070
- [72] Y. V. Kovchegov, *Unitarization of the BFKL pomeron on a nucleus*, Phys. Rev. **D61**, 074018 (2000), hep-ph/9905214
- [73] A. H. Mueller, *Unitarity and the BFKL pomeron*, Nucl. Phys. **B437**, 107 (1995), hep-ph/9408245
- [74] R. Baier, Y. L. Dokshitzer, A. H. Mueller, S. Peigne and D. Schiff, *Radiative energy loss and p_T -broadening of high energy partons in nuclei*, Nucl. Phys. **B484**, 265 (1997), hep-ph/9608322
- [75] S. Munier and R. B. Peschanski, *Traveling wave fronts and the transition to saturation*, Phys. Rev. **D69**, 034008 (2004), hep-ph/0310357
- [76] A. H. Mueller and D. N. Triantafyllopoulos, *The energy dependence of the saturation momentum*, Nucl. Phys. **B640**, 331 (2002), hep-ph/0205167

Bibliography

- [77] E. Levin and K. Tuchin, *Solution to the evolution equation for high parton density QCD*, Nucl. Phys. **B573**, 833 (2000), hep-ph/9908317
- [78] S. Munier and R. B. Peschanski, *Geometric scaling as traveling waves*, Phys. Rev. Lett. **91**, 232001 (2003), hep-ph/0309177
- [79] C. Marquet, R. B. Peschanski and G. Soyez, *Traveling waves and geometric scaling at non-zero momentum transfer*, Nucl. Phys. **A756**, 399 (2005), hep-ph/0502020
- [80] C. Marquet, R. B. Peschanski and G. Soyez, *QCD traveling waves at non-asymptotic energies*, Phys. Lett. **B628**, 239 (2005), hep-ph/0509074
- [81] M. Kozlov and E. Levin, *Solution to the Balitsky-Kovchegov equation in the saturation domain*, Nucl. Phys. **A764**, 498 (2006), hep-ph/0504146
- [82] M. Braun, *Structure function of the nucleus in the perturbative QCD with $N(c) \rightarrow \infty$ (BFKL pomeron fan diagrams)*, Eur. Phys. J. **C16**, 337 (2000), hep-ph/0001268
- [83] M. Braun, *High-energy interaction with the nucleus in the perturbative QCD with $N_c \rightarrow \infty$* (2001), hep-ph/0101070v2
- [84] M. Lublinsky, *Scaling phenomena from non-linear evolution in high energy DIS*, Eur. Phys. J. **C21**, 513 (2001), hep-ph/0106112
- [85] M. Lublinsky, E. Gotsman, E. Levin and U. Maor, *Non-linear evolution and parton distributions at LHC and THERA energies*, Nucl. Phys. **A696**, 851 (2001), hep-ph/0102321
- [86] N. Armesto and M. A. Braun, *Parton densities and dipole cross-sections at small x in large nuclei*, Eur. Phys. J. **C20**, 517 (2001), hep-ph/0104038
- [87] E. Levin and M. Lublinsky, *Parton densities and saturation scale from non-linear evolution in DIS on nuclei*, Nucl. Phys. **A696**, 833 (2001), hep-ph/0104108
- [88] K. J. Golec-Biernat, L. Motyka and A. M. Stasto, *Diffusion into infra-red and unitarization of the BFKL pomeron*, Phys. Rev. **D65**, 074037 (2002), hep-ph/0110325
- [89] R. Enberg, K. J. Golec-Biernat and S. Munier, *The high energy asymptotics of scattering processes in QCD*, Phys. Rev. **D72**, 074021 (2005), hep-ph/0505101
- [90] R. Enberg, *BKsolver: numerical solution of the Balitsky-Kovchegov nonlinear integro-differential equation*, <http://www.isv.uu.se/~enberg/BK/>
- [91] M. Bramson, *Convergence of solutions of the Kolmogorov equation to travelling waves* (American Mathematical Society, Providence, 1983)
- [92] R. A. Fisher, *The wave of advance of advantageous genes*, Ann. Eugenics **7**, 353 (1937)
- [93] K. A., I. Petrovskii and N. Piscounov, *A study of the diffusion equation with increase in the amount of substance, and its application to a biological problem*, Bull. Moscow Univ., Math. **A1**, 1 (1937)
- [94] D. Kharzeev, Y. V. Kovchegov and K. Tuchin, *Nuclear modification factor in $d + Au$ collisions: Onset of suppression in the color glass condensate*, Phys. Lett. **B599**, 23 (2004), hep-ph/0405045
- [95] J. T. de Santana Amaral, M. B. Gay Ducati, M. A. Betemps and G. Soyez, *$\gamma^* p$ cross section from the dipole model in momentum space*, Phys. Rev. **D76**, 094018 (2007), hep-ph/0612091
- [96] L. Motyka, K. Golec-Biernat and G. Watt, *Dipole models and parton saturation in ep scattering* (2008), 0809.4191 [hep-ph]

- [97] V. P. Goncalves, M. S. Kugeratski, M. V. T. Machado and F. S. Navarra, *Saturation physics at HERA and RHIC: An unified description*, Phys. Lett. **B643**, 273 (2006), hep-ph/0608063
- [98] F. Gelis, R. B. Peschanski, G. Soyez and L. Schoeffel, *Systematics of geometric scaling*, Phys. Lett. **B647**, 376 (2007), hep-ph/0610435
- [99] J. Bartels, K. J. Golec-Biernat and H. Kowalski, *A modification of the saturation model: DGLAP evolution*, Phys. Rev. **D66**, 014001 (2002), hep-ph/0203258
- [100] E. Gotsman, E. Levin, M. Lublinsky and U. Maor, *Towards a new global QCD analysis: Low x DIS data from non-linear evolution*, Eur. Phys. J. **C27**, 411 (2003), hep-ph/0209074
- [101] E. Iancu, K. Itakura and S. Munier, *Saturation and BFKL dynamics in the HERA data at small x* , Phys. Lett. **B590**, 199 (2004), hep-ph/0310338
- [102] J. Kwiecinski and A. M. Stasto, *Geometric scaling and QCD evolution*, Phys. Rev. **D66**, 014013 (2002), hep-ph/0203030
- [103] F. Caola and S. Forte, *Geometric Scaling from GLAP evolution*, Phys. Rev. Lett. **101**, 022001 (2008), hep-ph/0802.1878
- [104] R. D. Ball and S. Forte, *Double asymptotic scaling at HERA*, Phys. Lett. **B335**, 77 (1994), hep-ph/9405320
- [105] K. J. Eskola, H. Honkanen, V. J. Kolhinen, J.-w. Qiu and C. A. Salgado, *Nonlinear corrections to the DGLAP equations in view of the HERA data*, Nucl. Phys. **B660**, 211 (2003), hep-ph/0211239
- [106] B. Jager, A. Schafer, M. Stratmann and W. Vogelsang, *Next-to-leading order QCD corrections to high- p_T pion production in longitudinally polarized $p p$ collisions*, Phys. Rev. **D67**, 054005 (2003), hep-ph/0211007
- [107] K. J. Eskola and H. Honkanen, *A perturbative QCD analysis of charged-particle distributions in hadronic and nuclear collisions*, Nucl. Phys. **A713**, 167 (2003), hep-ph/0205048
- [108] K. J. Eskola, H. Honkanen, H. Niemi, P. V. Ruuskanen and S. S. Rasanen, *RHIC-tested predictions for low- p_T and high- p_T hadron spectra in nearly central Pb + Pb collisions at the LHC*, Phys. Rev. **C72**, 044904 (2005), hep-ph/0506049
- [109] F. Gelis, <http://ipht.cea.fr/Images/Pisp/fgelis/Soft/Saturation/>
- [110] J. Jalilian-Marian, A. Kovner, L. D. McLerran and H. Weigert, *The intrinsic glue distribution at very small x* , Phys. Rev. **D55**, 5414 (1997), hep-ph/9606337
- [111] K. J. Golec-Biernat and A. M. Stasto, *On solutions of the Balitsky-Kovchegov equation with impact parameter*, Nucl. Phys. **B668**, 345 (2003), hep-ph/0306279
- [112] E. Gotsman, M. Kozlov, E. Levin, U. Maor and E. Naftali, *Towards a new global QCD analysis: Solution to the non-linear equation at arbitrary impact parameter*, Nucl. Phys. **A742**, 55 (2004), hep-ph/0401021
- [113] J. L. Albacete, N. Armesto, J. G. Milhano, C. A. Salgado and U. A. Wiedemann, *Numerical analysis of the Balitsky-Kovchegov equation with running coupling: Dependence of the saturation scale on nuclear size and rapidity*, Phys. Rev. **D71**, 014003 (2005), hep-ph/0408216
- [114] C. Marquet and G. Soyez, *The Balitsky-Kovchegov equation in full momentum space*, Nucl. Phys. **A760**, 208 (2005), hep-ph/0504080
- [115] Y. V. Kovchegov and H. Weigert, *Triumvirate of running couplings in small- x evolution*, Nucl. Phys. **A784**, 188 (2007), hep-ph/0609090

Bibliography

- [116] V. Guzey, M. Strikman and W. Vogelsang, *Observations on d A scattering at forward rapidities*, Phys. Lett. **B603**, 173 (2004), hep-ph/0407201
- [117] D. Kharzeev, E. Levin and L. McLerran, *Parton saturation and N (part) scaling of semi-hard processes in QCD*, Phys. Lett. **B561**, 93 (2003), hep-ph/0210332
- [118] D. Kharzeev, Y. V. Kovchegov and K. Tuchin, *Cronin effect and high- p_T suppression in p A collisions*, Phys. Rev. **D68**, 094013 (2003), hep-ph/0307037
- [119] J. L. Albacete, N. Armesto, A. Kovner, C. A. Salgado and U. A. Wiedemann, *Energy dependence of the Cronin effect from non-linear QCD evolution*, Phys. Rev. Lett. **92**, 082001 (2004), hep-ph/0307179
- [120] R. Baier, A. Kovner and U. A. Wiedemann, *Saturation and parton level Cronin effect: Enhancement vs suppression of gluon production in p A and A A collisions*, Phys. Rev. **D68**, 054009 (2003), hep-ph/0305265
- [121] D. Kharzeev, E. Levin and M. Nardi, *QCD saturation and deuteron nucleus collisions*, Nucl. Phys. **A730**, 448 (2004), hep-ph/0212316
- [122] D. Boer, A. Dumitru and A. Hayashigaki, *Single transverse-spin asymmetries in forward pion production at high energy: Incorporating small- x effects in the target*, Phys. Rev. **D74**, 074018 (2006), hep-ph/0609083
- [123] Y. V. Kovchegov, *Quantum structure of the non-Abelian Weizsaecker-Williams field for a very large nucleus*, Phys. Rev. **D55**, 5445 (1997), hep-ph/9701229
- [124] J. Adams et al., *Evidence from $d + Au$ measurements for final-state suppression of high p_T hadrons in $Au + Au$ collisions at RHIC*, Phys. Rev. Lett. **91**, 072304 (2003), nucl-ex/0306024
- [125] I. Arsene et al., *On the evolution of the nuclear modification factors with rapidity and centrality in $d + Au$ collisions at $s(NN)^{1/2} = 200$ -GeV*, Phys. Rev. Lett. **93**, 242303 (2004), nucl-ex/0403005
- [126] J. Adams et al., *Forward neutral pion production in $p+p$ and $d+Au$ collisions at $s(NN)^{1/2} = 200$ -GeV*, Phys. Rev. Lett. **97**, 152302 (2006), nucl-ex/0602011
- [127] B. A. Kniehl, G. Kramer and B. Potter, *Fragmentation functions for pions, kaons, and protons at next-to-leading order*, Nucl. Phys. **B582**, 514 (2000), hep-ph/0010289
- [128] C. Adloff et al., *Deep-inelastic inclusive $e p$ scattering at low x and a determination of α_s* , Eur. Phys. J. **C21**, 33 (2001), hep-ex/0012053
- [129] J. Breitweg et al., *Measurement of the proton structure function F_2 at very low Q^2 at HERA*, Phys. Lett. **B487**, 53 (2000), hep-ex/0005018
- [130] S. Chekanov et al., *Measurement of the neutral current cross section and F_2 structure function for deep inelastic $e+p$ scattering at HERA*, Eur. Phys. J. **C21**, 443 (2001), hep-ex/0105090
- [131] E. Avsar and G. Gustafson, *Geometric scaling and QCD dynamics in DIS*, JHEP **04**, 067 (2007), hep-ph/0702087
- [132] D. G. d'Enterria, *Low- x QCD physics from RHIC and HERA to the LHC*, Eur. Phys. J. **A31**, 816 (2007), hep-ex/0610061
- [133] J. C. Collins, *Light-cone variables, rapidity and all that* (1997), hep-ph/9705393
- [134] R. Baier, Y. Mehtar-Tani and D. Schiff, *Has saturation physics been observed in deuteron gold collisions at RHIC?*, Nucl. Phys. **A764**, 515 (2006), hep-ph/0508026

- [135] M. A. Betemps and V. P. Goncalves, *Hadron and Photon Production in the Forward Region at RHIC and LHC*, JHEP **09**, 019 (2008), 0806.1467 [hep-ph]
- [136] K. Tuchin, *Forward hadron production in high energy pA collisions: From RHIC to LHC*, Nucl. Phys. **A798**, 61 (2008), 0705.2193 [hep-ph]
- [137] E. Iancu, C. Marquet and G. Soyez, *Forward gluon production in hadron hadron scattering with Pomeron loops*, Nucl. Phys. **A780**, 52 (2006), hep-ph/0605174
- [138] P. J. Mulders and R. D. Tangerman, *The complete tree-level result up to order $1/Q$ for polarized deep-inelastic leptonproduction*, Nucl. Phys. **B461**, 197 (1996), hep-ph/9510301
- [139] M. Anselmino, D. Boer, U. D'Alesio and F. Murgia, *Lambda polarization from unpolarized quark fragmentation*, Phys. Rev. **D63**, 054029 (2001), hep-ph/0008186
- [140] M. Anselmino, D. Boer, U. D'Alesio and F. Murgia, *Transverse Lambda polarization in semi-inclusive DIS*, Phys. Rev. **D65**, 114014 (2002), hep-ph/0109186
- [141] D. de Florian, M. Stratmann and W. Vogelsang, *QCD analysis of unpolarized and polarized Lambda baryon production in leading and next-to-leading order*, Phys. Rev. **D57**, 5811 (1998), hep-ph/9711387
- [142] M. Anselmino, D. Boer, U. D'Alesio and F. Murgia, *Transverse Lambda polarization in semi-inclusive DIS* (2002), hep-ph/0109186v1
- [143] A. Lesnik et al., *Observation of a Difference Between Polarization and Analyzing Power in Λ^0 Production with 6-GeV/c Polarized Protons*, Phys. Rev. Lett. **35**, 770 (1975)
- [144] G. Bunce et al., *Λ^0 Hyperon Polarization in Inclusive Production by 300-GeV Protons on Beryllium*, Phys. Rev. Lett. **36**, 1113 (1976)
- [145] A. D. Panagiotou, *Λ^0 polarization in hadron-nucleon, hadron-nucleus and nucleus-nucleus interactions*, Int. J. Mod. Phys. **A5**, 1197 (1990)
- [146] L. C. Bland, *private communication*.
- [147] T. Ullrich, *The Emerging QCD Frontier: The Electron Ion Collider*, J. Phys. **G35**, 104041 (2008), 0806.0048 [hep-ph]
- [148] A. H. Mueller, *Parton saturation at small x and in large nuclei*, Nucl. Phys. **B558**, 285 (1999), hep-ph/9904404
- [149] D. N. Triantafyllopoulos, *The energy dependence of the saturation momentum from RG improved BFKL evolution*, Nucl. Phys. **B648**, 293 (2003), hep-ph/0209121
- [150] D. Boer, C. J. Bomhof, D. S. Hwang and P. J. Mulders, *Spin asymmetries in jet-hyperon production at LHC*, Phys. Lett. **B659**, 127 (2008), 0709.1087 [hep-ph]
- [151] A. Accardi, *Cronin effect from backward to forward rapidity: A tale of two mysteries*, Acta Phys. Hung. **A22**, 289 (2005), nucl-th/0405046
- [152] S. D. Ellis, N. Fleishon and W. J. Stirling, *Logarithmic approximations, quark form-factors and quantum chromodynamics*, Phys. Rev. **D24**, 1386 (1981)

